ECOLE DOCTORALE ED352 : PHYSIQUE ET SCIENCES DE LA MATIERE

Discipline : Astrophysique et Cosmologie

Thèse présentée pour obtenir le grade universitaire de docteur

Nicolas PESCHKEN

Formation and evolution of galactic discs

Soutenue le 03/11/2016 devant le jury :

Philippe AMRAM	Laboratoire d'Astrophysique de Marseille	Directeur du jury
François HAMMER	GEPI Observatoire de Paris	Rapporteur
Olivier BIENAYME	Observatoire Astronomique de Strasbourg	Rapporteur
Carlos GARCIA GOMEZ	Universitat Rovira i Virgili	Examinateur
Albert BOSMA	Laboratoire d'Astrophysique de Marseille	Examinateur
Evangelie ATHANASSOULA	Laboratoire d'Astrophysique de Marseille	Directeur de thèse

Aknowledgments

I first want to thank my supervisor, Lia Athanassoula, for following, helping and supporting me consistently during these three years of PhD. She has been very present and available for me, allowed me to study many different and interesting aspects of galaxy simulations, and I learned a lot by working with her.

I would also like to thank the other people in our team, who were always very helpful when I needed it. Jean-Charles Lambert has been essential as the skillfull computer engineer of the group, and besides having developped or installed most softwares I was using, he has helped me countless times for fixing bugs or helping me with my codes, as I would drop by his office saying "It doesn't work!". Sergey Rodionov has always been available to help me with physics issues or giving me some of his codes to save time. I also want to thank Albert Bosma for helping me with my postodc applications, by patiently reviewing and correcting all my documents.

I also thank Marie Treyer for taking the time to listen about my research progress, and caring about the good proceeding of my PhD.

I would like to express my gratitude to the jury members Carlos Garcia Gomez, Philippe Amram and Albert Bosma for accepting to be part of my thesis committee, and especially to François Hammer and Olivier Bienaymé for their careful reading of my thesis, as well as their useful comments.

I want to thank all the PhD students, postdocs or interns, with which we would meet every day for lunch breaks, wich allowed me to chill out and stop thinking about work. They have truly become friends and have contributed very much to the excellent atmosphere I was feeling in the laboratory. Here are the names of some of them (I apologize for the ones I forgot) : Mario, Anna, Pedro, Miguel, David, Anna, Darko, Samuel, Javier, Ana, Marie, Axel, Deborah, Sergey, Grzegorz, Arthuro, Loren, Francesca, ...

Finally, a very special thanks Pauline for her love, support and patience during these three years. I asked her to follow me in the South for two years and she accepted without hesitation. She has always been here to hear me talk about my

PhD over and over again, in good and in bad times, and never complained once. I could not ask for more.

Contents

List of Figures

Introduction

The Milky Way has fascinated humanity for thousands of years, being very easy to observe in the night sky with its bright band shape. Already in the ancient Greece, philosophers such as Democritus (460–370 BCE) or Aristotle (384–322 BCE) were trying to understand what was this particular structure. They gave it the greek name *Galaxias*, which can be translated as *Milky One*, and the hypothesis of an agglomeration of distant stars was already proposed. Nervertheless, it was not until 1610 that this was finally proven by Galileo, using one of the first telescopes. The picture of the Milky Way being a rotating disc then first appears in 1750 with Thomas Wright, an english astronomer, as well as the idea that the solar system is part of it. The question of the formation and structure of the Milky Way thus becomes essential, since it is the big structure that allowed the creation of the Solar System, and the Earth. In the following centuries – and especially in the beginning of the 20^{th} century – this gradually led to the current view of the Milky Way, as being an *island universe* independent from other galaxies such as Andromeda.

We now know that the Milky Way is a spiral galaxy (as classified by Hubble in 1936), with a thin and a thick disc, a central bar, and a bulge with a boxy shape. We know approximately its size and mass, as well as the fact that the Sun is located at the periphery of the disc, in a spiral arm which is the bright band structure observed in the sky. We are thus much more aware of the Milky Way than the ancient Greeks were, but there are still a number of open questions remaining. How was the Milky Way created? Did it experience mergers in its history? Does it have a central classical bulge? What is the structure of its disc, in particular in the outer parts? How was the thick disc created? The main difficulty comes from the fact that we can only observe the Milky Way from the inside, from the position of the Sun, and only at a given time. This gives us a great precision on the stellar population of the solar neighborhood, but prevents us to clearly see other areas of our Galaxy, which are hidden by the objects surrounding us. In particular, dust clouds absorb the light going through them, preventing us to see what lies behind them. Objects vertically out of the disc can usually be observed with ease, but inside the thin disc our line of sight is limited. Although we continuously improve the resolution and depth of observations in the Milky Way, for example with the GAIA mission, we are still not able to have

a global picture of our Galaxy as reliable as for local external galaxies. The latter are much farther away, but can be observed as a whole, the intergalactic medium being almost empty compared to the solar vicinity.
In view of the above, it becomes clear that to understand the formation and structure of our Galaxy, we can use observations of external galaxies. The Milky Way is not unique, and disc galaxies with similar size and shape are very common in the Universe. By investigating how external galaxies formed, we can deduce how our own Galaxy was created. Furthermore, the light travelling at a limited speed, the farther we look, the younger the universe is, which allows us to look at galaxies of different ages. While we can only look at the Milky Way at the present time, with external galaxies we are able to see galaxies at different steps of their life, which helps us understanding how they formed and evolved. This approach has led to great progress in the knowledge of the structures and substructures of the universe since its creation. Thanks to the analysis of external galaxies, we discovered the presence of an invisible matter, called *dark matter*, which plays a decisive role in the creation of galaxies. This dark matter was discovered by Zwicky in 1933, by studying the velocity dispersion of galaxies in the Coma cluster, and led to the conclusion that the baryonic matter alone could not explain the observed velocities of these galaxies. We now know that this dark matter is present everywhere in the Universe in much higher quantity (or mass) than the baryonic matter, that it is collisionless, and mostly concentrated in galaxies, including ours. This is just one example of what the study of external galaxies can teach us about the Milky Way, and the Universe in general. This affects other research fields as well, since particle physicists are now trying to understand the nature of dark matter, using its properties derived from astronomical observations.

Furthermore, this dark matter is now believed to be the essential component allowing galaxies to form. Here is the current picture of how galaxies formed in the ΛCDM theory. Dark matter was first nearly homogeneously distributed in the universe, with only small local perturbations. Nevertheless, these inhomogeneities then grew due to gravitational forces, and dark matter concentrated hierarchically into filament structures, attracting gas into it. In the most concentrated parts of the filaments, this led to haloes of dark matter and gas in rotation, being the progenitors of the first galaxies. The gas in rotation cooled and fell inwards, forming a disc reaching concentrations allowing the birth of the first stars. This is how disc galaxies such as ours are thought to be born, from initially intergalactic gas attracted into dark matter haloes. The construction of this scenario was again allowed by observations of external galaxies being very far away (at high redshift), but also by running numerous simulations able to virtually reproduce this scenario. This is an important point, since the influence of simulations in astrophysics has kept growing in the last decades, as well as their resolution and the number of physical processes they include. This has led

to great progress in our knowledge of the universe, for example in cosmology or galaxy formation, where simulations are an indispensable tool nowadays, at the same level as observations. In simulations, galaxies can evolve over time, they can be seen under any line of sight, and their content, shape and velocity field are precisely known. This makes galaxy simulations an incredible asset to investigate how galaxies such as the Milky Way were formed. Nevertheless, the results must be taken with caution, since simulations are only an approximation of the reality, and their reliability depends on the quality of the physics and the initial conditions included in the model. This is why simulations need observations to confirm their findings, both being complementary.

Although the galaxy formation scenario described above works very well to explain how the first galaxies were born, it can not alone account for the diversity in masses, shapes and structures of the galaxies observed in the local Universe. In particular, some peculiar galaxies such as the Cartwheel Galaxy cannot be created by a simple halo of gas cooling down. To explain the formation of such bizarre structures, one has to invoke other mechanisms, and in particular the interaction and merger of galaxies. Galaxies are in constant movement in the expanding Universe, can be part of galaxy clusters, and are thus able to gravitationally interact, or even collide with each other. These merger events were very frequent when the Universe was young (at high redshift), and can consist in a big galaxy absorbing a smaller one (*minor merger*), or two galaxies of similar masses in collision. The latter case is called a *major merger*, and is a very violent event during which galaxies can totally change shape and structure, forming a new galaxy, called *remnant* galaxy. Studying the outcome (the remnant) of a major merger between two galaxies is crucial, since most local galaxies (potentially including the Milky Way) are thought to be the product of at least one major merger (Hammer, Flores, Puech, et al., 2009). To do this, simulations are a very useful tool, since they allow us to follow dynamically and morphologically the evolution of the merger and the creation of the remnant. Nevertheless, simulations sometimes happen to be in contradiction with observations, as it is the case for the result of a major merger between two disc galaxies. Such mergers were first believed to form elliptical galaxies (A. Toomre and J. Toomre, 1972), but observations at intermediate redshifts (e.g. Hammer, Flores, Yang, et al., 2009, Hammer, Flores, Puech, et al., 2009) recently showed that the remnant of the major merger of two gas-rich disc galaxies is actually a disc galaxy. In the meantime, simulations studied this particular problem, but were not able to produce extended discs such as in the local spiral galaxies. They found that the remnant could indeed have a disc component (e.g. Barnes, 2002, Springel and Hernquist, 2005, Cox, Jonsson, Primack, et al., 2006, Hopkins, Cox, Younger, et al., 2009, Borlaff, Eliche-Moral, Rodríguez-Pérez, et al., 2014), but with a small mass rather corresponding to a lenticular galaxy. The question of how to produce spiral galaxies in major mergers is thus still open.

During my PhD, I worked on simulations of galaxies created by merging two gas-rich disc galaxies. These simulations allowed us to show for the first time how to obtain a spiral galaxy from a major merger. In my work, I analyzed the morphological, dynamical and structural properties of the remnant galaxy in our simulations, with an emphasis on the surface density profile. Here is the outline of this thesis.

The first part presents the general properties of the remnant galaxy obtained from the major merger. I start with some global context about galaxies, with the Hubble sequence and the properties of disc galaxies. I then focus on our simulations, by presenting the main paper introducing them, studying the stellar migration, and computing the bar pattern speed.

In the second part, I focus on the study of the surface density profile of the remnant galaxies obtained in our simulations. I start again with some context about surface density profiles in disc galaxies, by describing the observations, and the bulge, bar and disc part of the profile. I then present my results in the next section, using two and one-dimensional density distributions, looking at the inner regions and the disc part, and finally studying the thick disc profile.

I. Study of simulated disc galaxies

1. Context

1.1. The Hubble sequence

Soon after the discovery of the first galaxies, observations showed that they could be of very different shape, size, luminosity and morphology.
The Hubble sequence is a way to classify them, according to their morphology (figure 1.1). It was invented by Edwin Hubble in 1926.
Hereafter I make a short presentation for each category of galaxies in the Hubble sequence.

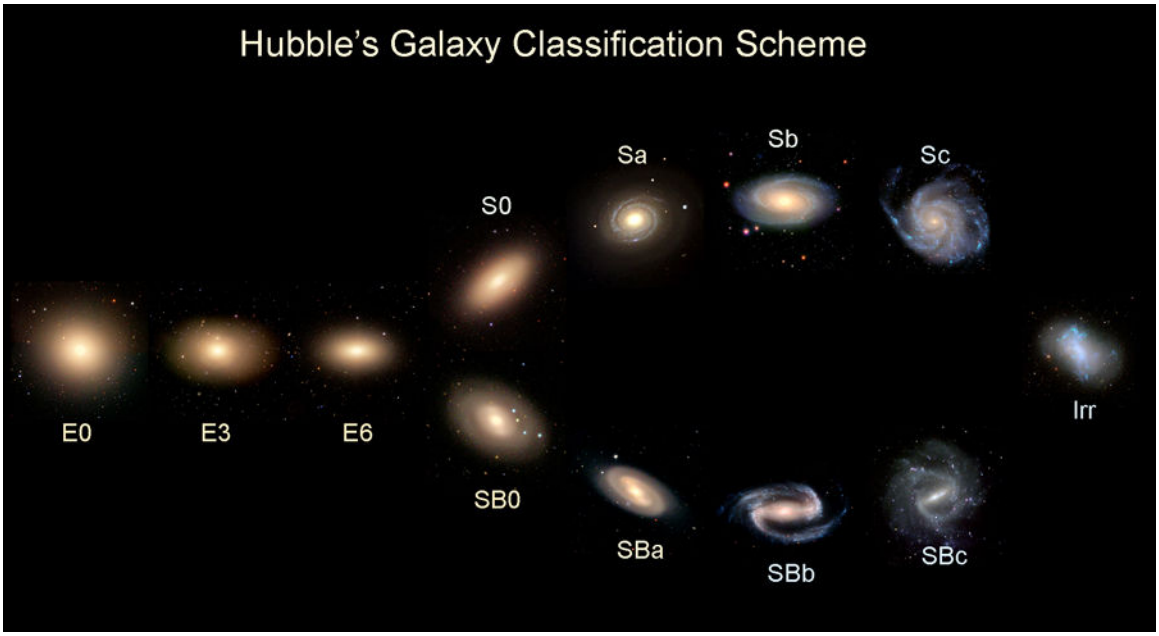

Figure 1.1.: The Hubble Sequence, a classification of the different galaxy types. On the left are the elliptical galaxies (sorted by their ellipticity), and on the right the spiral galaxies (barred and unbarred). Credit: GalaxyZoo.

1.1.1. Elliptical galaxies (Early Type)

Elliptical galaxies have a spheroidal, or ellipsoidal aspect. They can take various shapes, from nearly spherical to very flat. In the sky plane, they appear as el-

lipses, and were thus classified in 7 different types, from low ellipticity (E0) to high (E7). Nevertheless, this classification is rather arbitrary because the ellipticity depends highly on the angle at which the galaxy is observed (the line of sight), some E0 being actually much more elongated than they appear in the sky plane.
Their light is smoothly distributed, they are usually very massive and mostly populated by old stars. Indeed, they are poor in gas and do not form many stars (low star formation rate). They show little global rotation, contrary to disc galaxies.
Elliptical galaxies are also refered as early-type galaxies, together with lenticular galaxies.

1.1.2. Spiral galaxies (Late type)

Spiral galaxies are consisted of a flat rotating disc (e.g. figure 1.3). Their name comes from the typical spiral shaped structures found in their disc. These spiral arms usually extend from the center, and are areas with young bright stars, and high star formation rate (e.g. Silva-Villa and Larsen, 2012). Spiral galaxies often show a bulge at their center, which is a stellar structure going vertically out of the disc. The size, shape and nature of this bulge can vary from one galaxy to another. A stellar halo can also be present in spiral galaxies, which is a diffuse spheroidal component surrounding the disc.
Most spiral galaxies show a bar, which is an elongated structure extending across the center of the disc. One thus distinguish between the barred spiral galaxies (SB) and the unbarred ones (S), which make two distinct branches in the Hubble sequence. In the barred galaxies, the spiral arms extend from the ends of the bar.
Hubble further classified spiral galaxies as S(B)a, S(B)b, and S(B)c, mainly based on the opening of the spiral arms. Sa and SBa are unbarred and barred spiral galaxies with nearly circular tightly bound arms, whereas in S(B)c galaxies the spirals are very open and dominate the disc structure.
Spiral galaxies are also called late-type galaxies, as opposed to elliptical early-type galaxies.

1.1.3. Lenticulars

Lenticular galaxies (S0) are intermediate between elliptical and spiral galaxies, they are disc galaxies but show no or very weak spiral structures. They have little star formation, are mostly populated by old stars, and have significant dust in their disc. They have a prominent spheroidal central bulge, which is bigger than for spiral galaxies, and dominates the disc structure. They can also exhibit a central bar.

1.1.4. Irregulars

Irregular galaxies are all the galaxies which do not fit in any of the categories described above. They can sometimes show some similarities with a given category, for example the presence of a disc structure or a bulge, but with a peculiar aspect which prevents them to be classified as elliptical, lenticular, or spiral galaxies. These galaxies are called type I irregulars. On the other hand, they can also have a very chaotic and remarkable shape, and are then classified as type II. These galaxies can be formed by galaxies collisions or interactions disrupting their structure, and are then rather called peculiar galaxies, to distinguish them from secularly developped irregular galaxies, shaped only by their star formation.

1.1.5. From early type to late type?

Hubble made his classification with a left to right evolution, thinking that ellipticals evolve into spiral galaxies. That is why ellipticals are called “early type” and spirals “late type”. However, we now think that the evolution is in the other way, from spirals to ellipticals. Ellipticals are gas-poor while spirals are gas-rich, which leads to think that ellipticals have somehow depleted their gas, and are therefore older than spirals. Besides, looking at the Hubble sequence at higher redshift, we find more spirals and less ellipticals (Dressler, Oemler, Butcher, et al., 1994) than in the local universe, which argues in favor of ellipticals formed from spirals.
Looking at the color-magnitude diagram (the color of galaxies as a function of their mass, see figure 1.2), the ellipticals and the spiral galaxies tend to form two distinct groups, the former being redder than the latter (Strateva, Ivezić, Knapp, et al., 2001; Baldry, Glazebrook, Brinkmann, et al., 2004). These two groups are called the red (or passive) and the blue (or star-forming) sequence, and are a way to separate early-type from late-type galaxies. Between the red and the blue sequence, there is an area called $green\ valley$ (Wyder, Martin, Schiminovich, et al., 2007), which is less populated and represents the transition between blue and red galaxies (see figure 1.2). The galaxies in the green valley are often bulge dominated disc galaxies, with less star formation than spirals, and are often classified as lenticulars. They are usually considered as galaxies transiting from active star formation to quiescence due to gas quenching, which also supports the idea of ellipticals formed from spirals.

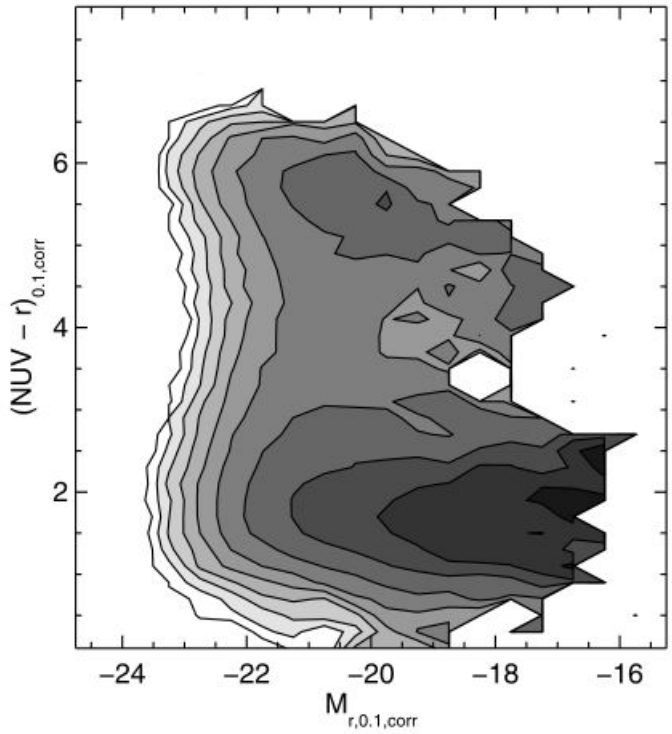

Figure 1.2.: UV-optical color-magnitude diagram (Wyder, Martin, Schiminovich, et al., 2007) showing the density of galaxies in grey scale. The blue sequence is the bottom dense part, while the red sequence is the top part. In between there is a less populated area, called $green\ valley$.

However, the question of how spiral galaxies evolved into ellipticals is still debated. The most probable scenario is that ellipticals were created by the merger of two spirals early in the age of the Universe (A. Toomre, 1977; Barnes, 1988; Hernquist, 1992; Bournaud, Jog, and Combes, 2005), possibly followed by a gas quenching phenomenon.

1.2. Disc galaxies

Figure 1.3.: NGC 4594, also called M104 or Sombrero galaxy, is a spiral galaxy seen edge-on. Credits: NASA/Hubble Heritage/STScI/AURA.

Disc galaxies are defined as galaxies having a disc component, and thus exclude elliptical galaxies. They include spirals and lenticulars. In this section I detail some properties of those galaxies.

1.2.1. How they form

The first galaxies are currently thought to be created with the "bottom-up" scenario, from hierarchical mergings of gas clouds embedded in dark matter clumps (Blumenthal, Faber, Primack, et al., 1984), following the ΛCDM theory. These early galaxies are therefore predicted to be very compact, clumpy and irregular, as confirmed by very high redshift (z∼8) observations (Oesch, Bouwens, Carollo, et al., 2010; Ono, Ouchi, Curtis-Lake, et al., 2013). The baryonic matter in the center of the remnant dark matter halo is rotating due to the angular momentum acquired from the gravitational interactions with the nearby structures. This rotation flattens the matter distribution, forming a gaseous and stellar disc, and creating a disc galaxy.

These disc galaxies often collide with each other, which is believed to form elliptical galaxies. Indeed, the observed fraction of massive disc galaxies increases with redshift while the ellipticals one decreases (Buitrago, Trujillo, Conselice, et al., 2013), supporting the picture of disc galaxies giving birth to ellipticals.
Nevertheless, not every present-day disc galaxy was formed at very high redshift, when the first galaxies were born. Observations have recently shown (Hammer, Flores, Elbaz, et al., 2005; Hammer, Flores, Yang, et al., 2009) that the merger of two disc galaxies at intermediate redshift could produce a new disc galaxy, and not only an elliptical. Some local spirals were thus created much later than the first galaxies, from a totally different process. This is the topic of section 2.1.

1.2.2. Bar

The presence of a central bar is very common, being observed in about 60-70% of local disc galaxies (Eskridge, Frogel, Pogge, et al., 2000; Laurikainen, Salo, and Buta, 2004; Menéndez-Delmestre, Sheth, Schinnerer, et al., 2007; Laine, Laurikainen, Salo, et al., 2014). The bar spins at a specific angular rate, called *pattern speed*, and has a very strong influence on the galaxy, being a non-axisymmetric feature. It exerts gravitational torques on the galactic structures, affecting the stellar orbits and the angular momentum distribution in the whole galaxy (Athanassoula, 2003), including the dark matter halo. The bar often shows a vertical component emerging out of the thin disc, called boxy/peanut bulge (section 1.2.3.2).
Bars form spontaneously from disc instabilities and then continuously evolve over time, changing their shape, length and rotation speed. They usually start rather thin, small and fast rotating, and then loose angular momentum to spherical features of the galaxy such as the DM halo (Athanassoula, 2003; Athanassoula, Machado, and Rodionov, 2013), which slows them down and makes them stronger, i.e. more elongated and more massive. However, the growth of the bar is not necessarily monotonic over time, and the bar strength can sometimes decrease up to the total disappearance of the bar, for example in the case of the interaction with a nearby galaxy.
Therefore, the strength and shape of the bar can vary from one galaxy to another, being directly dependent on the angular momentum exchanges with the different galactic (or extra-galactic) features.

1.2.3. Bulges

The true definition of a bulge is still not clear, as it can be described from a morphological, photometrical, or kinematical point of view. Using the morphology, a bulge can be described as a vertically thick component which swells out of the thin disc. On the other hand, in photometry a bulge is the central part of the

1D surface brightness profile which is above the exponential disc, being more luminous. Finally, in kinematics, the definition of the bulge is based on the value of V/σ (V being the velocity and σ the velocity dispersion) with the Binney diagram (J. Binney, 1978).
These three definitions can sometimes be in contradiction, as we will see below. Bulges are actually an inhomogeneous class of objects (Kormendy and Kennicutt, 2004; Athanassoula, 2005), and I present here the three types of bulges found in disc galaxies. Several different bulges can sometimes be found in the same galaxy.

1.2.3.1. Classical bulge

Classical bulges have a spherical (or spheroidal) shape, are found in the center of galaxies, and are very centrally concentrated. They are thought to be mainly formed by external accretion, during major (Katz, 1992, see Brooks and Christensen, 2016 for a review) or minor mergers (Bournaud, Jog, and Combes, 2005; Hopkins, Bundy, Croton, et al., 2010). Their stellar population is often old (Moorthy and Holtzman, 2006), suggesting that their formation can be prior to the disc. Another formation hypothesis is the coalescence of giant clumps in gas-rich primordial galaxies (B. G. Elmegreen, Bournaud, and D. M. Elmegreen, 2008). Their surface brightness profile shows a fast descreasing curve, usually fitted with a de Vaucouleurs law, as described in more details in section 3.2. Their properties are very similar to elliptical galaxies, having roughly the same morphology and kinematics (e.g. Davies, Efstathiou, Fall, et al., 1983, Kormendy and Bender, 2012).
The mass of the classical bulge is generally used to derive the bulge-to-total ratio (hereafter B/T), which is the ratio of the classical bulge stellar mass to the total stellar mass. Late-type galaxies usually show low B/T, while lenticulars have high B/T (Simien and de Vaucouleurs, 1986).
The most famous example of a classical bulge is seen in NGC 4594, also called the Sombrero galaxy (figure 1.3).

1.2.3.2. Boxy/peanut bulge

The boxy/peanut bulge has a peculiar aspect, with a boxy, peanut, or X shape seen from the edge (edge-on). It is sometimes called "pseudo-bulge", because it only fulfills the morphological definition of a bulge (being vertically thick). Although it was long considered as a separate component (as the classical bulge), it is actually part of the bar (Athanassoula, 2005). During the evolution of the bar, vertical instabilities of stellar orbits can lead to the thickening of the inner region of the bar, giving this particular boxy shape seen edge-on. This thickening is called *buckling*, usually happens on a short period of time, and coincides with

a bar weakening (Athanassoula, 2008).
The boxy/peanut bulge is shorter than the bar, and seen face-on constitutes a lens-like component called barlens.

1.2.3.3. Discy bulge

The discy bulge is a thin disc-like component in the center of the galaxy, in the galactic plane. It does not fulfill the morphological definition of a bulge, and is thus also called a pseudo-bulge. Nevertheless, it fulfills the photometrical definition, since its surface brightness profile stands clearly out of the exponential disc. The formation of discy bulges is usually linked to the bar attracting gas to the center of the disc due to gravitational torques. This gas then forms stars, leading to this small disc, which has a size of the order of 1 kpc. The discy bulge has thus a rather young stellar population, and as it is a disc structure, can sometimes show spirals or even bars (Carollo, Stiavelli, de Zeeuw, et al., 1997).

1.2.4. Disc

The galactic disc is the dominant part in late-type galaxies, extending far beyond the bulge in the galactic plane, and being more massive (low B/T). The formation mechanism of the disc is still unclear. Some think that discs are formed by gas inflows, for example from gas-rich minor mergers, or gradual accretion. On the other hand, it has also been proposed that discs can be formed by gas-rich major mergers, with the gas fueling a new disc creation. The latter will be described in section 2.1.
In the two following sections I describe some characteristics of the discs, namely their structure and their stellar orbits.

1.2.4.1. Disc structure

The stellar disc often shows subcomponents such as bars, spirals and rings, which are inhomogeneities formed from disc material. Spiral arms can have different opening angles (see section 1.1.2), going from nearly circular bound arms to very open ones. They can be smooth, representing just slight inhomogeneities in a rather continuous stellar disc, or very strong, concentrating the majority of the disc stellar content. In the case of barred galaxies, the spirals extend from the extremities of the bar (often being on the number of 2), while in non-barred galaxies they extend from the center. Their multiplicty and amplitude varies from one galaxy to another, and one can sometimes find two different sets of spirals, one in the center, and another in the outer parts.
The formation mechanism for spiral arms is still debated, and could not be unique. The density wave theory (Lin and Shu, 1964) states that spirals are actually density waves, and explains how stars can spend more time at a given

place in their orbit (usually due to deceleration), and thus locally create a region of higher stellar density. This means that the stars in the spiral arms do not stay inside them and rotate as a solid body, their orbits only cross them and make the stars spend more time inside the spirals than outside. These density waves would initially be formed by disc instabilities. Nevertheless, there is another possible mechanism, the manifold theory (Romero-Gómez, Masdemont, Athanassoula, et al., 2006), which is based on Lagrangian points located near the end of the bar. These Lagrangian points are unstable, and lead to specific stellar orbits, which will be the building blocks of the spirals. Therefore, here it is not about a high number of stars temporarily crossing the spiral arms in their orbit paths, but a fixed number of stars which sustainably follow and constitute the spiral structure.
Spiral arms are usually $trailing$, the outer part of the spiral being behind the inner part (with respect to the disc rotation), in opposition to $leading$ spirals where the inner part is behind.
Disc galaxies can also display rings in their discs. Rings can form by passing interactions, as in the Cartwheel galaxy, or by secular evolution linked to the bar, possibly following the manifold theory. There are also polar rings, which are perpendicular to the galactic plane, and are thought to be due to mergers as well.

The galactic disc can be vertically decomposed into two other subcomponents: the thin and the thick disc. Indeed, looking at the disc edge-on, the stellar density behaves differently at a given height from the galactic plane. This can be seen in figure 1.4, where the density as a function of the thickness z is plotted, for a given radius. This points out that the properties of the disc change from a given height (around 1500 pc in this example), suggesting the presence of a different component. Most disc galaxies show a thick disc (Yoachim and Dalcanton, 2006), including the Milky Way (Gilmore and Reid, 1983). The thin disc has a scale-height of about 300 pc, is composed of young and metal-rich stars, and displays substructures such as spiral arms and rings. On the other hand, the thick disc can extend up to 5 kpc height, is composed of old and metal-poor stars (Chiba and Beers, 2000), and is rather homogeneous. While the thick disc has long been considered as much less massive than the thin disc, it has recently been shown that in the Milky Way the mass of the thick disc represents around 50 % of the total stellar mass (Fuhrmann, 2008; Snaith, Haywood, P. Di Matteo, et al., 2014).
Several formation scenarios have been proposed for the formation of the thick disc, such as the heating from the thin disc by minor mergers (P. J. Quinn, Hernquist, and Fullagar, 1993; P. Di Matteo, Lehnert, Qu, et al., 2011) or radial migration (Loebman, Roškar, Debattista, et al., 2011).

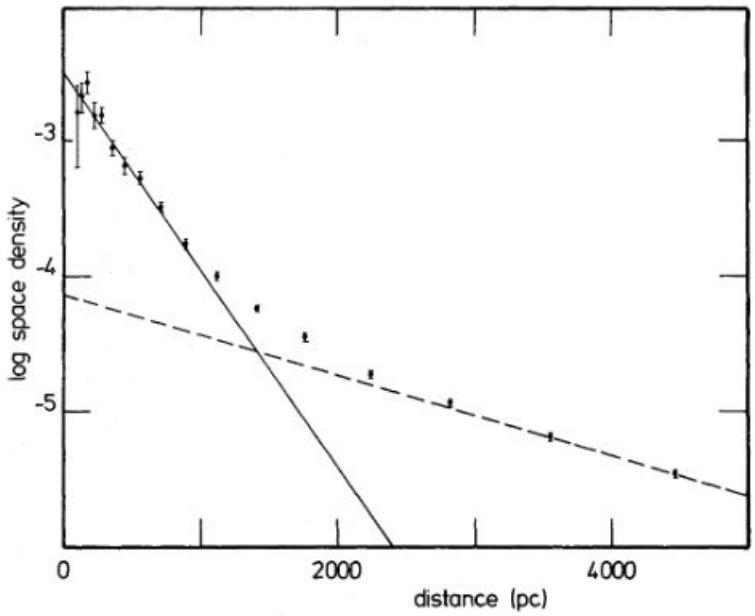

Figure 1.4.: Density distribution of stars as a function of the distance from the galactic plane (Gilmore and Reid, 1983), for the Milky Way. The dots represent the data, and the lines exponential fits for the thin and thick disc.

1.2.4.2. Orbits

The stars composing the disc tend to be trapped around several families of stable periodic orbits. These orbits are also called resonant orbits and are rather straightforward to derive. For example, in the case of a disc and a bar, a 2D galactic orbit in the corresponding potential can be characterized by its angular frequency of rotation around the galactic center Ω and its frequency of radial oscillations κ, also called epicyclic frequency. An orbit is then resonant if it closes after a certain number of revolutions and of radial oscillations, which gives for l and m being integers:

$$l\kappa + m(\Omega - \Omega_p) = 0 \tag{1.1}$$

in a frame of reference which rotates with the bar, where Ω_p is the angular velocity of the bar (or pattern speed).
The most important resonances for a bar (or any $m = 2$ pattern such as double armed spirals) are:
- The Corotation Resonance (CR): $l = 0$. This occurs when $\Omega = \Omega_p$, i.e. when the particle corotates with the bar.
- The Inner Lindblad Resonance (ILR): $l = -1$, $m = 2$. The orbit closes after two radial oscillations and one revolution around the center, which means that

a star following this orbit will feel the force of the bar at the same frequency as its epicyclic frequency. The ILR is located inward the CR radius since the star is faster than the bar ($\Omega - \Omega_p > 0$).
- The Outer Lindblad Resonance (OLR): $l = 1$, $m = 2$. Same as ILR, but located outward the CR radius since it is slower than the bar ($\Omega - \Omega_p < 0$).

These resonances are important since they trap many stars around them and create families of orbit. For example, the ILR supports the bar with the $x1$ orbit family (Contopoulos and Papayannopoulos, 1980). Furthermore, the CR has been shown to be an upper limit for the size of the bar, since bars cannot extend beyond their CR (Contopoulos, 1980). The ratio of the CR radius to the bar length allows to distinguish $fast$ bars from $slow$ bars.

2. Our simulations

2.1. Creating a disc galaxy from a major merger

This section is based on the paper Athanassoula, Rodionov, Peschken, et al. (2016, hereafter Paper I), and analyzes several aspects of our simulations tackled in this paper.

2.1.1. Paper I

The goal of our simulations is to see if we can obtain a realistic spiral galaxy from a major merger between two disc galaxies at high redshift. As described previously, this has been shown in observations, but so far simulations have not been able to reproduce this result. Although a disc component has been shown to form in the remnant in some cases (e.g. Wang et al. 2012), it is often too small to correspond to late-type galaxies. We thus proposed to try with our own simulations, by including a specific component in the models: a hot gaseous halo. It has been shown (e.g. Miller and Bregman, 2015) that disc galaxies have gas not only in their disc, but also in their halo. We will show here how the presence of this particular feature influences the outcome of a major merger.

Three fiducial examples of our simulations are described in detail in the paper below, as well as the main results, such as the morphology and properties of the remnant galaxies, the role of the halo gas or the presence of different stellar populations including the thick disc. I am the third author in this paper, and contributed to several parts, as described in the next section.

DRAFT VERSION FEBRUARY 16, 2016
Preprint typeset using LaTeX style emulateapj v. 5/2/11

FORMING DISK GALAXIES IN WET MAJOR MERGERS. I. THREE FIDUCIAL EXAMPLES

E. ATHANASSOULA, S. A. RODIONOV, N. PESCHKEN, J. C. LAMBERT
Laboratoire d'Astrophysique de Marseille (LAM), UMR7326, CNRS/Aix Marseille Université, Technopôle de Marseille-Etoile, 38 rue Frédéric Joliot Curie, 13388 Marseille Cédex 13, France

(Received; Revised; Accepted)
Draft version February 16, 2016

ABSTRACT

Using three fiducial Nbody+SPH simulations, we follow the merging of two disk galaxies with a hot gaseous halo component each, and examine whether the merger remnant can be a spiral galaxy. The stellar progenitor disks are destroyed by violent relaxation during the merging and most of their stars form a classical bulge, while the remaining form a thick disk and its bar. A new stellar disk forms subsequently and gradually in the remnant from the gas accreted mainly from the halo. It is vertically thin and well extended in its equatorial plane. A bar starts forming before the disk is fully in place, contrary to what is assumed in idealised simulations of isolated bar-forming galaxies. It has morphological features such as ansae and boxy/peanut bulges. Stars of different ages populate different parts of the box/peanut. A disky pseudobulge forms also, so that by the end of the simulation, all three types of bulges coexist. The oldest stars are found in the classical bulge, followed by those of the thick disk, then by those in the thin disk. The youngest stars are in the spiral arms and the disky pseudobulge. The disk surface density profiles are of type II (exponential with downbending), and the circular velocity curves are flat and show that the disks are submaximum in these examples: two clearly so and one near-borderline between maximum and submaximum. On average, only roughly between 10 and 20% of the stellar mass is in the classical bulge of the final models, i.e. much less than in previous simulations.

Subject headings: galaxies: structure — galaxies: kinematics and dynamics — galaxies: spiral

1. INTRODUCTION

What results from a merger of two disk galaxies of comparable mass? Toomre & Toomre (1972) were the first to propose that such a merger will form an elliptical. After some strong initial rebuttals, this was generally accepted (see e.g. Barnes 1998 and Schweizer 1998 for reviews), only to be questioned again in the last decade. Indeed, several observations at intermediate redshifts, suggest that the result of a merging of two gas-rich disk galaxies of comparable luminosity is actually not an elliptical, but a disk galaxy (e.g. Hammer et al. 2005, 2009a,b). Roughly concurrently, pioneering and seminal numerical simulations showed that the remnants of mergers of gas-rich disk galaxies do have a disk component (e.g. Barnes 2002, Springel & Hernquist 2005, Cox et al. 2006, Robertson et al. 2006, Lotz et al. 2010b, Governato et al. 2009, Hopkins et al. 2009, 2013, Wang et al. 2012, Borlaff et al. 2014, Querejeta et al. 2015). However, the relative mass and/or extent of these disks are in general considerably smaller than those of present day spiral galaxy disks. This formation mechanism could thus perhaps be appropriate for lenticulars, but not for spirals. Furthermore, although bars are present in about two thirds of disk galaxies in the local universe (Eskridge et al. 2000; Knapen et al. 2000; Menéndez-Delmestre et al. 2007; Buta et al. 2015, etc.) and are believed to be a major driver of secular evolution (see e.g. Athanassoula 2013; Kormendy 2013, for reviews of the theoretical and observational parts, respectively), these works provide little or no information on whether and when major merger remnants can have bars and on whether their bar properties and parameters are realistic.

It is thus necessary to return to this still open question and to test whether the remnants of major mergers could be spiral galaxies with the appropriate morphology, mass distribution, kinematics and substructures. In this paper, the first of a series, we present first results for three fiducial wet major merger simulations and their remnants. We first present the improvements we introduce in the modeling of the protogalaxies and in the simulation resolution and give information on the code we used and our initial conditions (Sect. 2). Sect. 3 presents and discusses our results. We show that the disk of the remnant can extend over several scalelengths, while the B/T ratio (classical-bulge-to-total stellar mass ratio) can reach sufficiently low values to be representative of spirals. We also discuss morphologies, including those of spirals and bars, show rotation curves and projected density radial profiles, and discuss when and how the various components are produced. We compare the morphology and kinematics of stellar populations with different ages (Sect. 3.6) and also present a simple scenario for the formation of disk galaxies (Sect. 4), before summarizing and concluding (Sect. 5). The nomenclature used in this paper is summarized in the Appendix. For brevity, we will hereafter often refer to our simulated galaxies simply as "galaxies", and to stellar particles in the simulation as "stars".

2. SIMULATIONS

2.1. *General context*

Compared to previous simulations on this specific subject, ours present one numerical and one conceptual advantage.

As a numerical advantage, we have a much better resolution than previous simulations tackling the specific question that we have set out to address in this project, namely whether major mergers of gas rich disk galaxies can form spirals, or not. Indeed, to answer this question necessitates a survey of simulations, as e.g. in Hopkins et al. (2009), so that the use of high resolution becomes computationally much more expen-

lia@lam.fr

sive than for problems necessitating only few simulations. For this reason previous attempts restricted themselves to considerably less than or of the order of half a million particles in total.[1]. We increased this number by more than an order of magnitude, adopting for each gas, or stellar particle a mass of m_g=5 $\times$ $10^4 M_\odot$ and a softening of 25 pc. The dark matter (DM) particles have a mass of $m_{\rm DM}$=2 $\times$ $10^5 M_\odot$ and a softening of 50 pc. We thus have in our simulations 2 and 3.5 million particles for the baryons and DM, respectively.

The conceptual improvement concerns the initial conditions of the simulations. In previous works, the progenitors resembled local disk galaxies, except for a higher content of cold gas in the disk. They consisted of a DM halo, a disk and sometimes a classical bulge with properties compatible to those of local galaxies. It is, however, well established that disk galaxies, except for the cold gas in their disk, have also hot gas in their halos (e.g. Miller & Bregman 2015). To include this, we start off our simulations with spherical protogalaxies consisting of DM and hot gas. Before the merging, a disk forms in each of the progenitors, so that we witness the merging of two disc proto-galaxies. The two gaseous halos merge into a single one enveloping the remnant and thus halo gas accretes onto the remnant disk all through the simulation (Sect. 3.2). Such gaseous halos exist also in mergings occurring in cosmological simulations (e.g. Governato et al. 2009), or in a couple of major merger studies (Moster et al. 2011; Kannan et al. 2015), whose remnants have a B/T ratio between 0.7 and 1., thus linking them to ellipticals with a small disk. Thus, to our knowledge, our study is the first one to include a hot gaseous component in dynamical simulations of major mergers whose remnants model realistic spiral galaxies.

2.2. *Code*

A full discussion of the code used in these simulations and of their initial conditions is the subject of the next paper in this series (Rodionov et al., in prep., Paper II). In this and the next two subsections we only summarise the main information necessary here.

We use a version of GADGET3 including gas and its physics (Springel & Hernquist 2002; Springel 2005). DM and stars are modeled by N-body particles, and gravity is calculated with a tree code. The code uses an entropy conserving density driven formulation of SPH with adaptive smoothing lengths (Springel & Hernquist 2002) and subgrid physics (Springel & Hernquist 2003).

Our feedback, star formation and cooling follow subgrid physics included in simple recipes given by Springel & Hernquist (2003) and were already used in a number of previous works cited in Sect. 1. It is beyond the scope of this paper to test other subgrid physics. Nevertheless, let us mention briefly that Cox et al. (2006) showed that the mass profiles of the major merger remnants are robust to substantial changes in subgrid physics parametrizations. Similarly, Hopkins et al. (2009) find that the efficiency with which gas avoids consumption during the merger and can reform a disk does not depend on the subgrid parametrization, unless the feedback is very weak. Most important, Hopkins et al. (2013) introduced detailed, explicit models for stellar feedback in their very high resolution major merger simulations and found that in all cases the mass profile results of explicit feedback models are nearly identical to those obtained with the subgrid physics we use here, except for some second order differences.

[1] Amongst the simulations with a resolution yet higher than ours we note two simulations of Milky Way sized galaxies with a resolution of four pc, i.e. roughly six times better than ours (Hopkins et al. 2013). Such a resolution, however, would be impossible for our project, since a few hundred simulations are necessary for an even cursory examination of the parameter space and in order for the three simulations discussed here to be fiducial they need to have the same resolution as the rest.

2.3. *Central, AGN-like feedback*

The code described above has already been used a large number of times to test the relevance of major mergers regarding the formation of disk galaxies, as e.g. in Hopkins et al. (2009, and references therein), albeit with initial conditions that do not include gaseous halos. We also used it in a number of our simulations, which always include gaseous halos. In those cases, we obtained merger remnants which are disk galaxies with thin and extended disks and realistic spiral arms, but with one serious drawback which is that the centermost part of the galaxy had a considerable central concentration, leading to an unrealistically high inner maximum of the circular velocity curve (Paper II). Furthermore, this high central mass concentration has the disadvantage of prohibiting bar formation, or at least delaying it beyond the 10 Gyr covered by our simulations. This is in disagreement with observations, since about 2/3 of local disk galaxies are barred (see references in Sect. 1).

Such excessive concentrations were also obtained in cosmological simulations of disk galaxy formation and were lately addressed by introducing additional feedback in the central regions, mainly in the form of AGN feedback. Very schematically, in this picture gas will flow inwards to the central black hole (BH). Feedback is then calculated as a given fraction of the luminosity which is radiated by the BH. This energy is distributed to the gas in the central region in the form of thermal energy, thus preventing excessive star formation.

In most studies, the inflow on to the BH is modeled using the Bondi accretion formalism (Hoyle & Lyttleton 1939; Bondi & Hoyle 1944; Bondi 1952), sometimes limiting it by the Eddington accretion rate to prevent excessive accretion. This inflow formalism has two free parameters, the accretion efficiency and the radiative efficiency (Springel et al. 2005). However, the physics of driving BH-generated outflows is still not well understood (e.g. Silk & Mamon 2012), and also necessitates resolutions much higher than what we have here. It has, furthermore, been criticized by Hopkins & Quataert (2012), who calculated the accretion directly from subparsec 'resimulations' of the central region of galaxy-scale simulations.

Our approach is based on the same physics, but since all we want is to solve the excessive mass concentration problem and not to model the BH accurately, we adopted a very straightforward, empirical and parametric method. As gas flows inwards, it will increase the density in the central regions. As in previous descriptions, we introduce two parameters, a density threshold $\rho_{\rm AGN}$ and a temperature $T_{\rm AGN}$. More specifically, at every time step we give internal energy to gas particles whose local density is larger than the threshold $\rho_{\rm AGN}$, by increasing their temperature to $T_{\rm AGN}$. This density threshold is chosen so as to ensure that the chosen particles are located in the centermost region. Furthermore, to ensure that the amount of energy that we thus inject is not excessive, we test at every step that the total energy distributed is below that of the Eddington rate (see e.g. Springel et al. 2005). We do this in a probabilistic manner, by setting the probability of a particle receiving internal energy equal to 1 if the energy to be distributed is less than the Eddington limit, or, if it is higher than

that limit, setting the probability as the ratio of the Eddington limit to the energy we were initially to distribute. A fuller description will be given in Paper II, where we describe all our computational and technical aspects in detail. Although very simple, this description includes the essentials sufficient for our purposes, namely it injects energy in the central regions to prevent excessive star formation. Compared to cases with no AGN feedback, it leads to mass distributions which are less concentrated in the centermost parts, more realistic circular velocity curves and allows bars to grow.

In our scheme there is no single particle representing the BH, as any spurious off-centering of such a particle, or its imperfect correction by analytical drag forces, could introduce errors because the BH mass is so much higher than that of the other particles in the simulation. Nevertheless, it is useful to keep track of the evolution of the BH mass ($M_{\rm BH}$) with time. We do this by measuring the energy released by our AGN-like feedback as a function of time and then following the simple formalism described in Springel et al. (2005, p. 783).

The following three questions need to be considered here:

1. *Does the thus described feedback model lead to unphysical results?* Several arguments argue against this:
   - The shape of the circular velocity curve, from unrealistic as in simulations without this central feedback, becomes very realistic, well compatible with observed rotation curves.
   - The mass of the BH at the end of the simulation, calculated using the energy of the feedback, is 1., 1.4 and 3.3 $\times$ $10^7 M_\odot$ for our three fiducial simulations. These are reasonable values for disk galaxies. Moreover, we calculated the velocity dispersion of the central parts, σ, directly from our simulation and found that this ($M_{\rm BH}$, σ) pair falls near the $M_{\rm BH}$ — σ relation (Ferrarese & Merritt 2000; Gebhardt et al. 2000), within the observational spread.
   - Qualitatively, the evolution of M_{BH} during the merging is similar to that obtained with other AGN feedback prescriptions, namely increases much more sharply during the merging than after it (e.g. Thacker et al. 2014).
   - Last, but not least, we ensure that at all times the amount of injected energy does not exceed the Eddington limit as described above.
2. *How is this energy distributed?* We followed during the simulations the locations of the gas particles to which the energy is deposited. We found that these particles cover a region around the dynamical center of the halo, i.e. around the position of the halo particle with the highest local density. The area they cover may vary from one run to another, but it is always much larger during the merging times. At such times, their characteristic size is of the order of half to one kpc, but becomes considerably smaller after the merging, when it is of the order of say 100 pc. This increase of the characteristic size during merging reflects the corresponding much larger feedback, while the extent during the merging time can be compared to the circumnuclear region which is very active during a merging (see e.g. Scoville et al. 1991 for the merging system Arp 220).
3. *Does this feedback affect the simulation results?* Indeed it does, as expected and required. Namely it changes the shape of the circular velocity curve, making it compatible with observations and, as a corollary, it allows the formation of bars, which we know are present in the majority of nearby galaxies (see references in Sect. 1). Moreover, changes in the values of the two adopted parameter ($\rho_{\rm AGN}$ and $T_{\rm AGN}$) should, and do, affect the simulation results. This is expected since they change the shape of the circular velocity curve and thus the bar properties, which, in turn, influences the dynamics and structure at least in the inner parts of the disk. These changes are most important in the central region hosting the bar, but much smaller at larger radii (Paper II).

To summarise, our simple parametric description of the central feedback has the desired effect without being unphysical. We thus adopt it for our simulations.

2.4. *Further information on the code*

Making a full comparison of the results of our simulations with those obtained with other codes, but with the same initial conditions and the same gas physics and subgrid physics, is beyond the scope of this paper. We, nevertheless, reran one of our fiducial simulation (referred to in the following as mdf732, see Sect. 2.6) using the GIZMO code (Hopkins 2013, 2014, 2015), after implementing to it the subgrid physics we use here. This code is a derivative code of GADGET, using the same MPI parallelization, domain decomposition, gravity solvers, etc. However, in contrast to that of GADGET, the SPH version of GIZMO is density independent, and it also includes a more sophisticated treatment of the artificial viscosity term (Cullen & Dehnen 2010), as described in Hopkins (2013, Sect. 3.1). It can thus handle better the phase boundaries, e.g. between the hot gas in the halo and the much cooler gas in the disk, or the description of cold dense clumps of gas in the otherwise hot halo.

The main difference we found between the results of these two codes is in the hot gaseous halo. This has small gaseous clumps in the simulation run with GADGET3, which are either absent, or much less prominent in the GIZMO run (see also Torrey et al. 2012 and Hayward et al. 2014). On the other hand, we find very good agreement when we compare the properties of the remnants, e.g. their gaseous or stellar projected density radial profile, their cumulative stellar mass, or the mean tangential velocity of the stars or gas and the stellar radial and vertical velocity dispersion profiles.

The good agreement between the properties of these two simulations argues that the clumps present in the halo of the GADGET simulation do not influence much the behaviour of the stellar component. Even the stellar vertical velocity dispersion or the thickness of the stellar disk are in good agreement, which shows that these clumps are not sufficiently massive and/or numerous to heat up noticeably the stellar disk.

2.5. *Initial density profiles of the protogalaxies*

We used idealised initial conditions with two identical protogalaxies composed of spherical DM and gaseous halos, of masses M_{DM} and M_{gas}, respectively, with $M_{total}/M_{gas} = 8$. The initial density of the DM and the gaseous halo is

$$\rho(r) = C \;\; sech(r/|r_t|) \;\; x^{-\gamma_i} \; (x^\eta + 1)^{-(\gamma_o - \gamma_i)/\eta}, \qquad (1)$$

where r is the spherical radius, $x = r/a$ and a and r_t are the scalelength and tapering radius of the halo, respectively.

The constants γ_i, γ_o and η characterize the shape of the radial density profile. The DM halo has $\gamma_i = 1$, $\gamma_o = 3$ and $\eta = 1$, while the gaseous one has $\gamma_i = 0$, $\gamma_o = 2$ and $\eta = 2$ (Beta model for $\beta = 2/3$, e.g. Miller & Bregman 2015 and references therein). For both we have r_t=100 kpc and a=14 kpc. The halo component was built following McMillan & Dehnen (2007), i.e. with a Cuddeford (1991) distribution function. We also add a small amount of spin to the halo. Let f be the fraction of particles with a positive sense of rotation. In cases with no net rotation f=0.5, while if all particles rotate in the positive (negative) sense f=1 (-1). The internal energy of the gas was set by requiring hydrostatic equilibrium (Paper II).

Stars do not exist in the initial conditions, but form during the evolution, so that, at the time of the merging, a stellar and a gaseous disk are present in the progenitor galaxies. Thus their density and velocity profiles are set by our initial setup for the hot halo gas distribution and its subsequent evolution, and not directly by the modeller seeking to match e.g. what is measured in nearby galaxies.

2.6. *Three fiducial examples*

In this paper we discuss three simulations (mdf732, mdf778 and mdf780). All three are 1:1 mergers of two identical protogalaxies. We start by adopting the simple case of coplaner mergers, while other orientations will be considered in forthcoming studies. We just mention briefly here that preliminary results show, as expected, that the orientations of the spin axes with respect to the orbital plane influence considerably the properties of the remnant, and that this may account for the spread observed in disk sizes, B/T ratios and gas fractions of nearby galaxies.

The orbits of the centers of density of the two protogalaxies, i.e. the orbits of the location where their DM density is highest, are given in Fig. 1a. Simulations mdf732 and mdf780 have f=0.6 and mdf778 has 0.55. The adopted AGN parameters are ρ_{AGN}=1 $M_\odot/pc^3$ for all three cases, and T_{AGN}=10^7 K for mdf732 and mdf778, and 2.5 $\times$ 10^7 K for mdf780. We continued all simulations up to 10 Gyr.

3. RESULTS AND DISCUSSION

3.1. *Early evolution of individual isolated galaxies*

In previous works (see papers cited in Sect. 1), the initial conditions consisted of two fully developed disk galaxies set on a given trajectory. Each consisted of a spherical halo, an exponential stellar disk and, in some cases, a classical bulge and/or a gaseous disk. Their properties were chosen so as to represent nearby galaxies; except for the fraction of gas in the disk, which was a free parameter varied at will. Thus gas fractions in the complete range between 0 and 1 were tried, even if this was not necessarily compatible with e.g. the adopted disk scale length (which was most times appropriate for low-redshift Milky-Way-like disk galaxies, i.e. 3 to 5 kpc), or with their B/T mass fraction. Although not ideal, these initial conditions allowed previous works to reach interesting conclusions, for example on the crucial role of the initial gas fraction on the nature of the merger remnant. This is presumably due to the fact that violent relaxation occurring during the merging wipes out all small details of the initial stellar structures.

We chose to start out with very different initial conditions for the progenitors (Sect. 2). However, before using these initial conditions in our major merger simulations we made sure that, when evolved in isolation, their t=10 Gyr snapshots gave reasonable approximations of local disk galaxies, and that during their early stages of evolution (up to say 2 Gyrs) they were compatible with the main properties of disk galaxies at such times. The latter entails that the disk should be considerably smaller and more perturbed than the disks in local isolated galaxies and that the fraction of gas in their disk should be higher (Bouwens et al. 2004; Ferguson et al. 2004; Elmegreen et al. 2005; Dahlen et al. 2007; Erb et al. 2006; Leroy et al. 2008; Daddi et al. 2010; Tacconi et al. 2010; Conselice et al. 2012; Rodrigues et al. 2012; Genzel et al. 2015, etc). More information on all this will be given elsewhere (Peschken et al., in prep.), but we summarise below some relevant information.

In our simulations, the protogalaxies at t=0 consist only of spherical distributions of DM and gas (Sect. 2.5). From the onset of the simulation, however, the gas in the halo cools radiatively and, getting out of equilibrium, falls inwards. Its density increases locally and the first stars form. Thus, the progenitors gradually acquire a disk. This, as expected, is much more perturbed and lumpy than the more settled exponential disks to which it evolves at later times. Fig. 2a shows the radial surface density profile at five times during the evolution (0.5, 1, 2, 5 and 10 Gyr). It is clear that the disk grows inside-out, relatively fast at early times and less so later on. The profiles are initially exponential-like, but it is not trivial to measure adequately their scale-length, so, instead, we measure the cylindrical radius R_{70}, containing 70% of the stellar mass. It is clear that this quantity increases considerably with time, as expected, particularly at early evolution stages (Fig. 2b).

Fig. 2c shows the fraction of gas in the disk component measured within $|\Delta z|$<0.5 kpc. We see that at the relevant times, i.e. the times corresponding to before the merging, the gas fractions are in the ball park of 60 to 30%, i.e. considerably larger than the corresponding gas fractions in nearby disk galaxies, in good agreement with observations of both local and intermediate redshift galaxies.

We do not claim that this is a perfect model of galaxies at intermediate redshifts, but it is still a considerable improvement over those used in previous studies. This improvement is a corollary of the existence of a hot gaseous halo in our initial conditions, as this entails a slow formation and evolution of the disk which becomes gradually more massive and more extended, while the gas fraction in the disk decreases monotonically with time.

3.2. *General evolution of a major merger*

The stellar disks of the progenitor galaxies are destroyed by the merging and their stars concentrate in the central regions of the remnant. As we will see in the following sections most of them form a classical bulge, while the remaining, albeit much smaller number of stars, contribute to a thick disk and its bar. The gaseous disks of the progenitors are also destroyed, and the gas which they included also concentrates in the innermost regions of the remnant, so that the stars that form from it contribute to the classical or disky pseudobulge.

After the end of the merging, gas continues to fall in mainly from the halo, but also, although in much smaller quantities, from the gaseous tails formed during the interaction. Thus a new disk is gradually formed, which very early on shows well-defined spiral arms. This gas accretion continues all through the simulation.

3.3. *Morphology of merger remnants*

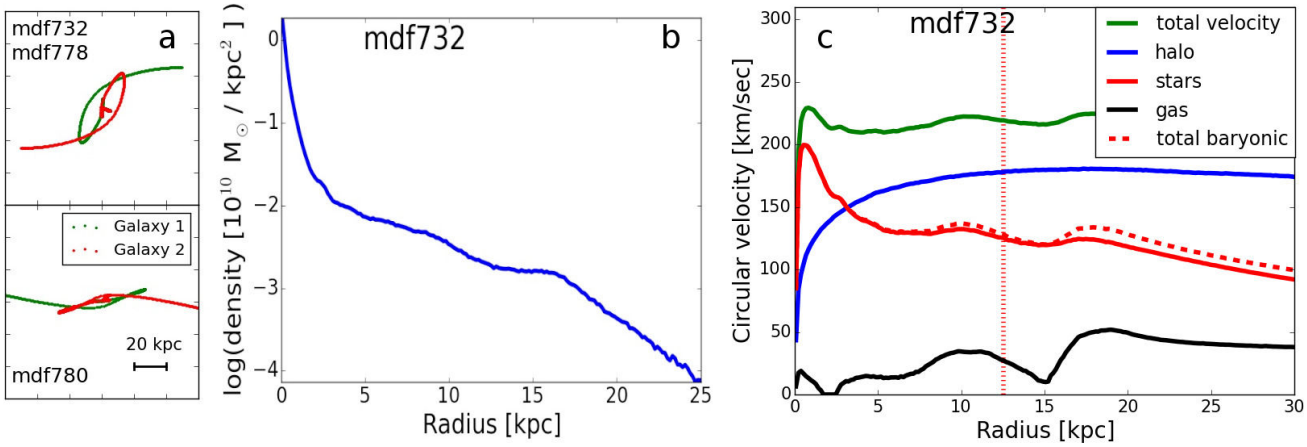

Figure 1. a: Orbits of the progenitors before the merging. b: Stellar radial surface density profile at t=10 Gyr. c: Circular velocity curves at t=10 Gyr, for the total mass, as well as separately for stars, gas, total baryonic mass and halo. The vertical red dotted line is located at 2.2 inner disk scalelengths.

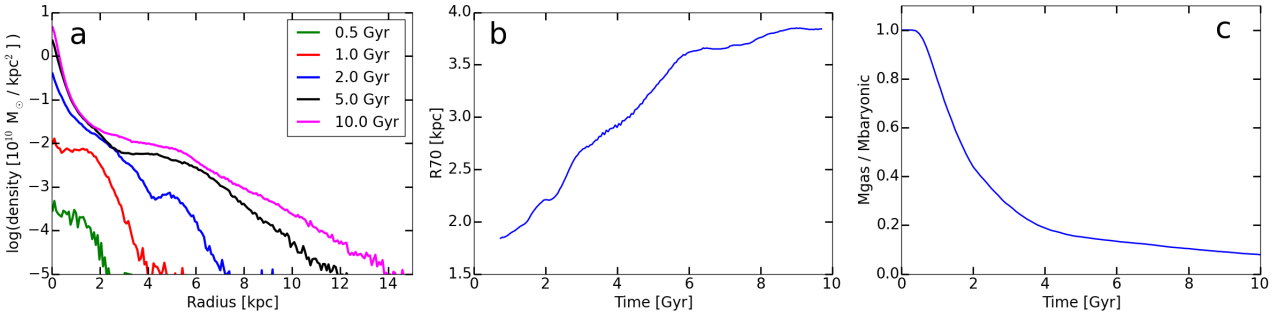

Figure 2. Properties of a simulated galaxy growing in isolation. Left: Radial surface density profile for times 0.5 (green), 1 (red), 2 (blue), 5 (black) and 10 Gyr (violet). Middle: Cylindrical radius containing 70% of the stellar mass. Right: Fraction of the gas in the disk ($|\Delta z|$<0.5) component as a function of time .

Fig. 3 gives the morphologies at the end of the simulations[2]. mdf778 has the largest disk extent and mdf780 the shortest. Seen face-on, all three galaxies have a clear and extended spiral structure. Let us denote by m the spiral arm multiplicity, i.e. the number of arms at any given radius. mdf778 is mainly bisymmetric (m=2), while mdf732 and mdf780 are m=2 in the inner parts and m>2 at larger radii, reaching m=5 at the edges of the disk. This increase of m with distance from the center is in good agreement with observations and was explained by Athanassoula et al. (1987, see also Athanassoula 1988 for models including accretion). These authors applied the swing amplification analytical formalism (Toomre 1981; see also reviews by Athanassoula 1984 and Dobbs & Baba 2014) to their rotation curve decompositions results and pointed out that, if the spiral structure was due to swing amplification, the arm multiplicity should increase with distance from the center. Thus the spiral structure in mdf732 and mdf780 is consistent with a swing amplification origin. Providing, however, tangible proof that these are swing amplification driven spirals is well beyond the scope of this paper.

mdf732 has an inner ring with a very asymmetric density distribution along it (Fig. 3, second row, where the lower half of the ring is clearly visible). Its semi-major axis has the same size as that of the bar and it is elongated in the same direction, both in good agreement with inner ring observations (e.g. Buta 1995, and references therein). Good examples of such inner rings can be seen in NGC 1433 and NGC 3660. mdf778 and mdf780 have m=2 spirals emanating from the ends of the bar roughly perpendicular to it and then trailing behind it, again in good agreement with what happens in observed local galaxies.

The bar size in all three simulations (2.5 to 4 kpc semi-major axis) is only slightly below the average for the stellar mass in question, and well within the range of observed values for external galaxies (lowest panel of Fig. 20 in Diaz et al. 2015). It should be noted that our three models presented here have a similar stellar mass as the Milky Way, and their barlength closely matches that of the Milky Way bar. To measure the bar strength, we Fourier decomposed the projected surface density of the face-on view as in Diaz et al. and used the maximum value of the relative m=2 Fourier component as the bar strength (see e.g. Diaz et al. for more information on this method). For our three simulations we find values between 0.32 and 0.35, which are in good agreement with observations. However this comparison is less constraining than the one concerning the bar length, because the observed values show a very large spread (second panel of Fig. 20 in Diaz et al. 2015).

We can also make meaningful comparisons concerning the bar morphology. Combining information from three different approaches, namely simulations following bar formation in isolated disk galaxies, orbital structure theory, and observations Athanassoula (2005, see also Athanassoula 2015 for

[2] Figs. 3, 4 and 6 were made using the glnemo2 software (http://projets.lam.fr/projects/glnemo2), which, in order to display morphologies best, uses color coding corresponding to the maximum of the spatial density along the line of sight.

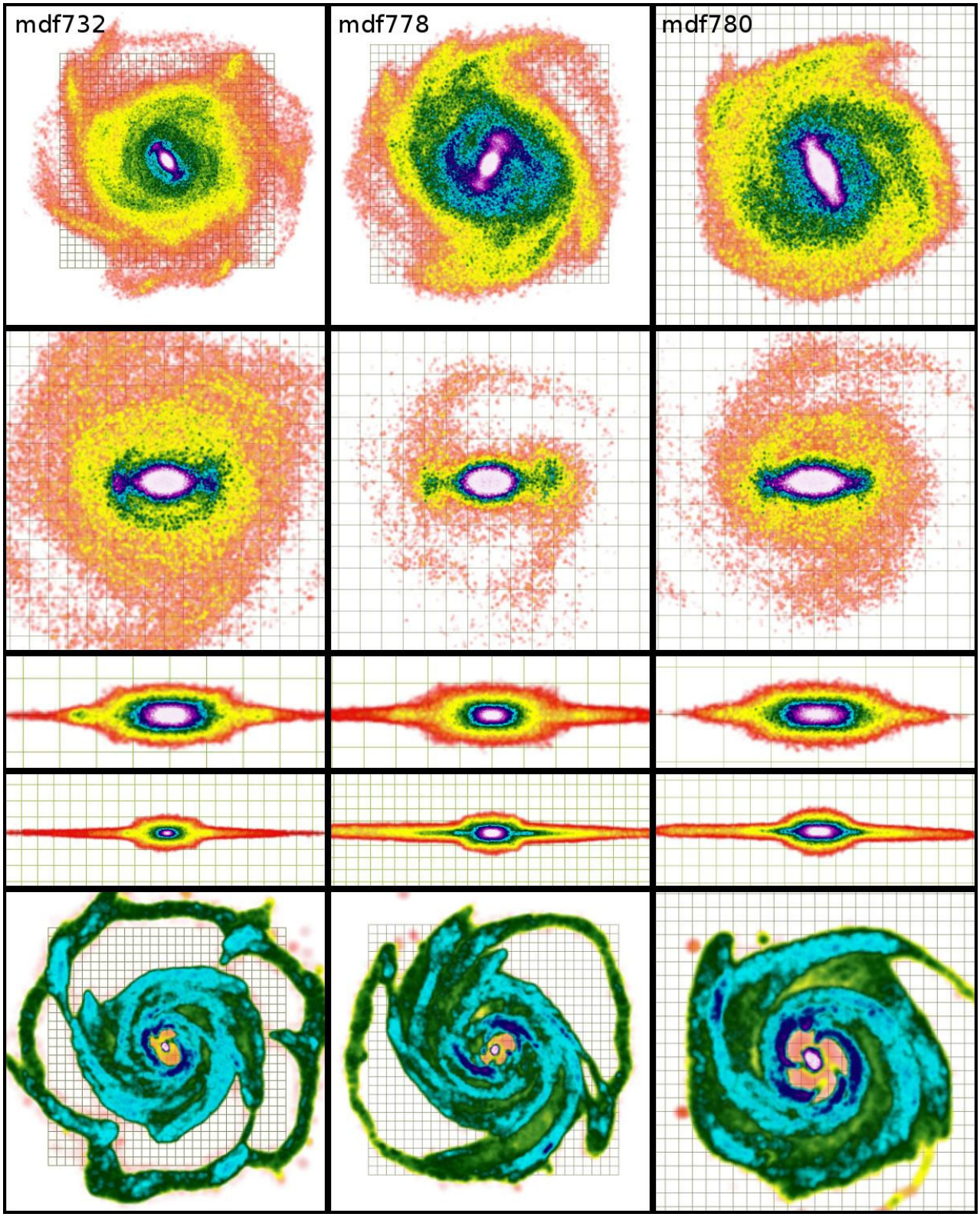

Figure 3. Morphology of the stellar (upper four rows) and gaseous (fifth row) disk components of our three fiducial simulations at t=10 Gyr. The uppermost panels give the face-on view and the second row zooms in the inner regions to highlight the face-on bar morphology. The fourth row shows the side-on view of the disk and the third row the side-on view of the bar region. The fifth row gives the face-on view of the gas distribution. To bring out best the features of interest (see text), we choose the color coding and linear resolution of each panel separately and include in the background a Cartesian grid with cells of 1×1 kpc size, to allow size estimates. In the second, third and fourth row the snapshot has been rotated so that the bar is along the x axis.

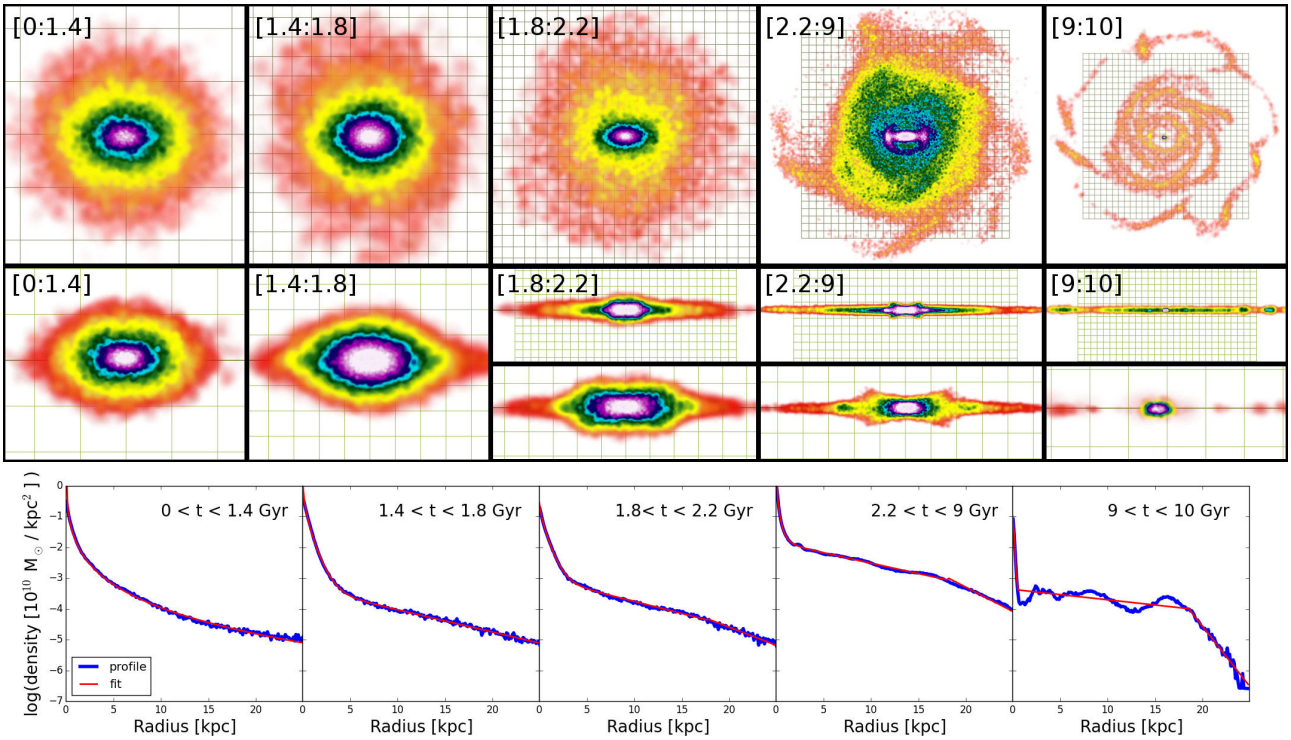

Figure 4. Five different stellar populations for mdf732 at t=10 Gyr, separated according to their time of birth (see text). Upper panels: Face-on views of the five populations. Middle panels: Edge-on views of the same populations. For the three youngest populations we include also a zoom of the inner parts to show best the morphology of the bar region viewed edge-on. For color coding and the background Cartesian grid see caption of Fig. 3. Lower panels: Surface density radial profiles of the five stellar populations as obtained from their face-on views (blue lines) and the corresponding decompositions (red lines). In the leftmost panel we used only one component, of Sérsic profile. The respective birth time ranges are given in the upper right corner of the lower panels.

a review, and references therein) came to the conclusion that bars have a rather complex shape. Namely their outer part is thin both when seen edge-on and face-on, while their inner part is thick again both viewed face-on and edge-on. Viewing the bars in our simulations from different angles, we find that they also have the above described morphology, arguing for a proper dynamical description of bars in our simulations and, most important, arguing that the observed bar shapes are compatible with a scenario of disk formation via major mergers.

The face-on bar morphology also agrees well with observations. In particular, the bar has ansae (Sandage 1961) and a barlens component (Laurikainen et al. 2014; Athanassoula et al. 2015). Seen side-on, the latter is usually referred to as a boxy/peanut/X bulge, but is in fact a part of the bar, i.e. consists of disk material and forms via disk instabilities (Athanassoula 2015, for a review).

The morphology of mdf778 shows a number of embedded structures, namely a bar of radial extent ∼3 kpc, an oval of radial extent ∼14.5 kpc outside the bar and two m=2 sets of spirals. The inner set is confined within the oval, while the outer one emanates from the ends of the oval, extends to larger radii (maximum ∼16.5 kpc) and falls back to the oval thus forming an outer pseudoring. Similar embedded structures can be seen e.g. in NGC 1566. The outer pseudoring and the oval have the same low pattern speed (∼18.5 km/sec/kpc), while the inner bar has a much higher pattern speed (∼43 km/sec/kpc). This morphology is very similar to that of manifold-driven outer spirals and pseudorings (Romero-Gómez et al. 2006; Athanassoula et al. 2009). Furthermore, for manifold theory the pattern speed of the oval and the outer spirals should be the same, as is the case in mdf778. The ultimate test, however, can be carried out with the help of the orbits of the particles in the spirals (Athanassoula 2012). Indeed in any density wave-based theory the orbits should traverse the arms, staying longer in the arm than in the interarm. On the contrary, in manifold theory the orbits of the particles start from one of the Lagrangian points nearest to the end of the bar (L_1 or L_2) and then follow the arm shape, outlining it, until they reach the opposite side of the bar. We followed the orbits of particles in the spirals and found that they stay within the spirals and outline them, i.e. these structures are manifold spirals as in the simulations of Athanassoula (2012). There is thus conclusive evidence for manifold spirals in mdf778.

The gas has, in all three cases, a qualitatively similar morphology to the stars. Note, however, that, contrary to the stars, the gas has a minimum in the central region of the galaxy of extent comparable to, but somewhat smaller than, the bar size. Further in, at a scale of 1 kpc or less, there is a strong concentration of gas. This morphology is in good agreement both with observations and with results of previous more idealised simulations (see e.g. Fig. 2 in Athanassoula 1992).

3.4. *Density and circular velocity profiles of the merger remnants*

The total stellar mass at the end of the simulation is around $5 \times 10^{10}\ M_\odot$ in all three simulations, i.e. these galaxies are Milky Way-sized. Fig. 1b shows the azimuthally averaged radial projected surface density profile of mdf732 at t=10 Gyr. Those of mdf778 and mdf732 are qualitatively the same. The outer parts in all three cases show a downbending truncation (i.e. of Freeman type II, e.g. Freeman 1970; Erwin et al. 2005; Muñoz-Mateos et al. 2013), which is the most common amongst the truncation types: ∼60% according to Pohlen & Trujillo (2006), or 42% according to Laine et al. (2014).

Fig. 1c shows the circular velocity curves for mdf732 at t=10 Gyr, both for the total mass in the galaxy, and for its basic components. It is calculated directly from the particle masses and positions in the simulation, without assuming spherical symmetry, contrary to a number of previous works. It is qualitatively the same for the other two cases. The total curve is fairly flat, with two shallow bumps due to the spirals. There is also a somewhat higher bump (15 – 20 km/sec) in the central region, due to the bulge. The ratio of the velocity due to the baryonic components to the total at 2.2 inner disk scalelengths is about 0.57 (mdf732), 0.62 (mdf778) and 0.69 (mdf780) of the total, Thus, relying on the Sackett (1997) criterion, mdf732 and mdf778 are clearly submaximal, while mdf780 is also submaximal but very near the borderline with maximum disks. Compared to the galaxies of the DISKMASS survey (Bershady et al. 2011, their Fig. 2), our three models have, for their circular velocity, amongst the highest fraction of disk mass of the survey, or even somewhat higher.

3.5. *Circularity parameter*

In a totally cold, perfectly axisymmetric disk, all stars will rotate with a velocity equal to the circular velocity. Stars in galactic disks, however, have some radial motion, albeit considerably less than their tangential one. At the other extreme, stars in classical bulges have strongly non-circular motions with considerable radial velocity components and with either direct or retrograde rotation. In between the two, there are stars in structures such as bars, ovals or lenses, whose motion is neither as circular as that of disk stars, nor as far from circular as that of classical bulge stars can be.

These different kinematics are reflected in the different values of the normalised angular momentum of a stellar orbit, known as the circularity parameter ε=J_z/J_{circ}, where J_z is the z component of the angular momentum and J_{circ} is the angular momentum of the circular orbit of the same energy (e.g. Abadi et al. 2003; Aumer & White 2013). Fig. 5a shows an example (red line) of a histogram of the number of particles as a function of their circularity for a snapshot with only a classical bulge and a disk component. This simulation is in all aspects identical to mdf732, except that no AGN feedback has been included (see Sect. 2.3 and Paper II). The classical bulge and the disk are clearly distinct and it is possible to distinguish disk from bulge stars simply by introducing a separation limit to their circularity value (ε_{lim}), which, as can be seen from Fig. 5a is situated around 0.5. We tested this kinematic way of distinguishing disk from classical bulge stars by viewing the spatial distribution of the two thus obtained populations separately and from various viewing angles and made sure that the disk is indeed adequately distinguished from the classical bulge component. After some trials, we found that ε_{lim}=0.5 gave quite satisfactory results and we adopted it. The stars that this method assigns to the disk(bulge) will hereafter be called 'kinematic disk(bulge) stars'.

A related, very useful quantity is the circularity at birth (ε_{birth}). As expected, this is very near 1 for stars born in the disk, but not for stars born in the bulge. Fig. 5b shows the fraction of stars of a given birth time which are born with $\varepsilon_{birth} > \varepsilon_{lim}$, as a function of their birth time, for mdf732 and as calculated for ε_{lim}=0.5 (red curve). Calculations using ε_{lim}=0.6 and 0.7 give quasi-identical results. Note that during the merging J_{circ} can not be adequately defined, so the curve includes only times after 1.55 Gyr. This curve shows considerable structure which will be discussed in the next subsection.

3.6. *Morphology and kinematics for populations of different ages*

It is expected that landmark times, such as the merging time, should set clear differences between the stellar populations born before and after them and we want to check whether this is indeed the case in our simulations and what the corresponding differences are. We will assess this by examining the t=10 Gyr snapshot of mdf732, to which all this subsection will pertain.

An obvious choice for the first landmark time is the merging time. In major mergers, however, there is no clearly and uniquely defined merging time and it is better to define a merging period, or time range. Furthermore, we want to avoid eye estimates of such times, because they can be biased and are not reproducible. We thus define the **b**eginning of the **m**erging period as the earliest time after which the distance between the centers of the two merging protogalaxies is always smaller than 1 kpc (t_{bm}). Although arbitrary, this time has the advantage of being clearly defined and reproducible. We define as the center of each galaxy what is often referred to as the center of density of its halo, calculated from the positions of the halo particles with the highest local density (as defined by the distance to their nearest neighbours, e.g. Casertano & Hut 1985). We measure the distance between the two progenitor centers and find the earliest time after which this distance stays smaller than 1 kpc. For mdf732 it is around 1.4 Gyr.

As a second landmark time, hereafter t_{bd}, we chose a time associated with the **b**eginning of the **d**isc formation and, more specifically, the time beyond which the vast majority of stars are born with disk kinematics. We estimate this by using ε_{birth}. Fig. 5b (red line, calculated for ε_{lim}=0.5) shows that the fraction of kinematic disk stars increases strongly with time of birth for up to 2.2 Gyr and that about 95% of stars born after this time have disk kinematics. We thus adopt t_{bd}=2.2 Gyr, after verifying that this value holds also for other reasonable values of ε_{lim}. We also introduced a third time at t_{by}=9 Gyr, which is somewhat arbitrary and not a landmark time, but is nevertheless useful because it sets a time such that any stars born after that can be considered **y**oung and thus allows us to focus on the distribution and kinematics of the youngest stars. For our snapshot, which is at 10 Gyr, the ages of the stars born at t_{bm}, t_{bd} and t_{by} are 8.6, 7.8 and 1 Gyr, respectively.

We can thus define five time intervals: namely [0,t_{bm}], [t_{bm},t_{hm}], [t_{hm},t_{bd}], [t_{bd},t_{by}] and [t_{by},10] where $t_{hm} = 0.5(t_{bm} + t_{bd})$. We then separate the stars in five groups according to which of the above time ranges they were born in, i.e. according to their age. We thus get five separate populations, and their respective number of stellar particles is 99369, 109035, 83960, 713081 and 47376. Their face-on and edge-on views are shown in Fig. 4. Corresponding kinematic information, separately for each of these five age groups, is given in Fig. 5c, which shows the distribution of stars as a function of their circularity at 10 Gyr (ε_{10}). Examining this morphological and kinematic information together, we find a number of important results:

- Stars born before the beginning of the merging period, i.e. that are older than 8.6 Gyr, (leftmost panels of Fig. 4) are concentrated in the innermost couple of kpc and their spatial distribution and radial density profile are that of a triaxial classical bulge. They are the oldest stars in the galaxy and experienced violent relaxation due to the strong evolution of the potential during the merging, thus explaining their very steep radial projected density profiles (Lynden-Bell 1967). Thus major mergers provide a mechanism for classical bulge formation. Some of these stars rotate prograde and others retrograde with respect to the disk, as expected for a classical bulge (Fig. 5c). There are, however, considerably more prograde than retrograde stars, i.e. the bulge has internal rotation. This is, at least partly, due to the bar, which can make the bulge more oblate (Athanassoula & Misiriotis 2002) and give it some spin (Athanassoula 2003; Saha et al. 2012).

- Stars born during the first half of the merging period (second column of panels in Fig. 4), i.e. with ages between 8.2 and 8.6 Gyr, have a density distribution similar to that of stars born before the merging, although more extended and more flattened. The outermost isodensities of the edge-on view are cusped, as one would expect from a relatively light underlying thick disk. This is corroborated from their angular momentum distribution (green line in Fig. 5c), which shows a considerable contribution of stars with ε_{10} near but somewhat less than 1.

- Stars born during the second half of the merging period (third column of panels) have a very different density distribution from that of the two previous groups. They trace in the outer parts a disk extending well beyond the bulge region and in the inner parts a bar with a vertically thick boxy bulge (Athanassoula 2005). Their circularity distribution (Fig. 5c, red line) also shows the existence of two components, a fast rotating component, i.e. a disk; and a slower component rotating with an average ε_{10} around 0.25. Checking out the spatial distribution of the stars in the latter component we found that it is the bar (see also Sect. 3.7). Thus the stars born in this time range contribute partly to the near-axisymmetric disk and partly to the bar.

- The stars within the two last age ranges (younger than 7.8 Gyr) were born during the disk formation era and are thus part of what is commonly referred to as the disk population. This disk is extended and quite thin. Except for the axisymmetric disk, the stars in the fourth age bracket contribute also to the spirals and to the bar. For this group of stars, the ansae at the extremities of the bar are clearly visible, and at smaller radii, there is an X-like edge-on shape, as in many barred galaxies. Note that both the disk and the bar are vertically thinner than the corresponding structures in the third age bracket.

  On the other hand, the stars which are younger than 1 Gyr do not participate in the bar structure, but are heavily concentrated in the spiral and ring structures, as well as in an innermost very thin structure, which can be called a disky pseudobulge (Kormendy & Kennicutt 2004; Athanassoula 2005). The latter may well exist in the third and fourth age brackets as well, but is less easily discernible in plots as in Fig. 4, because of the strong bar contribution to the central parts.

  The kinematics of these two youngest age ranges (Fig. 5c) corroborate the above. In particular, they show that the stars of the fourth age range contribute partly to the disk and partly to the bar (see also Sect. 3.7). On

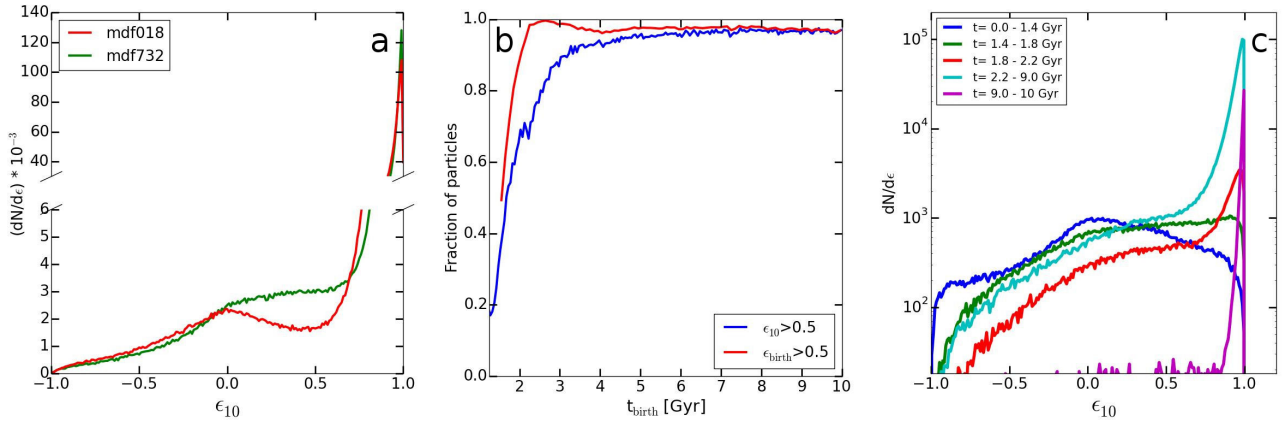

Figure 5. Identifying disk stars kinematically. Left: Distribution of the number of particles as a function of their circularity parameter for two snapshots. In one of these (red) the stars are basically either in a classical bulge, or in a disk. In the other (green) it is clear that there is a further component. Middle: fraction of stars with ε>0.5 at birth (red) and at 10 Gyr (blue). Right: Distribution at $t = 10$ Gyr of particles as a function of their circularity parameter ε_{10}, given separately for the stars in each of the five time of birth brackets as in Figs. 4. The adopted bin size in both the rightmost and the leftmost panel is $\Delta\varepsilon$=0.01.

the other hand, the stars in the youngest age bracket contribute essentially only to the disk, and more specifically (Fig. 4) to its spirals, rings and the disky pseudobulge.

In the lower panels of Fig. 4 we show the projected density radial profiles of each of the five stellar populations, obtained from their face-on views. The oldest population is well fitted by a single Sérsic component with an index between 4.5 and 6, i.e. corresponding to a classical bulge (Kormendy & Kennicutt 2004; Drory & Fisher 2007). At the other extreme, the youngest population can be fitted by three exponential disks, the innermost one corresponding to a disky pseudobulge, and the two next ones to the inner and outer disks, respectively. Thus, in general, the classical-bulge-to-total stellar mass ratio decreases with the age of the population from 100% to 0%.

3.7. *Coupling kinematics and morphology to identify disk stars*

In Sect. 3.5 we discussed a simple way of distinguishing the classical bulge population from that of the disk for snapshots with only these two components. We now extend this to snapshots with bars and/or ovals and apply it to mdf732 at t=10. The corresponding circularity histogram is given in Fig. 5a (green line). As expected, the distribution is now much more complex. Namely there is clearly additional material between the disk and the bulge components and applying a simple separating criterion to ε would not suffice if an important fraction of stars is in the bar component. Independent of their ε, bar stars should be considered as part of the disk component, since the bar forms from a disk instability which rearranges the disk material. We therefore conclude that not only all stars with $\varepsilon > \varepsilon_{lim}$ belong to the disk, but also a considerable fraction of those with $\varepsilon < \varepsilon_{lim}$. Thus a more elaborate analysis will be necessary for galaxies with bars.

We therefore divide stars into groups, depending on three physical properties, namely whether their time of birth is before or after t_{bd}, and on whether their kinematics at birth and at 10 Gyr are disk-like or bulge-like. The latter two are ensured by testing whether their circularity at birth and at 10 Gyr (ε_{10}) is bigger or smaller than ε_{lim}. In this section, as in Sect. 3.5, we describe results obtained with ε_{lim}=0.5. We tried, however, also other values and reported some of the corresponding results in Sect. 3.8.

This division creates in total eight groups of stars, described in Table 1. Groups G1 to G4 include all stars born after t_{bd}, while groups G5 to G8 all stars born before t_{bd}. We viewed each group separately in 3D from different angles to assess its shape and morphology and we also made projected surface density profiles, both radial and vertical and for different cuts. Whenever a bar is present in the group we calculated its position angle (PA) and, comparing the PA found for all groups, we found that they all agree to within 5°, i.e. to within the accuracy of the estimates. We now consider all this information together.

Group G1 consists of stars with disk kinematics, both at birth and at 10 Gyr. Fig. 6 (leftmost panels) reveals a thin disk with a strong global spiral structure and a rather weak bar. Its projected density profile (not shown) is exponential with a small central bump due to the bar. It is thus clearly a disk population and comprises 66% of the stars.

Stars in group G2 were born with disk kinematics, and by 10 Gyr evolved to non-disk kinematics. Morphology and photometry of G2 show that 95% of G2 stars form a bar and the remaining 5% a disk component around it. The bar in G2 has roughly the same orientation and length as that of G1, but is considerably fatter horizontally. Seen edge-on, it has a clear boxy/peanut structure. Most of the stars in G2 were born very soon after t_{bd}, while those of G1, G3 and G4 are more evenly spread between t_{bd} and 10 Gyr. Thus the stars in G2 are, on average, older than the stars in other groups. Their circularity argues that they were born in the axisymmetric disk and were trapped by the bar as this grew. G2 comprises 4.56% of the stars.

G3 has disk kinematics at 10 Gyr, but not at birth, while G4 does not have disk kinematics either at 10 Gyr or at birth. The stars in those two groups are concentrated in an inner triaxial object of size roughly 1.4:0.7:0.5, whose PA is, within the errors, the same as that of G1 and G2. Thus it can be considered as an inner part of the bar, presumably part of its barlens component (Laurikainen et al. 2014; Athanassoula et al. 2015). Together, G3 and G4 comprise only 1.65% of the stars.

Groups G5 to G8 consist of stars with $t_{birth} < t_{bd}$. For most of these stars it is not possible to calculate ε_{birth} because the center of the remnant at such times is not well defined. Instead, we calculate ε at t_{bd} (ε_{bd}), because, although this is early on in the evolution, it is sufficiently late for the center of

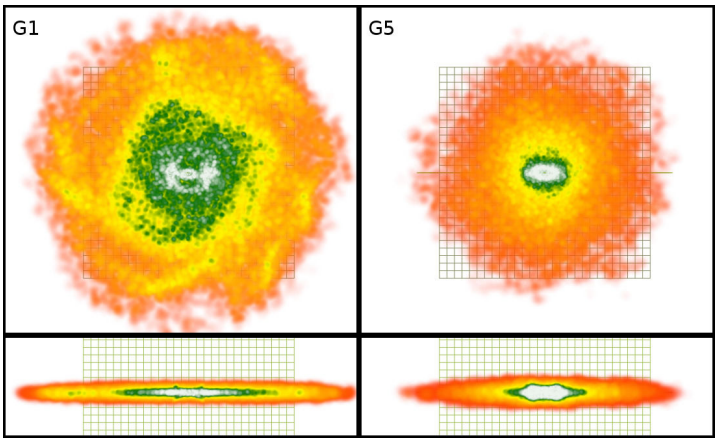

Figure 6. Components G1 and G5 at t=10 Gyr. Face-on (upper subpanels) and edge-on (lower subpanels) views of group G1 (left) and G5 (right) in mdf732 at 10 Gyr. All four subpanels have the same linear scale. The color coding was chosen so as to bring out best the morphological features of interest here.

Table 1
Basic properties of the eight groups

Group	Birth time	ε_{birth}, or ε_{bd}	ε_{10}	Fraction
G1	$t_{birth} > t_{bd}$	$\varepsilon_{birth} > \varepsilon_{lim}$	$\varepsilon_{10} > \varepsilon_{lim}$	0.660
G2	$t_{birth} > t_{bd}$	$\varepsilon_{birth} > \varepsilon_{lim}$	$\varepsilon_{10} < \varepsilon_{lim}$	0.046
G3	$t_{birth} > t_{bd}$	$\varepsilon_{birth} < \varepsilon_{lim}$	$\varepsilon_{10} > \varepsilon_{lim}$	0.003
G4	$t_{birth} > t_{bd}$	$\varepsilon_{birth} < \varepsilon_{lim}$	$\varepsilon_{10} < \varepsilon_{lim}$	0.013
G5	$t_{birth} < t_{bd}$	$\varepsilon_{bd} > \varepsilon_{lim}$	$\varepsilon_{10} > \varepsilon_{lim}$	0.091
G6	$t_{birth} < t_{bd}$	$\varepsilon_{bd} > \varepsilon_{lim}$	$\varepsilon_{10} < \varepsilon_{lim}$	0.040
G7	$t_{birth} < t_{bd}$	$\varepsilon_{bd} < \varepsilon_{lim}$	$\varepsilon_{10} > \varepsilon_{lim}$	0.024
G8	$t_{birth} < t_{bd}$	$\varepsilon_{bd} < \varepsilon_{lim}$	$\varepsilon_{10} < \varepsilon_{lim}$	0.123

the remnant to be clearly identified.

The stars of group G5 constitute at 10 Gyr a thick disk (Fig. 6) with no spirals and with a bar of roughly the same length and PA as that of G1, but much fatter in the plane and with no ansae. This thick disk comprises 9.08% of the stars.

Stars in group G6 basically compose a bar, similar in shape and outline to that of G5, while a few of them are in a thick disk, similar to that of G5. They comprise 3.99% of the stars.

Groups G7 has too few stars for us to be able to classify. It comprises 2.37% of the stars.

Most of the stars in group G8 belong to a flattened bulge, as argued by morphology, photometry and kinematics together. G8 isophotes have a bar like deformation in their central part, analogous to the 'halobar' found in the central parts of halos (Colin et al. 2006; Athanassoula 2007). G8 comprises 12.3% of the stars.

The above procedure distinguishes the disk from the classical bulge component. Groups G1, G2, G5, G6 are unambiguously linked to the disk, and this most probably is true also for G3 and G4. Indeed, they contribute mainly to the bar and, more specifically, to its inner parts. Most of group G8 is linked to the classical bulge. G7 is presumably linked to the bar, i.e. it is a disk population, but this is not as sure as for the other, above-mentioned disk components. Nevertheless, the uncertainty this entails is very small, 2 – 3%.

Note also that the stars in the thick disk are older than those in the thin one, as they were born earlier in the simulation and in a rather restricted time interval, roughly between 1.4 and 2.2 Gyr, i.e. at t=10 Gyr they have an age between 8.6 and 7.8 Gyr. Thus the oldest stars in this model are in the classical bulge, followed by those in the thick disk, while the youngest are in the thin disk.

3.8. *B/T mass ratio*

In Table 2 we give various estimates of the B/T ratio in our three fiducial simulations at t=10 Gyr, as well as some close upper limits. Columns 1 and 2 give the run number and t_{bd}, respectively. Columns 3 to 8 give results for the method described in Sect. 3.7, where we extended the simple kinematic decomposition of the stars into a disk and a bulge component, to cases with a bar. There we identified most of group G8 as the classical bulge component and the corresponding B/T values are given in columns 3 to 5 of Table 2. We were, however, unable to safely identify whether G7 should be considered as a disk or a classical bulge component, so we will for safety also include an estimate based on the sum of the two components, as an upper limit (columns 6 to 8). We applied this with ε_{lim}=0.5 (columns 3 and 6), the value we have found to be more appropriate (Sect. 3.5) and 3.7, but also with ε_{lim}=0.6 (columns 4 and 7) and even ε_{lim}=0.7 (columns 5 and 8), the last two, and particularly the last one, being more like upper limits. As expected, the smallest values are when identifying G8 to the classical bulge and using ε_{lim}=0.5, while the largest are the upper limits obtained when identifying G7 and G8 together to the classical bulge component and using ε_{lim}=0.7. It is, however, very reassuring that the differences are small, showing that the upper limits are close to the most probable values.

Hopkins et al. (2009) introduced a different, much simpler and more straightforward method to obtain an estimate of B/T. Namely, they assume that the bulge has no global rotation and that it is the only component that includes nega-

Table 2
Classical bulge to total stellar mass ratio, calculated in four different ways.

run	t_{bd}	G8 (0.5)	G8 (0.6)	G8 (0.7)	G8 + G7 (0.5)	G8 + G7 (0.6)	G8 + G7 (0.7)	Hopkins 2009	Surface density
mdf732	2.2	0.12	0.14	0.16	0.15	0.16	0.18	0.18	0.09 – 0.15
mdf778	2.2	0.11	0.13	0.15	0.13	0.15	0.17	0.19	0.10 – 0.18
mdf780	2.8	0.18	0.21	0.24	0.22	0.24	0.27	0.25	0.09 – 0.11

tive ε values. Under these assumptions the contribution of the bulge is equal to twice the mass of particles that have negative velocities. This was introduced for disk galaxies with no bars, where the two above assumptions are very reasonable to make. However, as discussed in Sect. 3.6 and the references therein, bars, although part of the disk population, do not have disk kinematics. Furthermore, they can transmit angular momentum to the classical bulge, so that for strongly barred galaxies the estimate from this method can be considered as approximate. We apply it to our simulations and find values to within 10% of our upper limits (Table 2). It is useful to have established this agreement, because the Hopkins et al. method is easy to apply and was used in a large number of previous cases.

To get a third, independent estimate of B/T, we used a decomposition of the radial projected density profile, obtained by averaging the density in cylindrical annuli in the face-on view of the disk. This decomposition is similar to the 1D decompositions used by observers for the radial luminosity profiles and, although 1D, it is not straightforward, since the innermost regions may include either both a classical and a disky pseudobulge, or one of the two only. Depending on exactly how the decompositions are done, we find values for mdf732 between 0.09 and 0.15, for mdf778 between 0.10 and 0.18 and for mdf780 between 0.09 and 0.11, i.e. somewhat lower than, but in good agreement with the kinematic estimates.

The values of the B/T ratio we find here are considerably smaller than those found in previous simulations with no hot gas in the halo. Such simulations are well summarized in Hopkins et al. (2009), where, out of several hundred simulations, only five have $B/T \leq 0.2$, and, moreover, these five have 1:8-1:10 progenitor mass ratios. On the contrary, our B/T values are compatible with those of observed spiral galaxies and do not exclude that such galaxies were formed from major mergers. This is a big improvement over past works and is due to the existence of a hot gaseous halo in the progenitors, which is carried over in the merger remnant. Indeed, as we showed in the previous subsections, the mass of the classical bulge (B) is roughly set by the number of stars that formed before the merging. On the other hand the mass of the disk is mainly due to stars that formed after the merging. Due to the gaseous halo, the accretion of gas on the disk continues well after the merging, up to the end of the simulation and presumably well after it. It thus leads to a more extensive and more massive disk than what would be found in the absence of a gaseous halo, and, therefore, smaller B/T values. Comparisons for more simulations and the effect of various progenitor properties and orbital parameters on the B/T values will be given elsewhere.

Observations show that there are spirals, in particular relatively small late types, with no, or hardly any, classical bulge (Kormendy et al. 2010). Our own Galaxy has a classical bulge of low mass (e.g. Shen et al. 2010; Ness et al. 2013a,b), but it is premature to state that it has no classical bulge at all. Our simulations produced considerably lower B/T values than previous ones considering major mergers. So far, however, none of our simulations gave results compatible with a total lack of classical bulge. This is a general problem of all disk galaxy formation studies and may be solved by changing the feedback recipes, as attempted in cosmological simulations (e.g. Brook et al. 2012; Brooks & Christensen 2015). Here let us simply note that major mergers should be rarer in low density environments, thus if bulgeless disks are found solely, or predominantly, in such environments their hosts may well not be major merger remnants. Moreover, our aim here is to test whether major mergers may produce disk galaxies, but certainly not to show that they are the only way of making them. Thus it is not necessary for our scenario to be able to form disk galaxies with no classical bulge at all. .

3.9. *The thick disk component*

When examining the group G5 in mdf732 at 10 Gyr (Sect. 3.7), we found that its stars form a thick disk (Fig. 6). We will now discuss its properties further and compare them to those of observed thick disks. Such a comparison can only be approximate because other groups may also host some thick disk stars. For example, thick disk formation will not stop abruptly at time t_{bd}, but will continue at subsequent times, albeit presumably at a tapered rate. Moreover, some stars born in the thin disk will be vertically heated, e.g. by the spirals, and thus contribute to the thick disk. Yet it makes sense to use G5 for comparisons with observations, because it is defined using physical criteria (Sect. 3.7) and, furthermore, it is a main, presumably *the* main, contributor to the thick disk. We will thus use here group G5 as a proxy, and loosely refer to it as the thick disk component. Note also that even in observations there is more than one way to define the thick disk. Thus Yoachim & Dalcanton (2006), Comeròn et al. (2011b, 2012) and Streich et al. (2015) use different methods and/or different fitting functions, thus introducing considerable differences in the results.

In the disk formation scenario which we consider, the thick disk forms naturally, in agreement with the observational claim of thick disk (near-)ubiquity (Yoachim & Dalcanton 2006; Comeròn et al. 2011a, but see also Streich et al. 2015).

Contrary to the thin disk, the simulated thick disk has no spirals, or then of such low amplitude that they are not discernible by eye. This should be linked to the fact that both density wave (Lin 1967) and swing amplification theories (Toomre 1981) show that hotter and thicker disks will harbour lower amplitude spirals. A similar result presumably holds also for a manifold origin, because it is more difficult to confine a hot stellar population than a cold one (see also Romero-Gómez et al. 2006), but no specific quantitative study has yet been made.

By definition, the stars in group G1 were born after t_{bd}, while those in group G5 before that. Thus the stars in the thick disk are older than the stars in the thin disk, in agreement with

observations (e.g. Mould 2005; Yoachim & Dalcanton 2008; Comeròn et al. 2015).

The bar in the thick disk has the same length and orientation as that of the thin one, but is much thicker in the disk plane than that of G1, as would be expected from previous work (Athanassoula 1983, see also Athanassoula 2003), where it was shown that the bar is thicker in the disk plane in the case of hotter disks. Note also that the bar in the thick disk has no ansae and, viewed side-on, it has a boxy/peanut bulge with a considerably larger vertical extent than that of the thin bar. According to this scenario, and since the thin and the thick disks co-exist, the bar component in observed galaxies will include contributions from both thin and thick disks, so that various parts of the bar may have different mean stellar ages.

Observations (Yoachim & Dalcanton 2006; Comeròn et al. 2012) show that the ratio of thick to thin disk mass is a decreasing function of the circular velocity, so that more massive galaxies have a relatively less massive thick disk. Yoachim & Dalcanton (2006, see caption of their Fig. 22) provide a simple fitting formula for this decrease, which, although poorly constrained for massive galaxies, has the advantage of fitting the whole mass range. Applying it for V_{circ}=210 km/sec, we find a ratio of thick to thin disk masses of 0.10, which, given the uncertainties due to the extrapolation, is in good agreement to the value of 0.14 we found in Sect. 3.7.

We calculated the mean tangential velocities of G1 and G5 in an annulus between 5 and 15 kpc from the center. This adopted radial range is not optimum, since it includes mainly large radii where the difference of the two means will be relatively small, but it was chosen so as to avoid the bar region, where the kinematics depend mainly on the strength of the bar, and only indirectly on the disk thickness. We find 209 and 197 km/sec for the thin and the thick disk respectively, values which are as expected in both sense and amplitude. They are also in agreement with the results of Yoachim & Dalcanton (2008), who find that for the higher mass galaxies in their sample, they fail to detect differences between the thin and the thick disk kinematics.

3.10. *On the role of the halo gas*

As already discussed in Sect. 2 and 3.1, our protogalaxies acquire a baryonic (stellar plus gaseous) disk before the merging. Thus our simulations describe the merging of two disk protogalaxies with a halo composed of DM and gas. We will here examine the role of the halo gas on the formation and evolution on the ensuing disk galaxy by tracking the origin of gaseous and stellar particles and by comparing cases with and without halo gas. We will thus use two different approaches:

3.10.1. *Tracking the origin of gaseous and stellar particles in the disk*

In this first approach we will use mdf732 to disentangle the gas which would be present in simulations with a gaseous disk but no gas in the halo, from the gas which is present in simulations including a gaseous halo (i.e. all the gas in our simulations). We track each of these two separately and follow how each one evolved up to 10 Gyr, i.e. the end of the run. We also take into account that each gas particle may have stayed in gaseous form or it may have turned into a stellar particle.

In order to disentangle the gas origin we use a snapshot at t=0.85 Gyr. This roughly corresponds to the time of the apocenter following the first pericenter. We also tried other times, between 0.7 and 0.9 Gyr and found qualitatively the same and quantitatively very similar results. Since the equatorial planes of the two protogalaxies coincide with the orbital plane, we can roughly define as halo gas all gas particles with $|\Delta z|$ >1 kpc, so that the gas which would be present in a simulation with no gaseous halo is only the gas with $|\Delta z|$ <1 kpc. The latter includes the gas in the two protogalactic disks before the merging as well as the gas in the tails formed during the interaction. It is important to include the gas in the tails because it moves initially outwards but eventually turns back at larger distances from the center and falls back towards the remnant disk. We can thus roughly assume that by tracking the gas with $|\Delta z|$ <1 kpc we follow the gas that would be present in a simulation with no gas in the halo. Of course the slab $|\Delta z|$ <1 kpc will also contain some halo gas, so that the above rough decomposition gives an upper limit of what the gas in cases with no halo gas can do. This upper limit, however, should be quite near the actual value.

Fig. 7a shows the mass found in the remnant disk still in gaseous form as a function of time, both including (red line) and excluding (blue line) the gas in the halo. The former shows a much weaker decrease with time (less than a factor of 2.5 between 3 and 10 Gyr) than the latter (more than a factor of 10 in the same time). This is clearly due to the gas accreted from the halo, which leads to much more gas-rich disks all through the simulation and a slower gas mass decrease.

Fig. 7b gives a similar comparison, but now for the stars. Here we compare the stellar mass formed in cases with no gaseous halo (blue line) to all disk stars (independent of the origin of the gas they were born from – red line). The latter shows a steady increase with time, compared to the former which is nearly constant. More specifically we witness an increase by a factor of 2.4 for the latter compared to barely a factor of 1.1 for the former.

Fig. 7c gives the ratio of gaseous to total baryonic mass as a function of time. This decreases from 0.37 at 3 Gyr to 0.092 at 10 Gyr when halo gas accretion is included, while it decreases from 0.1 to 0.01 in the same time range when accretion from the halo is not included.

To summarise, both the stellar and the gaseous disk are more massive when the accretion from the halo gas is taken into account, as expected, while the gas fraction in the disk is more compatible with that of spiral galaxies.

3.10.2. *A test simulation*

To deepen our understanding of the effect of the halo gas component on the disk galaxy formation and evolution we ran a further simulation. As initial conditions we used a snapshot of simulation mdf780 at t=1.77 Gyr, in which we replaced the low density gas particles (local density $< 5\times10^{-4}$ $M_\odot$ /pc^3) by collisionless particles. These had the same mass and positions as the gas particles they replaced, and their velocity was taken from the velocity distribution of the halo (as e.g. in Rodionov et al. 2009), in order to preserve as much as possible the dynamical equilibrium of the system. We also verified that this gas was essentially in the halo and that the gas in the disk and in the tidal tails was not affected by this change. This is run mdf223, which we compare to mdf780 in Fig. 8. Even a cursory glance shows that there is quite important differences between their mass distributions. The disk in mdf780 is much more extended and massive than that of mdf213. These results are in agreement with what we already discussed from the analysis of mdf732 in Sect. 3.10.1 and the two together show that the gaseous halo plays a crucial role in the formation and evolution of the disk.

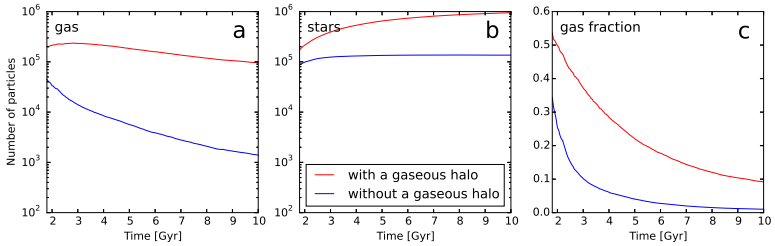

Figure 7. Number of gaseous (left panel) and stellar (middle) particles in the disk component as a function of time. The rightmost panel shows the gas fraction, again as a function of time. Red (blue) stand for a merging of two progenitors with (without) a gaseous halo (see Sect. 3.10.1 for a description).

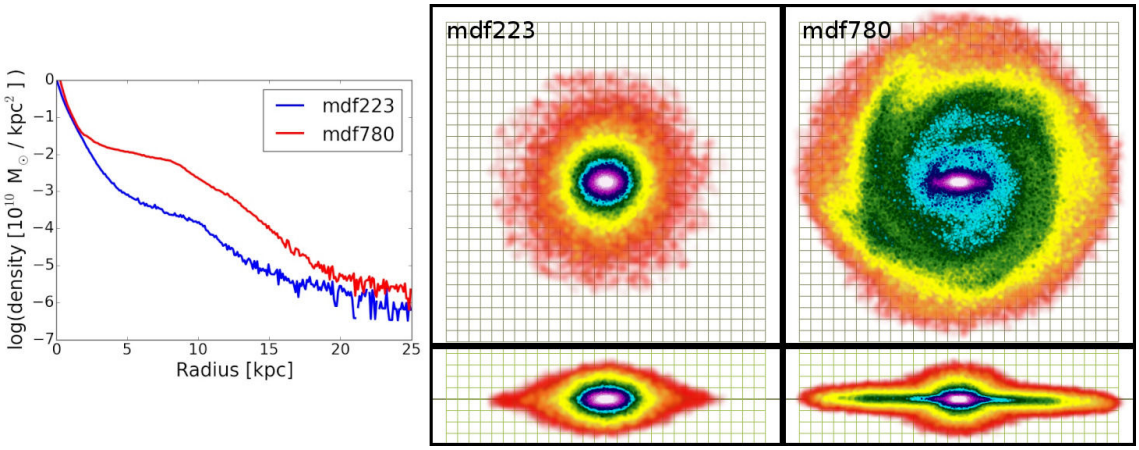

Figure 8. Comparison of two simulations, one with (mdf780) and the other without (mdf223) a hot gaseous halo, both at time t=10 Gyr. Left: The radial projected stellar surface density profiles. Middle: Face-on (upper) and edge-on (lower subpanels) views for mdf223. Right: Same for mdf780. Note the big difference in the disk extent and in its mass relative to the classical bulge component.

4. A SIMPLE SCENARIO FOR THE FORMATION OF DISK GALAXIES

Putting together the results from the previous section, we can outline the following simple scenario of disk formation via major mergers.

Two spherical protogalaxies, composed of DM and hot gas, are on an orbit leading to a merger. From the onset of the simulation, however, the gas in each halo cools radiatively and, getting out of equilibrium, falls inwards. Its density increases locally and the first stars form. Thus, the progenitors gradually acquire a disk and by the time the merging starts, the two progenitors can be described as disk protogalaxies, i.e. disk galaxies which are smaller and more gas rich than present day galaxies.

During the merging period the potential changes drastically during a relatively short period of time. Therefore most of the stars which were formed before the beginning of the merging period will undergo violent relaxation and will form a spheroidal bulge. Concurrently, a considerable fraction of the gas in the progenitor falls inwards and forms stars in the same bulge area. Most of the remaining disk gas moves outwards and forms, together with some of the outermost stars, extended tails.

A number of stars, particularly those born near the end of the merging period, will not be part of the bulge, but will form a thick disk.

After the end of this merging phase, the evolution stops being violent and becomes secular. The material in the tails gradually reach apocenter and fall back towards the center of the remnant. However, most of the gas accreting on the disk comes from the hot gaseous halo and forms a thin extended disk. In our three fiducial simulations this disk is bar unstable and a bar component grows concurrently with the disk. As in isolated disk simulations (Athanassoula 2015, for a review), this bar is composed of two parts an outer thin bar and an inner thick one. The latter is often referred to as the boxy/peanut/bulge but in fact is only the inner part of the bar grown from disk instabilities. The stars forming during the most recent times can be found in spirals, mainly grand design, as well as in a disky pseudobulge.

Very schematically, the formation of disk galaxies from a major merger can be seen as a three-stage process. The stars born before, or at the beginning of the merging period will undergo very strong and abrupt changes of the potential in which they evolve and therefore be subject to violent relaxation. They will constitute the classical bulge, and will be the oldest in the galaxy. Stars born around the end of the merging period will still feel considerable changes of the potential. These, however, are less strong and abrupt than those felt by the older stars, so that they are only strongly shuffled and end up in a thick disk component. Stars which are born well after the end of the merging period are born in near-circular orbits near the equatorial plane of the galaxy and form the thin disk. Thus, according to our scenario, the sequence from classical bulge, to thick disk, to thin disk should be a sequence of stellar age, with the stars in the classical bulge being the oldest and those in the thin disk being the youngest. The amount of perturbation they went through also decreases along the same sequence, from violent relaxation, to simple secular evolution. Furthermore their vertical thickness also decreases in the same way, from the triaxial classical bulge spheroid, to a thick and then a thin disk.

Of course once the thin disk is even partially in place, its evolution will be driven by its instabilities which will form the observed components of disk galaxies, such as bars, spirals, lenses, rings etc. Gas will be pushed inwards, either by the bar or spirals, or by various asymmetries in the merging or post-merging phases. This can form the disky pseudobulge, which will, therefore, have a considerable amount of young stars and gas, but also include some older stars.

Thus the major merger scenario can account for many observational constraints.

5. SUMMARY AND CONCLUSIONS

This paper is the first of a series using N-body simulations to test whether the remnants of early major mergers can be spiral galaxies. Our main improvement with respect to previous work on this specific subject is that each of the progenitor galaxies in our simulations has a hot gaseous halo component and these merge together in a hot gaseous halo of the merger remnant. We also have a larger number of particles, by as much as an order of magnitude compared to many previous simulations. Furthermore, we introduced a simple but effective AGN feedback model, which quenching star formation avoids excessive central mass concentrations of the remnants, thus leading to realistic shapes of the inner part of their rotation curves and allowing bars to form.

Contrary to previous work on this specific subject, our initial conditions do not mimic local galaxies, they are spherical distributions of DM and gas. Before including them in the merging simulations, we followed their growth in isolation and found that during the first few Gyr they form disk protogalaxies compatible with observations of disk galaxies at intermediate redshifts. In particular, they are dynamically less relaxed and much smaller than local galaxies, growing inside-out at a rate which is strong initially but decreases with time. They are also much more gas rich than local galaxies, with a gas fraction which decreases steadily with time, again at a faster rate during the earlier times. Thus what merges in our simulations are disk protogalaxies, more compatible with observations of galaxies at intermediate redshifts than with local ones.

To get both qualitative and quantitative estimates of the effect of the gaseous halo on the disk formation process in our scenario we used two different approaches. Both showed clearly that the presence of the gaseous halo leads to stellar and gaseous disks which are more massive and more extended. Star formation continues all through the simulation, so that there will be young stars at all times, as expected. On the contrary, if no gaseous halo is included, the amount of gas decreases with time and star formation grinds to a halt. Thus our improvement will allow us to discuss elsewhere in this series the chemical evolution and population synthesis in galactic disks.

In our model, the progenitor disks are destroyed by violent relaxation during the merging, but a new disk forms in the remnant, mainly composed of material that is gradually accreted from the halo after the merging and up to the present time. Thus, the formation of the bulge is due to a violent event, the merging, while the formation of the disk is secular. Furthermore, the existence of a sizeable disk in the major merger remnant by the end of the simulation does not argue that the disks survived major mergers, but that a new disk forms after the merging. This will have implications for the chemical composition and colors of the galactic disk, as expected, and as we will discuss in a future paper.

All three of our remnant examples have a thin, extended disk and a classical bulge. The projected radial density profiles of the disks are of type II, i.e. have downbending truncations. The rotation curves are flat and show that the disk is submaximum in all three cases, albeit only borderline so in one of the three. The disk has substructures, which our resolution allows us to examine. In particular we find bars, spirals, ovals, rings and disky pseudobulges. In all cases, their morphology is very realistic. Bars have both a thin and a thick component, the latter being better known as a boxy/peanut bulge. They also have ansae. Note that all three types of bulges – classical, disky pseudobulges and boxy/peanut/X – are simultaneously present, as in observations (e.g. Erwin 2008, and references therein), as could be expected from the scenario we present here. We also found ovals and realistic inner and outer rings and pseudorings. By following the orbits of individual stellar particles in the simulations, we found conclusive evidence that at least in one of the three simulations the spiral is of manifold origin.

A separate thick disk component forms naturally in our simulations, as would be expected from the very common, if not ubiquitous appearance of these structures in observed disk galaxies. Their properties – such as their mass, mean tangential velocities, substructures and the age of their stellar populations – are compatible with both observations and previous theoretical work.

We introduced a new method for distinguishing the bulge stellar particles from those of the disk and its substrucures. This couples information from stellar ages, kinematics, morphology, spatial distribution and projected surface density profiles. It is rather precise, albeit not straightforward. We compare the results with those of a straightforward method proposed by Hopkins et al. (2009) and find very good agreement for cases with no bar. This agreement, however, becomes less good for cases with bars and can be unsatisfactory for cases with very strong bars.

In our three fiducial simulations, we find that at t=10 Gyr, the mass of the classical bulge is, on average, between 10 and 20% of the total stellar mass, i.e. values much smaller than in previous works, as required in order to agree with the lower B/T values of spiral galaxies. This improvement is a corollary of the existence of a hot gaseous halo in our initial conditions, as this entails a slow formation and evolution of a massive disk. Indeed the mass of the classical bulge is set by the number of stars formed before the merging, i.e. depends relatively little on the existence of the gaseous halo, while the thin disk is much more massive in cases with such a component.

This, however, does not mean that all disk galaxies which are remnants of major mergers of protogalaxies with a gaseous halo will have such small classical bulges. We will present many examples with more massive classical bulges elsewhere. Note also that we were unable to form disk galaxies with no classical bulge at all. This is in agreement with the discussion in Kormendy et al. (2010), which argues that such bulgeless galaxies would be mainly found in low density environments where major mergers would be rather rare.

We are also able to build a sequence of components, according to the time of formation of their stars. The oldest stars are found in the classical bulge, since they are actually formed before the merging. The stars in the thick disk are the next to form, followed by the intermediate age stars in the disk and bar. The youngest stars can be found in the spirals and in a disky pseudobulge. Furthermore, based on the ensemble of our results, we are able to propose a simple scenario for the

formation of disk galaxies in major mergers.

We made a number of comparisons of our results with observations of spiral galaxies and found nothing that could exclude the possibility of forming such galaxies in major mergers of disk galaxies. We can thus consider the work presented here as a first "proof of concept" that remnants of major mergers of two disk galaxies with a hot gaseous halo component can be spiral galaxies. Elsewhere we will discuss more examples with various morphologies, B/T ratios, and kinematics, as well as specific dynamical aspects. We will thus be able to make more complete and detailed comparisons with observations which, in turn, will allow us to answer fully whether major mergers are a possible way of making disk galaxies, or not.

APPENDIX

In this appendix we briefly review the nomenclature we use in this paper regarding bulges. More extended discussion on this and specific references can be found in Kormendy & Kennicutt (2004), Athanassoula (2005,2015), Drory & Fisher (2007), and Fisher & Drory (2015).

Bulges are not a homogeneous class of objects. We here distinguish between classical bulges and disky pseudobulges. The former have a spheroidal shape and a Sérsic projected density profile with a large exponent, above say 2.5. They rotate relatively little, with V_{max}/σ values that are consistent with isotropic oblate rotators. On the other hand, disky pseudobulges have the shape of a thin disk and a Sérsic profile exponent below 2.5. They show rotation and also they harbour structures like inner bars and inner spirals. When we discuss here the B/T ratio, we refer to the ratio of the classical bulge mass to the total stellar mass.

Boxy/peanut/X bulges are called Boxy/peanut/X because of their shape and are called bulges because they protrude out of the galactic equatorial plane. Physically, however, they are just the thick part of the bar. The same structure, seen face-on, is often called a barlens. Although they are clearly not classical bulges, boxy/peant/X bulges should *not* be referred to as pseudobulges, so as not to be confused with disky pseudobulges.

ACKNOWLEDGMENTS

We thank Albert Bosma and F. Hammer for stimulating discussions, and Volker Springel for the version of GADGET used here. We also thank an anonymous referee for their useful report which helped us improve the presentation of this paper. We acknowledge financial support from CNES (Centre National d'Etudes Spatiales, France) and from the EU Programme FP7/2007-2013/, under REA grant PITN-GA-2011-289313, as well as HPC resources from GENCI/TGCC/CINES (Grants x2013047098 and x2014047098) and from Mesocentre of Aix-Marseille-Université (program DIFOMER).

REFERENCES

Abadi, M., Navarro, J., Steinmetz, M., Eke, V. 2003, ApJ, 597, 21
Athanassoula, E. 1983, in Internal kinematics and dynamics of galaxies, ed. E. Athanassoula, Dordrecht, D. Reidel Publishing Co., 243
Athanassoula, E. 1984, PhR, 114, 319
Athanassoula, E. 1988, in Towards understanding galaxies at large redshift, Dordrecht, Kluwer Academic Pub., 1988, 111
Athanassoula, E. 1992, MNRAS, 259, 345
Athanassoula, E. 2003, MNRAS, 341, 1179
Athanassoula, E. 2005, MNRAS, 358, 1477
Athanassoula, E. 2007, MNRAS, 377, 1569
Athanassoula, E. 2012, MNRAS, 426, 46
Athanassoula, E. 2013, in Secular Evolution of Galaxies, ed. J. Falcón-Barroso & J. H. Knapen, Cambridge, UK: Cambridge University Press, 305
Athanassoula, E. 2015, in Galactic Bulges, ed. E. Laurikainen, R. Peletier and D. Gadotti, Springer Verlag, Germany, p. 391
Athanassoula, E., Bosma, A., Papaioannou, S. 1987, A&A, 179, 23
Athanassoula, E., Laurikainen, Salo, H., Bosma, A. 2015, MNRAS, 454, 3843
Athanassoula, E., Misiriotis, A. 2002, MNRAS, 330, 35
Athanassoula, E., Romero-Gómez, M., Masdemont, J. J. 2009, MNRAS, 394, 67
Aumer, M., White, S. 2013, MNRAS, 428, 1055
Barnes, J. 1998, in Galaxies: Interactions and Induced Star Formation, ed. D. Friedli, L. Martinet and D. Pfenniger, Springer-Verlag Berlin/Heidelberg, p. 275
Barnes, J. 2002, MNRAS, 333, 481
Bershady, M., Martinsson, T., Verheijen, M., et al. 2011, ApJL, 739, 47
Bondi, H. 1952, MNRAS, 112, 195
Bondi, H., Hoyle, F. 1944, MNRAS, 112, 195
Borlaff, A., Eliche-Moral, M. C., Rodríguez-Pérez, C., et al. 2014, A&A, 570, 103
Bouwens, R., Illingworth, G., Blakeslee, J. 2004, ApJ, 611, L1
Brook, C., Stinson, G., Gibson, et al., 2012 MNRAS, 419, 771
Brooks, A., Christensen, C. 2015, in Galactic Bulges, ed. E. Laurikainen, R. Peletier and D. Gadotti, Springer Verlag, Germany, 317
Buta, R. 1995, ApJS, 96, 39
Buta, R., Sheth, K., Athanassoula, E., et al. 2015, ApJS, 217, 32
Casertano, S., Hut, P. 1985, ApJ, 298, 80
Colin, P., Valenzuela, O., Klypin, A. 2006, ApJ, 644, 687
Comeròn, S., Elmegreen, B. G., Knapen, J. H., et al. 2011b, ApJ, 741, 28
Comeròn, S., Elmegreen, B. G., Salo, H., et al. 2012, ApJ, 759, 98
Comeròn, S., Knapen, J. H., Sheth, K., et al. 2011a, ApJ, 729, 18
Comerón, S., Salo, H., Janz, J., Laurikainen, E., Yoachim, P. 2015, A&A, 584, 34
Conselice C., Mortlock A., Bluck A. F., Grützbauch R., Duncan, K. 2013, MNRAS, 430, 1051
Cox, T. J., Jonsson, P., Primack, J. R., Somerville, R. S. 2006, MNRAS, 373, 1013
Cuddeford, P. 1991, MNRAS, 253, 414
Cullen, L., Dehnen, W. 2010, MNRAS, 408, 669
Daddi, E., Bournaud, F., Walter, F., et al. 2010, ApJ, 713, 686
Dahlen, T., Mobasher, B., Dickinson, M. et al. 2007, ApJ, 654, 172
Díaz-Garca, S., Salo, H., Laurikainen, E., Herrera-Endoqui, M. 2015, arXiv:1509.06743
Dobbs, C., Baba, J. 2014, PASA, 31, id.e035
Drory, N., Fisher, D. B. 2007, ApJ, 664, 640
Elmegreen, B. G., Elmegreen, D. M., Vollbach, D. R., Foster, E. R., Ferguson, T. E. 2005, ApJ, 634, 101
Erb D. K., Steidel C. C., Shapley A. E., et al. 2006, ApJ, 646, 107
Erwin, P. 2008, in Formation and Evolution of Galaxy Bulges, ed. M. Bureau, E. Athanassoula, B. Barbuy, IAU Symp., 245, 113
Erwin, P., Beckman, J. E., Pohlen, M. 2005, ApJ, 626, L81
Eskridge, P. B., Frogel, J. A., Pogge, R. W., et al. 2000, AJ, 119, 536
Ferrarese L., Merritt D. 2000, ApJ, 539, L9
Ferguson, H., Dickinson, M., Giavalisco, M. 2004, ApJ, 600, L107
Fisher, D., Drory, N. 2015, in Galactic Bulges, ed. E. Laurikainen, R. Peletier and D. Gadotti, Springer Verlag, Germany, 41
Freeman, K. C. 1970, ApJ, 160, 811
Gebhardt K., Bender, R., Bower, G., et al. 2000, ApJ, 539, L13
Genzel, R. A., Tacconi, L. J., Lutz, D., et al. 2015, ApJ, 800, 20
Governato, F., Brook, C. B., Brooks, A. M., et al. 2009, MNRAS, 398, 312
Hammer, F., Flores, H., Zheng, X. Z., Liang, Y. C., Cesarsky, C. 2005, A&A, 430, 115
Hammer, F., Flores, H., Puech, M., et al. 2009a, A&A, 507, 1313
Hammer, F., Flores, H., Yang, Y. B., et al. 2009b, A&A, 496, 381
Hayward, C., Torrey, P., Springel, V., Hernquist, L., Vogelsberger, M. 2014, MNRAS, 442, 1992
Hopkins, P. F. 2013, MNRAS, 428, 2840
Hopkins, P. F. 2014, Astrophysics Source Code Library, record ascl:1410.003
Hopkins, P. F. 2015, MNRAS, 450, 53
Hopkins, P. F., Cox, T. J., Younger, J. D., Hernquist, L. 2009, ApJ, 691, 1168

Hopkins, P. F., Cox, T. J., Hernquist, L., et al. 2013, MNRAS, 430, 1901
Hopkins, P. F., Quataert, E. 2010, MNRAS, 407, 1529
Hoyle, F., Lyttleton, R. A. 1939, PCPS, 35, 405
Kannan, R., Macciò, A. V., Fontanot, F., et al. 2015, MNRAS, 452, 4347
Kormendy, J. 2013, in Secular Evolution of Galaxies, ed. Jesús Falcón-Barroso & Johan H. Knapen, Cambridge, UK: Cambridge University Press, 2013, 1
Kormendy, J., Drory, N., Bender, R., Cornell, M. 2010, ApJ, 723, 54
Kormendy J., Kennicutt R. C., Jr. 2004, ARA&A, 42, 603
Knapen, J. H., Shlosman, I., Peletier, R. F. 2000, ApJ, 529, 93
Laine, J., Laurikainen, E., Salo, H., et al. 2014, MNRAS, 441, 1992
Laurikainen, E., Salo, H., Athanassoula, E., Bosma, A., Herrera Endoqui, M. 2014, MNRAS, 444, L80
Lin, C. C. 1967, Annual Review of Astronomy and Astrophysics, 5, 453
Leroy A. K., Walter F., Brinks E., et al. 2008, AJ, 136, 2782
Lotz, J., Jonsson, P., Cox, T., Primack, J. 2010, MNRAS, 404, 590
Lynden-Bell, D. 1967, MNRAS, 136, 101
McMillan, P., Dehnen, W. 2007, MNRAS, 378, 541
Menéndez-Delmestre, K., Sheth, K., Schinnerer, E., Jarrett, T., Scoville, N. 2007, ApJ, 657, 790
Miller, M., Bregman, J. 2015, ApJ, 800, 14
Moster, B. P., Macciò, A. V., Somerville, R. S., Naab, T., Cox, T. J. 2011, MNRAS, 415, 3750
Mould, J. 2005, ApJ, 129, 698
Muñoz-Mateos, J. C., Sheth, K., Gil de Paz, A., et al. 2013, ApJ, 771, 59
Ness, M., Freeman, K., Athanassoula, E., et al. 2013a, MNRAS, 430, 836
Ness, M., Freeman, K., Athanassoula, E., et al. 2013b, MNRAS, 432, 2092
Pohlen, M., Trujillo, I. 2006, A&A, 454, 759
Querejeta, M., Eliche-Moral, M. C., Tapia, T., et al. 2015, A&A, 573, A78
Robertson, B., Bullock, J. S., Cox, T. J., et al. 2006, ApJ, 645, 986
Rodionov, S., Athanassoula, E., Sotnikova, N. 2009, MNRAS, 392, 904
Rodrigues, M., Puech, M., Hammer, F., Rothberg, B., Flores, H. 2012, MNRAS, 421, 2888
Romero-Gómez, M., Masdemont, J. J., Athanassoula, E., García-Gómez, C. 2006, A&A, 453, 39
Sackett, P. 1997, ApJ, 483, 103
Sandage, A. 1961, The Hubble Atlas of Galaxies (Washington:Carnegie Institution)
Saha, K., Martinez-Valpuesta, I., Gerhard, O. 2012, MNRAS, 421, 333
Schweizer, F. 1998, in Galaxies: Interactions and Induced Star Formation, ed. D. Friedli, L. Martinet and D. Pfenniger, Springer-Verlag Berlin/Heidelberg, p. 105
Scoville, N., Sargent, A., Sanders, D., Soifer, B. 1991, ApJ, 366, 5
Shen, J., Rich, M., Kormendy, J., et al. 2010, ApJ, 720, 72
Silk, J., Mamon, G. 2012, RAA, 12, 917
Springel, V. 2005, MNRAS, 364, 1105
Springel, V., Hernquist, L. 2002, MNRAS, 333, 649
Springel, V., Hernquist, L. 2003, MNRAS, 339, 289
Springel, V., Hernquist, L. 2005, ApJ, 622, 9
Springel, V., Di Matteo, T., Hernquist, L. 2005, MNRAS, 361, 776
Streich, D., de Jong, R., Bailin, J., et al. 2016, A&A 585, A97
Tacconi L., Genzel, R., Neri, R., et al. 2010, Natur, 463, 781
Thacker, R., MacMackin, C., Wurster, J., Hobbs, A. 2014, MNRAS, 443, 1125
Toomre, A. 1981, in The structure and evolution of normal galaxies, Fall, S. M. and Lynden-Bell, D., ed., Cambridge and New York, Cambridge University Press, 111
Toomre, A., Toomre, J. 1972, ApJ, 178, 623
Torrey, P., Vogelsberger, M., Sijacki, D., Springel, V., Hernquist, L. 2012, MNRAS, 427, 2224
Wang, J., Hammer, F., Athanassoula, E. et al. 2012, A&A, 538, 121
Yoachim, P., Dalcanton, J. 2006, AJ, 131, 226
Yoachim, P., Dalcanton, J. 2008, ApJ, 682, 1004

2.1.2. My contribution to Paper I

Here are the points I worked on in Paper I.
First, I made all the plots presented in this paper, mostly using $python$, and the interactive visualization 3D program $GLnemo2$ for the face-on and edge-on views of our simulated galaxies.
I worked on the morphology of our galaxies, using the $GLnemo2$ tools to highlight substructures such as the spirals, the bar or bulges. This allowed me to measure the size of the bar and of the boxy/peanut bulge by eye, and to study the morphological characteristics of the stellar populations based on the circularity parameter and age (sections 3.7, 3.8 in the paper).
As described in detail in section 4, I derived the surface density profiles of the final remnant galaxies, of an isolated galaxy at different times (Fig. 2a of the paper), and of several stellar populations based on their age (Fig. 4 of the paper). I made the fits of the latter using a $Fortran$ program (see section 4.2.1), and of the remnant galaxies profiles to derive the bulge-to-total ratio (table 2 of the paper), using one or two Sérsic functions for the classical and the discy bulges, and two exponentials for the disc.
I derived the Sackett parameter (section 3.4 in the paper) using the rotation curves, by measuring the circular velocity of the whole galaxy and the one of the baryonic component at 2.2 times the inner disc scalelength, which I derived from the fit of the surface density profile.
In section 3.10.1, I selected (using $GLnemo2$) and tracked the gas particles which would be in a simulation without a gaseous halo (i.e. only the disc gaseous particles), in order to follow over time their number as well as the number of stars formed from them, and compare these results to those including all the gas (i.e. the gaseous halo).

2.1.3. Beyond the three fiducial examples: whole sample

We presented only 3 simulations in Paper I, however several hundreds were run in total to cover a large amount of parameters. Here are the main parameters that we changed from one simulation to another. We call *protogalaxies* the merging galaxies, to avoid confusion with the remnant galaxy. The merger simulations are called mdf, for $merging\ disc\ formation$.

As described in Paper I, we defined a spin value f (not to be confused with the spin parameter λ used in section 4.4.2), representing the amount of initial spin in each protogalaxy. $f = 0.5$ corresponds to no global spin, whereas $f = 1$ represents the case where all the particles are rotating in the same direction. We used several values of f, between 0.55 and 0.8. This parameter affects the total angular momentum of the system, which is studied in section 4.4.2.
A further parameter contributing predominantly to the angular momentum is

the merging orbit of the protogalaxies. We used several types of orbits, each orbit having a different ellipticity, initial distance and perigee distance. Most of our simulations have rather low initial distances between the two protogalaxies, around 200 kpc. However, we ran some simulations with higher distances, which causes the collision to occur later. We call $early\ merger$ the mergers occuring around 2 Gyr after the start of the simulation, and $late\ merger$ the ones occuring later than 4 Gyr. The time of the merger is a crucial characteristic of the simulation, since for early mergers there is little stellar material colliding, the main part of the remnant galaxy being built by stars born after the merger, whereas the opposite can happen for late mergers. The late merger cases will be treated in a future paper.
One of the main parameters is also the inclination angle between the two protogalaxies. Most of our simulations have no inclination, so that both protogalaxies rotation axes are parallel, and both discs form in the orbital plane. The remnant galactic disc is then usually in the orbital plane as well. Nevertheless, for a number of simulations we tilted one protogalaxy with a chosen angle around the X or Y axis, Z being perpendicular to the orbital plane. This way, both discs are not parallel to each other, and collide with an angle which is the inclination angle. We made simulations mainly with 45, 90 and 180 degrees inclination angles. Although some discussion is made in sections 4.4.2.1 and 4.4.2.2, the effect of this angle still needs further analysis. In particular, for one simulation with a 45 degrees inclination angle we observed the presence of a polar bar in the remnant galaxy, i.e. a central bar perpendicular to the galactic plane.

We have some simulations without a central AGN; most of them were run before we realized that the central part of the velocity curve was unrealistic (see discussion in section 2.3 of Paper I). Nevertheless, the morphology and properties of the remnants with an AGN are similar to the ones without, since the AGN only affects the very central part, as will be shown in Rodionov, Athanassoula & Peschken (submitted, hereafter Paper II). Furthermore, we used two parameters to charaterize the AGN, T_{AGN} and ρ_{AGN} (see Paper I), and changed their values to test several possibilities. The effect of these parameters seems rather weak, but needs further investigation.
Most of our simulations have a 1:1 protogalaxies mass ratio, which means that both protogalaxies are initially identical, and start with the same number of gaseous and dark matter particles. However, we tried some different models, where one protogalaxy is bigger than the other. We took a ratio of 3:1, which can still be considered as a major merger, with one protogalaxy having a total of 2.75 million particles, and the other 0.917 million. The effect of changing the ratio from 1:1 to 3:1 will be shown in a future paper.
Before running our high resolution simulations described in Paper I (5.5 million particles), we ran some lower resolution simulations. These simulations have the same properties as the others, but have only 550 000 particles, no AGN and

no inclination. This low resolution makes them less interesting to analyze, their properties being less clear and less reliable. Nevertheless, they globally seem to be rather similar to the high resolution simulations, as for example in section 4.4.2.2.

Appart from the major merger simulations, we also ran isolated galaxies simulations, having the same properties of an individual protogalaxy, but without a merging. The goal of these simulations was to show that our merging protogalaxies were realistic when evolved for 10 Gyr in isolation (see Paper I). These simulations are called idf, for $isolated\ disc\ formation$, and have the same parameters as the mdf, except the orbit obviously. Further analysis is needed to study these simulations in detail, although some comparison with the mdf can be found in section 4.4.2.1 for the angular momentum.

2.1.4. Merging period

In this section I focus on the characteristics of the system in the period around the merging.

2.1.4.1. Morphology

Stars: Already before the merging, tidal forces act on the protogalaxies by stretching the disc and forming tidal tails after the first pericentre passage. These tidal tails are immediately accreted in the remnant galaxy during the merging event. I show some illustrating snapshots in Appendix A. The collision is a violent event, which completely destroys the structures present in both protogalaxies (such as the spirals), and creates an important concentration of stars in the center. Some stars are spread out by the collision, but stay in the remnant galaxy, either being accreted to the center later, or taking excentric orbits around it. Right after the merging, some lump structures can be seen in the remnant, which are the future spirals of the disc.

Gas: The gas also feels the tidal forces after the first pericentre, but is much more affected than the stars. The tidal tails induced are much more extended, and are accreted for a long time after the merging, sometimes several Gyr after. During the merging, the gas structure is also completely destroyed, and forms a very concentrated part in the center, while the accreted tidal tails form a ring around it. This ring will then give birth to the spiral structure. During the merging, star formation mainly occurs in the concentrated central part, with about 10% (for $mdf732$) occuring in the ring. I show snapshots illustrating this in Appendix A.

2.1.4.2. How to define a merging time

The merging is not an instantaneous event, the process of the protogalaxies collisioning and merging to form an unique remnant galaxy takes time. Therefore, deriving the time of the merging, for example to isolate the stars born before or after the merger, is not straightforward. In Paper I we used the distance between the centers of density of the protogalaxies (hereafter COD) to define the start of the merging, but here are some alternatives we worked on.

SFR: An interesting way to find the merging time is to look at the star formation rate (SFR). During the secular evolution of the galaxy, the total star formation rate is expected to be more or less constant, or slowly decreasing. Indeed, the star formation is linked to the gas density, which remains more or less the same after the merging, gas being depleted by star formation and filled by accretion from the halo. There is no sudden supply of gas which would brutally increase the density and thus the star formation. This is true before the merging as well, when both protogalaxies evolve independently. Nevertheless, the merging is a violent phase, during which the two protogalaxies and their gas are colliding, which locally creates high density clumps of gas in the center. This will trigger a burst of star formation in these clumps, and therefore the star formation rate of the merging system will be much higher than before and after the merging. By plotting the total SFR as a function of time, we thus see a very high peak of star formation at the time of the merging, which is easy to detect (see figure 2.1, left panel). This peak is very narrow and thus gives a rather precise estimate of the merging time.
Unfortunately, this only works when there is no AGN in the center. The presence of an AGN makes it more complicated, since the central black hole distributes energy to the gas, which prevents excessive star formation in the center. Therefore, during the merging the gas suddenly accreted in the center will not be able to form as many stars as without an AGN, and the SFR will not be as high. Furthermore, the heated gas will eventually cool down and form stars, so that the AGN delays part of the star formation. We plotted the SFR as a function of time for simulations with AGN, which constitute the majority of our sample, and found that indeed during the merging the star formation is very chaotic, being higher than for the secular evolution but showing a large number of peaks extending over a relatively long period of time (figure 2.1, right panel). Therefore, the SFR cannot be used to derive the merging time in the presence of an AGN, although the beginning and the end of the chaotic period can give an estimate for the merging period.

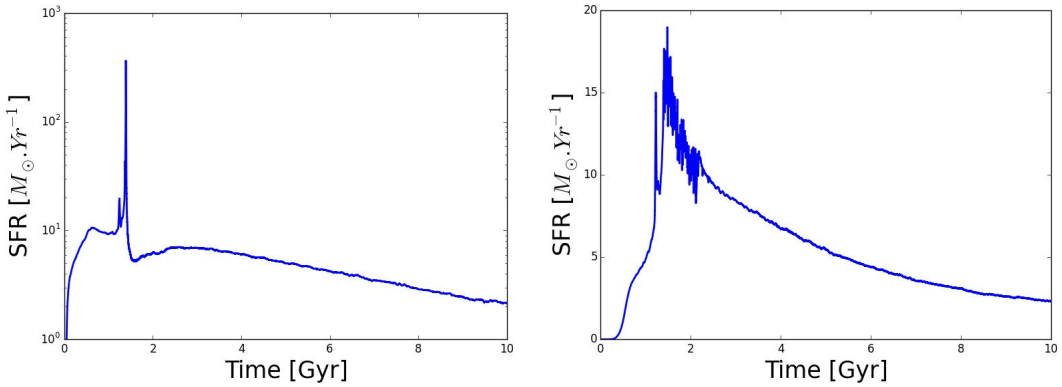

Figure 2.1.: Total star formation rate as a function of time in a simulation without AGN (left) and a simulation with an AGN (right). The SFR in the left panel is in logarithmic scale.

Black Hole Mass: We were thus looking for a way to derive the merging time for simulations including a central AGN. The AGN prevented us to use the SFR, so we looked at the black hole properties as a function of time. The black hole accretes mass, and it is thus possible to measure its mass at a given time, using the energy released by the AGN feedback. This is explained in Springel, T. Di Matteo, and Hernquist (2005). During the merging, the mass accreted by the black hole will be higher, since many particles will end up in the center. Therefore, by looking at the mass of the black hole as a function of time, there should be a sudden increase of mass during the merging. We thus tried to use this phenomenum to derive the merging time.
I show the mass of the black hole as a function of time in figure 2.2. There is indeed a brutal increase of the mass between 1.4 and 2.2 Gyr, corresponding to the merging. This increase is not instaneous though, so that this method cannot give a precise value for the time of the merging. Nevertheless, it can give us a good approximation for the merging period, more precise than for the SFR. I thus wrote a *python* program to systematically locate the start and the end of this increase in the black hole mass profile for all our simulations. To do this, I used the derivative of the profile, expecting the derivative to suddenly change when the mass starts increasing, and when it becomes flat again after the merging. Nevertheless, the mass profile, and consequently its derivative, show many fluctuations in the flat parts, so that detecting the change in the derivative corresponding to the merging is difficult. I thus smoothed the mass profile using a Savitzky-Golay algorithm, with a 101 window size and order 5.
The first step is now to derive the start of the increase, corresponding to the start of the merger. When the mass increases, the derivative suddenly jumps to a high value. I used this pattern by looking for the last time at which the derivative reaches 20% of its maximum (before it reaches its maximum). To be sure that

the derivative does not reach that value with a temporary peak, I added a condition on the mean of the derivative over 10 points to be higher than these 20% as well. This method seemed to work well for most simulations, as shown in figure 2.2.
The next step is to derive the time at which the mass stops increasing and becomes flat, which causes the derivative to be nearly constant and zero. To do this, I computed the variance of the derivative as a function of time, and looked for the first time at which the derivative drops below a given value (empirically fixed) and stays so (low variance). Although empirical, this method seems to work well (figure 2.2).
We now have the time interval where the black hole mass increases, which corresponds to the merging interval. We can go further and use the black hole mass to derive the time at which the bar starts forming. Indeed, we noticed that after the merging, the mass stays nearly constant, until a specific time at which it slowly starts increasing again, which corresponds to the time at which the bar appears. Since the bar is well known for funneling gas to the center of the galaxy (Athanassoula, 1992; Friedli and Benz, 1993), it seems coherent that it will start fuelling the central black hole again. Here I used again a combination of empirical values for the derivative and its variance to derive the bar formation time, and the result can be seen in figure 2.2.
In the end, we chose not to keep the AGN mass method to derive the merging interval, since the COD distances method was more straightforward and reliable, being easy to apply for every simulation.

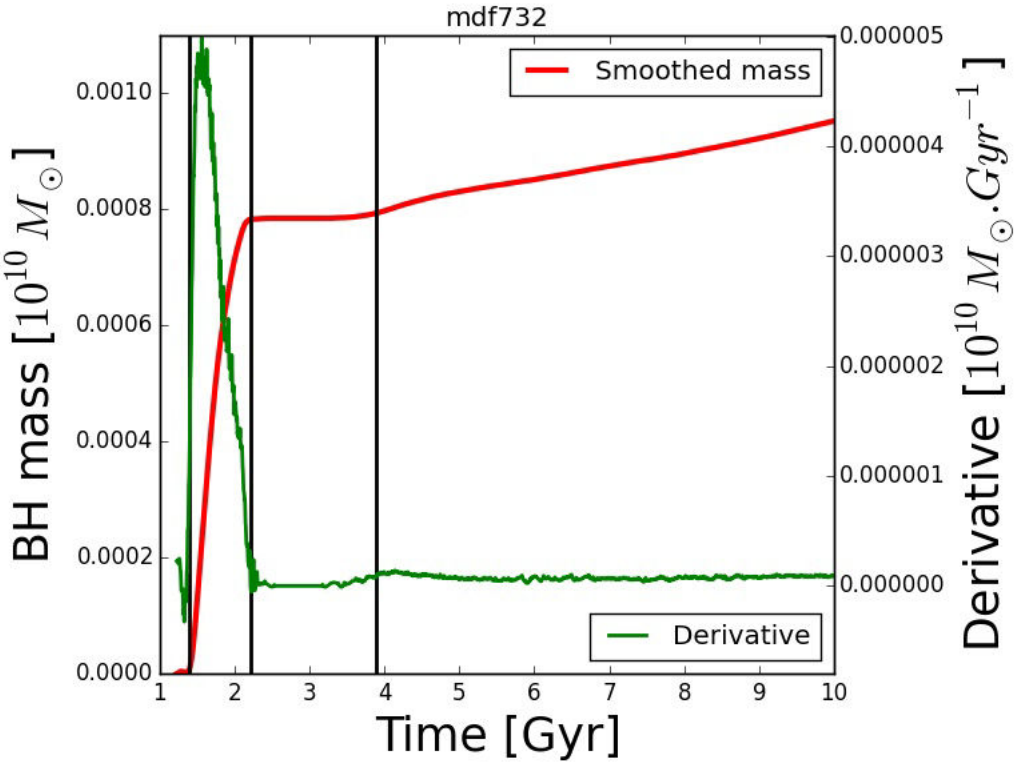

Figure 2.2.: Smoothed black hole mass as a function of time in a simulation with AGN. The three vertical lines represent respectively the beginning and the end of the merging, and the start of the bar formation, all three times being derived from the analysis of the derivative.

2.1.4.3. Start of disc formation

When the merging is over, the new disc starts to form in the remnant. Nevertheless, the end of the merging is not always well defined, and does not necessarily corresponds to the start of the disc formation. We wanted to have an independent value for the time at which the new disc appears (herefater T_{bd}, for *beginning of disc*), and to do this we used the circularity parameter ϵ at birth as a function of time, as explained in Paper I (section 3.6 in the paper). We defined T_{bd} as the first time at which 95% of the stars were born with $\epsilon > 0.5$, i.e. with disc dynamics.
Although this method worked well for our fiducial example $mdf732$ (see Paper I), I applied it for the other simulations of our large sample, and found that it was not accurate for some of them. I show two examples in figure 2.3, where T_{bd} derived this way seems to occur well after the merging, and after the disc started forming. This seems to be due to the fact that while for $mdf732$ the fraction reaches almost 1 at the end of the simulation, it is not always the case for

other simulations (see figure 2.3). So I tried to define T_{bd} as the time at which the fraction reaches 95% of the maximum fraction of the profile, instead of 0.95. This seemed to work well (see figure 2.3, left panel), T_{bd} being more consistent for the problematic simulations shown previously. Nevertheless, there were still some simulations that did not give a consistent value for T_{bd} (figure 2.3, right panel).

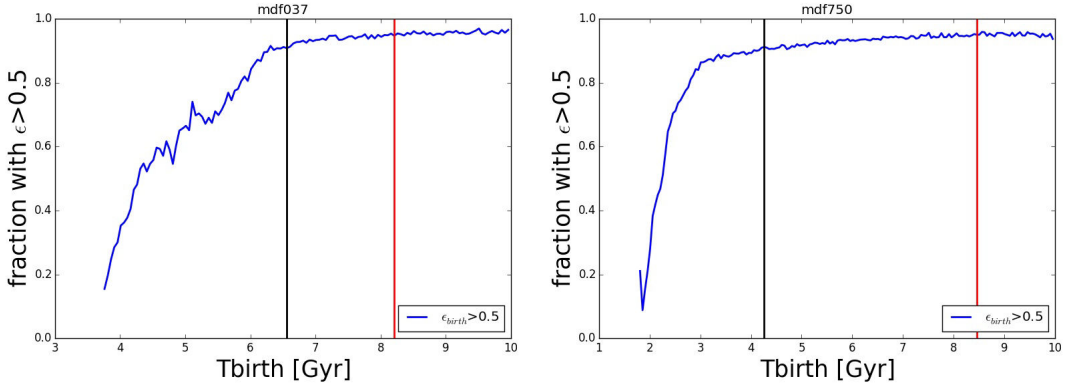

Figure 2.3.: Fraction of particles born with $\epsilon > 0.5$, as a function of time, for two different simulations. The red vertical line corresponds to the time at which the fraction reaches 0.95, and the black one to the time at which it reaches 95% of the maximum fraction. The latter seems to be an improvement compared to the former, but is still not satisfying for the right panel.

We thus tried a new method to derive T_{bd} with the ϵ fraction, using the fact that the fraction shows a brutal increase over time, which stops when the disc starts forming (see figure 2.3). We defined T_{bd} as the end of the increase, when the fraction becomes rather flat, which means that the star formation has reached the start of the secular disc growth phase. This usually corresponds to the T_{bd} defined with the 95% (see figure 2.3, left panel), but the goal was here to find it also for the cases where the 95% does not work. To do this, we used the derivative of the fraction – as in section 2.1.4.2 with the black hole mass. Nevertheless, we chose not to use exactly the same method, since it was highly based on empirical values and not always reliable. I first smoothed the curve again with a Savitzky-Golay algorithm, with a 21 window size and order 3. Looking at the derivative (figure 2.4), we saw that it is usually rather flat and low after T_{bd}, and abruptly takes high values just before. I thus wrote a $python$ program to derive the time at which the derivative changes from very high to very low and flat. We chose not to rely on a value threshold to determine when this occurs, since the values of the derivative are very different from one simulation to another. Instead, the program will try to fit the flat part with a straight line, and find its intersection with the abrupt increase of the derivative. To do this, it starts from

the final time (10 Gyr), and goes backwards to fit straight lines on the derivative within 1 Gyr intervals (figure 2.4, top). The goal is to find two consecutive intervals where the straight lines show almost the same slope. When the program goes past the end of the flat part (still going from high to low times), the 1 Gyr wide fitted straight line will suddenly show a very different slope than the previous interval, and will thus be discarded. Furthermore, this method discards any interval in the flat part where a bump of the derivative is observed. Once the two consecutive intervals have been found, we define those two intervals as the fitting base for the whole flat part after T_{bd}, and fit a straight line on the corresponding 2 Gyr interval to modelize this flat part. Of course this only works if $T_{bd} < 8$ Gyr, i.e. if the merging does not occur too late. Once the final straight line is derived, T_{bd} is defined as the first time at which the line intersects the derivative. Some illustrations are shown in figure 2.4.
This method works well overall, including for the cases where the 95% method was not accurate (as $mdf750$, see figures 2.3 and 2.4), but it is not perfect. In some cases the straight line does not intersect the derivative, no consecutive intervals are matching, or the slope of the final straight line is too high to appear flat. I thus implemented several warnings in output, which allow us to go back to the plot, check what went wrong and potentially make an eye estimate of the value of T_{bd} if the method did not work.

The derivation of T_{bd} required to have the fraction of particles with $\epsilon_{birth} > 0.5$ as a function of time, so that I first needed to derive ϵ_{birth} for all the particles at each time step. I wrote a $python$ program allowing me to do this, and described the method in Appendix B.

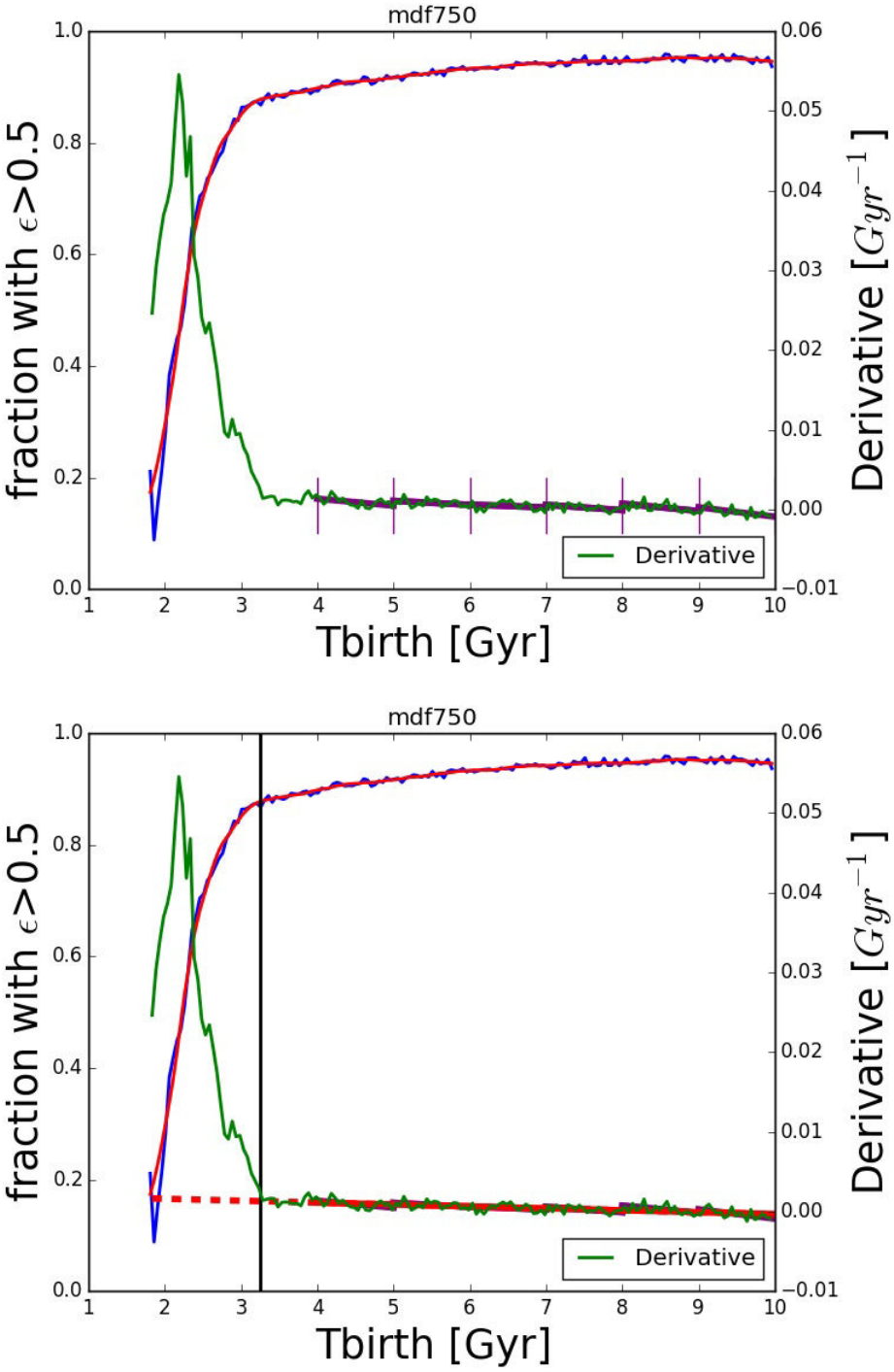

Figure 2.4.: Same as figure 2.3, but with a smooth of the fraction (red curve), and the derivative of this smooth (green curve). The top panel shows how the derivative is cut and fitted into several intervals. The final fit is shown in the bottom panel (red straight line), and T_{bd} (vertical black line) is defined as the intersection between the fit and the derivative.

2.2. Stellar migration

In this section I study the radial migration of stars in our remnant discs, throughout the whole simulation.

2.2.1. Presence of radial stellar migration

Stars in galactic discs do not stay at their birth radius their whole life: radial displacements have been shown to occur in the disc (e.g. Haywood, 2008). Those displacements can be radial oscillations around the radius of a given orbit (epicyclic motions), or stars migrating from an orbit to another (Roškar, Debattista, T. R. Quinn, et al., 2008). The former does not have a huge impact on the disc structure and properties since the star's radius does not change significantly over time. On the other hand, stars changing orbit can affect the distribution and mix stellar populations in the disc. This is the migration we will be investigating here.

The stellar migration has been shown to play a role in building the outer disc in spiral galaxies with a downbending disc, by populating the outer parts through inside-out motions (Roškar, Debattista, Stinson, et al., 2008). Our remnant galaxies showing a downbending disc (Paper I, section 2.1.1), we investigated whether radial migration could be found in our simulations too. I first plotted for one simulation the final radius of every star as a function of its birth radius (figure 2.5, left panel). Since the migration takes place in the new disc formed after the merging, for all the stars born before the start of the disc formation (T_{bd}) I took their radius at $t = T_{bd}$ as birth radius. If there was no migration, the stars would all concentrate around the $y = x$ line. However, we see that there are many stars located far from this line, having travelled sometimes more than 10 kpc inwards or outwards since their time of birth. This plot is very similar to the one found in Roškar, Debattista, Stinson, et al. (2008) (figure 2 in the paper), and shows the presence of radial stellar migration in our disc.
Furthermore, we can see that most stars ending up beyond the 10 Gyr break radius (i.e. break radius measured at t=10 Gyr, dashed horizontal line at 25 kpc) have migrated inside-out to get there. This is shown also with the radial density profile in Paper III (section 4.4.2.1). Nevertheless, to investigate whether a star migrated from one disc to another (inner and outer discs) since its birth, one needs to take into account the break radius at the star's time of birth, since the break radius changes with time (Paper IV, section 4.4.3.1). A discussion about this can be found in Paper III. I thus plotted (figure 2.5, right panel) for each star its radial distance from the break at 10 Gyr (final radius – 10 Gyr break radius), as a function of the radial distance from the break at its time of birth (birth radius – birth time break radius). This requires to know the break radius at each time step, for each star's birth time. The method used to derive this break radius

is described in detail in section 4.2.1. Looking at figure 2.5 (right panel), we see that there are 4 parts, the top right and the bottom left ones showing the stars staying in the outer and inner disc, and the others showing the stars migrating from one disc to the other. In particular, the top left part shows the particles that migrated from the inner to the outer disc. This part seems dominant among the stars ending up in the outer disc, but this is not always the case for other simulations. This actually depends on the total angular momentum in the galaxy, as discussed in Paper III.

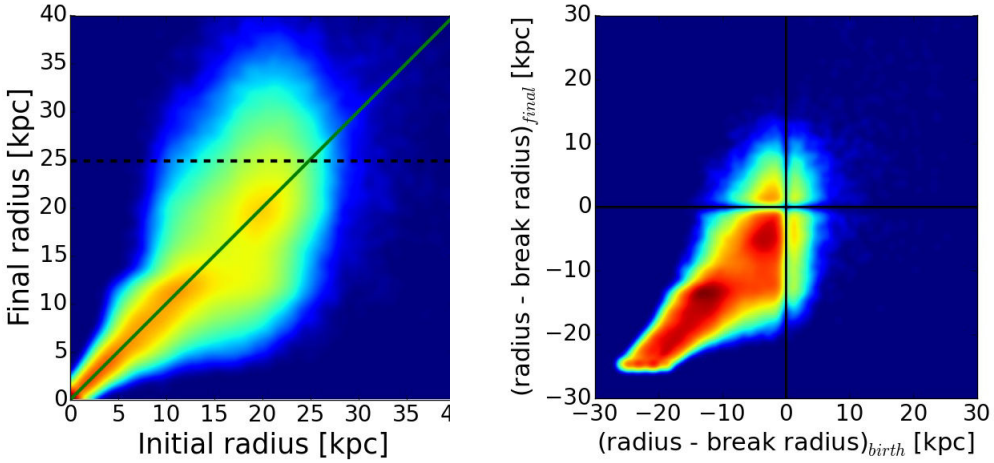

Figure 2.5.: Left panel: Final radius as a function of the birth radius for all the stars in the disc. The green line is $y = x$, while the black dashed line is the final break radius. Right panel: Final radius – final break radius, as a function of the birth radius – birth break radius. The stars around the break radii have been removed for clarity.

Furthermore, to see which parts of the disc are the most concerned about inward or outward migration, I plotted the mean migration distances as a function of the radius, i.e. looking at the particles ending up at a given radius, which distance they travelled on average to get there. The mean migration distance at a given radius is thus the difference between the final and the birth radius, averaged for all the particles at this final radius. To get rid of the radial oscillations of the stars around their orbit which can affect the results, I took here the guiding radius instead of the real radius. The guiding radius R_G of a star is defined as the radius of the circular orbit corresponding to its angular momentum L_z:

$$R_G = \frac{L_z}{v_{circ}(R_G)} \tag{2.1}$$

where v_{circ} is the circular velocity at the guiding radius (see Appendix C for more details).

I show the corresponding plot of the mean migration distance as a function of the radius in figure 2.6 (left panel). We can see that the inner parts are mostly composed of stellar particles which have migrated inwards, while in the outer parts they mostly migrated outwards. We can do the same plot but as a function of the birth radius (figure 2.6, right panel), but here the resulting profile seems less easy to interprete, although we can globally see that at most birth radii the stars tend to migrate slightly more inwards than outwards.

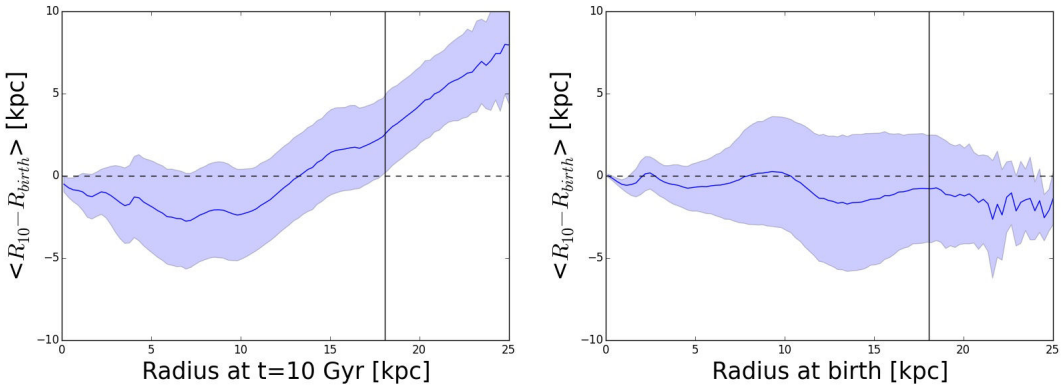

Figure 2.6.: Mean migration distance (using the guiding radii) as a function of the final guiding radius (left panel) and the birth guiding radius (right panel). The blue shaded area gives the 1 σ region. The dashed line is the limit between dominant inward and outward migration. The solid line represents the break radius at t=10 Gyr.

2.2.2. What causes this migration?

Having established the presence of radial migration in our galactic discs, the next step is to understand how this migration works, and what causes it. In particular, I investigated whether it is associated to a specific component or feature in the disc. I thus looked at the positions over time of stars migrating inwards or outwards, separately. Nevertheless, there are many stars whose migration is very small, or just represent radial oscillations around their orbit. These stars needed to be excluded to be able to observe the mechanism ruling the migration, so that I could study only the ones showing a clear migration from one orbit to another. One way to do this would be to fix a minimum distance that stars should travel over time, but the radius can sometimes be misleading, since stars are oscillating radially and some stars are not always at the radius we expect them to be from their angular momentum. I thus used the angular momentum as as tracer for the migration instead. When a stellar particle changes its orbit, its angular momentum changes as well. Therefore, a star looses angular momentum as it migrates inwards, and gains it by migrating outwards (assuming the orbit is not too excentric). To select the stars showing a clear migration inwards or outwards, I

thus used an empirical minimum (absolute) value for the change of angular momentum ($5 * 10^{60}\ kg.m^2.s^{-1}$) between their birth and the end of the simulation. This value is above the average change of angular momentum of the stars during their lifetime, to make sure that the selected particles are significantly migrating. I ended up with two distinct populations: the stars showing a clear inward migration, and the ones with a clear outward migration. For each group I plotted their position over time since their birth in the galactic plane, to see if a pattern emerged. Since there are stars born throughout the whole simulation, I further separated the stars into several birth time intervals to have a constant number of stars over time, and plotted for a given interval their position in the galactic plane at different times, from their time of birth to the end of the simulation. I show an example for the stars born between 4 and 6 Gyr in figure 2.7 (inward migration) and in figure 2.8 (outwards). We can clearly see the stars expanding or shrinking their radius over time, and it is interesting to see how they still form a sort of ring throughout their migration, and how at some point they reproduce the spiral pattern.

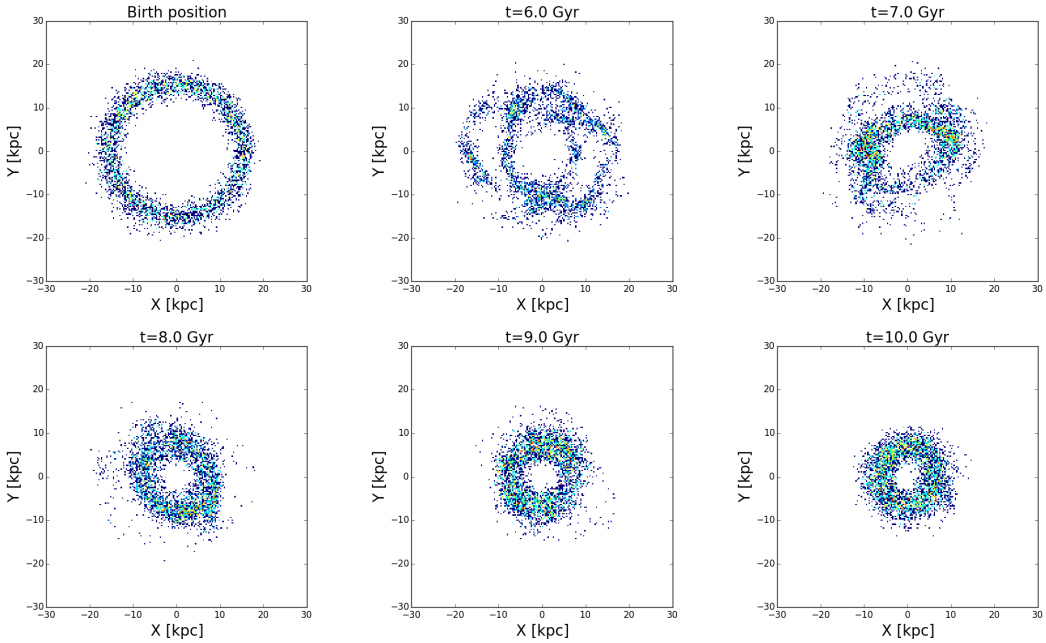

Figure 2.7.: Evolution over time of the position of stellar particles showing a clear inward migration. Here are displayed only the particles born between 4 and 6 Gyr.

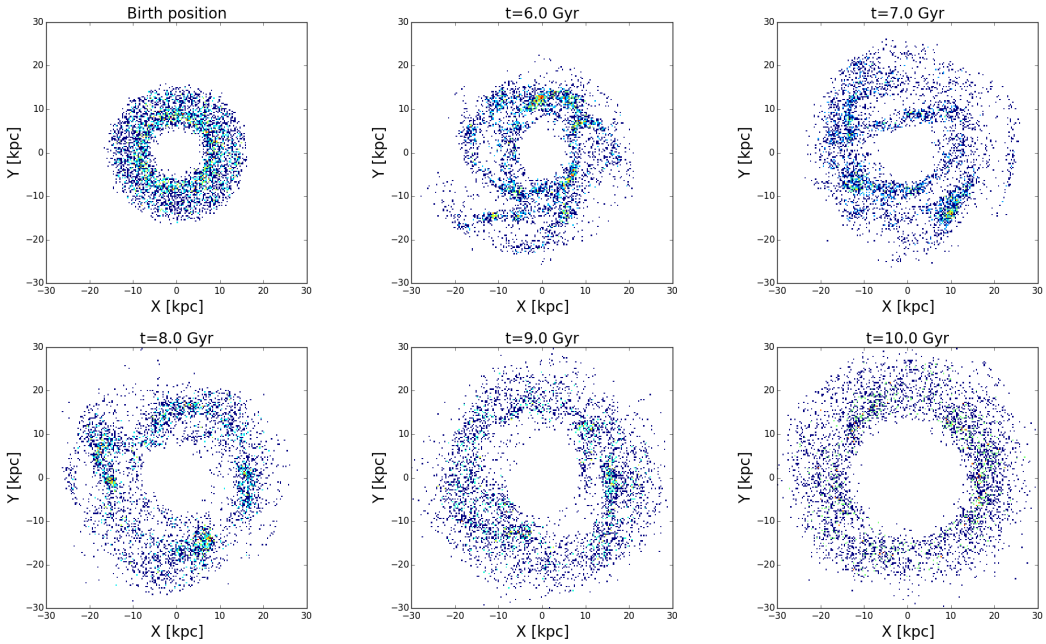

Figure 2.8.: Same as figure 2.7, but showing the particles with a clear outward migration.

To investigate whether the migration is related to a particular feature in the disc, I tried to link these positions to the corotation resonance (hereafter CR, see section 1.2.4.2) of the spirals. The CR has been shown to play a role in the migration (Sellwood and J. J. Binney, 2002; Minchev and Famaey, 2010), with the help of the density waves in the spiral arms. The CR radius in our simulations was computed at several times using the circular velocity and the pattern speed(s) of $m = 2$ structures. I thus compared the CR radius to the distributions shown in figure 2.7 and 2.8, and found that for the stars migrating outwards, the birth radius is around the 5 Gyr CR radius of the spirals. I did this for several birth time intervals and confirmed this result. The outward migration thus seems to be directly linked to the CR, which seems to point out that the migration is due to resonances in the disc, possibly with a spiral - bar resonance overlap (Minchev and Famaey, 2010) since our simulations often show a bar. Nevertheless, the birth radius of the stars migrating inwards does not seem to be directly related to a resonant orbit.

2.3. Bar pattern speed

In this section I present a study about the bar pattern speed, and how to derive it using the Tremaine-Weinberg method.

2.3.1. What is the pattern speed?

The pattern speed of a component is its rotation speed, or angular velocity. Stars do not rotate independently, there are some structures in the galaxy that keep their coherence over time and thus rotate at a given angular rate, called the pattern speed. In particular, bars and spirals are usually rather long-lived, and rotate around the galactic center as a whole. This does not mean that the stars in this structure rotate all at the same speed, a substructure such as a spiral arm is not a solid rotating structure. In fact, the stars composing this structure change continuously in the density wave theory, their orbit making them go in and out over time (see section 1.2.4.1).

I focused on the bar pattern speed, and used the Tremaine-Weinberg method to derive it in simulations. In particular, I wanted to know if this method is also valid in the case of thick discs, and for this I used a reference value of the pattern speed. This reference value was computed beforehand by deriving the bar angle over time with a Fourier analysis of the $m = 2$ component in the central region.

2.3.2. Description of the Tremaine-Weinberg Method

The Tremaine-Weinberg (hereafter TW) method is based on the paper Tremaine and Weinberg (1984), where the two authors propose a new method to compute the bar pattern speed in observations of disc galaxies, using the surface brightness and the radial velocities. Here is a brief summary of this method.
Three main assumptions are made:
- the disc of the galaxy is perfectly flat (zero thickness)
- it has a well-defined pattern speed (constant surface brightness for an angular speed Ω_p)
- the surface brightness of the tracer obeys the continuity equation (tracer conserved).

The first assumption allows the authors to simplify the analysis by getting rid of the vertical coordinates, the second one to express the surface brightness as a function of Ω_p, and the third one to obtain an equation involving the surface brightness and Ω_p. After some simple calculations, they derive a formula for the pattern speed, as a function of integrals of the surface brightness and the velocities:

$$\Omega_p \sin i = \frac{\int_{-\infty}^{+\infty} \int_{-\infty}^{+\infty} h(Y)\Sigma(X,Y)V_{\parallel} dX dY}{\int_{-\infty}^{+\infty} \int_{-\infty}^{+\infty} h(Y)\Sigma(X,Y)X dX dY} \tag{2.2}$$

where i is the inclination of the galaxy, $h(Y)$ an arbitrary weight function, $\Sigma(X,Y)$ the surface brightness, and $V_{\parallel}$ the radial velocity ($V_{\parallel} = v_y \sin i$). The coordinates (X,Y) used here are the sky plane coordinates, whereas (x,y) are the coordinates in the galactic disc plane, with $(X,Y) = (x, y\cos i)$.
As the pattern speed expression depends on the inclination, this method works for face-on discs as well as inclined ones. This formula is also valid in case of non-zero thickness, as long as the vertical velocities of the disc are zero.

The main problem here is the fact that this is only valid for conserved tracers, i.e. particles which are not created or destroyed over time. This cannot be achieved in the simulations I described previously, since the number of stars is not conserved due to constant star formation in the disc. I thus used different simulations for the computation of the pattern speed, which are briefly described in the following section.

2.3.3. Computing the pattern speed with the TW method in simulations

The goal is to test the TW method in our simulations, and check whether we can find values close to the reference value.

2.3.3.1. Description of the simulations used

The simulations I used to compute the pattern speed are not the merging simulations presented previously, but slightly older ones presented in Athanassoula, Machado, and Rodionov (2013). The asset of these simulations is that we included a stellar population which is conserved throughout the whole simulation, which allows these stars to follow the continuity equation, as required for the Tremaine-Weinberg method. Here is a short summary of the technical aspects of these simulations, which can be found in more detail in Athanassoula, Machado, and Rodionov (2013).
The simulations are made using GADGET2 (Springel, Yoshida, and White, 2001; Springel and Hernquist, 2002), using N-body particles to model the stars and the dark matter, and N-body SPH particles to model the gas. Sub-grid physics is used to model star formation, as described in Paper I. The galaxy is evolved in isolation, and gravity is computed with a tree code. These simulations use two distinct types of particles for the stars: the ones which were already present in the initial conditions, called DISK, and the ones born afterwards from the gas, called STARS.

The baryonic matter starts in a disc built in near-equilibrium in the potential of the whole galaxy, while the dark matter is distributed in a halo which can be axisymmetric or triaxial. The initial amount of gas in the disc is varying from one simulation to another, from 0% to 100% of the baryonic matter. Short animations of the full evolution for all simulations and components can be found at http://195.221.212.246:4780/dynam/movie/gtr/.
In the plots shown in the following sections, I use $gtr106$, which is a simulation with an axisymmetric halo and 20% of gas in the disc, and includes a well developed bar. Nevertheless, I did the analysis with other simulations as well, and found similar results.
I used these specific simulations only for the bar pattern speed study; every other analysis presented in this thesis was made using the mdf (or sometimes idf) simulations.

2.3.3.2. Parameters

I took the simulations face-on for simplicity ($i = 0$), and used the surface density instead of the surface brightness. A further parameter is the angle of the bar θ_{bar}. Contrary to observed galaxies, in our simulations we can rotate the galaxy to have the bar at the angle we want. This has an impact on the results since we take particles inside parallel slices, as shown in the following section. If the slices completely miss the bar (being for example parallel to the bar and outside it), the pattern speed computed will probably be wrong. I thus kept the bar angle as a free parameter, $\theta_{bar} = 0$ being the bar along the X axis. Finally, a decisive choice for the computation of the pattern speed is the weight function.

2.3.3.3. Weight function

Tremaine and Weinberg (1984) argue that the most useful weight functions are odd in Y. I thus used the weight function:

$$h(Y) = \frac{1}{1 + (\frac{Y-Y_0}{n_w})^2} - \frac{1}{1 + (\frac{Y+Y_0}{n_w})^2} \tag{2.3}$$

which is equivalent to taking particles only in Y slices around Y_0 and $-Y_0$, Y_0 being a free parameter. n_w determines the level of smoothing for the slices, which I fixed to n_w=10.
I thus obtained 2 free parameters for my computation of the pattern speed, Y_0 and θ_{bar}, so that by computing Ω_p for different values of Y_0 and θ_{bar} I could fill the parameter space (figure 2.9, left panel).

2.3.3.4. Bar particles

To be able to derive the pattern speed of the bar consistently, I needed my slits to select particles from the bar. But with some combinations of θ_{bar} and Y_0, there can be situations where the particles taken by the weight function do not take enough particles being part of the bar. I thus put a constraint on the number of bar particles taken into account for the derivation of Ω_p to be reliable.
To do this, I first needed to be able to define which particles are part of the bar. I derived the isophotes of the face-on view of the galaxy, and fitted them with generalized ellipses:

$$(\frac{|x|}{\alpha})^c + (\frac{|y|}{\beta})^c = 1 \tag{2.4}$$

α, β and c being free parameters.
I then defined the bar contour as the generalized ellipse with the major axis being the closest to the bar length (estimated by eye beforehand), and counted all the particles inside it as being part of the bar.
Being now able to know which particles are in the bar, I fixed 1000 as the minimum number of bar particles necessary for the pattern speed derivation to be reliable.
In figure 2.9 I show the results of the relative difference between the computed value of Ω_p and the reference value in the parameter space (θ_{bar}, Y_0), with and without the bar particles constraint. One can see that by removing the parameters with not enough bar particles, the results are in better agreement with $\Omega_{p,ref}$.

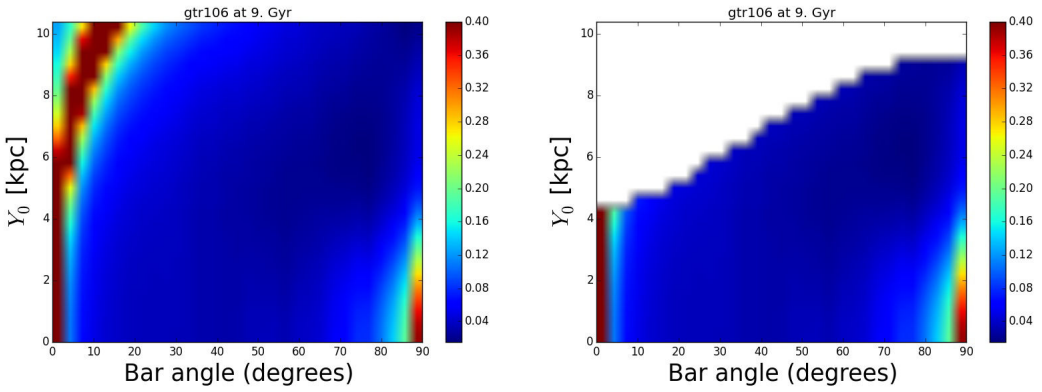

Figure 2.9.: Relative differences between the pattern speed reference value (11.8 $km.s^{-1}.kpc^{-1}$ here) and the value computed with the TW method, in the parameter space (angle of the bar, position of the slit). On the right panel the parameters leading to taking less than 1000 bar particles are removed.

2.3.3.5. Time chosen and buckling

The bar pattern speed changes with time, and can be derived at any time of the simulation, as soon as the bar appears. Nevertheless, to fulfill the flat disc condition, it should be better to take a time at which the galaxy is rather flat. This can be difficult to achieve in a barred spiral galaxy, since the bar often shows a vertical component, called boxy/peanut bulge (see section 1.2.3.2). This thick part of the bar appears during a buckling event, after the apparition of the bar. Since the TW method is only valid in a flat galaxy – or at least in a galaxy with no vertical motion, which is not the case here since the orbits in the bulge are three-dimensional – I expected the results to be in better agreement with the reference value before the buckling event, i.e. before the emergence of the boxy/peanut bulge. I thus computed the pattern speed at several times before and after the buckling for different simulations, to see if I could observe the effect of the bar thickening. The time of the buckling was derived using vertical asymmetry as a function of time (see Athanassoula, 2008).
Suprisingly, I found the agreement between my computations of Ω_p and the reference value to be the best at the end of the simulation (see figure 2.10), well after the buckling. This points out that the boxy/peanut bulge does not seem to interfere with the computation of the pattern speed, despite its thickness. An explanation for the fact that the results are better at the end of the simulation could be that the bar is more developed and stable then, which makes the computation of the pattern speed more reliable both for the Tremaine-Weinberg method and for the reference value.

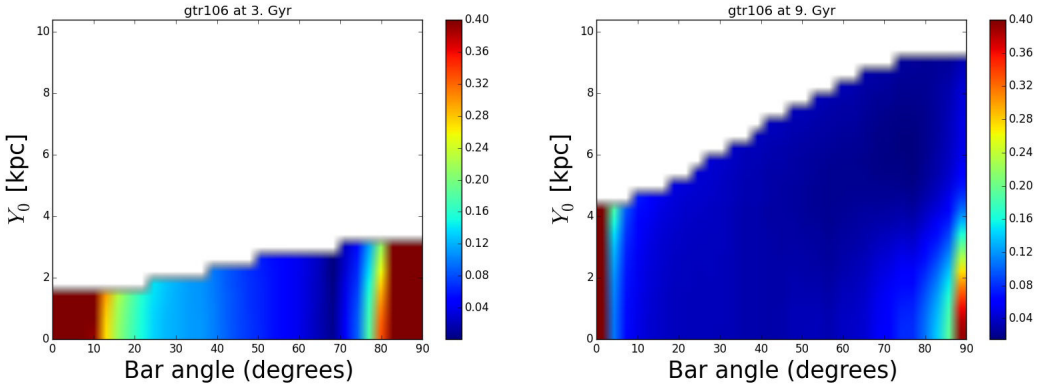

Figure 2.10.: Same as figure 2.9 for two different times: 3 (left panel, $\Omega_{p,ref} = 22.4\ km.s^{-1}.kpc^{-1}$) and 9 (right panel, $\Omega_{p,ref} = 11.8\ km.s^{-1}.kpc^{-1}$) Gyr. The slits for which there are less than 1000 bar particles are removed (white parts). The bar is smaller at 3 Gyr, which explains why more slits are removed for the lack of bar particles.

2.3.3.6. Effect of thickness

To further test the flat disc condition, I added several vertical constraints on the particles used to compute the pattern speed, at the end of the simulation.

I first applied a vertical cut by keeping only the particles close enough to the plane, with $|z| < 1$ kpc. To insure that there are no vertical motions, I also put a constraint on the vertical component of the velocities, by selecting only particles with $|v_z| < 2$ km/s.
Nevertheless, these constraints do not lead to pattern speed values in good agreement with the reference values, and the constraint on the vertical velocities is very strong, cutting out a large number of particles. The number of selected particles may thus be too low to derive Ω_p consistently. Increasing the limit value of v_z gives better results, but still not as good as with no vertical contraints.

I then tried another method to constrain the thickness of the disc. Instead of constraining the velocities, I kept only the particles staying in the plane, by applying a vertical cut at each time step – and not only the time taken for the computation of the pattern speed. I removed every particle going out of the plane (with $z_{lim} = 1$ kpc) between $t - 2$ and $t + 2$ Gyr, t being the time at which the pattern speed is computed. This method allowed me to keep a higher number of particles than the velocity constraint, and also gave better agreements with the reference value of Ω_p.
Nevertheless, the results are still better if I do not put any vertical constraint on the particles, selecting every particle regardless of its height with respect to the galactic plane. It thus seems that the thickness of the disc does not influence the derivation of the pattern speed in our simulations.

2.3.4. Conclusion about the pattern speed

To conclude, I managed to derive values of the pattern speed in good agreement (<10%) with the reference value at late times (close to the end of the simulation), and as long as the bar angle is not too high or too low (see figure 2.9). I added a constraint requiring the slit to contain a minimum number of particles in the bar for the analysis to be reliable. Contrary to what was expected, the thickness of the disc does not seem to affect the derivation of Ω_p with the Tremaine-Weinberg method, since the presence of the thick boxy/peanut bulge, as well as the thick disc component, do not reduce the quality of the results. Futhermore, the results are better after the buckling, and without putting any constraint on the thickness of the disc.

II. On the surface density profile of disc galaxies

3. Context

3.1. Observations

In observations, a simple way to get information on a galaxy is to study its photometry, i.e. the amount of light emitted by the different regions of the galaxy. At a given wavelength, the more light is received from a given area, the more stars emitting in this wavelength are expected to be found there. This allows to find which parts are the densest, as well as the distribution of stellar content in the galaxy. Because an observed galaxy can only be seen from the Earth line of sight, the light emitted is received in the sky plane, and this photometrical image is called surface brightness distribution. The surface brightness is a flux, and is measured in magnitude per square arcsecond ($mag.arcsec^{-2}$).
To analyze the properties of the surface brightness derived in a galaxy, and be able to compare it to other galaxies, the simplest solution is to suppose that the light distribution is axisymmetric, and therefore look at the surface brightness as a function of the cylindrical radius in the sky plane. It requires averaging the flux emmited at a given radius to obtain a one-dimensional luminosity profile, called surface brightness profile. This has the advantage of providing a single curve to describe the whole luminous distribution, as well as being easily reproducible for every galaxy. Examples of surface density profiles for observed galaxies are given in section 3.4.

The first attempt to derive and study this surface brightness profile was made in 1913 by J. H. Reynolds to study the luminosity radial distribution of the bulge in M31. Nowadays, surface brightness profiles are widely used to analyze every region of the galaxies, especially in disc galaxies.
These 1D profiles are also used for simulated galaxies, to compare them to observations. Nevertheless, in simulations there is no light emitted, we just know the position (and mass) of each star. Although it is possible to add special features allowing to simulate the stellar light emission (e.g. SUNRISE, Jonsson, 2006) and thus receive a simulated flux from a chosen line of sight, the simplest solution is to replace this luminous flux by stellar density. As light concentration can usually be directly linked to stellar density, we expect to find similar profiles if we plot the logarithm of the density of stars as a function of the cylindrical radius, instead of the surface brightness. This plot is called surface density profile (or ra-

dial density profile), and will be studied in detail for our simulations in section 4.

The study of surface brightness (or density) profiles is based on the assumption that each galactic component, such as the bulge or the disc, has a typical density distribution. For example, the classical bulge shows a very rapid decrease in density when moving away from the center, whereas the disc shows a slowly (or at least slower) decreasing density as a function of the radius (see section 3.4). This allows the decomposition of the profiles into several parts, each associated to a distinct component. These components can thus be analyzed separately, based on the corresponding radius interval of the profile, and using fitting functions to characterize them. The classical bulges of two different galaxies will show a typical rapid central decrease in the radial profile, but the properties of this decrease will vary from one bulge to the other, and can be derived by fitting a function on the central part with free parameters. The values of these parameters are directly linked to the component properties, for example its mass or extent, and can then be used to understand and constrain its nature or even its formation scenario.
Nevertheless, the analysis of the surface brightness profiles has some limitations. First of all, the assumption that the galaxy is axisymmetric is not always true, some components such as the bar or the spiral arms are clearly non-axisymmetric. This means that the profile of the bar at a given radius shows the average between the bar brightness and the surrounding disc, instead of only the bar. Although this does not prevent the analysis of the bar profile, as shown in sections 3.3 and 4.3.2, it makes it less reliable and more difficult to isolate. The other major limitation is linked to the fact that the light received comes from the superposition of several components, since each component is not located at a distinct radius interval. Therefore, to isolate a component, several superposed functions need to be fitted, which can lead to free parameters degeneracy. Furthermore, we only receive the light in the sky plane, whereas the galaxy is triaxial, and thus several structures can be vertically added in the observed radial profile, resulting in more uncertainties for the profile decomposition. Nonetheless, in nearly face-on disc galaxies the components are usually rather flat, so that this does not significantly affect the decomposition, although the presence and effect of a thick disc is discussed in sections 4.3.1.3 and 4.5.

In the following sections, I present the surface brightness profile parts associated to different components in disc galaxies, as well as their properties. It is important to note that the surface brightness is usually plotted in magnitude units, whereas the fit is based on the intensity, so that the logarithm of the fitting functions are actually displayed on the surface brightness profile. For example, if we fit the disc part with an exponential function, it will appear as a linear fit on the plot.

3.2. Bulge part

The central part of the surface brightness profile is dominated by the classical bulge (if there is one), as it is more luminous than the underlying disc. As mentioned in the previous section, the bulge shows a rapid decay in luminosity, so that the profile is dominated by the disc usually after a few kiloparsecs from the center. As specified in section 1.2.3.1, classical bulges are very similar to elliptical galaxies, and this is also true for the surface brightness profile. De Vaucouleurs first proposed to fit elliptical galaxies profiles with a power law function, named after his name:

$$I(R) = I(0)e^{-kR^{1/4}} \tag{3.1}$$

k being a constant. Using the radius of the isophote containing half the total luminosity R_e and the corresponding surface brightness I_e, this can be also written:

$$I(R) = I_e e^{-7.67((\frac{R}{R_e})^{1/4}-1)} \tag{3.2}$$

This typical $R^{1/4}$ law has long been used to fit the surface brightness profile of the classical bulge as well (e.g. Shaw and Gilmore, 1989; Byun and Freeman, 1995), but later a generalization of this power law has been shown to be more accurate (Möllenhoff and Heidt, 2001; MacArthur, Courteau, and Holtzman, 2003), the Sérsic law (Sérsic, 1968):

$$I(R) = I(0)e^{-kR^{1/n}} \tag{3.3}$$

where n controls the curvature of the profile (figure 3.1), $n = 4$ corresponding to the de Vaucouleurs law. n can be set as a free parameter to fit the bulge, and is usually found to be close to 4 for classical bulges, as predicted by de Vaucouleurs.

Nevertheless, as described in section 1.2.3, there is more than one type of bulge, and the discy and boxy/peanut bulges show a very different shape than the classical one, which prevents them to be fitted with the same function. Kormendy and Kennicutt (2004) showed that these "pseudo-bulges" can be fitted using a Sérsic function as well, with a Sérsic index $n \sim 1 - 2$.

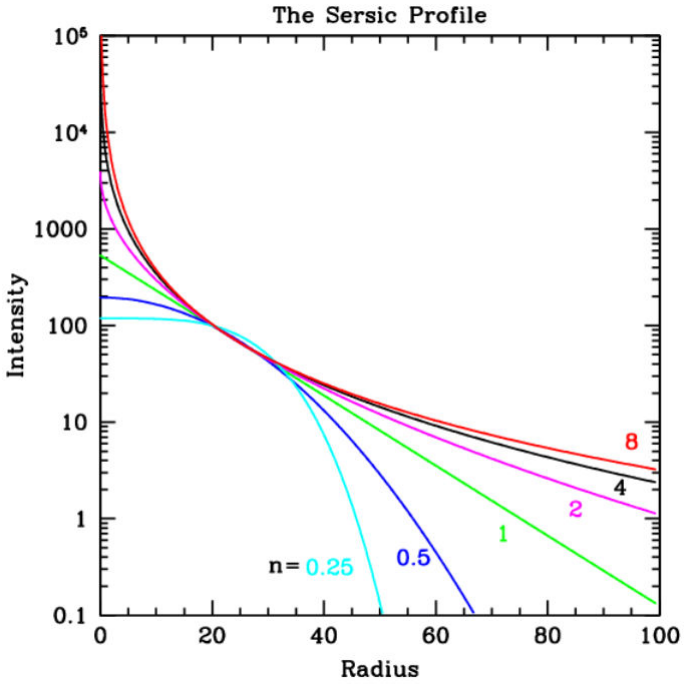

Figure 3.1.: Shapes of the Sérsic function by varying its index n, while other parameters are fixed. The intensity is in logarithmic scale, to represent the luminosity.

3.3. Bar

The bar is not always easy to detect in the surface brightness profile, depending on its shape, strength and extent. Small bars will usually be difficult to observe, being dominated by the bulge brightness profile. On the other hand, strong and long bars will go out of the bulge part and extend through the disc profile, which makes them easy to see in the surface brightness profile, being much brighter than the local disc.
In the profile, a strong bar usually show a rather constant (or slowly decreasing) brightness, followed by a small drop, corresponding to the end of the bar. These are called flat bars. On the other hand, weak bars have a brightness profile decreasing in an exponential way, and are also called exponential bars. Examples of surface brightness profiles including bars can be found in section 3.4.
The bar has the specificity of being non-axisymmetric, which makes it difficult to fit reliably since the observed brightness is a circular average between the bar and the local disc. However, it is possible to use a function to reproduce the bar profile, with free parameters allowing to adapt for different types of bars. One function used for the fit is the Ferrers function, but a Sérsic function can also be appropriate (e.g. Laurikainen, Salo, and Buta, 2005), with a low n parameter.

3.4. Disc part

The disc is usually the dominant part of the surface brightness profile in late-type galaxies, being the most extended. It is also the part I focused my analysis on during my PhD, as will be seen in section 4.4. Although the disc was first thought to be easily characterized with a single exponential profile, it has then been shown to be more complex, displaying several types of profiles from one galaxy to another. This is described in details in the following sections.

3.4.1. Single Exponential

The first attempts to fit the surface brightness profile of disc galaxies showed that a single decreasing exponential function was the most appropriate (Freeman, 1970), before later works found the presence of a break in the radial profile of most disc galaxies (van der Kruit, 1979; van der Kruit and Searle, 1981; Pohlen, Dettmar, Lütticke, et al., 2002). Nevertheless, single exponential discs are still observed in about 10 to 30 % of disc galaxies (Pohlen and Trujillo, 2006; Erwin, Pohlen, and Beckman, 2008; Gutiérrez, Erwin, Aladro, et al., 2011; Laine, Laurikainen, Salo, et al., 2014), and are also called *type I* discs. This name was first proposed by Freeman (1970), to distinguish single exponentials from *type II* (and later *type III*) discs, where a break is observed in the profile (see following sections). The typical function used to fit the luminosity in type I profiles is:

$$I(R) = I(0)e^{-\frac{R}{R_0}} \tag{3.4}$$

where $I(0)$ and R_0 are free parameters. R_0 is called the scalelength, and is an essential parameter to characterize the extent of the disc. Large scalelengths correspond to extended discs, whereas low values show rapidly decreasing profiles. A single exponential has been argued to be the canonical profile for a disc (Gunn, 1982; Yoshii and Sommer-Larsen, 1989; Ferguson and Clarke, 2001; B. G. Elmegreen and Struck, 2013). An example of a type I disc is shown in figure 3.2 (left panel), with the corresponding fit. As mentioned in section 3.1, the exponential disc appears as a decreasing straight line in the surface brightness profile, as the plot displays the common logarithm of the intensity.

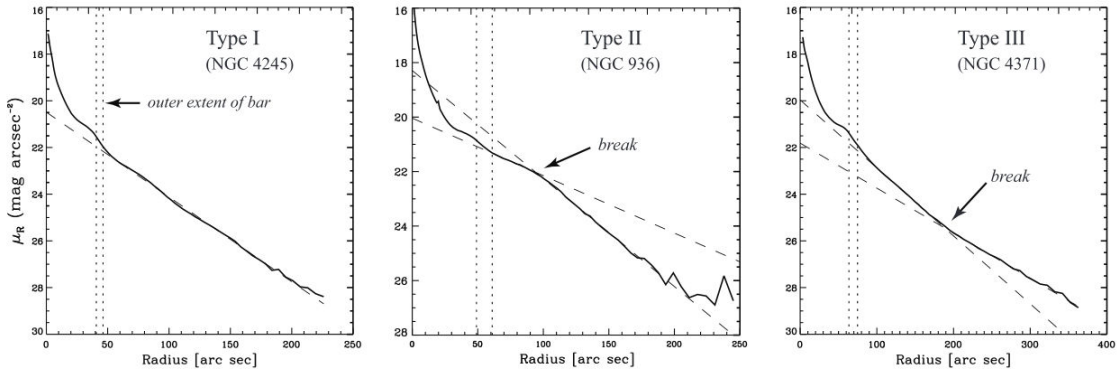

Figure 3.2.: Surface brightness profiles for three galaxies with different disc types (Erwin, Pohlen, and Beckman, 2008). The vertical dotted lines represent the estimate of the bar size, and the dashed lines are the exponentials fits of the different disc parts.

3.4.2. Downbending disc

The increasing size of the telescopes allows astronomers to explore more and more the outer parts of galaxies, which improves the quality, but also the radius range of the surface brightness profiles. This is how in 1979, van der Kruit showed that in some disc galaxies, the radial profile cannot be well fitted by a single exponential profile, the outer parts showing a very sharp edge. Indeed, we now know that for most disc galaxies, the exponential profile is only valid in the inner regions, until a break in slope occurs. This break marks the separation between the *inner disc* and the *outer disc*, and it was shown that the outer disc can also be well fitted by an exponential (e.g. Naeslund and Joersaeter, 1997, Pohlen, Dettmar, Lütticke, et al., 2002), different from the inner disc one. The best way to fit this type of profile is thus with a double exponential function, also called *broken exponential*:

$$
\begin{aligned}
&I(R) = I_{in}(R) + I_{out}(R),\\
&I_{in}(R) = I_{0,in} e^{-\frac{R}{R_{in}}} \quad \text{for} \quad R < R_{break}, \quad I_{in}(R) = 0 \quad \text{for} \quad R > R_{break},\\
&I_{out}(R) = I_{0,out} e^{-\frac{R}{R_{out}}} \quad \text{for} \quad R > R_{break}, \quad I_{out}(R) = 0 \quad \text{for} \quad R < R_{break},
\end{aligned}
\tag{3.5}
$$

$I_{0,in}$, $I_{0,out}$, R_{in} and R_{out} being free parameters, and R_{break} the break radius.
The break is sometimes also called $truncation$ (corresponding to a $truncated$ profile).
Those broken-exponential profiles can be of two types: the outer disc can be either steeper than the inner disc, or shallower. The first case is called downbending, or type II (Pohlen and Trujillo, 2006) and corresponds to an inner disc scalelength R_{in} (hereafter inner scalelength) being larger than the outer disc

scalelength R_{out} (outer scalelength). These discs are the most common ones, representing between 40 to 60 % of late-type galaxies (Pohlen and Trujillo, 2006; Erwin, Pohlen, and Beckman, 2008; Gutiérrez, Erwin, Aladro, et al., 2011; Laine, Laurikainen, Salo, et al., 2014). I show an example of a downbending disc in figure 3.2 (middle panel), with the corresponding fit.

Different types of downbending discs have been observed. II.i discs have a break related to the galactic bar, being located in the bar region, while II.o are located farther, as classified by Erwin, Pohlen, and Beckman (2008). These authors further decomposed II.o discs into II.o-CT profiles, as *classical truncation*, and II.o-OLR, as Outer Lindblad Resonance (see section 1.2.4.2 about resonances). This shows that the origin of downbending discs is not unique, and several formation scenarios have been proposed. They are thought to be created by star formation thresholds (II.o-CT, Schaye, 2004; Pohlen and Trujillo, 2006; B. G. Elmegreen and Hunter, 2006), by bars via the Outer Lindblad Resonance (Pohlen and Trujillo, 2006; Muñoz-Mateos, Sheth, Gil de Paz, et al., 2013; Kim, Gadotti, Sheth, et al., 2014), or connected with morphological components such as rings or spirals (Laine, Laurikainen, Salo, et al., 2014). The stellar migration is also found to be important in the creation of type II profiles, being able to redistribute the stars from the inner disc to the outer disc (Yoachim, Roškar, and Debattista, 2010; Yoachim, Roškar, and Debattista, 2012), and can be coupled with a star formation threshold (Roškar, Debattista, Stinson, et al., 2008).

3.4.3. Upbending disc

Upbending discs are the second case of broken exponential profiles, when the outer disc is shallower than the inner disc, and is also called type III disc (Erwin, Beckman, and Pohlen, 2005). This means that the outer scalelength is larger than the inner scalelength, and occurs for 20 to 40 % (Pohlen and Trujillo, 2006; Erwin, Pohlen, and Beckman, 2008; Gutiérrez, Erwin, Aladro, et al., 2011; Laine, Laurikainen, Salo, et al., 2014) of disc galaxies. I show an example in figure 3.2 (right panel), with the corresponding fit.
The origin of upbending discs remains poorly understood. They are sometimes associated with a spheroidal component such as a stellar halo (Erwin, Beckman, and Pohlen, 2005; Bakos and Trujillo, 2012), and are then called type III-s. The other type III discs are called III-d, when the outer part is a disc component instead of a spheroid. This outer disc can be formed by the superposition of a thin and a thick disc (Comerón, B. G. Elmegreen, Salo, et al., 2012), could be the result of minor mergers (Younger, Cox, Seth, et al., 2007), or linked to a strong bar (Herpich, Stinson, Rix, et al., 2015).

In some cases, combinations of type II and type III discs have been observed, showing a triple exponential profile, with two different breaks. Those profiles are

generally II+III profiles, which means that a downbending profile is followed by a third exponential with a shallower slope (e.g. Pohlen and Trujillo, 2006; Erwin, Pohlen, and Beckman, 2008; Gutiérrez, Erwin, Aladro, et al., 2011; Minchev, Famaey, Quillen, et al., 2012; Laine, Laurikainen, Salo, et al., 2014), as in figure 3.3. This type of profile is not yet fully understood, and could be associated to a combination of several features, each break being formed by a different mechanism.

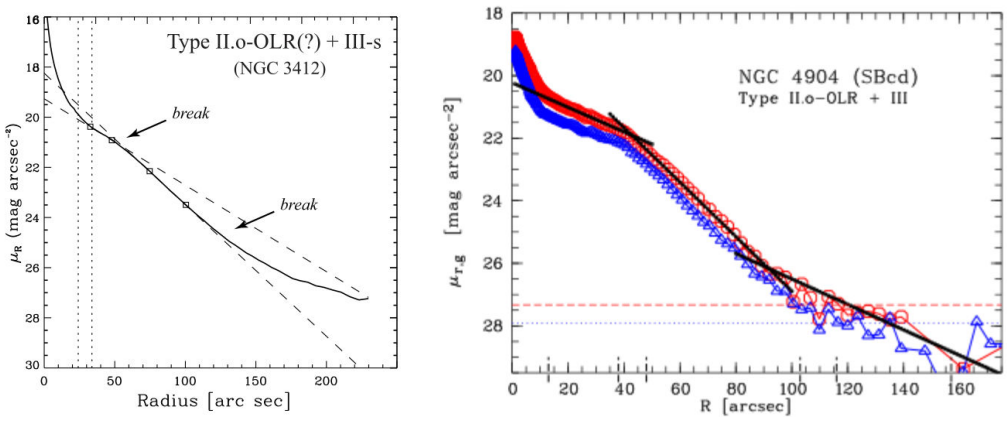

Figure 3.3.: Examples of composite surface brightness profiles: downbending disc + upbending end (II+III). The left panel is from Erwin, Pohlen, and Beckman, 2008, while the right panel is from Pohlen and Trujillo, 2006.

3.4.4. Disc types frequencies and Hubble sequence

The fractions of type I, II and III discs I presented above are an average for all disc galaxies. Nevertheless, it has been observed that these fractions vary along the Hubble sequence of disc galaxies (lenticulars and spirals). This is an interesting result, because different mechanisms can be involved in the formation of different Hubble type galaxies (for example mergers for lenticulars), which can help us to constrain and understand how each disc type is formed.
Gutiérrez, Erwin, Aladro, et al. (2011) and Laine, Laurikainen, Salo, et al. (2014) have studied the frequencies of the different disc types as a function of Hubble type in large samples of observed galaxies, and both found that type I discs are more frequently observed in early-type disc galaxies (S0 or Sa) than in late-type (see figure 3.4). On the other hand, type III discs do not seem to show any dependence on the Hubble type, while type II discs were found to be more frequent in late-type disc galaxies than in early type. Nevertheless, the quantitative results vary heavily from one study to the other, and are different for barred and non-barred galaxies.

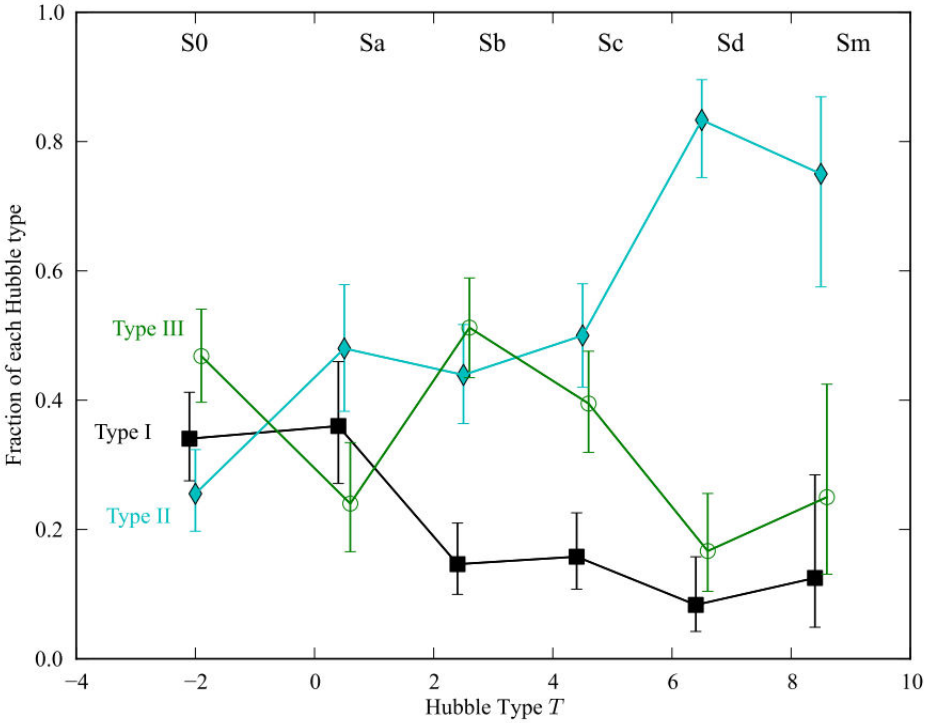

Figure 3.4.: Fractions of type I, II, and III discs as a function of the Hubble type, from Gutiérrez, Erwin, Aladro, et al. (2011) on a sample of 183 early and late-types galaxies. Error bars are 68% confidence limits based on the Wilson confidence interval.

4. Study of the density distribution in our simulations

4.1. Two-dimensional analysis

The surface brightness of a galaxy can be characterized using the radial profile, but as described in section 3.1, this method shows some limitations. To get rid of the axisymmetrization problem, one can study the surface brightness in two dimensions, instead of projecting it on the radius. As with the radial profile, the goal is to fit the surface brightness and its different components, but this time directly on an image of the galaxy. This can be done using softwares such as GALFIT or BUDDA, which can be used both for observations and simulations, taking a given number of functions to reproduce the luminosity (or density) 2D distribution of a snapshot. I tried to use those tools to fit some snapshots at the end of our major merger simulations, taken face-on for simplicity.

4.1.1. GALFIT

GALFIT is a program fitting 2D analytic functions to galaxies directly to digital images, the number and nature of the functions being chosen by the user. The optimization of the fits is based on the Levenberg-Marquardt algorithm, and a residual image is given in output (along with a file containing the free parameters retained), which is the substraction of the resulting surface brightness of the fit to the original image. This way one can see if some parts of the galaxy were well or badly fitted (see an example in figure 4.1), since a perfect fit would result in a totally black residual. The fitting functions are applied on generalized ellipses with a given ellipticity (or axis ratio $b/a < 1$), position angle (PA), and diskiness/boxiness $C0$, which allows to fit non-axisymmetric components such as bars or oval discs. The available functions are the Sérsic profile, the exponential disc, the edge-on disc, the Nuker law, the gaussian, the modified Ferrer profile, the empirical King and the Moffat profiles. A detailed description of GALFIT can be found in Peng, Ho, Impey, et al. (2002); Peng, Ho, Impey, et al. (2010). GALFIT takes a single input file containing all the parameters needed for the fit, such as the name of the input $fits$ image, of the analytical functions to use, and their

initial parameters. Several additional parameters can be chosen, such as a PSF image or a bad pixel mask, which I did not need for my analysis on simulations.

An important part of the work is to determine the correct initial parameters of the fitting functions, for example the half-light radius and the integrated magnitude for an exponential disc, as well as the ellipticity and position angle. Indeed, the fit is very sensitive to the initial parameters, and with completely wrong first guesses – especially when there are many functions to fit – the fit will probably either fail or be completely wrong as well. As often stated in computer sciences: *"Garbage in, garbage out"*. The estimate of the ellipticity and position angle of a component can be done using IRAF with the task $ellipse$, fitting ellipses to the isophotes of the corresponding component on the snapshot. To get good first guesses on the function's parameters, one can derive the 1D radial profile, and estimate by eye the parameters on the plot. For example, for an exponential disc, by extending the estimated exponential function to the center ($r = 0$), one gets a good estimate of the integrated magnitude.

I thus used GALFIT on snapshots (transformed into $fits$ files beforehand) of our remnant galaxies, and tried to fit first a bulge (with a Sérsic function) and an exponential disc. Nevertheless, despite trying many different initial parameters (first guessed from the radial profile, and then extented to other values), I was not able to fit the central part correctly ; the residual image was still showing a bright very central part (see figure 4.1). The only way I found to solve this problem was by adding another Sérsic function in the central part, representing a second bulge. This gave me a correct residual in the central part,with one fitted Sérsic of index close to 1 (discy bulge, see section 3.2), and another close to 2.5. The second one, although being lower than the typical $n = 4$ de Vaucouleurs index, is associated to a classical bulge. I checked that these result were consistent with the radial density profile by fitting it also with two distinct Sérsic functions, and found similar results (see section 4.3.1.2). This method thus allowed me to find the presence of two distinct bulges in our simulations: a discy and a classical bulge. Note that this was not obvious from the radial density profile only, since a single bulge could have been good enough in 1D.

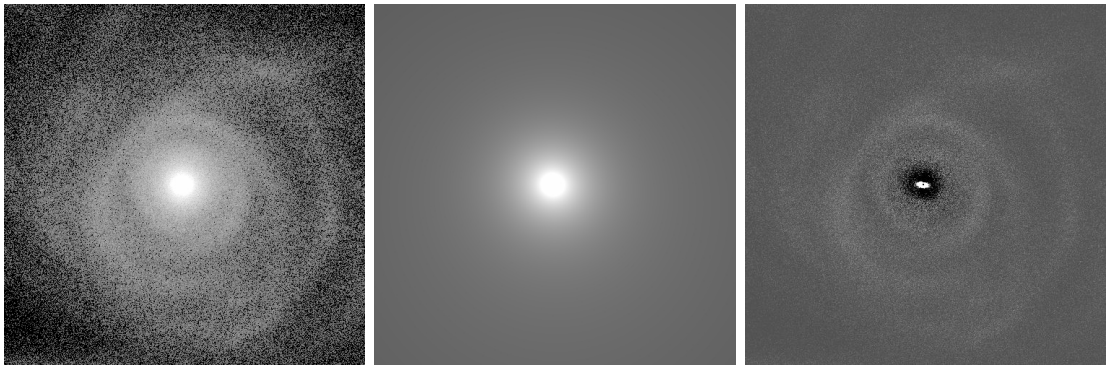

Figure 4.1.: From left to right: simulation's original snapshot, fitted 2D model, and residual image. The 2D fit was made using GALFIT with a Sérsic function for the bulge and an exponential for the disc. The very central bright part in the residual shows that the fit was not able to reproduce the whole bulge part correctly, and suggests the presence of a second bulge, possibly a discy pseudo-bulge.

I then extended my study to the disc part. The exponential disc I used in GALFIT reproduced well the inner part of the disc, and was in agreement with the radial density profile, but as mentioned in section 2.1.1, our remnant galaxies have truncated downbending discs. I thus needed to fit the outer part with a second exponential disc. The fit of truncated discs is possible in GALFIT, by using two exponential functions, truncated inwards for the outer one and outards for the inner, by a truncation function defined independently. I thus used this truncation function alongside the two exponentials to reproduce the downbending discs observed in our simulations. I estimated the break radius on the radial profile, which I used as first guess for the truncation function. Nevertheless, I did not manage to recreate the break observed in the snapshot, the fitted surface brightness showing a discontinuity (instead of a simple break in slope) at the break radius. The problem is that the fitting method of GALFIT for truncations does not constrain the surface brightness to be continuous, so that the two exponentials fitted do not have to be at the exact same luminosity (or density) at the break radius. Despite trying many initial parameters, and constraining the value of some of them (such as the break radius), I was not able to get reasonable (i.e. continuous) surface brightness fits for our downbending discs.

4.1.2. BUDDA

I thus decided to try another 2D fitting algorithm, BUDDA. BUDDA allows to fit 4 major components in a galaxy: a bulge, a disc, a bar and a central source of light such as an AGN. The bar and the bulge are fitted by two Sérsic profiles, and the disc by an exponential. As for GALFIT, the fitting functions are expressed along

the semi-major axis of generalized ellipses. However, contrary to GALFIT, where the user can choose the number and nature of the fitting functions, in BUDDA there can only be two Sérsic functions for the bulge and the bar, one exponential for the disc and one Moffat profile for the AGN. No other functions or components are allowed, but the sky contribution and the atmosphering seing can be taken into account, and most importantly here, a double exponential disc can be used. The fit is also very sensitive to the initial conditions, provided in an input file. A detailed description of BUDDA can be found in de Souza, Gadotti, and dos Anjos (2004).
I thus tried to fit again the disc surface density of our simulations, using a double exponential disc. As with GALFIT, I tried several initial parameters, and even found empirically the best fitting parameters. However, again I failed to find a free consistent fit, the two discs being discontinuous at the break radius, even when the empirically derived parameters were set as initial conditions. Constraining the values of some parameters did not help, the only way to get a continuous profile was to fix both scalelengths to the right (empirically found) values, which was not interesting for my analysis. Facing the same problem as with GALFIT, I decided to give up on the 2D analysis of our simulations.

4.2. One-dimensional analysis

Since the 2D fitting was not successful, I focused on the 1D profile, i.e. the surface density profile.

4.2.1. Fitting Procedure

The first step is to derive the surface density profile for our remnant galaxies. To do this, I used axisymmetric radial bins, taking circular and concentric annuli in the galactic plane and counting the number of stellar particles located inside, using their cylindrical radius (not considering their vertical positions). To derive the density in a given annulus, I then summed the masses of the stars found inside, and divided by the area covered by the annulus. This gave me the stellar density as a function of the radius, and by taking the natural logarithm of the density I got the surface density profile (or radial density profile), which can be directly compared to the surface brightness profile in observations. For simplicity, I computed the profile face-on for a given snapshot, meaning that I just take the particles positions and the concentric annuli in the galactic plane, without assuming any angle in the line of sight. I defined the center of the annuli as the center of density computed for the whole galaxy (including gas, stars and dark matter).

Another way to derive the radial density profile would be to use ellipses instead of circles, based on the isophotes. This can be achieved for example using the $ellipse$ task in IRAF, which computes the isophotes on a 2D image of a galaxy, and tries to fit them using concentric ellipses. One can then derive at every semi-major axis the density averaged over the corresponding ellipse, which gives a surface density profile. This method is often used for observed galaxies, which are not perfectly face-on and thus cannot be fitted with circular averaging. There are two ways to do it: by keeping the position angle and the ellipticity of the ellipses constant with radius – usually fixed on the outer disc values (e.g. Pohlen and Trujillo, 2006; Erwin, Pohlen, and Beckman, 2008), or let them as free parameters, allowing them to vary with radius (or semi-major axis). The former is the most frequent, and is equivalent to circular averaging for face-on galaxies, since these ellipses are just circles inclined with the inclination angle of the galaxy (assuming that the outer disc is circular). A study of the effect of inclination on the radial density profile can be found in Paper IV (section 4.4.3.1). On the other hand, letting the ellipticity and position angle vary with radius is a different method, since the ellipses will be different depending on the components fitted (for example for the bar and the disc). It has the advantage of giving the real density of isophotes, which can be more physically consistent than a circular average, for example for the bar. Nevertheless, the resulting density is not expressed as a function of the radius but as a function of the semi-major axis, which is sometimes more difficult to visualize in the case of varying ellipticities, and besides isophotes are not always ellipse shaped. This last point can make the ellipse fit – and thus the surface brightness profile – unreliable, especially in the case of local inhomogeneities such as spirals. On the other hand, circular averages (or fixed ellipse fitting) are not dependent on the isophotes and on local components, and despite being sometimes less consistent for non-axisymmetric components, are more reliable overall. A discussion about the comparison between free ellipse and fixed ellipses fitting can be found in Erwin, Pohlen, and Beckman (2008).

Once the radial profile is derived for a given snapshot, it is time to decompose it into different parts and fit them using functions such as those described in section 3. For this, I wrote a $Fortran$ program allowing me to interactively select the interval to fit. This program first computes the radial density profile with the procedure described above, and displays it in an interactive window. In this window, one can manually choose the radius interval to fit on the profile, as well as the function to fit it with (exponential, Sérsic, etc.). The program then fits the selected part of the profile by finding the best free parameters with a least square algorithm (starting from initial values fixed beforehand), and displays again the density profile, with the fitted function superposed. One can then select a new interval to fit with another function, which will be added to the previously fitted ones. Indeed, the density of the bulge adds to the density of the underlying disc,

so that the resulting profile should be the sum of the two. In the case of a break in the disc profile, one can choose the position of the break manually, and fit the outer disc part separately from the inner disc part. In this particular situation, the inner disc and outer disc exponential fitted functions do not add, as a broken exponential profile is not the sum of two exponentials but the stack of two distinct exponentials, each on a different radius interval.
To optimize the free parameters, the least square algorithm uses the relative differences between the function and the profile, and not the absolute differences. This allows the fit to be as reliable for the high values of density as for the low values.

Although the number of stars in the halo is very low, I did not want these stars to be included in my density profiles, since I am interested in the galactic disc profile. I thus decided to fix a maximum height from the disc for the stellar particles to be taken into account. After several trials, I took $zmax = 1$ kpc ($|z| < 1$ kpc) to keep only the thin disc.

4.2.2. Difficulties

4.2.2.1. Difficulties about axisymmetrisation

As mentioned in section 3.1, one of the major problems of radial profiles is that they do not give an accurate description of non-axisymmetric components. In particular, the bar is non-axisymmetric, and can be washed out by the circular averaging, especially in the case of small and weak bars. To solve this, I tried to limit the analysis to a band in the galactic plane going accross the galactic center. By setting a band in the bar direction, one can get the density along the bar only, instead of an average between the disc and the bar. This band is set by fixing a maximum width and an angle.
I thus implemented this band method to my fitting program, with a 2 kpc wide band placed along the bar, to see if it could help me to fit the bar more accurately. As shown in figure 4.2 for a simulation with a big bar, the bar part (around 5 kpc) is indeed slightly more prominent, which should make its fit easier and more reliable. However, the effect is not outstanding, and the disc part is much worse than in the circular average method, being very noisy and badly defined. This is due to the fact that there are much less particles taken in the band method, and the spirals can locally disturb the density profile along the band. The break (around 10 kpc) can hardly be seen in the band method, and the bulge central part has a strange behaviour.
To conclude, if I gain some accuracy on the description of the bar part with the band method, I loose much more in the resolution of the bulge and disc part, which makes the overall fit very difficult. I thus chose to discard this method,

and kept the circular averaging to derive the density profile, even if the bar is not always well described this way.

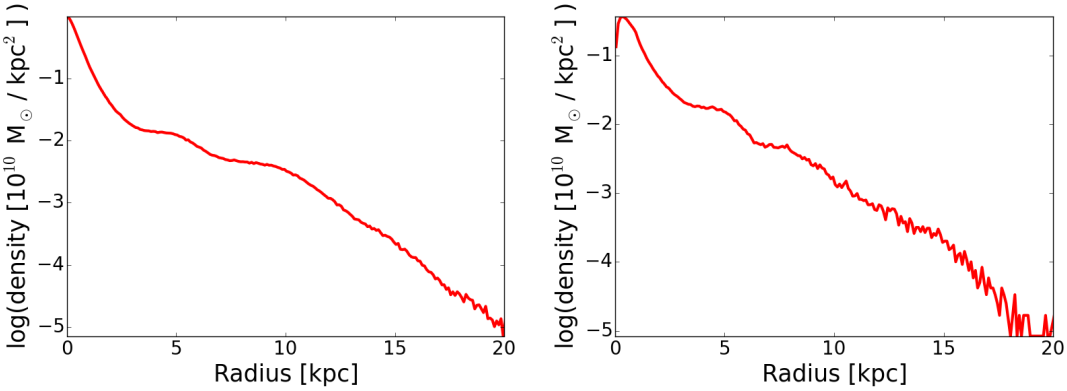

Figure 4.2.: Radial density profile of a snapshot with a prominent bar, derived in the standard way on a 360 degrees arc angle (left image) and by taking only a 2 kpc wide band along the bar (right image). The bar is located around 5 kpc, and is more prominent on the profile with the band method.

4.2.2.2. How spirals can interfere with the fit

In an ideal exponential disc, the light distribution would be smooth and axisymmetric, and would decrease monotonically with the radius. Nevertheless, in late-type galaxies, some components such as bars, spirals or rings often represent a local excess of light, which can be well seen in surface density profiles. They appear as local small bumps in density (see examples in figure 4.3), which prevents the profile to be a perfect exponential, and makes the fit less reliable. The bar is sometimes located in the bulge dominated part, and can be fitted as a separate component (see sections 3.3 and 4.3.2), so that it does not represent a serious problem here. However, spirals (or rings) are located in the disc dominated area, and their number and extent vary from one galaxy to another. They are thus difficult to avoid in the fit, especially when there are two different sets of spirals, so that the majority of the disc is covered by them (see $mdf732$ in figure 3 of Paper I, section 2.1.1). This makes the fit of the inner disc difficult (the outer disc is less concerned by spirals since the break is usually located at the end of the spirals, see Paper IV in section 4.4.3.1), and can prevent the localization of the break, when a spiral is located on it. Furthermore, when spirals are located close to the center (for example for the inner set of spirals in $mdf732$), they can be confused with a bar, showing a bump of similar amplitude. The only way to be sure about the presence of a bar is by visual inspection on the face-on image of the galaxy.

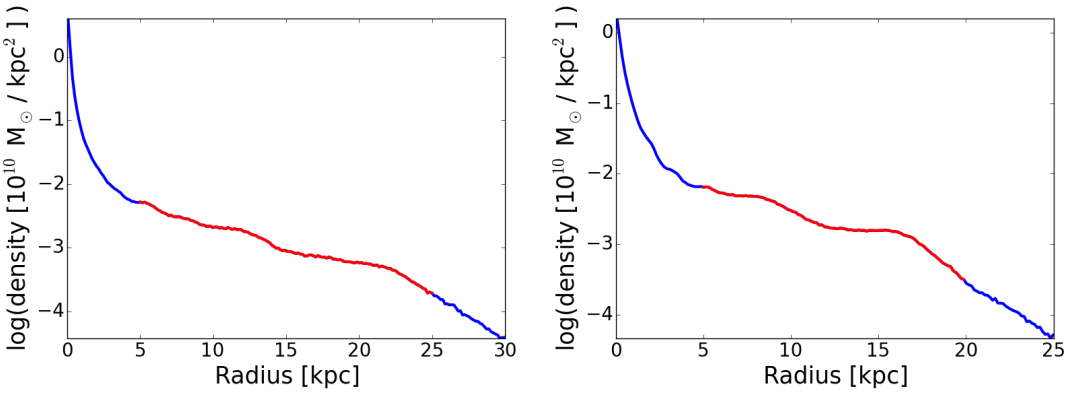

Figure 4.3.: Radial density profiles of two different simulations snapshots. Spirals make little bumps appear on the profile, as around 6 and 13 kpc on the left panel, and 9 kpc on the right. The red parts of the profiles are covered by spirals, as determined by eye on the 2D images of the galaxies.

These spiral arms are thus annoying for the fit, and I tried to find a way to get rid of them. I removed them from the fits, by marking beforehand the radius interval covered by spirals on the face-on image of the snapshot, and removing them from the fitting interval. To do that, I implemented in my $Fortran$ program a subroutine displaying a face-on image of the galaxy with isophotes, which allows to interactively determine the radii of the start and the end of the spirals. Nevertheless, as mentioned in the previous paragraph, spirals can cover a large part of the disc, which makes the remaining fitting range very small – or even non existent (see figure 4.3) – so that I gave up on this method.

Rather than remove them from the fit, I then tried to take only the minimum in density of the spirals, not taking into account the excess of density forming the bump. This method is based on the assumption that spiral arms are excess of matter in the disc, and I aimed here to get the underlying disc (minimum of density) for my fit. I show an example of a fit in figure 4.4 (left panel). This allowed me to get a more reliable fit than the whole spiral removal method presented in the last paragraph, since it keeps some parts of the density profile in the spiral, and thus provides a more extended radius range (although still rather small) for the fit.
Nevertheless, spiral arms are made from matter content taken from the disc, and are usually considered as being part of it, rather than as an additional component. This makes the former assumption doubtful. Furthermore, this method did not give consistent results for time evolution (fitting the disc for different times), showing large scatters in the fitted exponentials parameters such as the inner scalelength. I thus decided to give up on this method too.

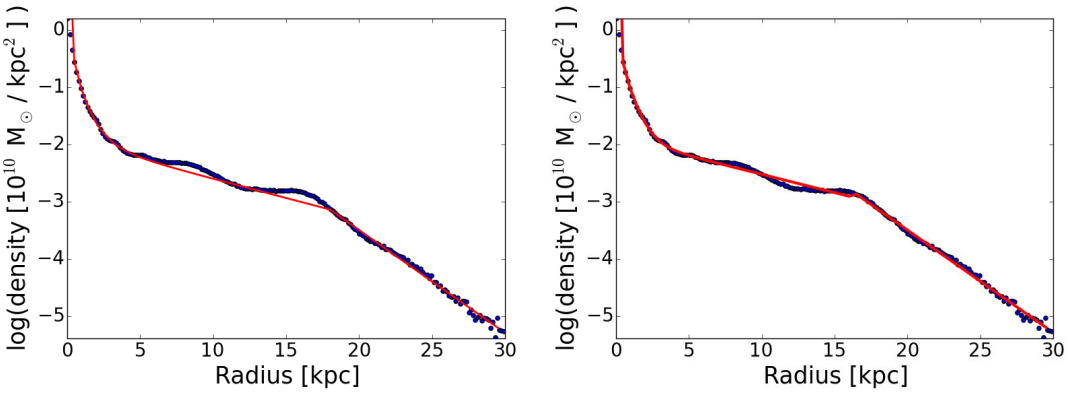

Figure 4.4.: Radial density profile of a snapshot, fitted (red curve) with two different methods with respect to the spirals. The left image shows a fit which tries to reproduce the underlying disc, discarding the spiral arms. This implies to take only the minimum of the profile, ignoring the bumps corresponding to the spirals. The right image takes the spirals into account, and fits an exponential through them, using the whole inner disc interval.

Finally, the best method I found was to simply fit the exponential through the spirals (see figure 4.4, right panel), by assuming that they are part of the disc and should therefore be taken into account for the fit. This gives more consistent time evolution results (see section 4.4.3.1), and uses the whole disc interval. Most of the time (especially for late times), the spiral bumps are rather small and do not disturb the fit in an important way (see figure 4.5, left panel). However, for the case of spirals being very strong and making the fit unreliable (see figure 4.5, right panel), I added a quality parameter Q in the output of the fit, fixed to 1 for reliable fits, and 0 otherwise. Although being purely subjective (I decide after each fit if it is reliable or not), this parameter helped me keeping track of which fits should be trusted or not for an analysis of the derived parameters.

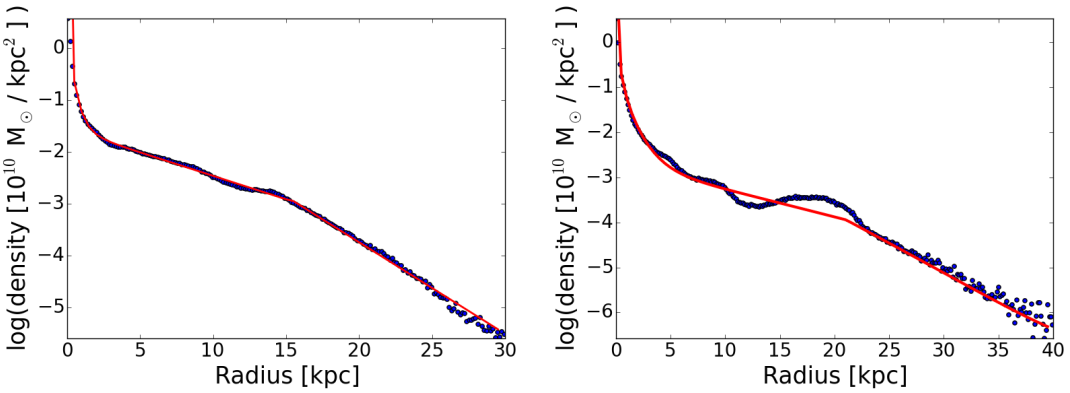

Figure 4.5.: Radial density profiles for two different snapshots including spirals, one where the spirals appear rather small in the profile and the fit (red curve) is thus reliable (left panel), and the other where the spiral bumps are very important in the profile, making the fit unreliable (right panel).

4.3. Inner regions

4.3.1. Bulge

4.3.1.1. Single Bulge

I first used a single Sérsic function to fit the bulge part, expecting a Sérsic index n close to 4 (classical bulge). I thus fixed $n_i = 4$ as initial value for the Sérsic index. The fit seemed to work for the bulge, as shown in figure 4.6 (left panel), and the resulting Sérsic index was as expected around 4.
I used this method to derive the classical bulge-to-total ratio in Paper I, by computing the mass of the fitted bulge and divide it by the mass of the total fitted profile, including the bulge and the downbending disc. The mass of each component can be derived from their fitting function by integrating it over the radius. The integral of a Sérsic is not trivial, but has an analytic solution, which gives the mass of the bulge M_b:

$$M_b(r) = a_b * 2\pi r_b^2 * n * \gamma(2n, (\frac{r}{r_b})^{1/n})$$

for a Sérsic function $\Sigma(r) = a_b * exp(-(\frac{r}{r_b})^{1/n})$, γ being the incomplete gamma function.
I made several trials to have a range of possible values for the bulge-to-total ratio, the fit with a Sérsic being very sensitive to the fitting interval selected.

Fitting the simulations at different time steps, I found that the Sérsic index is more or less constant over time, oscillating around 4 (figure 4.6, right panel).

On the other hand, the bulge effective radius seems to fluctuate heavily over time, with no obvious trend. This seems to point out the fact that the fit of the bulge is not always reliable, and indeed the central part is often not perfectly reproduced.
Therefore, to improve the quality of the central part fit, I added another bulge, as described in the following section.

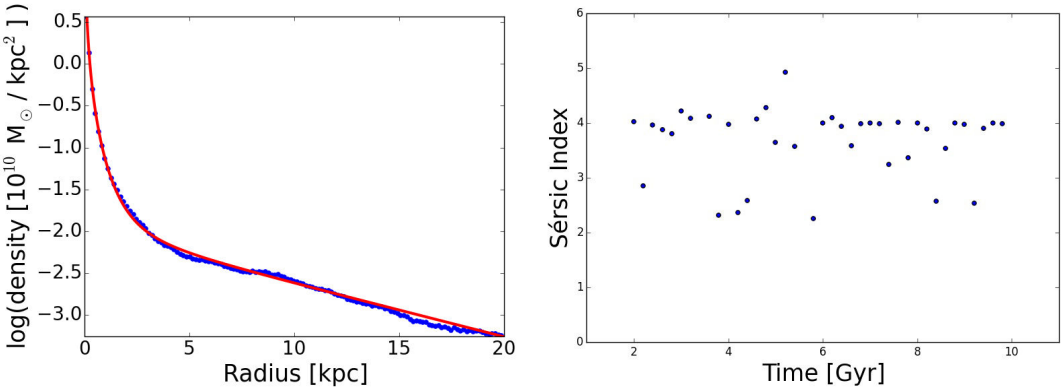

Figure 4.6.: Left panel: Fit (red curve) of the radial density profile with one Sérsic for the bulge (+ one exponential for the inner disc). Right panel: Sérsic index as a function of time.

4.3.1.2. Double bulge: discy + classical

As mentioned in sections 1.2.3 and 4.1.1, there can be pseudo-bulges in the central part of the galaxy, which have to be fitted as well. I thus used an additional Sérsic function in my fits to account for a pseudo-bulge, with a lower n than the classical bulge.
The problem is that there are now two Sérsic functions to fit on a relatively small interval, which leads to degeneracies in the fit and makes it uncertain, since 6 free parameters are used to fit the bulge area (3 per Sérsic). To be sure to fit a classical bulge and a discy pseudo-bulge with the Sérsic functions, the initial values of the parameters are often not enough, so I added some constraints to the fit parameters. In particular, I constrained the Sérsic index n of both bulges to be above 0.5. This prevents one of the Sérsic to fit a small bump in the profile rather than the bulge.

The resulting fits are now better than in section 4.3.1.1, the central part being better reproduced (figure 4.7, left panel). The Sérsic indexes are coherent, one being around 4 and the other around 1 (see figure 4.7, right panel), which is consistent for respectively a classical and a discy bulge (see section 3.2). Note that depending on the simulation, these values can be slightly lower or higher.

Although it is still consistent with a classical bulge, the first Sérsic index can sometimes be closer to 3 or 5. On the other hand, the second Sérsic tends to be often between 1 and 2, and sometimes closer to 2. This could point out the presence of a boxy/peanut bulge, the fact that the discy bulge is not perfectly discy, or in the worst case scenario a degeneracy problem in the fit.

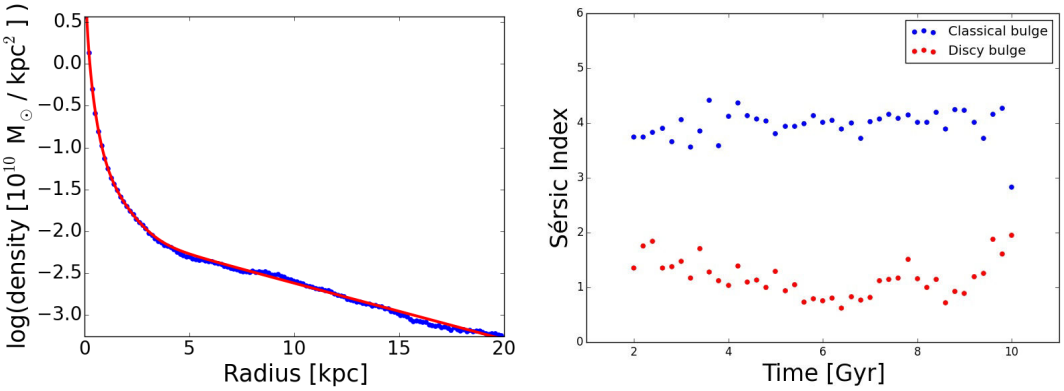

Figure 4.7.: Left panel: Fit of the radial density profile with two Sérsic functions for the bulge (+ one exponential for the inner disc). Right panel: Sérsic indexes as a function of time.

I could have used two Sérsic functions for the pseudo-bulges, one for the discy bulge and one for the boxy/peanut bulge (when there is a bar), but these components are not necessarily both present at the same time, and putting too many fitting functions for a small radius interval can make the fit difficult and cause even more degeneracy problems, as described previously.

4.3.1.3. End of the profile: part of the bulge?

Looking at the outer parts of the radial profiles of our galaxies, I found that the end of the outer disc often shows a flattening. This is shown in figure 4.8. I found that feature for most of our simulations, with a variable extent: sometimes it seems very negligeable, as it is only at the very end of the outer disc and does not disturb the fit. Nonetheless, for some cases it occurs not far away from the break so that the downbending outer disc has a rather short extent – being rapidly dominated by this flattening – which makes the fit difficult and less reliable (see example in figure 4.8).
This flattening could be an upbending disc, as composite downbending followed by upbending (II+III) profiles have been found in observed galaxies (see section 3.4.3). Nevertheless, these composite profiles are not very common, while I find this flattening end in almost every profile. I thus tried to find another explanation.

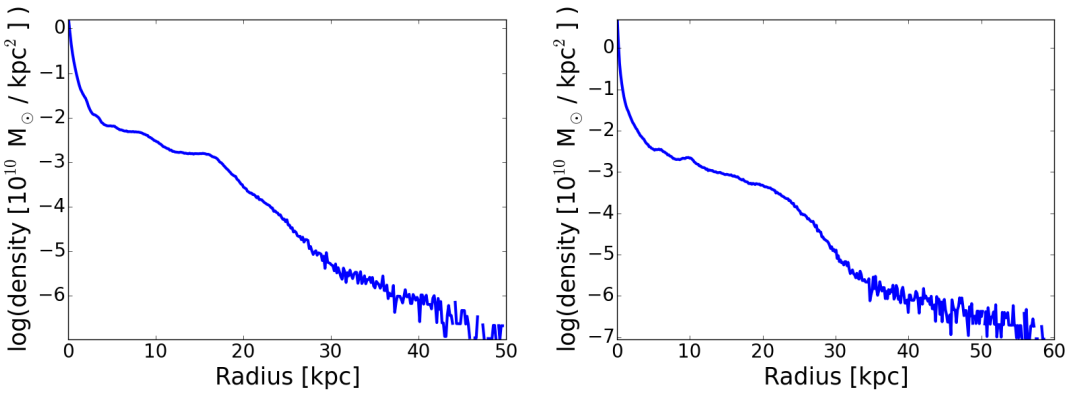

Figure 4.8.: Radial density profiles of two different simulations snapshots, which show a flattening (or upbending) part at the end of the profile, in the outer disc. The left profile shows this feature starting around 30 kpc, but the downbending outer disc part is still big enough to allow a reliable fit (from 16 to 30 kpc). On the other hand, the profile on the right also shows this upbending part around 32 kpc, but the downbending outer disc is difficult to fit reliably, since it extends only between $\sim$ 24 to 32 kpc.

A further possibility would be that this flattening is part of the central classical bulge, at a radius where the disc is too faint and the bulge would be dominant again. This would be likely since it could often easily be fitted with a Sérsic. I thus fitted a Sérsic which would both fit the central part (with the help of a second Sérsic for the discy bulge) as well as the end of the profile. It required to select a fitting interval for the classical Sérsic which includes the whole profile, from the center to the very outer parts. This seemed to work well, as the fit reproduced the profile correctly (see figure 4.9).
To test the accuracy of this fit, I took the two fitted Sérsic functions (classical + discy) and integrated them over the radius (as in section 4.3.1.1) to get the mass of the two bulges as a function of the radius. I plot in figure 4.9 (right panel) the typical shape of the two masses as a function of the radius, for the fit described above. We can see that the classical bulge mass grows slowly in the center, while the discy bulge grows rapidly and is thus dominating the inner part. This does not seem realistic, as the mass of the classical bulge should be mostly concentrated in the center. Here the mass of the classical bulge grows too slowly, the mass included inside 1 kpc radius is only 30% of its total stellar mass. Therefore, it seems that this fit actually reproduces the central part with one Sérsic (with n $\sim$ 1), and the outer part with the other one (with n $\sim$ 4), which was not the goal of this analysis since the classical Sérsic was supposed to reproduce both the central and the outer parts.

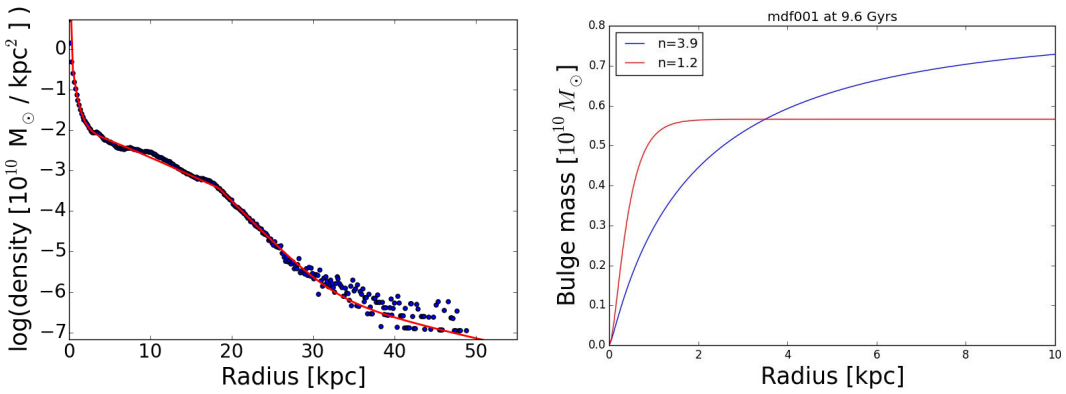

Figure 4.9.: Left panel: Radial density profile of a snapshot, fitted by trying to reproduce the upbending end of the profile with the central classical bulge. The fit is made using two Sérsic functions for the bulge part, one for the classical bulge and one for the discy pseudo-bulge, and two exponentials for the disc. The Sérsic corresponding to the classical bulge is fitted using the whole disc interval, to be able to reproduce the central part as well as the very end of the profile. Right panel: Inside mass of the fitted bulges, as a function of the radius.

I tried several ways of fitting this particular profile (e.g. changing the fitting interval of both Sérsic, putting constraints on their parameters), but I could not achieve to fit both the center and the end of the profile, as any function fitting the end would have to be faint in the center. Having a bulge extending so far (over 40 kpc for some simulations) was very doubtful anyway, and I thus discarded the hypothesis of this flattening to be due to the bulge.

If the end of the profile is not due to a disc or a bulge, what is it? I tried to remove the vertical cut I was using to derive the profile ($|z| < 1$ kpc, see section 4.2.1), and found that this flattening part was even bigger (see figure 4.10). I thus concluded that it was part of a vertically thick component, discarding the hypothesis of a thin upbending disc. It could be a thick disc or a stellar halo, being dominant in the outer part of the disc when the thin disc is too faint. As it seemed to be unrelated to the components I was fitting (bulges, thin inner and outer discs), I decided to ignore this particular part in the profile, and just classify the fit as unreliable (quality parameter $Q = 0$) when the outer disc was too difficult to fit due to this flattening.

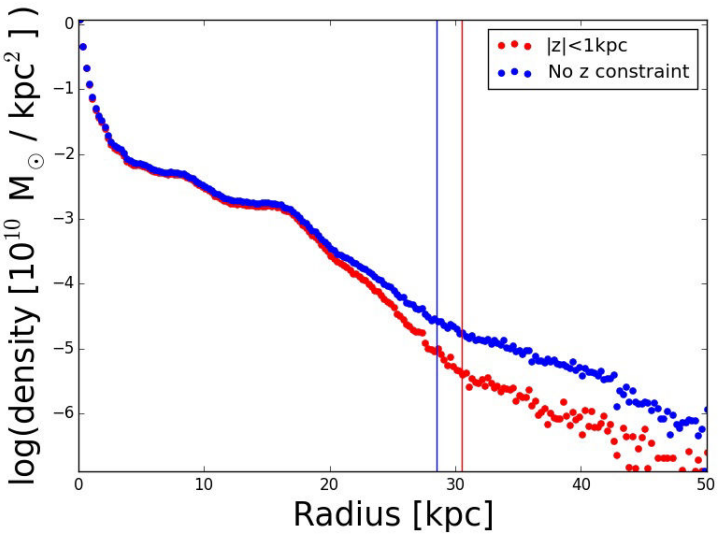

Figure 4.10.: Radial density profiles derived differently for the same snapshot: once with no vertical constraint, and once by taking only the stars being less than 1 kpc distant from the disc. The vertical lines show for each profile where the upbending part starts.

4.3.2. Bar

Most of our remnant galaxies show a bar in the center of the galaxy, which can be of different size, from 1 kpc semi-major axis to $\sim$ 8 kpc. While the smaller bars are often difficult to detect in the radial density profile, the bigger ones can appear as a big bump in the inner disc. In the latter case not fitting the bar could lead to a bad fit of the inner disc and a doubtful value of the inner scalelength. It is thus necessary to fit the bar in the profiles, using a new Sérsic function with a low Sérsic index ($n < 1$, see section 3.3) in my $Fortran$ program. Most of the time the bars are small in our simulations, and fitting them is difficult and does not make a big difference (see figure 4.11, left panel). However, for some simulations the bar is bigger, and the parameters of the fitting functions (such as the inner scalelength or the bulge Sérsic index) are different when a bar is taken into account in the fit (see figure 4.11, right panel).

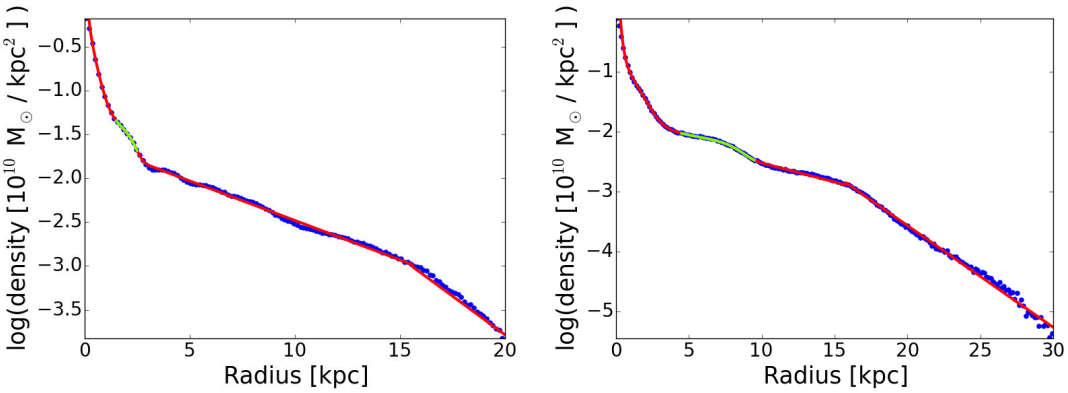

Figure 4.11.: Radial density profiles of a simulation at two different times: when the bar is small (left panel), and later, when it is bigger (right panel). The green part of the fit is the one corresponding to the bar.

One of the main problems is to know what part of the profile corresponds to a bar. While we can guess that a bar will be found between the end of the bulge part and the beginning of the inner disc, as shown in section 4.2.2.2 there are other features in the galaxy that can produce bar-like bumps in the profile, such as the spirals. As in section 4.2.2.2, I used my $Fortran$ subroutine displaying the face-on image of the galaxy to select the radii corresponding to the bar.
Another major problem is that by implementing a bar in the fit, I now have 3 Sérsic functions to fit in the central part, which makes a total of 9 free parameters for a rather small fitting interval (usually less than 5 kpc). As in section 4.3.1.2, there is thus again a degeneracy problem between these different functions, and fixing the appropriate initial parameters is often not enough. To make sure the Sérsic corresponding to the bar fits the bar and nothing else, I put some strong constrains on its parameters. I implemented in my $Fortran$ program the possibility to interactively give the radius corresponding to the end of the bar (estimated by eye on the profile) and fix the bar effective radius to this value. I also constrained the Sérsic index of the bar to be lower than 0.5, to distinguish it from the bulges. This might prevent the fit of exponential bars ($n_{bar} \sim 1$), but these correspond to weak bars, which are usually very discreet in the profile. Bars that really need to be fitted usually have a lower Sérsic index (see figure 4.11).

The bar has a limited life time, and changes over time. Fitting my profiles at different time steps, I could see in some simulations the bar appear, grow, and sometimes decrease in size until it disappears. I show in Appendix D the resulting profiles as a function of time for $mdf992$, alongside face-on images. The resulting bar effective radius tends to follow the growth of the bar, which is consistent since it is fixed by eye estimate. On the other hand, the Sérsic index n_{bar} does not seem to have a consistent behaviour over time. This might be due to the fact

that the area covered by the bar is often too small to give a precise fit, since the Sérsic index is very sensitive to the radius interval.

4.4. Disc part

I fitted our disc profiles using two exponential functions, one for the inner disc and another for the outer disc. The analysis of these fits gave very interesting results, and therefore I dedicated an important part of my work to it, as shown in the following sections.

4.4.1. Understanding the profile

The very vast majority of our galaxies shows downbending discs at the end of the simulation. In this section we try to understand what are the mechanisms involved in the creation of these type II discs.

4.4.1.1. Gas profile

I investigated whether the radial density profile of the gas in the disc was connected to the stellar distribution. I used the same conditions as for the stars, with a 1 kpc maximum height constraint (which is crucial here because of the presence of the hot gaseous halo) and averages over circular annuli. I show some resulting density profiles in figure 4.12. The profile is not as straightforward to fit as the stellar one, and from one galaxy to another some features seem to be very different. Nevertheless, I found a pattern which could be found in most cases: the density shows a peak in the very center, but is then more or less flat (sometimes with bumps), until a rapid drop of density occurs. After this drop the density is slowly decreasing, and rather flat.

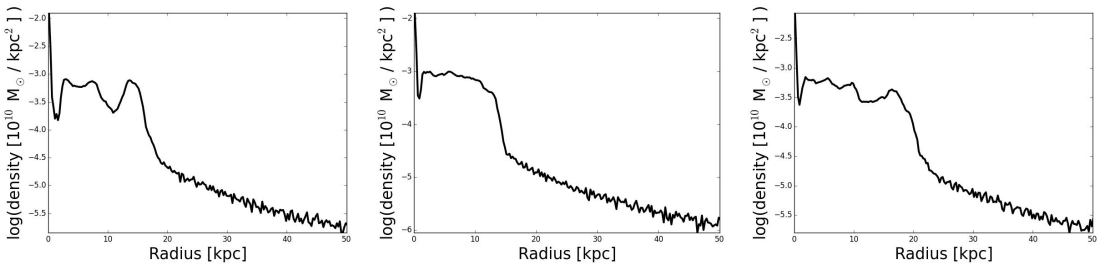

Figure 4.12.: Examples of gas radial density profiles for 3 different simulations.

To characterize this profile and compare it to the stars, I needed to find a fitting function able to successfully reproduce this pattern for most simulations. After trying several functions, I decided to decompose the profile into three parts, each

fitted with a different exponential function, corresponding to the inner flat distribution, the drop, and the outer slowly decreasing part. It could be considered as a II+III composite disc, with two breaks corresponding to the beginning and the end of the drop. Some of the profiles seem to be well fitted by these 3 exponentials (see figure 4.13, left panel), while for others it seems very far-streched (figure 4.13, right panel). Nevertheless, even when the inner part does not look like an exponential at all, we always find this rapid drop in the profile.

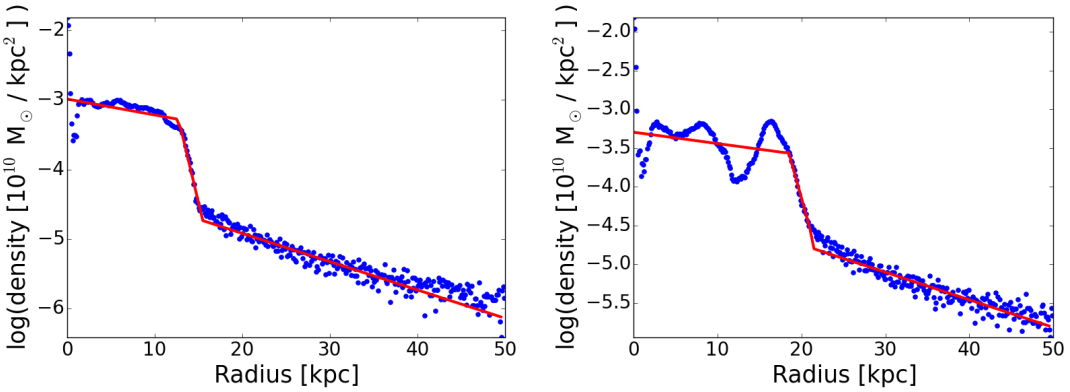

Figure 4.13.: Radial density profiles of two different simulations, fitted with 3 exponential functions. The fit (in red) seems appropriate for the left panel, but not for the inner part of the right panel.

I then proceeded to link the results of my fits to the ones of the stellar profiles. Since the inner part of the gaseous profile shows more or less a downbending profile as the stellar profile, I first tried to see if the scalelengths of the inner and outer discs of both distribution showed similar values. But the drop of the gaseous disc seems to be decreasing much faster than the outer stellar disc, while the inner scalelength of the gaseous inner disc seems to be higher than the inner stellar scalelength. The value of the gaseous inner scalelength seems to be very unreliable though; sometimes the fit even gives a negative value, corresponding to an increasing exponential. This confirms that the inner part may not be well described by an exponential.
Since the scalelengths of the stellar and gaseous distributions do not seem to be related, I looked for a correlation between the breaks. Taking the position of the stellar break, I plotted it against the position of the first gaseous break (beginning of the slope). I found a very good correlation (see figure 6 in paper IV, section 4.4.3.1, and figure 4.14 for all times), the two breaks being located at the same radius for both.

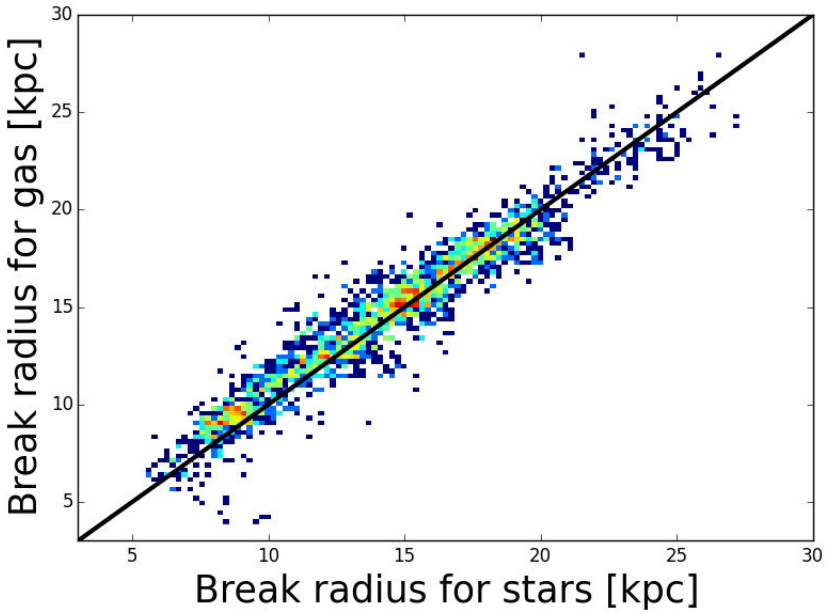

Figure 4.14.: Correlation between the gaseous and the stellar break radii of the radial density profiles, for a sample of 100 simulations taken each at 40 time steps. The colors represent the density of points. Only the break radii for which the fits of the gaseous and stellar density profiles were reliable are plotted.

It is thus interesting to see that the start of the drop of gas density corresponds to the break of the stellar density profile. How can we explain this relation? The stellar disc is linked to the gas distribution, since the density of gas determines the star formation: according to the subgrid physics used for star formation in GADGET3, the probability of a gaseous particle to transform into a star depends on the local gas density. Therefore, the denser a region is in gas, the more we expect to find a high concentration of stars as well. This is why on the gas density profiles I could often see the spiral regions, corresponding to a high gas density (inner bumps in figure 4.12 or 4.13). But this should work in the other way too: low densities of gas should correspond to areas where few stars – or at least few young stars – can be found. Therefore, the drop in the gaseous profile being followed by a region where the gas density is suddenly much lower, we expect to find less stars in this area, and with a different density distribution. This corresponds to the stellar outer disc, and the sudden change in the stellar density distribution gives the break.

If the stellar distribution was directly linked to the gaseous one, we would expect to find a link between the scalelengths of both profiles. Nevertheless, the gas density only determines the amount of young stars found at a given radius, whereas the stellar profile is the sum of all stars, young and old. The old stars

could have been formed at the same radius, when the local density was different, or at a different radius and have migrated since then. In both cases the old stars do not correlate with the gas density at the considered time, which would explain the lack of correlation between the scalelengths. It is probable that we would find a link between the scalelengths of the very young stellar distribution and the ones of the gas at a given time. As a matter of fact, the radial density profile of the youngest star often shows an inner disc which does not look like an exponential (see figure 4 in Paper I), just as the gaseous profile.

The third exponential of the gas profile, the very outer part after the drop, shows a density slowly decreasing up to more than 100 kpc. This seems too far to still be part of the disc, and thus probably corresponds to the hot gaseous halo.

4.4.1.2. Star formation rate

To confirm that the break and the outer disc in the stellar profile are linked to a decrease of star formation (due to a drop of the gas density), I plotted the star formation rate as a function of the radius in the disc. I derived the star formation rate by counting at each radius the number of stars born in the last 0.2 Gyr in the corresponding annulus, and dividing by the surface and the time interval (0.2 Gyr). This gives a SFR expressed in number of stars per square kiloparsec per Gyr. I show some examples of the resulting profile in figure 4.15, with the stellar density profile for comparison.
We can see that the stellar break corresponds to a brutal drop of the SFR, as expected from the drop in the gas density profile. In fact there is very little star formation in the outer disc, which confirms that the outer disc is – at least partly – populated by stellar migration. Nevertheless, there are still some stars formed in the outer disc, but with a different proportion from one simulation to another. A discussion about this can be found in Paper III (section 4.4.2.1).

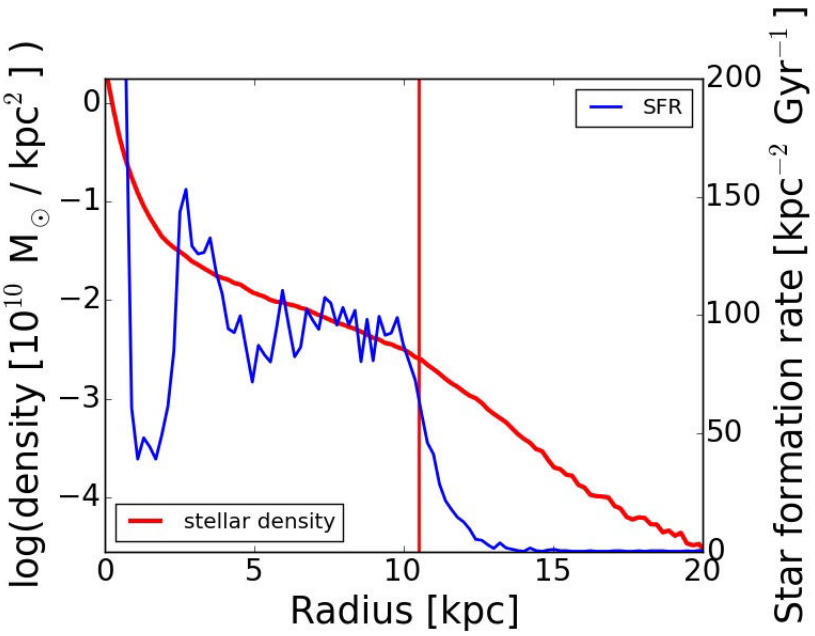

Figure 4.15.: Star formation rate (SFR) as a function of the radius, along with the radial density profile. The stellar break is indicated with a red vertical line, and seems to correspond to a brutal drop of the SFR.

4.4.1.3. Break and spiral morphology

As shown in Paper IV (section 4.4.3.1), the stellar break in our simulations seems to be systematically related to the spirals, being located at the outer edge of the spiral arms. Furthermore, we found that in some of our galaxies, the spiral arms show a strange behaviour at the break radius. I plotted in figure 4.16 a face-on view of one of our simulated galaxies to illustrate this phenomenon. The spiral arms are abruptly changing their pitch angle at the break radius, as if they could not extend beyond the break. The break thus seems to be breaking the spiral, but if it can be seen clearly in this example and a few other simulations, for most simulations this feature is not as obvious. This effect of the break on the spiral morphology is interesting, although we did not find a satisfactory explanation for this phenomenon yet.

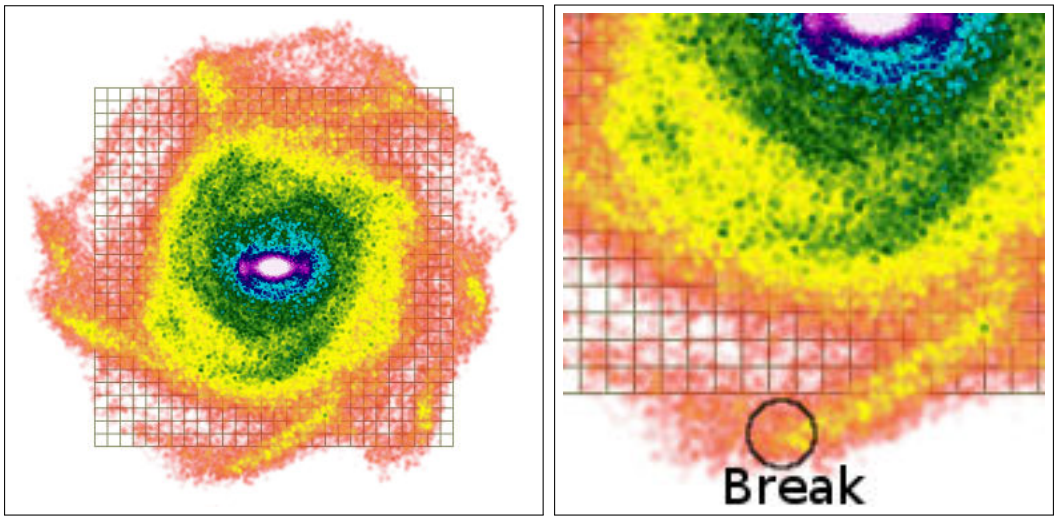

Figure 4.16.: Face-on view of $mdf732$ (zoomed in the right panel), which is a striking example of the effect of the break on the spirals. At the break radius, the spirals seem to change abruptly their pitch angle.

4.4.2. Paper III: Linking the profile with angular momentum

I analyzed and fitted the radial density profiles of many simulations, and found that if almost all of them are type II discs, the shape, extent and properties of these discs can be very different from one simulation to another. In particular, the values of the scalelengths fitted on the inner and outer disc are different, ranging from 3 to 10 kpc for the inner disc, and 1 to 3.5 kpc for the outer disc. The break is also located at different radii depending on the simulation, going from 5 to 25 kpc. The total masses in our simulations were mostly very similar, so that these differences could not be linked to the mass of the disc. I thus looked at another parameter of our simulations, the total angular momentum. The results of this analysis are presented in Peschken, Athanassoula & Rodionov (submitted, hereafter Paper III), which is given below.

4.4.2.1. Paper III

MNRAS **000**, 1–?? (2016) Preprint 2 November 2016 Compiled using MNRAS LATEX style file v3.0

Forming disc galaxies in major mergers : III. The effect of angular momentum on the radial density profiles of disc galaxies

N. Peschken[1]★, E. Athanassoula[1], S. A. Rodionov[1]
[1]*Laboratoire d'Astrophysique de Marseille, 38, rue Frédéric Joliot-Curie 13388 Marseille cedex 13 FRANCE*

2 November 2016

ABSTRACT
We study the effect of angular momentum on the surface density profiles of disc galaxies using high resolution simulations of galaxy pairs major mergers. The disc of the remnants shows a downbending radial density profile (type II). We find that both the inner and the outer disc scalelengths of the remnant disc, as well as the break radius, correlate with the total angular momentum of the initial merging system, those quantities being larger for high angular momentum systems. To understand this result, we study the angular momentum redistribution in our galaxies, and find that such correlations can be understood in the framework of disc galaxy formation from major mergers of progenitors with extended gaseous haloes. In such cases the initial angular momentum is transferred to the disc by accretion from the gaseous halo. Adding simulations of isolated galaxies to our sample, we find that our correlations are valid also for disc galaxies evolved in isolation. We show that the outer part of the disc at the end of the simulation is populated mainly by inside-out stellar migration, and that in galaxies with high angular momentum, stars travel radially further out. We point out that not taking into account the fact that the break radius changes with time can lead to a misinterpretation of the origin of the outer disc. Indeed, while some previous studies argued that outer disc stars (in type II discs) were mostly born in the inner disc, we show that this can be wrong if we take into account the time dependence of the break radius.

Key words: galaxies: spiral – galaxies: structure – galaxies: kinematics and dynamics

1 INTRODUCTION

The surface density profile of disc galaxies was first thought to be well fitted by an exponential (Freeman 1970). Later work (Van der Kruit 1979, and later e.g. Pohlen et al. 2002, Erwin, Beckman & Pohlen 2005, Gutiérrez et al. 2011) revealed the presence of a break in the profile of most galactic discs, as well as the fact that both the inner and the outer parts are well described by exponentials.
The break can be of two kinds, depending on the scalelengths of the two exponentials. If the slope of the outer part of the disc, hereafter called outer disc, is steeper than the slope of the inner part (inner disc), the profile is called downbending, or type II (Pohlen & Trujillo 2006). This is the most common profile for disc galaxies (e.g. Pohlen & Trujillo 2006, Azzollini, Trujillo & Beckman 2008, Laine et al. 2014), and corresponds to the case where the inner disc scalelength (hereafter inner scalelength) is greater than the outer disc scalelength (outer scalelength). In the opposite case, the outer disc is shallower than the inner disc, and the profile is called upbending, or type III. The single exponential case, where no break is observed, is called type I.
The mechanisms producing those different types of discs are diverse. While it has been argued that a single exponential is the canonical profile for a disc (Gunn 1982, Lin & Pringle 1987, Yoshii & Sommer-Larsen 1989, Ferguson & Clarke 2001, Elmegreen & Struck 2013), many formation scenarii have been proposed for the downbending discs, sometimes related to each other. They are thought to be created by bars via the Outer Lindblad Resonance (Debattista et al. 2006, Pohlen & Trujillo 2006, Muñoz-Mateos et al. 2013, Kim et al. 2014), by star formation thresholds (Schaye 2004, Pohlen & Trujillo 2006, Elmegreen & Hunter 2006), or connected with morphological components such as rings or spirals (Laine et al. 2014). The stellar migration is also found to be important in the creation of type II profiles, being able to redistribute stars from the inner disc to the outer disc, and can be coupled with a star formation threshold (Roškar et al. 2008). On the other hand, type III profiles (upbending discs) remain poorly understood. They are sometimes associated with a spheroidal component such as a stellar halo, or with the superposition of a thin and a thick disc, could be the result of minor mergers, or be linked to a strong bar (Erwin, Beckman & Pohlen 2005, Younger et al. 2007, Bakos & Trujillo 2012, Comerón et al. 2012, Herpich et al. 2015b).
Although the majority of the present-day spirals is thought to have experienced at least one major merger in their history (e.g. Hammer et al. 2009), so far most of the simulated galaxies used to investigate the formation of these different disc types have been evolved in isolation. Recent simulations, however (Athanassoula et al. 2016,

★ Contact e-mail: nicolas.peschken@lam.fr

hereafter A16), showed that it is possible to form spiral galaxies from major mergers. In A16, we presented three fiducial examples from a large sample of high resolution simulations of a major merger between two disc galaxies with a hot gaseous halo each, and showed that the remnants are good models of spiral galaxies, with type II discs. In this paper, we aim to study the role of angular momentum on shaping those type II profiles, using our large sample of major merger simulations.

The outline is as follows. In section 2, we briefly summarise the necessary parts of A16, and describe the fitting procedure for the radial density profiles. We compute the initial angular momentum and link it to the scalelengths in section 3. In section 4, we follow the angular momentum redistribution to explain how the initial angular momentum can affect the final disc properties. We discuss our results in section 5, and conclude in section 6.

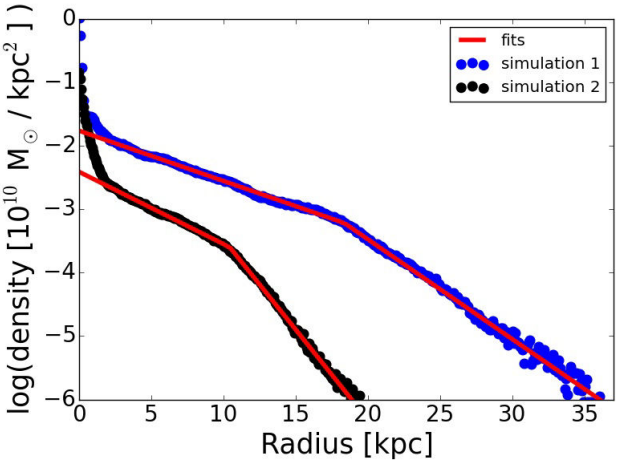

Figure 1. Projected surface stellar density radial profiles for two simulations together with the corresponding fits for the disc part. For clarity, the second simulation (in black) has been shifted down by 1 logarithmic unit. Simulation 1 has a higher initial spin parameter than simulation 2.

2 TECHNICAL ASPECTS

2.1 Description of the simulations

In this section we will briefly summarise the simulation characteristics, which have been obtained and described in some detail in A16. Our simulations start from two spherical protogalaxies consisting only of dark matter (DM) and hot gas, on a given orbit. We have a total of 5.5 million particles (2 million for the baryons, 3.5 million for the DM), with softenings of 25 pc for the gas and 50 pc for the DM. Each particle's mass is $5*10^4$ $M_\odot$ for the gas and stars, and $2*10^5$ $M_\odot$ for the dark matter. By the time of the merging, a disc has formed in each of the progenitors, which is completely destroyed by the merging, its stars ending up mainly in a classical bulge. Gas continues to fall from the halo and a new disc is gradually formed in the remnant. Well-defined spiral arms soon develop in this disc, as well as a bar and a boxy/peanut bulge. Each simulation ends after 10 Gyr evolution, showing a remnant with a classical bulge-to-total ratio which is consistent with that of real spiral galaxies.

Our simulations are made using the N-body/SPH code GADGET3, including gas and its physics. The description of this code can be found in Springel & Hernquist (2002) and Springel (2005). Stars and dark matter are modeled by N-body particles, and gas by SPH particles, with fully adaptive smoothing lengths. Each SPH particle represents a region of the ISM containing both cold and hot gas in pressure equilibrium. Gravity is computed with a hierarchy tree algorithm, and the code uses subgrid physics for the feedback, star formation and cooling, described in Springel & Hernquist (2003).

For a description of the technical aspects of the simulations we refer the reader to Rodionov, Athanassoula & Peschken (submitted).

To avoid an excessive central concentration in our simulated galaxies, which leads to unrealistic circular velocity curves and delays the formation of the bar (Rodionov et al., submitted), we added AGN feedback. The physics underlying this feedback is described in detail in A16, and is based on a density threshold ρ_{AGN} and a temperature T_{AGN}. Every gas particle whose local density is larger than ρ_{AGN} receives internal energy, and changes its temperature to T_{AGN}.

The simulations used in this paper have different orbits for the two merging protogalaxies. These orbits are characterized by their ellipticity, and the initial distance between the two progenitors. Each orbit leads to a different merging time, which is difficult to define precisely but can be approximated by deriving the time beyond which the distance between the two centers of density stays below 1 kpc (see A16). The simulations used in this paper have rather early merging times, between 1.7 and 2.2 Gyr after the start of the simulation.

The two protogalactic haloes start with an initial spin, which, in the simulations discussed here, is the same for both. This spin is characterized by a spin value f, representing the fraction of particles rotating with a positive sense of rotation. $f = 1$ thus corresponds to all the particles rotating in the same sense, while $f = 0.5$ is the case whith no net rotation. Most of the simulations have spin axes perpendicular to the orbital plane, but for 32 simulations we tilt one protogalaxy with a chosen angle, to see the effect of the spin axis orientation.

A central AGN is present in the remnant galaxy of the majority of our simulations, as described in A16, but we include 18 simulations without AGN to cover a larger part of the available parameter space. Nevertheless, the presence of our AGN affects mainly the central part of the disc (Rodionov et al., submitted), and should not have an impact on the analysis presented in this paper.

We also added 6 simulations where one protogalaxy is more massive than the other by a factor 3. These simulations have a total of 3.67 million particles (1.33 millions for the baryons, 2.33 millions for the DM).

In total, we have a sample of 100 simulations.

2.2 Fitting the radial density profiles

To derive the stellar radial density profile of the remnants at the end of the simulations, we use axisymmetric concentric annuli, and choose z_{lim}=1 kpc as maximum height when we wish to keep only the thin disc profile. As shown in A16, the disc at the end of our three fiducial simulations is composed of an inner and a downbending outer disc (type II), separated by a break. This is also the case for the 100 simulations of the sample used in this paper, therefore we fit the disc part of our profiles with two exponential functions. We use a "piecewise" fit, which means that we fit the inner and the outer disc separately with an exponential :

$$\Sigma_{in}(r) = \Sigma_i \ \exp(\frac{-r}{h_i}), \qquad r < r_{break} \tag{1}$$

$$\Sigma_{out}(r) = \Sigma_o \ \exp(\frac{-r}{h_o}), \qquad r > r_{break} \tag{2}$$

where Σ_i, Σ_o are normalization factors, h_i and h_o the inner and outer disc scalelengths, and r_{break} the break radius. The latter is derived by taking the intersection between the inner and the outer disc fits. The interval to fit for each part of the disc is selected manually, and we exclude, after visual inspection, every simulation for which the fit is not reliable. Two examples of the fits are shown in Fig. 1. Another way to make this fit would be to use a double exponential function (or "broken-exponential") for the whole disc, which has been shown to give very similar results (differences in the scalelengths < 5%, Erwin et al. 2008). We chose the present approach because of its simplicity.

The scalelengths change with time in the simulations, and to be able to compare consistently the scalelengths derived for the different simulations, we need the evolution time of the disc formed after the merging to be the same for each galaxy. We thus take a fixed evolution time of 7.8 Gyr after the merging for every simulation. Given that the merging times have values between 1.7 and 2.2 Gyr, the times at which we now study the disc are therefore between 9.5 and 10 Gyr, depending on the simulation. We will hereafter refer to this time as the final state.

We here aim to investigate the role of angular momentum on the formation of the new disc formed after the merging, in the secular evolution period of the galaxy. Nevertheless, some of the stars formed before or during the merging were spread all over the galaxy by the merging, and can pollute our density profiles. These stars represent between 10 and 30% of the total stellar mass in the thin disc. Most of them are located in the bulge region (about 65%), but they can also form a stellar halo or a thick disc, which will add particles in the outer disc, changing the value of the outer scalelength by up to 20%. These stars are not related to the new disc formation and its dependance on the angular momentum, and we thus choose to remove them, selecting only the stars formed after the merging to derive our density profiles and the corresponding scalelengths.

3 THE ROLE OF ANGULAR MOMENTUM

3.1 Definition of the global, dimensionless spin parameter

Our goal is to investigate the effect of the global angular momentum on the disc structure in our simulations. To have a definition of the angular momentum which is valid for every simulation, we use the dimensionless spin parameter λ (Peebles 1969) :

$$\lambda = \frac{J|E|^{1/2}}{GM^{5/2}}, \tag{3}$$

where J, E and M are respectively the total angular momentum, energy and mass of the system including its dark matter, gas and stars, computed with respect to the center of density of the system, and G is the gravitational constant. The total energy is computed adding the kinetic energy, the gravitational potential energy and the gas internal energy. The center of density is derived using the *nemo* package (Teuben 1995); we also used the center of mass with very similar results. The total angular momentum J is a conserved quantity, so that its value is constant in time. However, the total energy varies with time because of processes such as the cooling of the gas and the stellar feedback. Therefore, λ is not conserved and the time chosen to compute it matters.

We aim to explore the effect of the initial angular momentum on the disc migration in the remnant for all the simulations, so that the time used to compute λ has to be consistent for every simulation. We cannot take t=0 as initial state to derive the angular momentum since the merging time is different depending on the orbit (see section 2.1), so that t=0 does not represent the same state in the merging process for every simulation. Indeed, we are only interested in the disc formed after the merging, and the time to be defined as *initial* has to be consistent with respect to the new disc formation in the remnant for every simulation. The simplest solution would be to take some reproducible definition of the merging time, but the merging is a very violent phase during which the total energy can vary quickly and the center of density is not defined precisely, so that λ can be derived less reliably. We thus chose to take 1 Gyr before the merging as the initial state, because the total energy and the center of density are more stable then.

3.2 Angular momentum and scalelengths

How is the disc affected by the global spin parameter λ computed above? From the definition of angular momentum we expect that for two galaxies of the same total mass, the galaxy with the highest angular momentum is more extended, and this has been shown in previous studies (e.g. Dalcanton, Spergel & Summers 1997 and Kim & Lee 2013). We thus expect the disc to be globally larger for high spin parameter galaxies. However, since the disc is constituted of an inner and an outer part, which part of the disc is affected? We expect at least one of the two discs (inner or outer) to be larger at higher spin parameter. To investigate this, we study the dependance of the scalelengths of both discs with λ.

We look at the disc of the remnant at the final state (as defined in section 2.2) to see how its scalelengths are affected by the initial angular momentum. We plot the three parameters derived from the fits of the radial density profiles (inner, outer scalelength and break radius) as a function of the initial spin parameter for each simulation (Fig. 2). As described in section 2.2, we excluded all the simulations for which there was some uncertainty in the fit of the corresponding parameter, which explains why the number of points is different for each plot. We thus have a total of 75 values for the inner scalelength, 80 for the outer scalelength and 64 for the break radius (for which the fits of both the inner and the outer disc have to be reliable).

We see that the inner scalelength, the outer scalelength and the break radius *all* increase linearly with λ, so that large angular momentum systems produce discs with higher inner, outer scalelengths and break radii. This confirms the results of Herpich et al. (2015a) for the inner scalelength and the break radius (see discussion in section 5.1), and adds a further argument that the remnant of a major merger possesses all the characteristics of a disc galaxy.

We show an illustration of the resulting radial density profiles in Fig. 1, where one of the simulations (in blue) has a higher initial λ than the other (in black). We can see that the scalelengths of the former are indeed larger than the latter, and its break is located further out.

The correlation coefficients of the fits in Fig. 2 are good, especially for the break radius. The scalelengths show a larger spread,

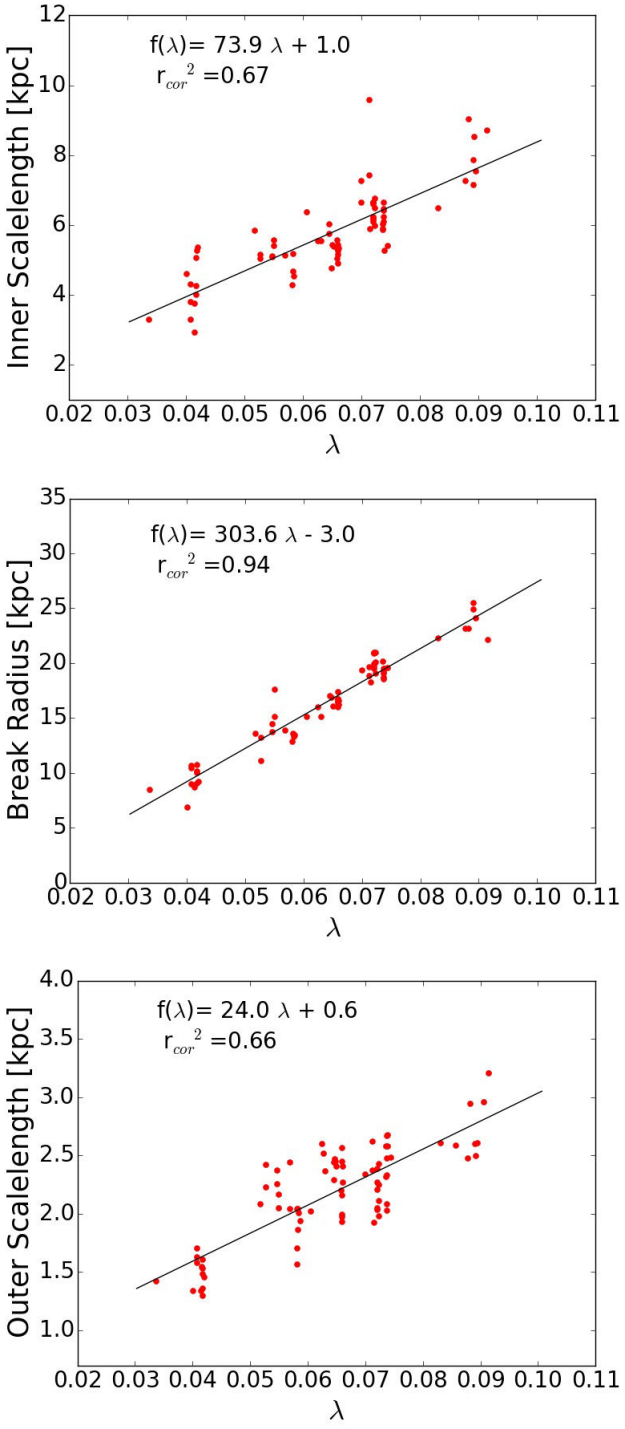

Figure 2. From top to bottom we plot respectively the inner scalelengths, the break radii and the outer scalelengths derived from the fits at the final state, each as a function of the spin parameter taken at the initial state. The corresponding linear fits are plotted in black, with the equation and correlation coefficient given in the top left corner of each plot.

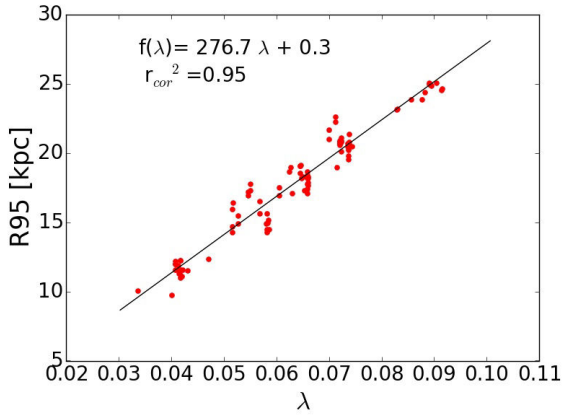

Figure 3. Radius containing 95% of the stellar mass as a function of the spin parameter of the simulations.

probably because their values can vary easily in the presence of morphological components such as bars, spirals or rings.

We further plot the size of the galaxies at the final time as a function of λ. As an estimate of the galaxy's size, we take R95, the cylindrical radius containing 95% of the total stellar mass. We can see on Fig. 3 that the size of the final galaxy also increases linearly with the spin parameter, with a very good correlation coefficient. This is consistent with the results, in the case of isolated simulations, of Dalcanton, Spergel & Summers (1997) and Kim & Lee (2013), where the disc is larger for higher λ.

4 ANGULAR MOMENTUM EXCHANGES

The spin parameter is computed 1 Gyr before the merging, and is dominated by the halo (hot gas and DM), the discs of the proto-galaxies then being small and of low mass since the merging is early in our sample of simulations. Therefore, λ does not seem to be directly linked to the remnant final disc and to its properties such as the scalelengths.
In this section we will try to understand how the halo can influence the disc, by looking at angular momentum transfers in our simulations.

4.1 Baryonic and dark matter

To illustrate the angular momentum exchanges in our simulations, we will focus on one fiducial simulation, *mdf*732, presented in A16. Note, however, that we made the same analysis with other simulations, and found similar results.

We first look at the exchanges between the baryonic and the dark matter. The number (and mass) of both dark matter and baryonic (gas + stars) particles is conserved since the system is isolated, and since the star formation transforms a gas particle into a stellar particle of same mass. Therefore, the total angular momentum should be conserved, and it is possible to look for angular momentum exchanges between dark and baryonic matter just by looking at their angular momentum in time. We plot for *mdf*732 the total angular momentum L as a function of time for both groups in Fig. 4, starting from the time at which the disc starts forming (2.2 Gyr, see

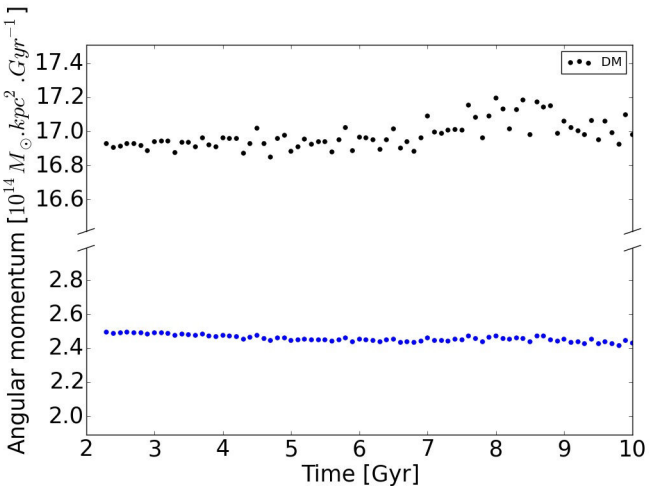

Figure 4. Total angular momentum of the baryonic (gas + stars) and dark matter as a function of time.

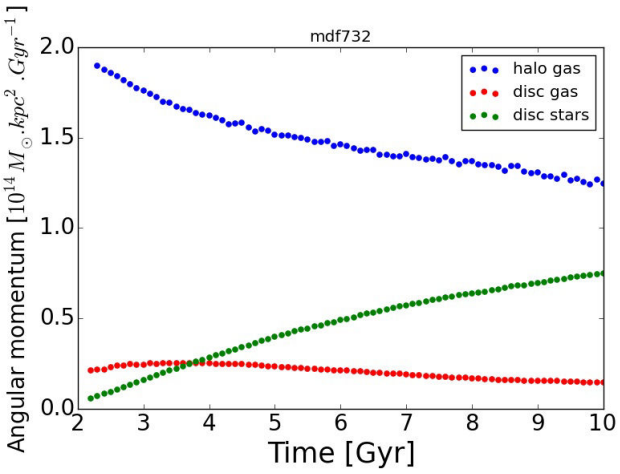

Figure 5. Total angular momentum of the gaseous halo, the gaseous disc and the stellar disc as a function of time.

A16). The angular momentum is nearly constant over time for both the dark and the baryonic matter, with small variations of less than $5 * 10^{65}\ kg.m^2.s^{-1}$ for the baryonic matter (3.3%) and $2.2 * 10^{66}\ kg.m^2.s^{-1}$ for the dark matter (2%). The variations over time of the total angular momentum (including all components) are around $2.4 * 10^{66}\ kg.m^2.s^{-1}$ (2%), therefore the variations of the dark and baryonic matter are within the errorbars of the simulation. We thus conclude that the exchanges of angular momentum are negligible between those two components, and that the baryonic angular momentum can be considered as conserved over time.
This angular momentum conservation only works because our system is isolated. Nevertheless, this is often not the case in real galaxies, where interactions are expected to happen with their environment. These interactions can be of gravitationnal nature, or represent matter exchanges between the galaxy and its neighbors. In either case, the total angular momentum in the galaxy will not be conserved, and the angular momentum exchanges studied in the following section do not apply.

4.2 Baryonic halo and disc

Having shown that the baryonic angular momentum is conserved, we can now look at the exchanges between the baryonic halo and the disc, without having to worry about the dark matter. We define the disc as a 40 kpc radius pill-box, of 2 kpc thickness ($|z| < 1$ kpc), and the halo as everything else. The baryonic halo is mainly constituted of gas, but a few stars are expected to be found as well. Nevertheless, we find the total angular momentum L of these stars to be a thousand times lower than the halo gas, and we thus choose to neglect them.
We plot in Fig. 5 the angular momentum of the halo gas, as well as the angular momentum of the gas and the stars in the disc, as a function of time. We can see that the halo gas is loosing angular momentum to the disc. We further plot the mass of these three components as a function of time (Fig. 6), to see if it can account for the angular momentum changes. We see that the gaseous halo looses mass while the stellar disc gains it. This is due to the accretion of the halo gas on to the disc, where it forms stars (A16). The stellar disc is thus gaining angular momentum by gas accretion and star formation.
The disc grows from material taken from the gaseous halo, which directly gives angular momentum to the disc. Therefore, the initial properties of the halo – and in particular its angular momentum – affect the final disc structure, which constitutes a plausible explanation for the disc properties (scalelengths and break radius) being linked to the initial halo-dominated spin parameter.

Looking at the specific angular momentum L/M as a function of time in Fig. 7, we see that it increases for the three components. It is important to note that this is not in contradiction with the angular momentum conservation, since the specific angular momentum is not conserved (the number of particles changes in time for each component). This result is not suprising for the gas and stars in the disc since the gas particles accreted from the halo have a higher angular momentum, which also explains why the gas in the disc has a higher specific angular momentum than the stars. We explain the increase of the specific angular momentum in the halo by the fact that the particles accreted by the disc are the ones closest to the disc, which are also the particles with the lowest angular momentum in the halo. By removing the lowest angular momentum particles in the gaseous halo, the accretion thus increases the specific angular momentum of the halo. Note that this does not deplete the gas reservoir around the disc, since the particles accreted are replaced by particles coming from farther layers of halo gas.

5 DISCUSSION

5.1 Robustness of the correlations

It is important to note that all our simulations show similar total stellar masses at their final state, so that the spread of scalelengths cannot be simply due to a mass dependence. The total masses (gas, stars and DM) at the final time are also similar, and therefore do not account for the spread of λ. Thus the spread is due to the different parameters of the initial conditions in the various simulations, such as the halo spin value, and, in particular, to the different orbits of the two progenitors.

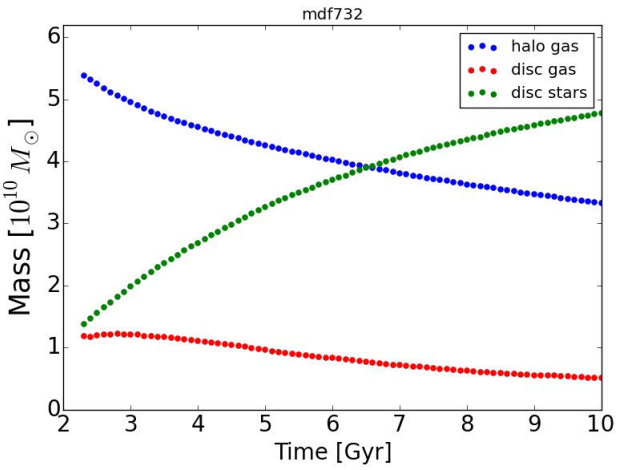

Figure 6. Total mass of the gaseous halo, the gaseous disc and the stellar disc as a function of time.

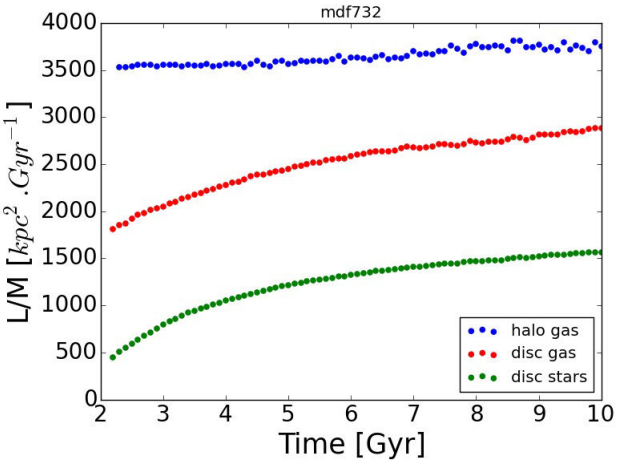

Figure 7. Specific angular momentum (angular momentum normalized by the mass) as a function of time, for the gaseous halo, the gaseous disc and the stellar disc.

To test the robustness of our results with respect to the time defined as final state, we changed this quantity, fitting the radial density profiles 5.8 Gyr after the merging, instead of 7.8 Gyr. The values of the correlation coefficients are reported in Table 1. As expected, the individual values of the scalelengths and the break radii are different, but we still find increasing linear trends with λ. Therefore, the time chosen as final state does not seem to be important for this study, as long as it is consistent for all simulations ; the increasing trend with λ is valid regardless of the disc evolution time. We can thus keep 7.8 Gyr after the merging as the final state without having to worry about its relevance.

We also changed the time at which we take the spin parameter (the initial state) and used the merging time. We found very little difference in the results, and the correlation coefficients are similar (Table 1), although somewhat lower, as expected since the center of density and the total energy are somewhat less reliable (section 3.1). We repeated this analysis with different times covering the range between the start of the simulation and the merging,

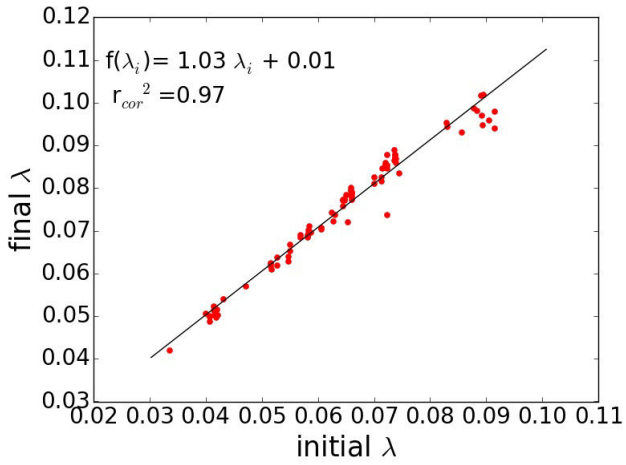

Figure 8. Correlation between the final and the initial values of the spin parameter.

and concluded that the time chosen does not change the results significantly. We can also use the spin parameter at the final state, thus not taking it as an initial parameter, but looking at the correlation between the angular momentum and the disc structure at a given time. We found again the same increasing trends, with the correlation coefficients reported in Table 1. This seems to point out the existence of a correlation between the initial and final λ, which we confirmed by plotting one against the other in Fig. 8, and argues that for an analysis of this type, one can take the value of angular momentum at any time, as long as it is consistent for all simulations.

This last conclusion allows us to plot again the disc parameters as a function of the final λ, but this time including two different final states (5.8 and 7.8 Gyr after the merging) in the same plot, allowing us to double our sample and check if the two subsamples match together. As shown in Fig. 9, the two samples fit very well with each other, and we find a correlation for each plot, albeit considerably less tight for the inner disc scalelength and somewhat less tight for the outer one and the break radius.

We also changed the definition of λ, taking the total energy at t=0 Gyr (instead of the initial state). This is equivalent to deriving λ at t=0 Gyr, since the total mass and angular momentum are constant in time. Using this definition, we loose the time consistency between the simulations, but we get a single value for λ based on t=0 Gyr. We find correlations for the scalelengths and the break radius, but the correlation coefficients are somewhat lower (Table 1).

We also tried to compute λ in a different way, to see if it changes the results : we took the angular momentum of the dark matter only, and of the baryonic matter only (gas+stars). Again, we find increasing trends for the three parameters, and put the correlation coefficients in Table 1.

To see if the results obtained for our merger simulations are also valid for isolated galaxies, we added to our sample 39 simulations which take only one of the protogalaxies used in the merger simulations described in section 2.1, and see how it evolves in isolation. To be able to compare the merger to the isolated simulations, we define the initial state as the start of the new disc formation for both, being at the end of the merging for the former, and at t=0 for the

latter. We take 7 Gyr after the initial state as the final state. We find that the isolated galaxies fit very well with the merger simulations (see Fig. 10), which means that the increasing linear trends of the two scalelengths and the break radius with the angular momentum seem to be the same if the disc is formed in isolation or from a major merger. Our results are therefore also valid for isolated galaxies.

Herpich et al. (2015a) did a similar analysis to ours, looking at the dependence of the scalelengths and the break radii with the angular momentum, but with a sample of 9 simulations of galaxies evolved in isolation. They computed the spin parameter λ of the dark matter halo at the start of the simulation, and found that the inner scalelength and the break radius increase with λ, in agreement with our results. However, they observed a decreasing trend of the outer scalelength with λ, while we have an increasing one. We explain this difference by the fact that they included upbending discs in their analysis, whose outer scalelengths are naturally much higher than for downbending discs, while we only have downbending discs in our sample. Upbending profiles will be discussed in detail in a future paper (Athanassoula, Peschken, Rodionov, in prep, hereafter Paper IV). As a consequence, Herpich et al. (2015a) also find an increasing trend with λ for the ratio of the inner scalelength to the outer scalelength, while we do not (see Fig. 11), our values showing no correlation with λ.

We mentioned in section 2.1 that in 32 of our 100 major merger simulations, the spin axis of one protogalaxy is tilted by a given angle with respect to the other. This angle can be around the X or the Y axis, Z being the axis perpendicular to the orbital plane. We wanted to see if these simulations behave differently in our results than the simulations where both protogalactic spin axes are parallel, and perpendicular to the orbital plane. In Fig. 12 we plotted again our correlations between the scalelengths and the spin parameter, but showing the angles between the two protogalactic spin axes. We can see that the simulations where the spin axes are not parallel (angle $\neq 0$) fit reasonably well with the others, although their inner scalelengths show some larger scatter. We can thus conclude that our results seem to be valid regardless of the spin axis orientation.
We also looked at the effect of the presence of a central AGN on our correlations, and found that the simulations without AGN also fit well with the ones having an AGN. This confirms that our AGN only affects the central part of the galaxy (Rodionov et al., in prep).
We also used 6 simulations where the two protogalaxies are not of the same mass (section 2.1), one being 3 times more massive than the other. These simulations also fit well with the others in the correlations, showing that our results also work in the case of non identical progenitor galaxies.

5.2 Migration and angular momentum

The formation of outer discs in downbending profile galaxies is still debated, but one of the main possible scenario includes the presence of outwards stellar migration to build the outer dic (Roškar et al. 2008). We thus look where the stars in the outer disc of our remnant galaxies come from, by calculating the radius at which they were born. The stellar discs of the two protogalaxies are separate before the collision and thus the birth radius with respect to the remnant galaxy cannot be defined. We therefore use in our analysis only the stars born after the merging, as in section 2.2.
We define the stars of the outer disc as all the stellar particles located beyond the break. We plot in Fig. 13 the distribution at their time of birth of the stars which by t=10 Gyr end up in the outer disc. Since every star is born at a different time, this distribution does not represent a real stellar distribution at any time of the simulation, but it helps visualizing the fraction of stars born at a given radius throughout the whole simulation. We can see that most stars of the outer disc (81 ± 11 %) were born at a radius less than the break radius at t=10 Gyr. This means that these stars have migrated radially outwards to form the outer disc, showing the presence of inside-out stellar migration in the disc. This is in agreement with the results of Roškar et al. (2008) presenting simulations with a downbending disc profile induced by a star formation threshold and outward migration, and with observations e.g. in Radburn-Smith et al. (2012) and Zheng et al. (2015), and thus adds a further argument to those presented in A16 that the remnant of a major merger is a disc galaxy and behaves in all aspects as such.

Having established that there is inside-out stellar migration in our discs, we explore the effect of angular momentum on this phenomenon. To characterize the migration, we look at the distances travelled by these migrating stars towards the outer disc, throughout the whole simulation. To derive the migration distances for a a given simulation, we first compute the radial distance travelled by each star ending up in the outer disc between its time of birth and the final state (as defined in section 2.2) :

$$D_{mig} = R_{final} - R_{birth}, \quad (4)$$

where R_{final} and R_{birth} are the radii at the final state and at birth for each star. We remove again the stars born before the merging since migration only starts after the collision, or, more precisely, after the disc forms stars (A16). Since we are only interested in the outward migration towards the outer disc, we also remove the stars migrating inwards, which represent only about 5% of the outer disc population. We then take the mean over all the stars to get a single value for each simulation, which allows us to plot it versus the spin parameter. We repeat this for all simulations and plot the result in Fig. 14. We see a clear increasing trend of the migration distances with λ, allowing us to conclude that higher initial angular momentum systems lead to discs with higher migration distances towards the outer disc. In fact, we find the same result if we consider inside-out migration in the whole disc, and not restrict ourselves to outer disc stars. The stars travel globally further out in high angular momentum systems, and this is particularly important in the outer disc, where 95% of the stars have undergone inside-out migration (compared to 45% for the whole disc).
The angular momentum thus seems to play an important role in the radial outward migration, by redistributing the stellar content in the outer disc efficiently (with large travelling distances) or not.
This result is consistent with outer disc in high λ simulations having larger scalelengths : if stars travel further out, their final distribution will be more extended, resulting in a larger outer disc.

5.3 Migration and birth radius

In section 5.2, we showed that most particles ending up in the outer disc were born inside the break radius, as calculated at t=10 Gyr. However, the stars whose birth distribution has been plotted in Fig. 13 were born throughout the whole simulation (after the merging). As will be shown in Paper IV, the break radius is not constant with time, so that stars which are born inside the 10 Gyr break in Fig. 13 could in fact be born beyond the break taken at their time of birth.

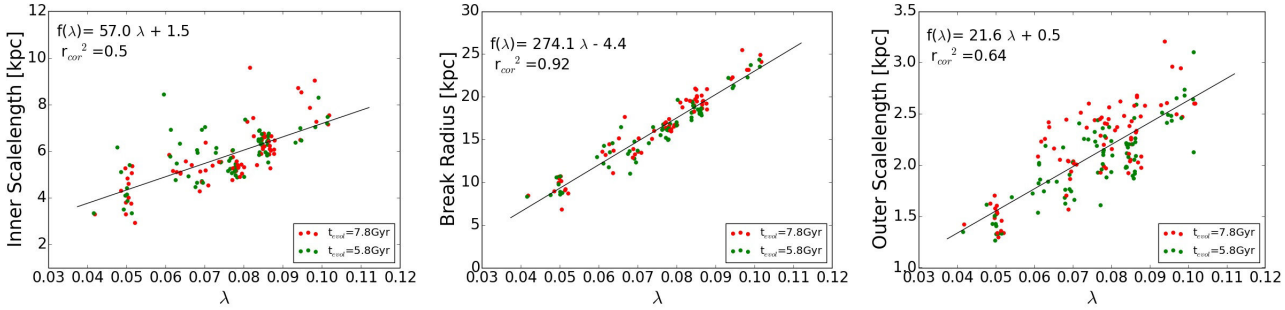

Figure 9. Same plots as in Fig. 2, by taking each simulations two times : with an evolution time of 5.8 Gyr, and 7.8Gyr. The spin parameter λ is here computed at the final state.

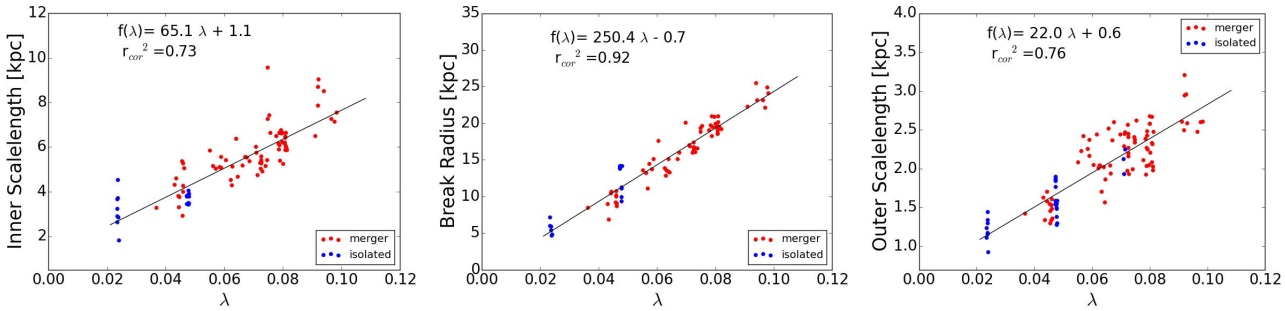

Figure 10. Same plots as in Fig. 2, but adding isolated simulations (in blue).

Table 1. Parameters of the linear fits for different plots of λ versus the inner scalelength, break radius and outer scalelength. t_i, t_f and t_{merg} are respectively the times of the initial state, the final state and the merging, and r_c^2 is the correlation coefficient for the linear fit with equation : $f(\lambda) = a\lambda + b$.

	Inner Scalelength			Break Radius			Outer Scalelength		
	r_c^2	a	b	r_c^2	a	b	r_c^2	a	b
$\lambda_{t=t_i}$	0.67	73.9	1.0	0.94	303.6	-3.0	0.66	24.0	0.6
$\lambda_{t=t_{merg}}$	0.60	67.1	1.2	0.93	286.1	-3.0	0.61	22.0	0.7
$\lambda_{t=t_f}$	0.60	66.6	0.7	0.93	285.2	-5.0	0.63	22.3	0.5
$\lambda_{halo,t=t_i}$	0.67	59.6	0.9	0.93	244.1	-3.2	0.67	19.5	0.6
$\lambda_{bary,t=t_i}$	0.75	5.2	0.6	0.88	19.5	-2.7	0.59	1.5	0.7
$\lambda_{t=t_i}$, $t_f = t_{merg} + 5.8$	0.43	51.7	2.5	0.94	285.4	-2.5	0.72	22.5	0.6
$\lambda_{t=t_f}$, $t_f = t_{merg} + 5.8$	0.40	47.0	2.2	0.92	263.7	-4.1	0.67	21.0	0.4
$\lambda_{t=t_f}$, $t_f = t_{merg} + 7.8$ & $t_f = t_{merg} + 5.8$	0.50	57.0	1.5	0.92	274.1	-4.4	0.64	21.6	0.5

Therefore, we cannot claim that 81 ± 11% of the outer disc's stars that were born at a radius which corresponds to the inner disc at 10 Gyr were actually born in the inner disc, since their birth radius could be in the outer disc at their birth time. Although this does not change the fact that most of these stars clearly migrated outwards, it could question the claim that they travelled from the inner disc to the outer disc.

To solve this, we took the same stars (the ones in the outer disc at 10 Gyr), and computed the fraction which was born in the inner disc defined with respect to the break at their time of birth. However, the derived fraction of stars born in the inner disc depends strongly on the value taken for the break radius, since the break is often located on spirals, which are high star formation areas (A16 for simulations and e.g. Silva-Villa & Larsen 2012 for observations). Besides, the break radius can be difficult to measure precisely at early times (a few Gyr after the merging). We thus defined errorbars for the estimated break position at each time step, and excluded all the particles born closer to the break radius than these errorbars. To

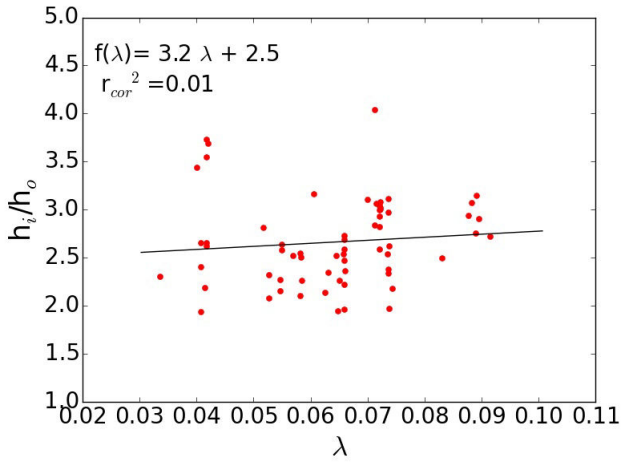

Figure 11. Ratio of the inner to the outer scalelength as a function of the spin parameter λ.

make sure our 10 Gyr outer disc definition is also reliable, we also defined the particles of the outer disc as the ones located beyond the external errorbar of the break radius.

To exclude the effect of radial displacements due to epicyclic radial oscillations of stars in their orbit, we chose to use R_G, the guiding radius of each star, instead of their regular radius to derive their position with respect to the break. R_G is the radius of the circular orbit associated to the angular momentum of a given star, and can be derived by solving the equation :

$$R_G = \frac{L_z}{v_{circ}(R_g)}, \quad (5)$$

where L_z is the vertical component of the angular momentum of the star, and v_{circ} is the circular velocity at the guiding radius.

The fractions of outer disc stars that are born in the inner disc derived with this method cover a wide range of values depending on the simulations, from 10% to 80%. Nevertheless, we find globally lower fractions than the ones from section 5.2, which can be explained by the fact that the break radius tends to increase with time (see paper IV), so that some stars were born inside the 10 Gyr break but outside their birth time break, and are now considered as outer disc stars.

To understand the spread of values derived for the fraction of stars born in the inner disc, we tried to plot these fractions again versus λ (taken for all the components, 1 Gyr before the merging) in Fig. 15. Although having a large scatter (probably because of the sensitivity of the values to the break location and its errorbars, and the difficulty to define them precisely at early times), this plot shows again an increasing trend of the fractions with λ. Therefore, galaxies with high angular momentum will have an outer disc which is populated by a majority of stars coming from the inner disc, whereas in low angular momentum galaxies, stars in the outer disc will mostly be born in the outer disc. This is consistent with the results of the migration distances found in section 5.2, since stars in high angular momentum galaxies travel further, and can more easily leave the inner disc for the outer disc. It is important to note that the trend found in Fig. 15 does not imply that low angular momentum galaxies form more stars in their outer parts, since the number of stars in the outer disc is different in every simulation.

We thus have simulations which have outer discs formed mostly by radial migration, but with a significant amount of stars in the outer parts which were born in the outer disc. We conclude that not taking into account the fact that the break radius changes with time, can lead to overestimating the fraction of stars born in the inner disc in the context of radial migration. Therefore, the picture of outer disc stars mostly coming from the inner disc (~ 85%, Roškar et al. 2008) has to be used with caution, since it depends on the efficiency of radial migration. Only very efficient radial migration, in galaxies with high angular momentum (λ>0.08 in our simulations), seem to be able to have more than 80% of their outer disc stars born in the inner disc. In rather low angular momentum galaxies (λ<0.06 in our simulations) this fraction drops below 50%, disclaiming the inner disc as the main origin of the outer disc stars.

6 SUMMARY AND CONCLUSION

In this work, we used a sample of 100 high resolution major merger simulations as these described in A16, where after the merging a new disc forms in the remnant from gas accreting from the halo. We derived the radial density profiles of these remnants at the end of the simulations, found only downbending (type II) profiles, and explored the effect of the total angular momentum on this profile. To do this, we derived the inner and outer disc scalelengths, as well as the break radius, by fitting the radial density profile near the end of the simulation. We used the spin parameter λ computed 1 Gyr before the merging to have a definition of the angular momentum consistent for all our simulations. Plotting for our sample of 100 galaxies the values derived from the radial density profiles fits as a function of λ, we found that the inner, the outer scalelength and the break radius increase with the spin parameter. Therefore, both the inner and the outer discs are larger for higher angular momentum systems.

To explain how the initial angular momentum of the merging system, being dominated by the halo, can affect the properties of the final remnant disc (mostly composed of stars born after the merging), we looked at the angular momentum redistribution in our simulations. The angular momentum of the total baryonic matter is conserved, the system being isolated and the exchanges between dark and baryonic matter negligible, which allows us to focus on the baryonic angular momentum redistribution. In the framework of disc galaxy formation from a major merger of two progenitors with extended gas-rich haloes, it is easy to understand that the gaseous halo gives angular momentum to the disc by accreting its gas onto it. To investigate this, we focused on one fiducial simulation presented in A16, and found that the total angular momentum of the stellar disc increases in time while the angular momentum in the gaseous halo decreases due to mass loss. Naturally this scenario is only valid for an isolated system whith no interactions between the galaxy and the environment. Therefore, we cannot state that our results would apply to galaxies in a cosmological context, since interactions could interfere with the angular momentum exchanges between the gas and the disc.

The correlations of the scalelengths and the break radius with the spin parameter are robust and do not change with the time at which we fit the radial density profiles, the time used to compute the spin parameter, or the components (dark and/or baryonic matter) used to compute the spin parameter. Furthermore, simulations of isolated galaxies follow the same trends, so that our results are

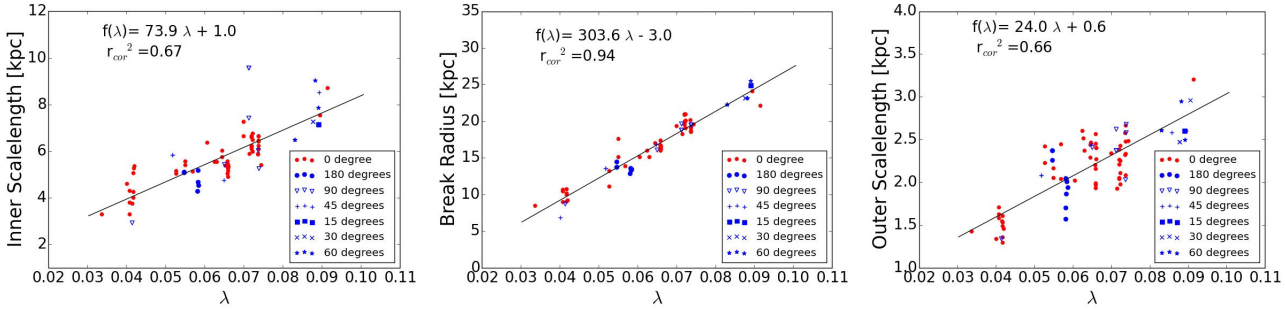

Figure 12. Same plots as in Fig. 2, but showing the effect of spin orientation on our correlations.

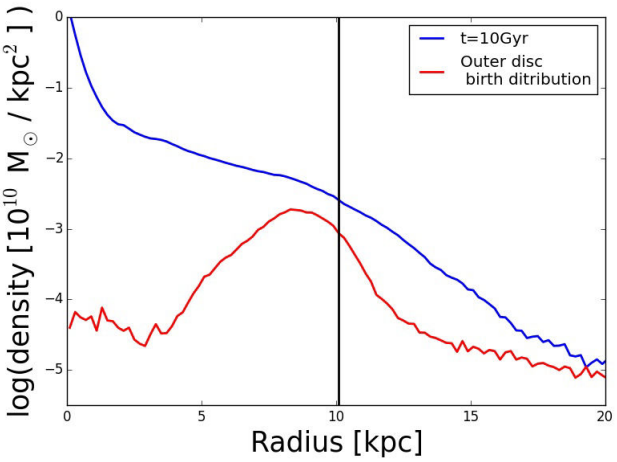

Figure 13. Radial density profile for a snapshot at t=10 Gyr (in blue), and distribution at time of birth of the stars ending up in the outer disc (in red). The break radius at t=10 Gyr is indicated with a black vertical line.

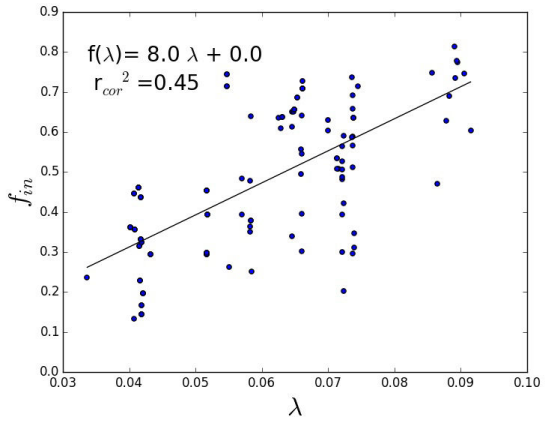

Figure 15. Fraction of outer disc stars which were born in the inner disc, as a function of the spin parameter. For each star, the inner disc is defined here with respect to the break radius derived at its time of birth, as explained in section 5.3.

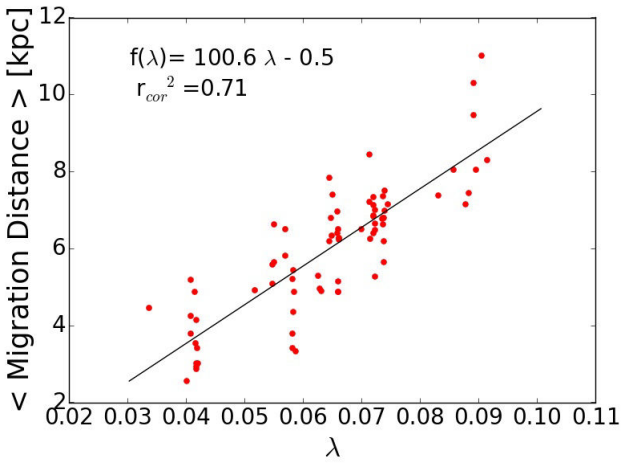

Figure 14. Mean inside-out migration distance of the stars ending up in the outer disc, as a function of the initial spin parameter.

valid for discs formed both in isolation and in major mergers. In some simulations one protogalaxy spin axis is tilted by a chosen angle with respect to the other, and we showed that the spin axis orientations of the two merging protogalaxies do not seem to play a role in this analysis.

We analyzed the outer disc origin, and found that the stars ending up in the outer disc were mostly born at smaller radii (~95%), suggesting inside-out migration as the main formation driver for the outer disc. To see the effect of the angular momentum on this migration, we computed the distance radially travelled by the stars towards the outer disc, and plotted it against the spin parameter for the simulations of our sample. We found a correlation, galaxies with higher angular momentum having larger inside-out migration distances.

Furthermore, we showed that to study the origin of the outer disc, we have to take into account the fact that the break location changes with time, so as to avoid overestimations of the fraction of stars born in the inner disc. While ~80% of the outer disc stars were born inside the break at t=10 Gyr, this fraction can take low values under 50% using the time dependent break, which could set doubt to the picture of the outer disc mainly formed from the inner disc. This fraction depends on the angular momentum, and is higher in high angular momentum galaxies, which is consistent with the larger stellar migration distances found in such high

angular momentum systems.

Therefore, the angular momentum seems to be a key parameter in the creation of disc structures, as it affects radial migration, and can explain the large range of values observed for the inner and outer scalelengths in disc galaxies for a given mass.

AKNOWLEDGEMENTS

We thank Jean-Charles Lambert for computer assistance. This work was granted access to the HPC resources of [TGCC/CINES/IDRIS] under the allocations 2014-[x2014047098], 2015-[numero] and 2016-[numero], made by GENCI, as well as the HPC resources of Aix-Marseille Université financed by the project Equip@Meso (ANR-10-EQPX-29-01) of the program « Investissements d'Avenir » supervised by the Agence Nationale de la Recherche.

REFERENCES

Athanassoula, E., Rodionov, S., Peschken, N., Lambert, J.C. 2016, ApJ, 821, 90
Azzollini, R., Trujillo, I., Beckman, J. E. 2008, ApJ, 684, 1026
Bakos, J., Trujillo, I. 2012, preprint (arXiv:1204.3082)
Comerón, S., Elmegreen, B. G., Salo, H., et al. 2012, ApJ, 759, 98
Dalcanton, J. J., Spergel, D.N., Summers, F. J. 1997, ApJ, 482, 659
Debattista, V. P., Mayer, L., Carollo, C. M., et al. 2006, ApJ, 645, 209
Elmegreen, B. G., Hunter, D. A. 2006, ApJ, 636, 712
Elmegreen, B. G., Struck, C. 2013 ApJ, 775, L35
Erwin, P., Beckman, J. E., Pohlen, M. 2005, ApJ, 626, L81
Erwin, P., Pohlen, M., Beckman, J. E. 2008, AJ, 135, 20
Fathi, K., Gatchell, M., Hatziminaoglou, E., Epinat, B. 2012, MNRAS, 423, L112
Ferguson, A. M. N., Clarke, C. J. 2001, MNRAS, 325, 781
Freeman, K. C. 1970, ApJ, 160, 811
Gunn, J. E. 1982, in Astrophysical Cosomology Proceedings, 233
Gutiérrez L., Erwin, P., Aladro, R., Beckman, J. E. 2011, ApJ, 142, 145
Hammer, F., Flores, H., Puech, M., et al. 2009, 507, 1313
Herpich, J., Stinson, G. S., Dutton, A.A., et al. 2015a, MNRAS, 448, 99
Herpich, J., Stinson, G. S., Rix, H. W., et al. 2015b, preprint (arXiv:1511.04442)
Kim, J., Lee, J. 2013, MNRAS, 432, 1701
Kim, T., Gadotti, D., Sheth, K., et al. 2014, ApJ, 782, 64
Laine, J., Laurikainen, E., Salo, H., et al. 2014, MNRAS, 441, 1992
Lin, D. N. C., Pringle, J. E. 1987, ApJL, 320, L87
Muñoz-Mateos, J.C., Boissier, S., Gil de Paz, A., et al. 2011, ApJ, 731, 10
Muñoz-Mateos, J.C., Sheth, K., Gil de Paz, A., et al. 2013, ApJ, 771, 59
Peebles, P.J.E. 1969, ApJ, 155, 393
Pohlen, M., Dettmar, R. J., Lütticke, R., Aronica, G. 2002 A&A, 392, 807
Pohlen, M., Trujillo, I. 2006, A&A, 454, 759
Radburn-Smith, D. J., Roškar, R., Debattista, V. P., et al. 2012, 753, 138
Roškar, R., Debattista, V. P., Stinson, G. S., et al. 2008, ApJ, 675, L65
Schaye, J. 2004, ApJ, 609, 667
Sheth, K., Regan, M., Hinz, J. L., et al. 2010, PASP, 122, 1397
Silva-Villa, E., Larsen, S. S. 2012, A&A, 537, A145
Springel, V. 2005, MNRAS, 364, 1105
Springel, V., Hernquist, L. 2002, MNRAS, 333, 649
Springel, V., Hernquist, L. 2003, MNRAS, 339, 289
Tueben, P. 1995, in ASP Conf. Ser., Vol. 77, Astronomical Data Analysis Software and Systems IV, Shaw R. A., Payne H. E., Hayes J. J. E., eds., p. 398
van der Kruit, P.C. 1979, A&AS, 38, 15
Yoshii, Y., Sommer-Larsen, J. 1989, MNRAS, 236, 779
Younger, J.D., Cox, T.J., Seth, A.C., Hernquist, L. 2007, ApJ, 670, 269
Zheng, Z., Thilker, D. A., Heckman, T. M. et al. 2015, APJ, 800, 120

4.4.2.2. Further analysis on the effect of angular momentum

In this section I present additional results about the angular momentum and the density profile of our remnant galaxies.
First, I did not describe in detail how I derived the spin parameter λ in Paper III, but the computation of λ can be found in Appendix E, both for all the components and for only one component (dark or baryonic matter).
Looking at the value of λ for different simulations, I found that the main contributor to the initial angular momentum (and therefore λ) in our merger simulations is the orbital angular momentum. We used several types of orbits (see section 2.1.3) for the two protogalaxies, and I show their effect on λ in figure 4.18 (top panel). The next important parameter is the spin f, which determines the position on the plot of a simulation inside an orbit group (figure 4.18, bottom panel). The angle also plays an important role, two simulations having the same orbit and f but a different angle will not have the same value of λ. In particular, the more inclined a protogalaxy is with respect to the other (until 180 degrees), the lower its spin parameter will be. This is easily understandable, since two parallel protogalaxies will have a very high angular momentum z-component (axis perpendicular to the orbital plane), while two protogalaxies at 180 degrees will cancel each other's spins in the computation of the angular momentum. And indeed, I found that a simulation with a 180 degrees angle will have a lower λ than a simulation having the same orbit but no angle, whatever the value of f. Other parameters, such as the AGN properties, might affect (slightly) the disc properties, but do not contribute to λ in a significant way.

To further check the reliability of our correlations, I added to the sample 38 low resolution major merger simulations, described in section 2.1.3. Although less reliable than the high resolution simulations, their characteristics are generally in agreement with the latter. I show the plot including those simulations in figure 4.17. The low resolution simulations are in good agreement with the correlations found for the high resolution ones.

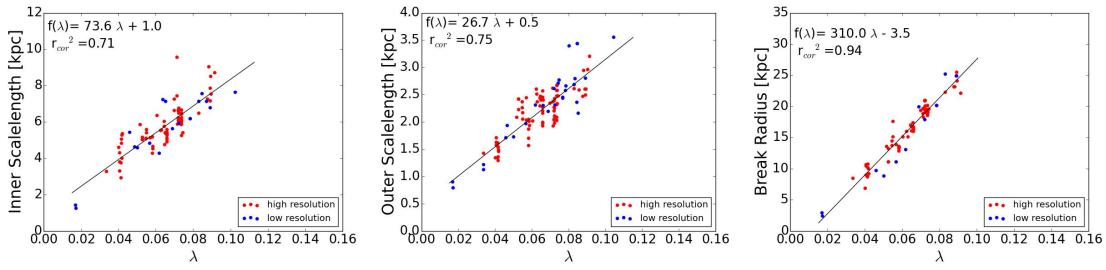

Figure 4.17.: Break radius, inner and outer scalelengths as a function of the spin parameter λ (see Paper III), by adding low resolution simulations to the sample.

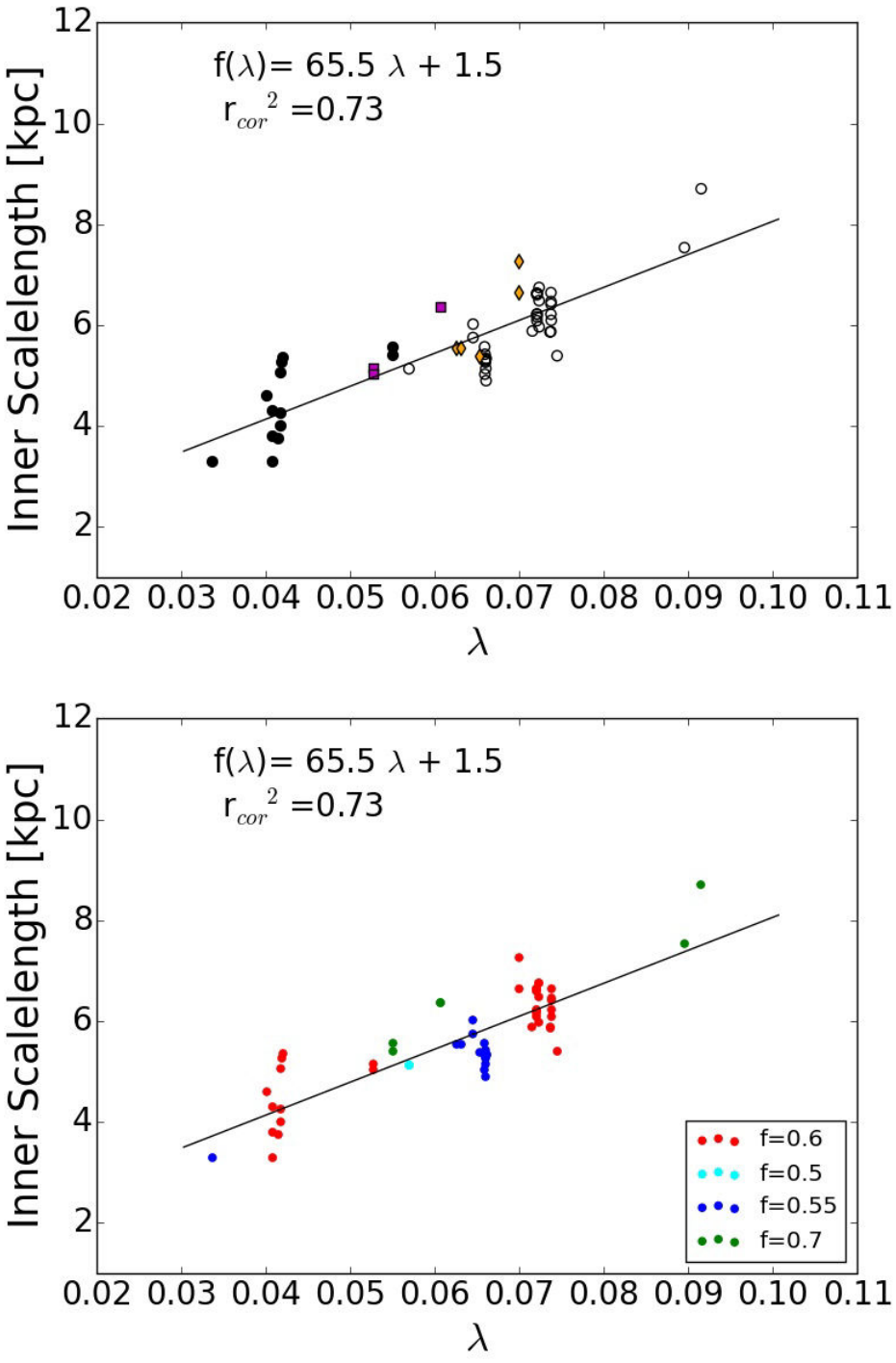

Figure 4.18.: Inner scalelength as a function of the spin parameter λ (see Paper III) by showing the effect of the orbit (top panel) and the spin of the protogalaxies f (bottom panel). On the top panel, each symbol represents one of the 4 orbits used in the sample, each having different initial positions and velocities (see section 2.1.3). Only the simulations with no inclination angle between the protogalaxies are plotted here.

In section 5.2 of Paper III, we showed the presence of a correlation between the distances of migration towards the outer disc and λ. We mentioned that this correlation exists also if we consider the whole outward migration, and not only the particles ending up in the outer disc. I show this result in figure 4.19 (left panel). Furthermore, I found that the inward migration also correlates with λ (figure 4.19, middle panel). In high angular momentum galaxies, the stars thus seem to travel further both inwards and outwards, which means that the overall distances of migration are larger. I checked this by plotting the migration distances for all the stellar particles as a function of λ, taking the absolute values of the distances (figure 4.19, right panel) to take into account both the inward and outward migration. The resulting correlation is very good, which is an interesting result, but needs further investigation to explain it.

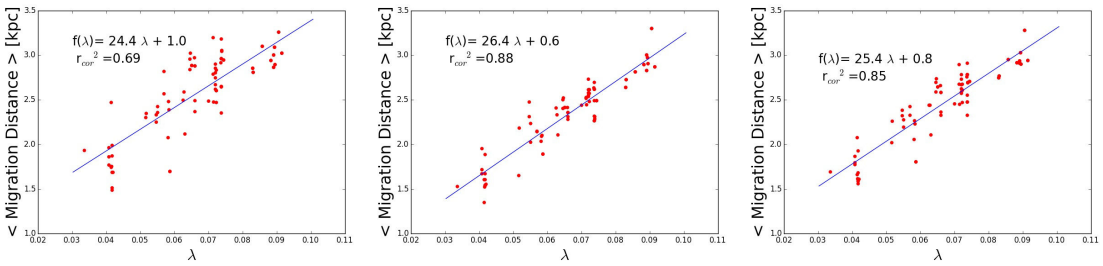

Figure 4.19.: Mean migration distances as a function of the spin parameter λ, for stellar particles migrating outwards (left panel), inwards (middle panel) and for all stars (right panel). For the latter the distances are taken in absolute value, to add the effect of inward and outward migration.

4.4.3. Paper IV: Radial projected surface density profiles

4.4.3.1. Paper

In the continuity of Paper III (section 4.4.2.1) and the study of radial density profiles in our remnant galaxies, we are preparing the next paper (hereafter Paper IV) where I stand as a second author. The goal of this paper is to make an extended analysis of our radial density profiles and the quantities derived from their fits as a function of time, stellar age and inclination, link them with the the galaxy's properties such as the spirals, and compare them to observations. This paper is not finished yet, but I present here a draft that should be completed and sumbitted within a few weeks.

Mon. Not. R. Astron. Soc. **000**, 1–10 (2012) Printed September 6, 2016 (MN LATEX style file v2.2)

Forming disc galaxies in wet major mergers IV: Radial projected surface density profiles

E. Athanassoula⋆, N. Peschken, S. A. Rodionov

Laboratoire d'Astrophysique de Marseille (LAM), UMR7326, CNRS/Aix Marseille Université, Technopôle de Marseille-Etoile, 38 rue Frédéric Joliot Curie, 13388 Marseille Cédex 13, France

Accepted . Received -

ABSTRACT

Key words: galaxies: structure – galaxies: kinematics and dynamics – galaxies: spiral

1 INTRODUCTION

Radial luminosity profiles have been observed for a very large number of disc galaxies, both spirals and lenticulars, and in many wavelengths. The inner parts of these profiles are dominated by the light from a bulge, be it classical or discy pseudobulge[1]. At larger radii, where the disc is the main contributor to the luminosity, the radial profile shows single, double, or even multiple segments of exponential profiles (e.g. Freeman 1970, Pohlen et al. 2002, Pohlen & Trujillo 2006, Erwin, Pohlen & Beckman 2008, Gutiérrez et al. 2011, Muñoz-Mateos et al. 2013, Laine et al. 2014, Kim et al. 2014). Profiles with a single exponential are called type I, while those with two profiles are called type II or downbending, if the decrease of the luminosity with radius in the outer part is steeper than that of the inner part. Inversely, if it is less steep, the profiles are called type III or upbending, or anti-truncating (Erwin, Beckman & Pohlen 2005). The radius at which the inner and outer exponential profiles intersect is known as the break radius.

Laine et al. (2014) analysing a sample of 328 galaxies from the S4G (Spitzer Stellar Structure Survey of Galaxies, Sheth et al. 2010), or the NIRS0S samples (Laurikainen *et al.* 2011) and noted that nearly all Type II profiles are associated with galactic subcomponents, such as rings, pseudorings, spirals etc, or strong star formation regions, while this is generally not true for the type III ones.

Statistics of the fraction of galaxies in each of the three types have been given in various studies, but there is no good global agreement, arguing that these fraction should depend on parameters such as the galaxy mass or type. Yet all agree that, in the field, the type II profiles are considerably more frequent than the rest. The percentage of Type III ones increases clearly from Sc-Sd galaxies to S0-Sa ones (Erwin, Pohlen & Beckman 2008; Ilyna & Silchenko 2012; Gutiérrez et al. 2011; Maltby et al. 2015), which suggests the existence of a link between type III profiles and a spheroidal component, while such a link does not seem to exist for type II ones.

Here we will discuss the formation and evolution of such profiles in the context of models in which a disc galaxy forms from a major merger. Such models are described in some detail in Athanassoula et al. (2016), which we will hereafter refer to as A16, while their salient features are summarised in the Sect. 2, where we also present our sample and techniques. Sect. 3 is devoted to type II profiles, their evolution in time (Sect. 3.2), their fossil records (Sect. 3.3), the location of the break (Sect. 3.4) and how they correlate with each other and with the corresponding densities (Sect. 3.5. Type III profiles, their formation and properties are the subject of Sect. 4. In Sect. **??** we discuss the age radial profiles and their links to the the surface density profiles. We summarise and conclude in Sect. **??**. In this paper, for brevity, instead of "stellar particle", we often say "star", and instead of "snapshot", or "simulation" we often say "galaxy", or "simulation galaxy", or "simulated galaxy".

2 SIMULATIONS

2.1 General context

Our models start with two protogalaxies, each consisting of a spherical halo consisting of dark matter and gas, both with a small spin around a given axis. These protogalaxies are set on orbits bringing them to a merger. Before this occurs, however, the halo gas starts cooling by radiation and falls towards a plane perpendicular to its spin axis. Thus a protodisc starts forming in each protogalaxy separately. Its properties are nearer to those of galaxies at intermediate redshifts than to local galaxies, namely it is more gas rich, smaller and less relaxed than local galaxies. The stars in these protodiscs experience violent relaxation during the merging and end up mainly in a spheroidal object, at the centre of the forming galaxy with a density distribution and kinematics similar to those of classical bulges. Stars born during the merging period or close to it, are considerably shuffled by the merging and end up in a thick disc. During that time the two gaseous haloes also merge into one. After

⋆ E-mail: lia@lam.fr

[1] See Kormendy & Kennicutt (2004) and Athanassoula (2005, 2016) for a discussion of the different types of bulges.

the end of the merging period the gas accreting from the gaseous halo will fall onto the equatorial plane of the new galaxy and start forming the thin disc. Several of the properties of the thus formed disc galaxy were compared to observations in A16 and showed good agreement. According to this scenario the stars in the classical bulge should be the oldest, followed by those in the thick disc and then those in the thin disc. The youngest stars are found in the spiral arms and the discy pseudobulge.

2.2 Radial projected density profiles and their analysis

The merging does not take place instantaneously. It is thus more correct to talk of a time range over which the merging occurs. For many reasons, however, it is often useful to have a given single time. In this paper, for example, we need to compare our simulations at an equivalent time. We thus follow A16 and define as merging time, t_{merge}, the earliest time after which the distance between the centres of the two merging galaxies stays always less than 1 kpc. We also used a second characteristic time, again calculated as in A16, namely the time when the disc starts forming, t_{bd}, for *b*egin *d*isc formation.

To calculate the surface density radial profile we first set the centre of coordinates at the centre of the galaxy and set the equatorial plane on the z=0 plane. We then viewed the disc face-on and integrated the stellar mass in cylindrical annuli. Since we want to focus on the disc component we omit stars with $|z|$ >1 kpc and stars born before the merging time, as these will mainly contribute to the bulge component (A16). The effect of these restrictions will be discussed further in Sects. 2.4 and 4.

The inner and outer radii were measured interactively by "piece-wise" fits, also known as the broken exponential function fit. We first plotted the log of the surface density as a function of radius and the radial extents to which a straight line was to be fitted were chosen by eye after some trials. This method gives a similar results as more standard decompositions (Erwin, Pohlen & Beckman 2008). The scalelength of each component was obtained from the slopes of the fitted straight lines, while its central surface density from the extrapolation of this straight line to R=0. The break radius was then calculated as the radius at which the two straight lines intersect.

In the following we will compare the characteristic disc lengths not only as a function of time, to get information on temporal evolution, but also across the sample. We chose to compare all radial density profiles not at the same time from the beginning of the simulations, but at the same time after the beginning of the merger, so as to compare, in as much as possible, simulated galaxies at the same phase of their evolution, roughly 8 Gyrs after the merging. We found that, at that time, all the profiles are of type II. Profiles of type III will be discussed in Sect. 4. We found profiles that can be classified as Type I only in very few cases, right after the merging.

2.3 Sample

In the following analysis we analysed ∼100 simulations of the type described above. In all these the ratio of the baryonic to total mass is 1/8 and the initial mass distribution in the two components initially follows in all cases the analytic functions given in A16. However the numerical values of the free parameters vary from one simulation to another. We considered two values of the spin parameter of the halo, namely f = 0.55, 0.6 and 0.7, which bracket a reasonable range of values since bigger values would lead to big values of the total angular momentum of the system while smaller ones would be too near the no net rotation case (f = 0.5).

We also considered both 1:1 and 1:3 mergers, various orientations of the initial spin axes and various orbits for the merging. We also included cases without and with AGN feedback, the latter with AGN of different strengths. None of the galaxies in our sample has a very strong bar, although we have a number of weak, or of intermediate strength bars.

We performed the above described analysis for all simulations of our sample and, in many cases, for a number of times. We then examined the quality of each fit and kept this information to use later in the analysis and particularly in the correlations between various characteristic quantities. By keeping only results from fits of a sufficient quality we of course reduce the size of our sample, so that e.g. for high quality type II fits at a time of t_{merge} + 7.8 Gyr our sample reduces to 64 simulations. In this way, however, we also very considerably improved the sample quality and therefore the strength of our results and conclusions.

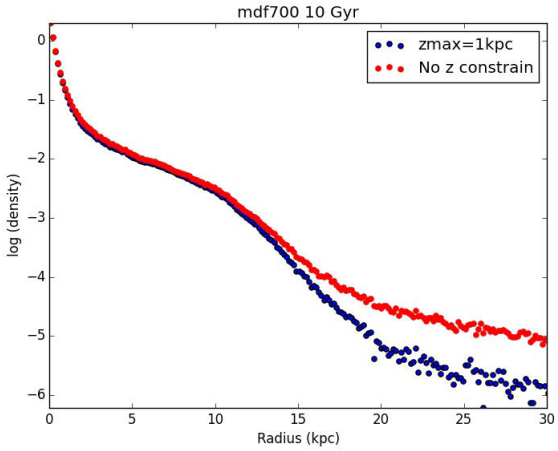

Figure 1. Comparisons of projected surface densities obtained with no cut-off and with a cut-off at $|z| = 1$ kpc.

2.4 Comparing profiles from face-on, edge-on and intermediate views

As mentionned in Sect. 2.2, when calculating the surface density we used a cut-off and omitted all the mass with $|z| > 1$ kpc. This of course can not be done in observations. To test whether it could influence comparisons, we compared projected surface density profiles with and without that cut-off for a number of our snapshots and we show a typical example of such a comparison for a type II profile in Fig. 1. It shows clearly that the cut-off does not influence the inner disc scalelength and the break radius. As expected, however, it does influence the outermost low density parts of the profile, i.e. the part beyond the region from which we measure the outer disc scalelength. The radial extent of the region from which we can measure the outer disc scale length also changes, being considerably smaller for the case with no cut-off. This could also have been expected, as the cut-off eliminates the low density background of stars which are in fact outside the disc. By measuring the outer disc cut-off for the cases with and without cut-off we find 1.6 and 1.9, respectively, i.e. a difference of about 17%. Note, however, this difference is not noise, but more like a bias, the background material

making the outer disc drop shallower and thus the outer disc scale length larger. This does not introduce any substantial change to our results, but should be taken into account if any detailed quantitative comparison of a model to the observations of a given galaxy.

The above comparison was made for type II profiles. In Sect. 4 we saw that such a cut-off will eliminate a large fraction of the outer region density.

3 TYPE II PROFILES

We used the projected surface density radial profiles of our simulation snapshots at t=10 Gyr to measure the inner and outer disc scalelengths as well as the break radius for all galaxies in our sample. After eliminating the non-satisfactory fits, we compare these values to the S^{4}G observations in Fig. 2. we compare the inner and outer disc scale lengths obtained from satisfactory fits to to the observations of the disc galaxies in the S4G sample (Sheth et al. 2010) as measured by Munoz-Mateos. Our simulations do not cover all stellar masses, as we only have two values of baryonic mass in our initial conditions. Thus our simulations with 1:1 progenitor mass ratios give stellar masses around 5.2 $\times 10^{10}$, while those with 1:3 ratios give masses around 3.1 $\times 10^{10}$.

We note that there is a good general agreement, but that the simulations compare well mainly with the big observed values.

3.1 Following the evolution

There are two possible ways of tracking evolution in galaxies. The first one is to observe galaxies also at higher redshifts and make comparisons so as to obtain the evolution as a function of time. The disadvantage of this approach is that observations at higher redshifts are more difficult to make, have lower resolution and do not reach as low surface brightness levels as observations of local galaxies. In the second way, one can observe and analyse separately different stellar populations, as a function of their age. This can be done in nearby galaxies, including our own Milky Way. For external galaxies colour is often used as a proxy of age. This way is often referred to as "near-field cosmology". It can be carried out easier than the previously discussed way, because it requires less telescope time and can be done on relatively smaller telescopes. Because of the proximity, its results have higher resolution and can reach lower surface brightness levels. On the disadvantages side, let us note that it relies on models to tell us what ages (and therefore what lookback times) we are examining. An important point to note here is that the two approaches do not give us the same information. The first one gives us information on the galaxy at a given lookback time, i.e. information on the stellar populations at some lookback time, while the second one about what a given population has evolved to and what its properties are now. Thus the two approaches are complementary. Simulations have an advantage here over observations, namely they can provide both perspectives and thus are able to link the two views.

3.2 Evolution of radial density profiles with time

We measured the inner and outer scalelengths and the break radius for a number of our simulations and at different times during its evolution. The results for one of them are given in Fig. 3. For both the merging time and the time at which the disc formation starts (t_{bd}) we use the same definition as in A16. Thus the start of the merging period, or as more commonly referred to simply the merging time, is the earliest time after which the distance between the centres of the two galaxies is always smaller than 1 kpc.

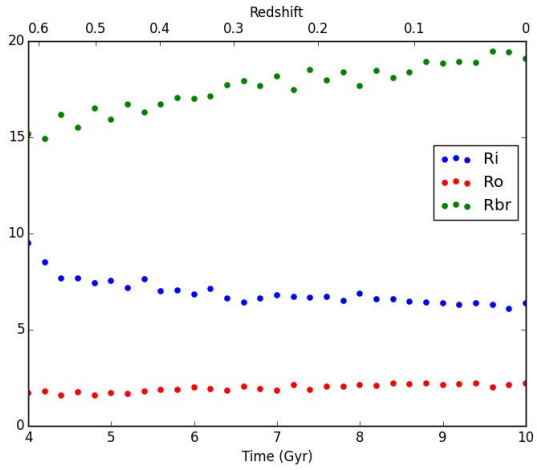

Figure 3. Evolution of the inner disc scale length (blue), the outer one (red) and the break radius (green). The time on the lower abscissa is not the lookback time, but the time since the beginning of the simulation. On the upper abscissa we give the redshift.

Fig. 3 shows that the characteristic lengths of the density distribution evolve secularly. Over the last 4 Gyr the increase of the break radius, of the inner disc scale length and of the outer disc scale length is roughly 3.4 kpc (19%), -2.2 kpc (26%) and 0.54 kpc (27%), respectively, the relative values being calculated with respect to the value at time t=10 Gyr.

The above are in good qualitative agreement with the observations of Perez (2004), of Azzolini, Trujillo & Beckman (2008b) and Muñoz-Mateos et al. (2011), as well as with a general inside-out growth of the disc component.

The comment of Trujillo : Observations show that R-break increases with time. There is also some global evolution (increase or decrease for inner and outer disc scale length

3.3 Examining the fossil record

Let us now try the second way of following the evolution, i.e. with the help of the fossil records of this evolution and examining separately populations of different ages, also known as mono-age populations. We will define the mono-age populations Martig, Minchev & Flynn (2014) in two different ways. In the first way, we follow the above mentioned paper and divide the simulation time (from 0 to 10 Gyr) in age brackets of equal duration. Since the evolution is not very rapid we use only five age brackets, calculating the radial profiles and measuring the breaks and the inner and outer disc scale lengths for each age bracket separately. In the second way, we divide the time into brackets of unequal lengths whose limits are set by landmark times, i.e. times that strongly mark the evolution, like the merging time and the time after which the thin disc starts forming (see A16). As there are only two such landmark times and we deemed three mono-age populations too little, we split the times between the landmark times in two or three. We thus have one mono-population with stars born before the merging starts, two (of equal duration) for stars born between the beginning of the merging time and the beginning of the thin disc formation and three, of roughly equal duration, after that.

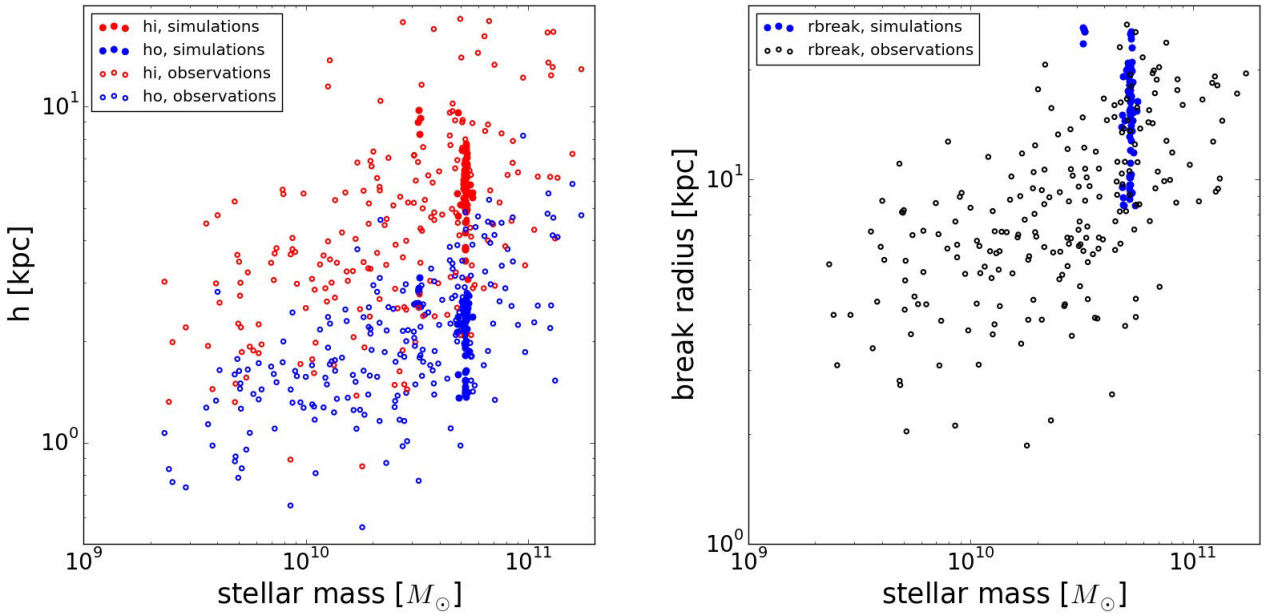

Figure 2. Left panel: Inner and outer disc scale lengths as a function of stellar mass. Right panel: Break radius as a function of stellar mass. Observations are from Muñoz-Mateos et al. 2013 and are plotted with open symbols. Simulation results are plotted with full symbols. Red and blue symbols stand for inner and outer scale lengths, respectively.

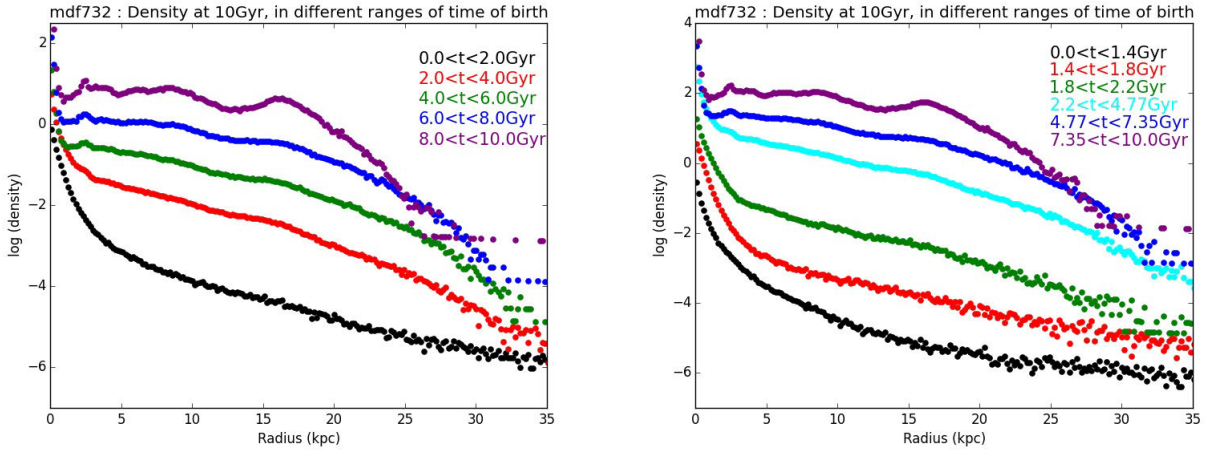

Figure 4. Surface density as a function of radius for stars of different ages, as shown on the plots. For the left panel, we have five mono-populations, each covering 2 Gyr. For the right panel, we have the mono-populations set by the two landmark times, i.e. the merging time and the time after which the thin disc starts forming, as described in the text.

The corresponding density profiles are given in the left and right panels of Fig. 4, respectively. We see that the latter mono-populations are more informative than the former. They show clearly that the surface density of the stars born before the merging (black line) follows a Sersic law with a higher index than that of the exponential, i.e. a bulge, as already found in A16. The two mono-populations with age brackets between the two landmark times have both a bulge and a disc component, while the three last ones are dominated by the disc, again in good agreement with what was found in A16. It is also clear, now from both time decompositions, that younger populations have flatter inner disc profiles, i.e. larger inner disc scale lengths, and steeper outer profiles, i.e. smaller outer disc scale lengths. Finally the break radius hardly changes from one mono-age population to another.

Our results are in good agreement with observations as shown e.g. for NGC 4244 by de Jong et al. (2007), for NGC 7793 by Radburn-Smith et al. (2012) and for our Galaxy e.g. by Sale et al. (2010), and by references therein.

Fig. 5 plots the values of the characteristic scalelengths and includes results from both the above definitions of the mono-age populations. In both cases we find that the break radii are, to within the measuring errors, independent of the age bracket chosen, while inner (outer) disc scale length decreases (increases) as the age of the population increases.

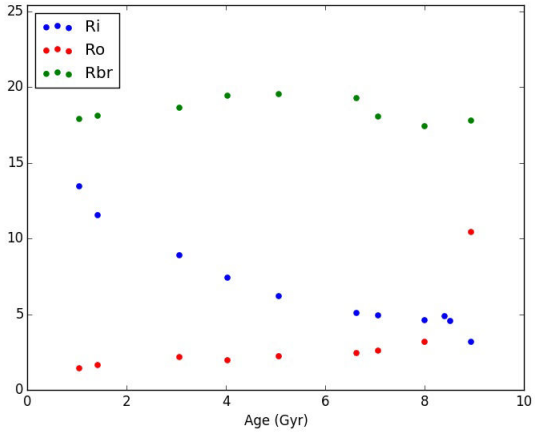

Figure 5. Characteristic disc lengths for various stellar populations. We plot the inner disc scale length (blue), the outer one (red) and the break radius (green), as a function of the age of the population.

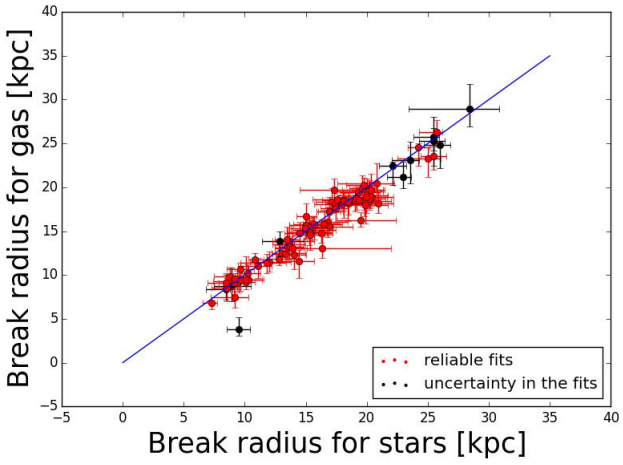

Figure 6. Comparison of the break radius of the star forming gas to that of the total stars for all the simulations of this sample at t=10 Gyr, i.e. the end of the simulations. The solid blue line is the diagonal. Data from reliable fits are given in red, while those in black correspond to less reliable ones.

Radburn-Smith et al. (Fig. 5) shows that $R_{d,out}/R_{break}$ is an increasing function of age (in agreement with Roskar et al. 2008b).

To test an extreme population difference, we also measured the break radius of the star forming gas at t=10 Gyr and compared it to that of the total stellar component for the same simulations and time. We find the two break radii to be equal to within the measuring errors, again in good agreement with observations. Indeed, this is what was found by Muñoz-Mateos (2014), who compared the radial projected density profile of the molecular gas to that of the old stellar population of NGC 5985, as obtained by the Spitzer Survey of Stellar Structure in Galaxies (S^{4}G, Sheth et al. (2010)).

3.4 Association of breaks with substructures and star formation regions

Laine et al. (2014) found that, for the vast majority of type II profiles, the break radius is connected with structural components such as spirals, rings and lenses, or the outer edge of a star-forming disc.

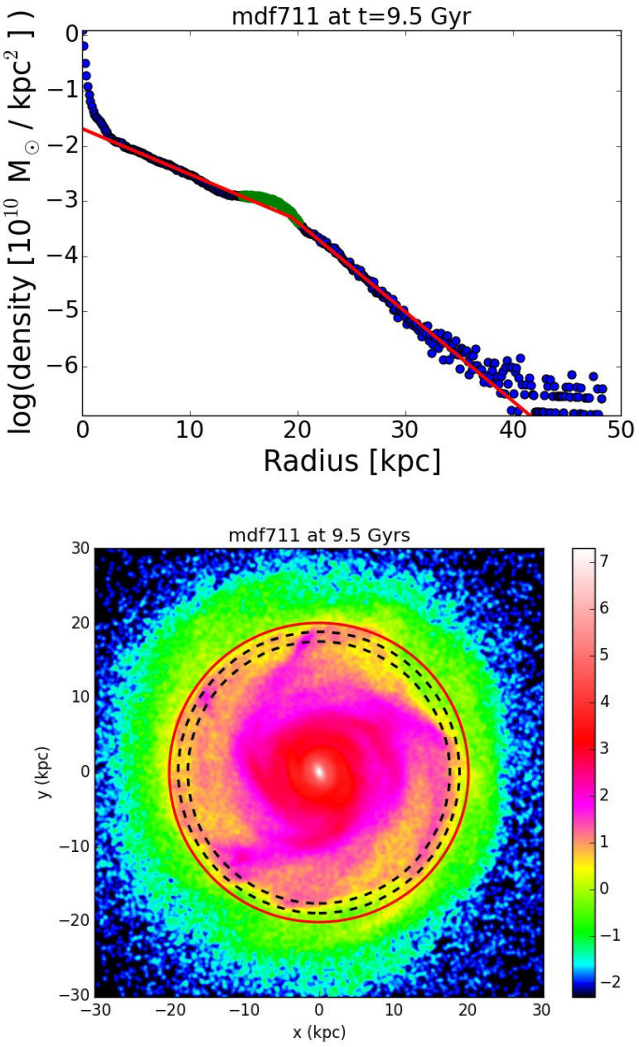

Figure 7. Upper panel: An example of a radial surface density profile with a bump very near the break radius. The radial surface density profile is given with blue filled circles, except for the region around the bump where the projected stellar density is higher than the corresponding inner pr outer exponential profile, where we use green filled circles. The exponential profile fits for the inner and outer discs are given by red lines, the intersection of which is at the break radius. Lower panel: 2D plot of the projected stellar surface density in logarithic scale. The red circle shows the location of the break radius and the black dashed ones the radius of the maximum amplitude of the outer spiral arms and their outer edge, respectively.

In order to see whether this is true also for our simulations we visualised the radial surface density profiles at roughly 7.8 Gyr after the merging time t_{merge} and superposed the two exponential profile fits, one for the inner and one for the outer disc. We noted that typically the surface density reached a local shallow maximum (hump) at radii around, and in most cases within the break radius. A good example if given in the upper panel of Fig. 7. In the lower panel of this figure we show the 2D plot of the stellar surface density distribution. The full red circle shows the position of the break radius. There are also two circles in black dashed lines. The inner one shows the location of the maximum of the hump, while the outer one shows the outer end of the region where the projected surface brightness exceeds the two line fit. These two radii can be considered as the radius of the maximum amplitude of the spiral or

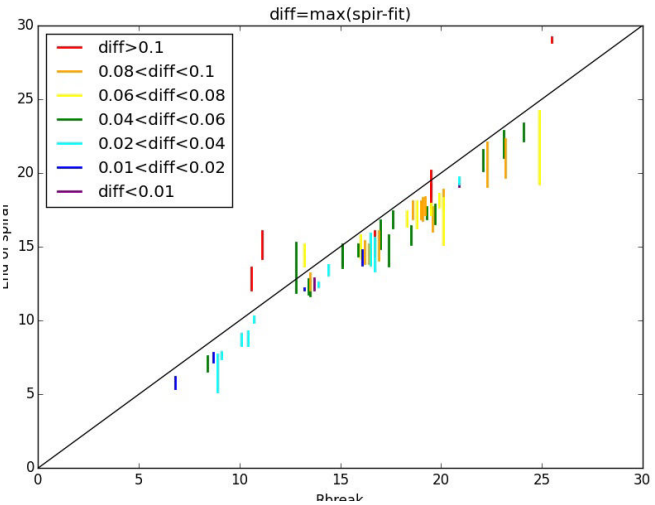

Figure 8. Link between the break radius and the location of spirals and rings. The vertical line joins the radius of the maximum amplitude to the apparent outermost radii of the spirals. Its abscissa is at the break position and its colour depends on the value of the maximum deviation of the surface density from the two line fits, as given in the plot. In this figure we include only the simulations for which the fit at the chosen time is satisfactory.

ring and its outer edge, respectively. We note that both these radii, and particularly the outer limit of the spiral, are very near the break radius, as already found in observations by Laine et al. (2014).

We then extended this analysis to all 64 galaxies with good estimates for the inner and outer disc scale lengths and the break radius (see Sect. 2.3). We found that, like in observations, our simulations have a break radius that is very near the end of a structure. In both simulations and observations this feature can be an outer ring or pseudo ring, or the end of an outer spiral, or the radius where this spiral contributes most to the stellar projected surface density, or where the star forming disc ends. We include all the results in Fig. 8, where we plot the radial extent of the region from the radius of the maximum amplitude of the spiral density to its outermost part, both radii being obtained from radial surface density profiles as in the upper panel of Fig. 7 where the projected density is higher than the two line fit as a function of the break radius.

We note that in most of our simulations the break radius is near the end of the feature, not the point of the maximum star formation. In fact it is very often slightly beyond the the end of the feature. There are, however, cases for which the break radius is nearest to the radius of maximum density of the spiral or ring, while in three cases the both radii are beyond the break radius.

3.5 Correlations

We so far discussed three characteristic quantities of the profile, namely the inner and outer disc scale lengths and the break radius. To these we will add r_{95} (the spherical radius including 95% of the total stellar mass) and three characteristic densities, namely the central density $\Sigma_{inner}(R=0)$ and $\Sigma_{outer}(R=0)$ (obtained by extrapolating the fits to the inner and outer part of the disc profile), and Σ_{break} (the projected surface density of the fitted exponentials at $R = R_{break}$). Fig. 9 shows the correlations between R_{break} and all the remaining quantities at t=5.8 Gyr and 7.8 Gyr after the merging time (Sect. 2). Values obtained from satisfactory (unsatisfactory) fits to the surface density profiles are given in full (open) circles. The third to sixth columns of Table 3.5 summarise the corresponding information, namely the correlation coefficient (r^2), the coefficients a and b of the fitted regression line ($y = ax + b$) and the ?Kendal? rank correlation coefficient (r_{rank}). When calculating these values, only the data from the satisfactory fits are taken into account.

		Rbr, all		Rbr, same mass	
		5.8 Gyr	7.8 Gyr	5.8 Gyr	7.8 Gyr
r_{95}	r^2	0.96	0.97	0.96	0.96
	a	0.88	0.88	0.88	0.87
	b	3.55	3.62	3.49	3.66
	r_{rank}	0.98	0.97	0.98	0.97
R_{in}	r^2	0.42	0.62	0.39	0.58
	a	0.20	0.22	0.19	0.20
	b	2.71	2.0	2.82	2.35
	r_{rank}	0.68	0.85	0.67	0.83
R_{out}	r^2	0.59	0.59	0.57	0.58
	a	0.07	0.07	0.07	0.07
	b	0.95	1.03	0.96	1.07
	r_{rank}	0.67	0.67	0.65	0.63
$\ln(\Sigma_{in})$	r^2	0.54	0.63	0.52	0.64
	a	-0.09	-0.10	-0.09	-0.08
	b	-2.67	-2.33	-2.79	-2.60
	r_{rank}	-0.73	-0.83	-0.72	-0.80
$\ln(\Sigma_{out})$	r^2	0.10	0.11	0.12	0.19
	a	0.07	0.07	0.08	0.09
	b	-0.23	-0.49	-0.40	-0.81
	r_{rank}	0.34	0.37	0.38	0.47
$\ln(\Sigma_{break})$	r^2	0.92	0.95	0.92	0.95
	a	-0.07	-0.08	-0.07	-0.07
	b	-1.89	-1.81	-1.91	-1.86
	r_{rank}	-0.95	-0.98	-0.98	-0.98

We note that the correlations at t=5.8 Gyr after t_{merge} are less tight than those at t=7.8, which could be expected since at the former time the density profile is not as well settled, the stellar populations are younger and the spiral perturbations are stronger than in the latter. Correlations between any two radii are present and most of them are quite tight. There is also a correlation with the density at the break position and with the central density of the inner part of the disc, but not with that of the outer part. One could have been tempted to dismiss these results simply as a result of more massive galaxies having larger radii and larger surface densities. For this reason we repeated these comparisons using only galaxies with roughly the same stellar mass. The results are shown in Table 3.5 and show that the regression values are the same, or at least very similar. We can thus conclude that the galaxies with different stellar masses follow very similar, if not the same regression lines.

Similar correlation are found also for observations. For example, Laine et al. (2014, see their figure 13) find correlations of the inner disc central surface brightness with inner disc scalelength. On the other hand, plotting this quantity for the corresponding outer disc quantities they find that there is no correlation. We show the same plots for our sample in Fig. 10 and find the same behaviour.

4 TYPE III PROFILES

As already mentionned, all our simulations, when considered at a time sufficiently long after the merging, have a type II profile. We

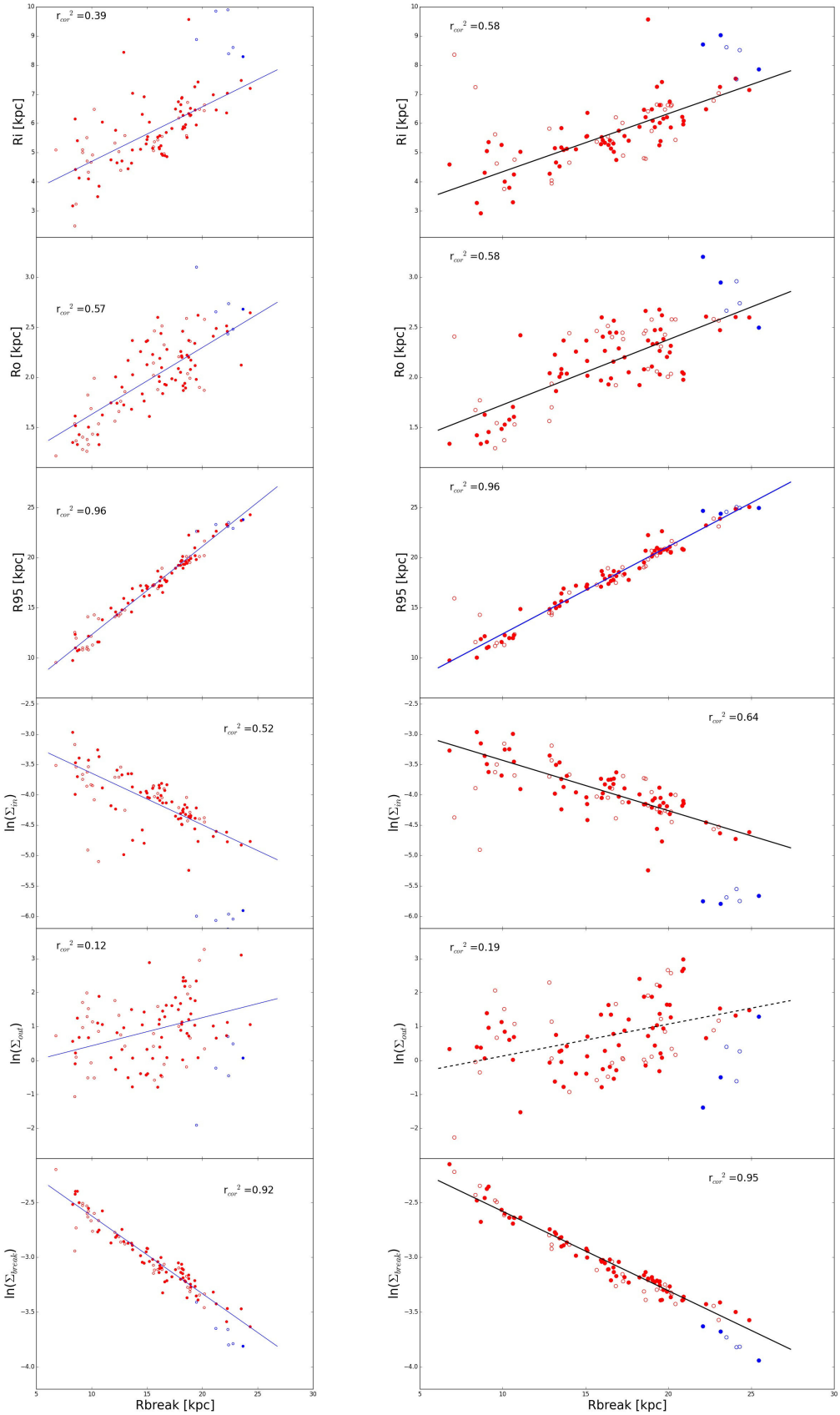

Figure 9. Correlations of the break radius with, from top to bottom, R_{95}, R_{inner}, R_{outer}, $\Sigma_{inner}(R=0)$, $\Sigma_{outer}(R=0)$ and $\Sigma_{break}(R=R_{break})$, all calculated at *t*=5.8 Gyr (left panels), or 7.8 Gyr (right panels). Open symbols are for unsatisfactory fits to the surface density profiles and thus are not taken into account when calculating correlation coefficients and properties of the regression line. Red symbols represent simulations of roughly the same stellar mass ($5.2 \times 10^{10}\ M_{solar}$), while blue symbols are for simulations of other masses.

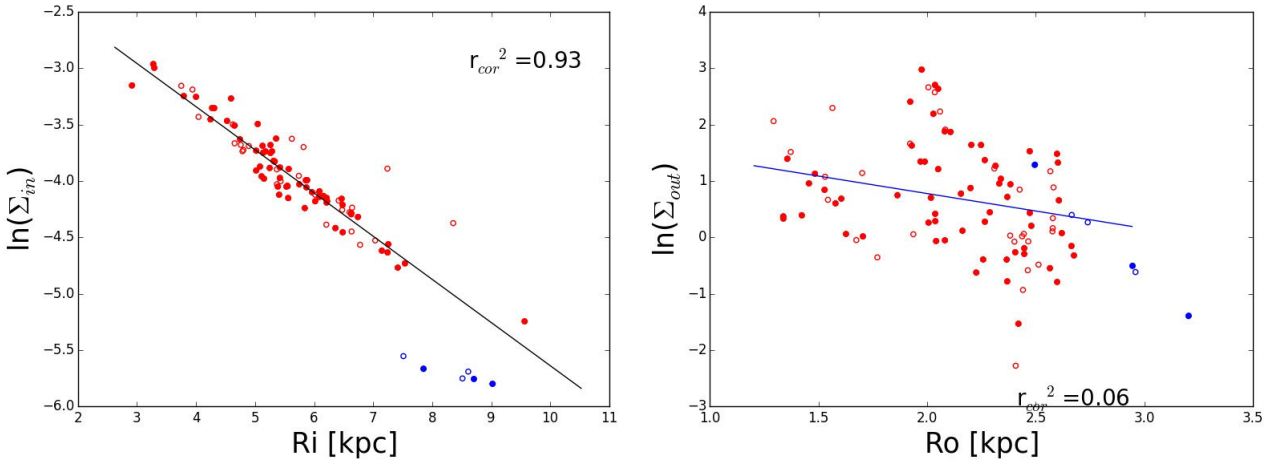

Figure 10. Correlations between inner and outer disk characteristic parameters. Left: Central surface density of the inner disc as a function of its scale length. Right: Same, but for the outer disc. The quantities are measured for all simulations 7.8 Gyr after t_{merge}. Symbols, colours etc. are as in Fig. 9.

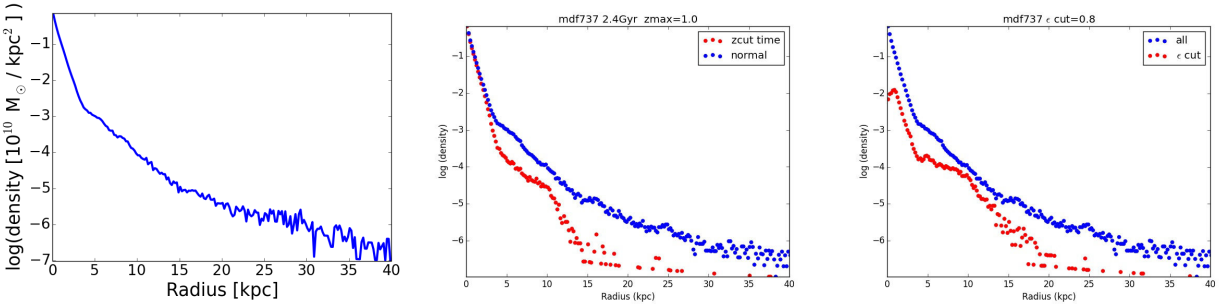

Figure 11. Left panel: Example of a radial projected surface density type III profile (blue filled circles in all panels) Middle panel: The same example together with another profile (red filled circles) after eliminating all stars which are not confined within $|z|$ <1 over a period of at least 2.4 Gyr (see text). Right panel: The same, but now eliminating all stars with a circularity parameter which is less than 0.8 (red filled circles).

did, however, find type III profiles when we considered profiles at a time near to the merging time. This is true for all but a handful of the simulations, but the quality of the profile varies quite considerably from one simulation to another. A good example is given in the left panel of Fig. 11 at a time 0.6 Gyr after t_{merge}. This time was chosen because the profile reproduces best a type III. In the next two subsections we will discuss the formation and evolution of such profiles.

4.1 Formation

To understand better how such profiles are formed, we make radial surface density profiles in two more ways. Namely, we wish to include in the profile only stars from the disc, i.e. stars which are and stay near the equatorial plane, and/or have near-circular orbits. We tried this in two different ways, all illustrated in Fig. 11. In the upper left panel we include only stars which are within $|z|$ <1 kpc from the equatorial plane not only at the time we make the radial profile, but over a range of time starting 0.4 Gyr before the time under consideration and ending 2 Gyr after it. In this way we also eliminate non-disc stars that happen to traverse the disc at the time of the measurement. We note that a considerable number of stars are eliminated, from nearly all radii except for innermost part where there must be a discy pseudo-bulge. Thus stars are eliminated not only from the outer disc region (R >9 kpc), but also from the inner disc region, which might be excessive. The important point to note, however, is that the remaining disc profile is of type II.

We then repeated this, eliminating all stars with clearly non-circular motions. For this, we first calculated for each star its circularity parameter ε=J_z/J_{circ}, where J_z is the z component of the angular momentum of the star and J_{circ} is the angular momentum of the circular orbit of the same energy as the star (e.g. Abadi et al. 2003, Aumer & White 2013, A16) and then eliminated all that have ε <0.8 (see A16 for this choice). We note that relatively few stars were eliminated from the inner disc region, while many stars were eliminated from the outer disc and the classical bulge area.

The two ways of eliminating particles discussed above have a similar effect, i.e. they exclude a number of stars in a bulge or corona component. None of the three ways, however, is well defined quantitatively, because we do not have an optimum value for the vertical height, or for the circularity parameter below which the excluded stars describe best the bulge and corona components. They were simply obtained after some trial and error, and could well differ from one simulation to another. For this reason we added a third way, in which a star was excluded when it fulfilled at least one of the two above criteria.

We note that all three profiles obtained after restricting ourselves as much as possible to the disc component have one property in common: they are of type II, contrary to the profile from which

they emanated. The importance of this result will be discussed in the next subsection.

4.2 Discussion

In Sect. 4 we found that the radial projected surface density profiles can be of type III for times right after the merging. This, however, can not explain the formation of type III profiles of nearby galaxies. Indeed if a major mergings occured about say 2 - 3 Gyr ago, the stars in its disc should be very young, so that their colours would not be compatible with observations. Our scenario, however, could explain the type III profiles observed at higher redshifts [(REF)]. It has, furthermore, provided strong evidence that type two profiles are linked to stars which have strongly non-circular motions and are well off the equatorial plane. I.e. type III profiles are linked to stars which are not part of the thin disc. This is an important step in the understanding of type III formation.

Maltby et al. (2012) examined the radial surface density profiles for a sample of 78 spiral galaxies and found that in $\sim$15% of the cases the outer antitruncated region can be accounted for simply by the extension of the central bulge component, so that the antitruncations are of type III-s (s for spheroidal). In the remaining $\sim$85%, however, this is either negligible ($\sim$70%) or simply not sufficient ($\sim$15%) and the antitruncations are named of type III-d, i.e. the antitruncations are assumed to be of pure disc origin. Although it is clear that an extra component is necessary to explain such profiles, it is unclear why this should necessarily be a disc. The only obvious link, in the absence of kinematics and of 3D viewing, is the fact that the profile is exponential. Using our simulations, however, we were able to show that, contrary to the outer discs of type II profiles, the material in the outer antitruncated discs extends considerably off the galactic equatorial plane and its kinematics is not that of discs. We would thus argue more for a corona or a thick disc extending well outside the inner thin disc.

We also inspected the break regions of type III profiles and found that in the majority of cases they are not associated with features, contrary to the breaks in type II profiles (Sect. 3.4). This is a further considerable difference between type II and type III profiles.

Thus all arguments seem to converge to a view where type III outer discs are a corona or a thick disc, formed by some merging event, most probably minor. Links between outer extensions and minor mergers have already been suggested in the literature as e.g. by Pe narrubia, McConnachie & Babul (2006) and Younger et al. (2007), but no explicit link with type III profiles has yet been discussed.

ACKNOWLEDGEMENTS

We thank Albert Bosma for stimulating and useful discussions and Jean-Charles Lambert for computer assistance We acknowledge financial support from CNES (Centre national d'tudes spatiales). This work was granted access to the HPC resources of [TGCC/CINES/IDRIS] under the allocations 2014-[x2014047098], 2015-[x2015047098] and 2016-[x2016047665] made by GENCI, as well as the HPC resources of Aix-Marseille Université financed by the project Equip@Meso (ANR-10-EQPX-29-01) of the program Investissements dAvenir supervised by the Agence Nationale de la Recherche.

REFERENCES

Abadi, M., Navarro, J., Steinmetz, M., Eke, V. 2003, ApJ, 597, 21
Athanassoula E., 2005, MNRAS, 358, 1477
Athanassoula, E., 2016, in "Galactic Bulges", Astrophysics and Space Science Library, Volume 418, E. Laurikainen, R. Peletier and D. Gadotti (eds.), Springer Verlag, Germany, 391
Athanassoula, E., Rodionov, S., Peschken, N., Lambert, J.C. 2016, ApJ, 821, 90
Aumer, M., White, S. 2013, MNRAS, 428, 1055
Azzolini, R., Trujillo, I., Beckman, J.E. 2008a, *ApJ*, 679L, 69
Azzolini, R., Trujillo, I., Beckman, J.E. 2008b, *ApJ*, 684, 1026
Bakos, J., Trujillo, I. 2012, preprint (arXiv:1204.3082)
Bakos, J., Trujillo, I., Pohlen, M. 2008, *ApJ*, 683, L103
Comerón, S., Elmegreen, B. G., Salo, H., et al. 2012, ApJ, 759, 98
Dalcanton, J. J., Spergel, D.N., Summers, F. J. 1997, ApJ, 482, 659
de Jong, R.S., Seth, A.C., Bell, E.F. et al. 2007, *ApJ*, 667, L49
Elmegreen, B. G., Hunter, D. A. 2006, ApJ, 636, 712
Elmegreen, B. G., Struck, C. 2013 ApJ, 775, L35
Erwin, P., Beckman, J. E., Pohlen, M. 2005, ApJ, 626, L81
Erwin, P., Pohlen, M., Beckman, J. E. 2008, AJ, 135, 20
Fathi, K., Gatchell, M., Hatziminaoglou, E., Epinat, B. 2012, MNRAS, 423, L112
Ferguson, A. M. N., Clarke, C. J. 2001, MNRAS, 325, 781
Freeman, K. C. 1970, ApJ, 160, 811
Gunn, J. E. 1982, in Astrophysical Cosomology Proceedings, 233
Gutiérrez L., Erwin, P., Aladro, R., Beckman, J. E. 2011, ApJ, 142, 145
Hammer, F., Flores, H., Puech, M., et al. 2009, 507, 1313
Herpich, J., Stinson, G. S., Dutton, A.A. 2015a, MNRAS, 448, 99
Herpich, J., Stinson, G. S., Rix, H. W., et al. 2015b, preprint (arXiv:1511.04442)
Ilyna, M. A., Silchenko, O. K. 2012, Astron. Astroph. Trans., 27, 313
Kim, J., Lee, J. 2013, MNRAS, 432, 1701
Kim, T., Gadotti, D., Sheth, K., et al. 2014, ApJ, 782, 64
Kormendy J., Kennicutt R. C., Jr., 2004, ARA&A, 42, 603
Laine, J., Laurikainen, E., Salo, H., et al. 2014, MNRAS, 441, 1992
Laurikainen, E., Salo, H., Buta, R., Knapen, J. 2011, MNRAS, 418, 1452
Lin, D. N. C., Pringle, J. E. 1987, ApJL, 320, L87
Maltby, D. T., Hoyos, C., Gray, M. E., Aragn-Salamanca, A., Wolf, C. 2012, MNRAS, 420, 2475
Maltby, D. T., Aragn-Salamanca, A., Gray, M. E., Hoyos, C., Wolf, C., Jogee, S., Bhm, A. 2015, MNRAS, 447, 1506
Martig, M., Minchev, I., Flynn, C. 2014, *MNRAS*, 442, 2474
Muñoz-Mateos, J.C., Boissier, S., Gil de Paz, A., et al. 2011, ApJ, 731, 10
Muñoz-Mateos, J.C., Sheth, K., Gil de Paz, A., et al. 2013, ApJ, 771, 59
Muñoz-Mateos, J.C. et al. 2014, http://www2.lowell.edu/workshops/expdisks2014/presentations/munozmateos_talk.pdf
Pe narrubia, J., McConnachie, A., Babul, A. 2006, MNRAS, 650, L33
Perez, I. 2004, *A&A*, 427, L17
Pohlen, M., Dettmar, R. J., Ltticke, R., Aronica, G. 2002 A&A, 392, 807
Pohlen, M., Trujillo, I. 2006, A&A, 454, 759
Radburn-Smith, D. J., Roškar, R., Debattista, V. P., et al. 2012,

753, 138
Roediger, J.C., Courteau, S., Sãnchez-Blãzquez, P., McDonald, M. 2012, *ApJ*, 758, 41
Roškar, R., Debattista, V. P., Stinson, G. S., et al. 2008, ApJ, 675, L65
Ruiz-Lara, T., Perez, I., Florido, E., et al. 2016, *MNRAS*, 456, L35
Sale, S.E., Drew, J.E., Knigge, C. et al. 2010, *MNRAS*, 402, 713
Schaye, J. 2004, ApJ, 609, 667
Schweizer, F. 1976, ApJS, 31, 313
Sheth, K., Regan, M., Hinz, J. L., et al. 2010, PASP, 122, 1397
Silva-Villa, E., Larsen, S. S. 2012, A&A, 537, A145
Tueben, P. 1995, in ASP Conf. Ser., Vol. 77, Astronomical Data Analysis Software and Systems IV, Shaw R. A., Payne H. E., Hayes J. J. E., eds., p. 398
van der Kruit, P.C. 1979, A&AS, 38, 15
Yoachim, P., Roškar, R., Debattista, V. P. 2010, ApJ, 716, L4
Yoachim, P., Roškar, R., Debattista, V. P. 2012, ApJ, 752, 97
Yoshii, Y., Sommer-Larsen, J. 1989, MNRAS, 236, 779
Younger, J.D., Cox, T.J., Seth, A.C., Hernquist, L. 2007, ApJ, 670, 269
Zheng, Z., Thilker, D. A., Heckman, T. M. et al. 2015, APJ, 800, 120

In this paper we studied the time evolution of the radial density profile in our simulations, and found that soon after the merging the simulations show a type III disc. Following the evolution of the radial profile over time, I could see the evolution of the profile, and observe the apparition of the type II disc, from the initially type III profile. I show this evolution in Appendix F. One can see how the upbending part of the early profiles is gradually replaced by a downbending part, but is always present underneath, being relegated to the end of the profile. This remaining outer upbending end is the one I observed in my profiles in section 4.3.1.3. The latter is thus not part of the thin disc, as shown in section 4.1 of the paper by keeping only the particles with thin disc characteristics (circularity parameter, thickness). This confirms that it was the right choice to ignore this part in the the thin disc fit.

4.4.3.2. My contribution

I describe here briefly my contributions to Paper IV.
As in Paper I and III, I made all the plots of the paper, using $python$. I derived all the stellar radial density profiles presented in the paper, and fitted them for different times, age brackets and galaxy inclinations to derive the disc scalelengths, the break radius, as well as the disc central surface densities. I also derived the gaseous radial density profiles, and measured its break.
I wrote a $python$ program to locate the outer edge and the maximum amplitude radii of the spiral arms, using the bump in the radial density profile.
Plotting the density profiles of the remnant galaxies at several times soon after the merging, I classified them as type I, II or III, finding mostly type III profiles. I then wrote the program keeping only a specific stellar population to plot the radial density profiles: the stars staying in the thin disc over time, or the stars with a circularity parameter higher than 0.8 (see section 4.1 in the paper).

4.4.4. Type III isolated

As shown in Paper IV, in the first times after the merging our remnant galaxies often show a type III disc. These type III are probably what some call type III-s (see section 3.4.3), meaning that the upbending part is due to a spheroidal component. Nevertheless, this type III does not last, as the new disc formation soon makes a type II appear in the profile. By the end of the simulation the type II is dominant, and none of our remnant galaxies still shows a type III at t=10 Gyr, at least for the early merging simulations.
However, I also analyzed the radial density profiles of our isolated galaxies simulations, and if most galaxies also have a type II at $t = 10$ Gyr, I found 3 simulations with a type III disc (figure 4.20). What makes these 3 simulations different from the others? I computed their spin parameter λ as in Paper III (section

4.4.2.1) and found that it was lower than any other simulation we have. The isolated simulations tend to have a lower λ than the merger simulations because the merging orbits contributes significantly to the total angular momentum, and is absent for the idf. Besides, these three type III idf simulations have the lowest spin value f (see section 2.1.3) that we fixed for our simulations, $f = 0.55$. This explains why their spin parameter is the lowest. It is interesting to note that finding a type III at low λ is in agreement with the results of Herpich, Stinson, Dutton, et al. (2015), who find in their simulations that high spin parameter haloes lead to type II discs, while low λ values lead to type III.

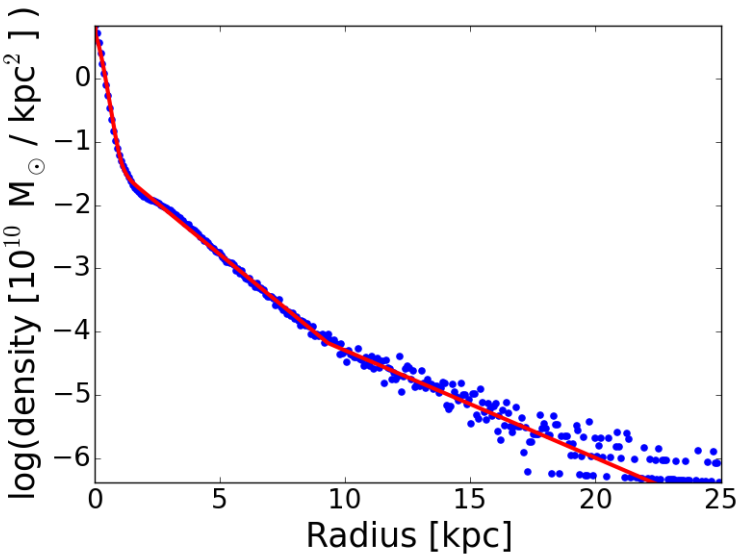

Figure 4.20.: Radial density profile of $idf022$, one of the three type III disc isolated galaxies in our sample, at t=10 Gyr with the corresponding fit in red.

I fitted the radial density profiles of the three type III simulations to derive the scalelengths and the break radius, and be able to compare them with the other simulations. Doing this analysis at 7.8 Gyr, I could add the values of these three simulations in the correlation plots between the scalelengths (or break radius) and λ (see Paper III). As shown in figure 4.21, the three simulations do not fit well with the others. The inner scalelength is slightly too small (although compatible with the other simulations), and the outer scalelength and the break radius are clearly too large. This is easily understandable, since we compare type III to type II discs. Our correlations thus seem to work only for type II discs.

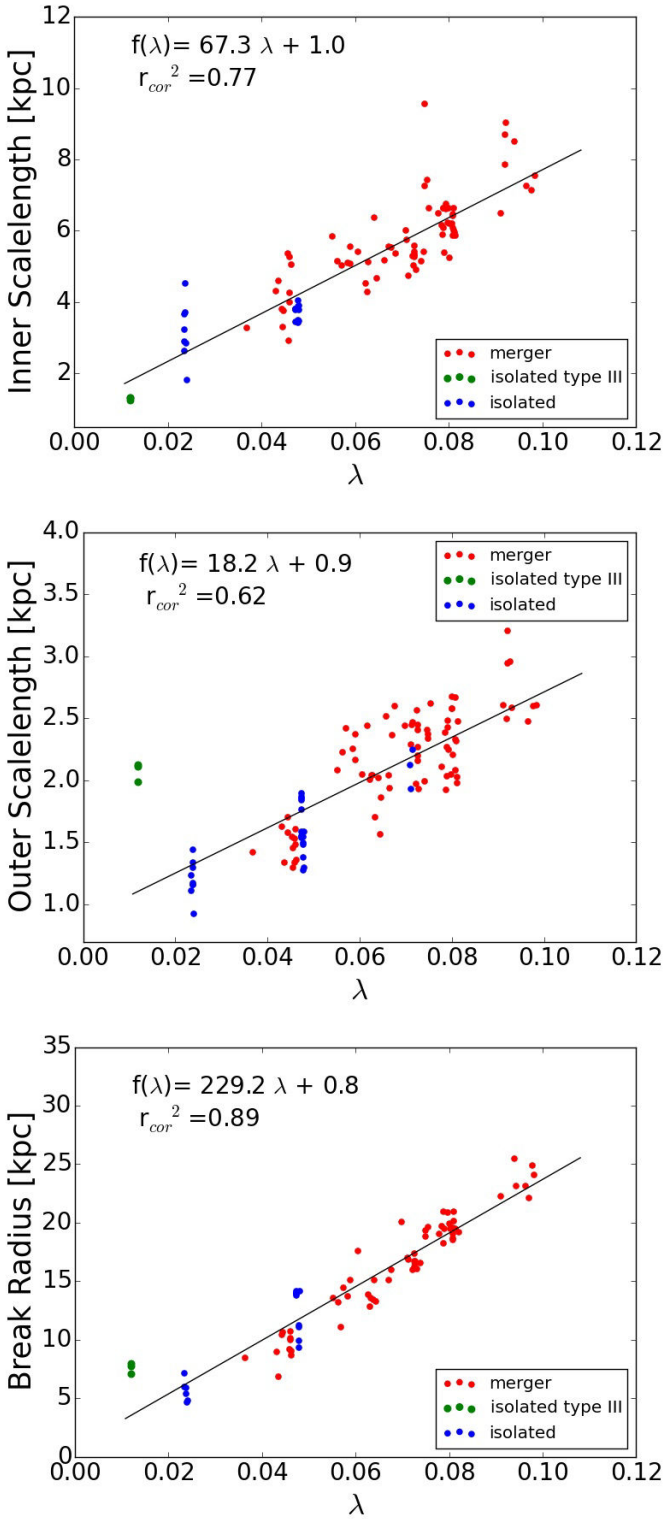

Figure 4.21.: Scalelengths and break radius as a function of the spin parameter λ, with both merger and isolated galaxies simulations, by adding 3 isolated galaxies showing a type III profile. These 3 simulations are sometimes superimposed, e.g. in the top panel.

In Paper IV, we applied several cuts in thickness and circularity parameter (section 4.1 in the paper) to the radial density profiles of our type III discs found close to the merging, to derive a type II disc underneath. I applied the same cuts to the type III idf simulations, using $\epsilon_{min} = 0.8$ and $z_{max} = 1$ kpc. This is shown in figure 4.22, and the radial density profiles of the remaining particles clearly shows a type II disc with a break around 4 kpc. Therefore, as in Paper IV, we find again that in these simulations there is a type II disc covered by a spheroidal component, which makes the profile appear as a type III. This type III is thus not of (thin) disc nature, since keeping only the particles with thin disc characteristics (circularity parameter, thickness) makes it disappear. It is consequently probably again a type III-s profile.

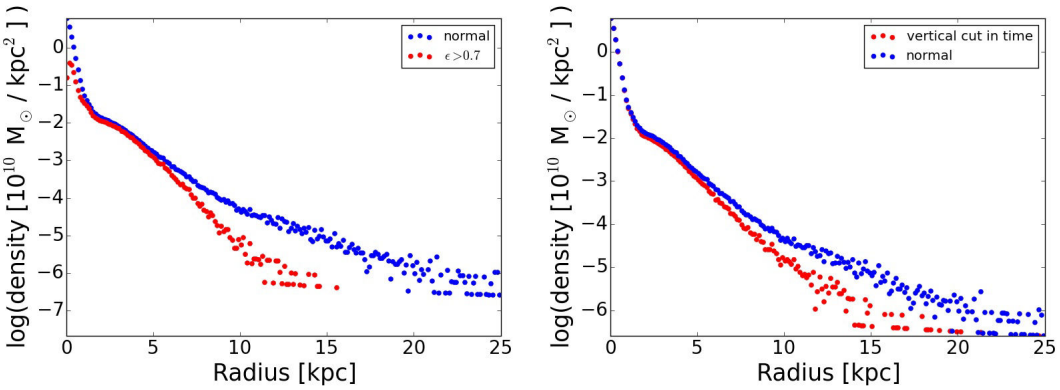

Figure 4.22.: Radial density profile of $idf022$ at t=10 Gyr, an isolated galaxy simulation with a type III profile, with a circularity parameter cut (left panel) and a vertical cut over time (right panel).

Using the newly derived type II profiles for the three idf simulations, I put the corresponding scalelengths and break radius in the correlation plots with λ. This time the three simulations fit well with the others (figure 4.23), which confirms the consistency of the type II underneath, as well as the reliability of the correlations at low λ.

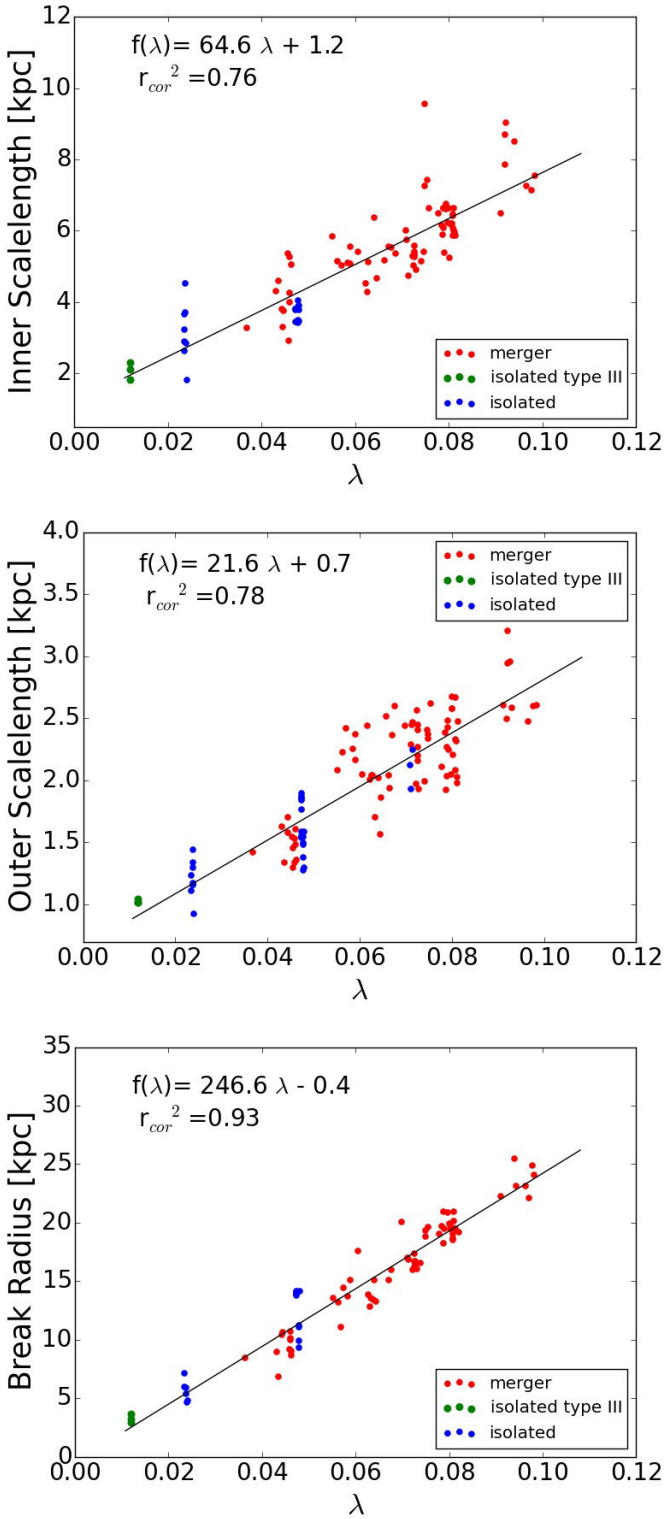

Figure 4.23.: Same as figure 4.21, but the three idf type III simulations are fitted with downbending exponentials using the ϵ cut (figure 4.22).

Nevertheless, the question of why these very low λ simulations have this spheroid dominating the profile is still open. Herpich, Stinson, Rix, et al. (2015) proposed a mechanism where the bar affects the stellar orbits due to resonances, making them excentric and creating a low rotating disk-like component. This could be our (flattened) spheroid, our three idf simulations showing a bar throughout the whole simulation. Furthermore, applying several age cuts to the radial density profile, I found that the type III was mostly composed of old stars, the youngest stars forming a type II disc. This could be consistent with the bar resonances gradually changing the circular orbits into excentric orbits. However, more investigation is necessary to confirm or disprove this theory, and determine the origin of these type III profiles.

4.4.5. Comparison to observations: Scaling relations

When working with simulations, a crucial part of the analysis is to compare the results with observations, to make sure that our analysis is consistent. In particular, I wanted to check the reliability of the values derived from my fits, i.e. the scalelengths and the break radius. It would be interesting to test the values of the effective densities as well, but observations give values in magnitude, so that we cannot compare our values directly with real galaxies. For the comparisons, I used the results from Muñoz-Mateos, Sheth, Gil de Paz, et al. (2013), and Laine, Laurikainen, Salo, et al. (2014), who study the surface brightness profiles of galaxies observed by S^{4}G and NIRS0S. The samples are using nearly face-on disc galaxies (Hubble stage $-3 \leq T \leq 7$) in the 3.6 μm wavelength of S^{4}G and the K_s band of NIRS0S. Two comparison plots have already been shown in Paper IV (figure 2 in the paper, section 4.4.3.1) for both scalelengths and the break radius, as a function of the total stellar mass. These plots only used the fit of one snapshot per simulation (at the final state, see Paper III in section 4.4.2.1), but I did the same plot again using several time steps (20 per simulation) to have a larger number of points. I removed all the time steps for which the fit was not reliable. The plot can be found in figure 4.24, and confirms the good agreement between our simulations and the observations, although the break radius is sometimes slightly too high.

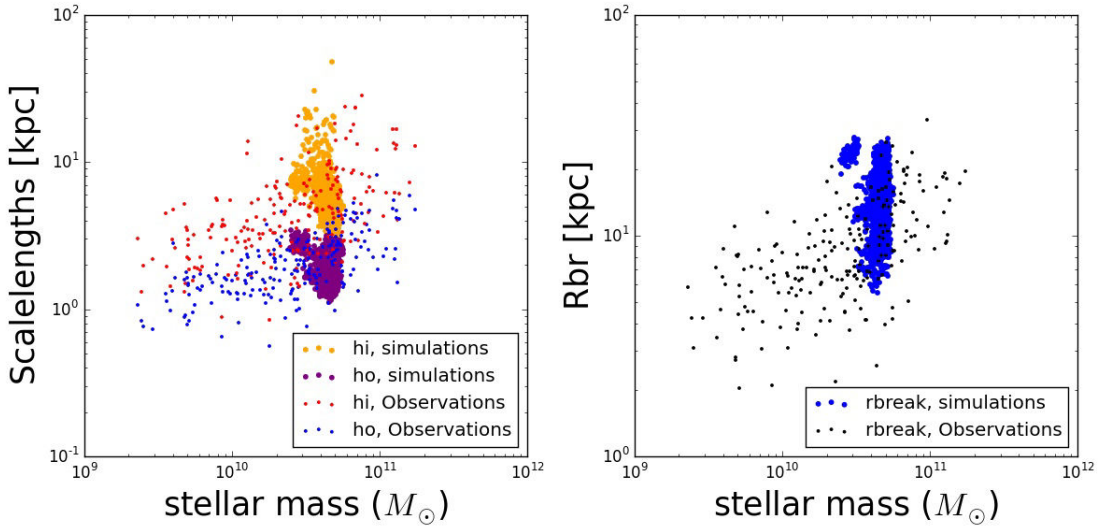

Figure 4.24.: Scalelengths and Break radius as a function of the total stellar mass, for observations (Muñoz-Mateos, Sheth, Gil de Paz, et al., 2013; Laine, Laurikainen, Salo, et al., 2014) and our simulations (for 20 time steps).

I did the same analysis for our galaxies evolved in isolation, and show the plot in figure 4.25. Again, we find a good agreement with the observations, except maybe for the break radius.

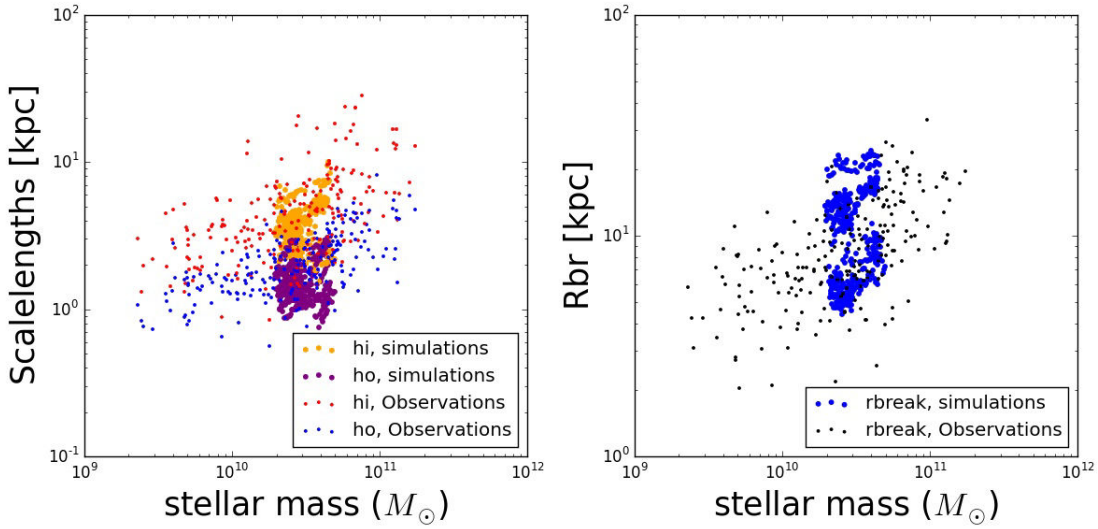

Figure 4.25.: Same as figure 4.24, but for our simulations of galaxies evolved in isolation (idf)

Furthermore, Laine, Laurikainen, Salo, et al. (2014) showed the presence of scal-

ing relations between these quantities. To check the compatibilty of my results with the observations, it is not enough to see if the values are consistent with the observed ones, they should also follow the same trends. I thus reproduced the plots of this paper to see if my values showed the same relations.
I thus present in figure 4.26 the break radius divided by the inner scalelength, as a function of the logarithm of the outer scalelength divided by the inner scalelength, for type II discs. Although both our simulations and the observations seem to follow the same trend, there seems to be an offset between the two samples, our values of R_{break}/h_i being a bit too high for a given $log(h_o/h_i)$. This could be due to the fact that our break radii are sometimes too large, while our outer scalelengths are in the lower part of the observations.

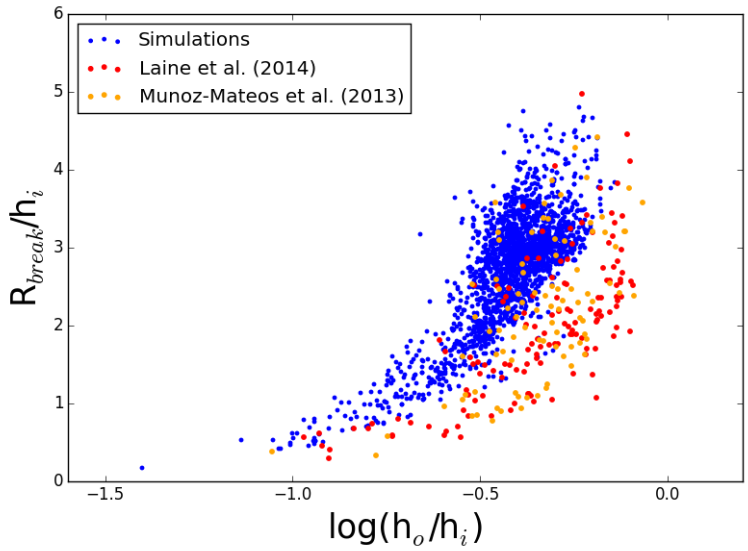

Figure 4.26.: Break radius, as a function of the logarithm of the scalelengths ratio, plotted for our simulations and from the observational results of two papers. Only downbending profiles (type II) are taken into account here. For our simulations, about 20 time steps for a hundred simulations are used in this plot, with the condition that the fit of the radial density profile has to be reliable.

Another plot made by Laine, Laurikainen, Salo, et al. (2014) is the central surface brightness of the inner and the outer disc as a function of the scalelengths. As explained above, here we cannot directly compare our values with theirs because the units are different. Nevertheless, we can check whether the trends are the same for our type II discs. I thus plotted the effective densities of the inner (outer) disc as a function of the inner (outer) scalelength in figure 4.27, alongside the results of Laine, Laurikainen, Salo, et al. (2014). We see that we also find a decreasing trend for the effective density as a function of the scalelength

in the inner disc, as well as the outer disc. Our results thus seem consistent with the observations.

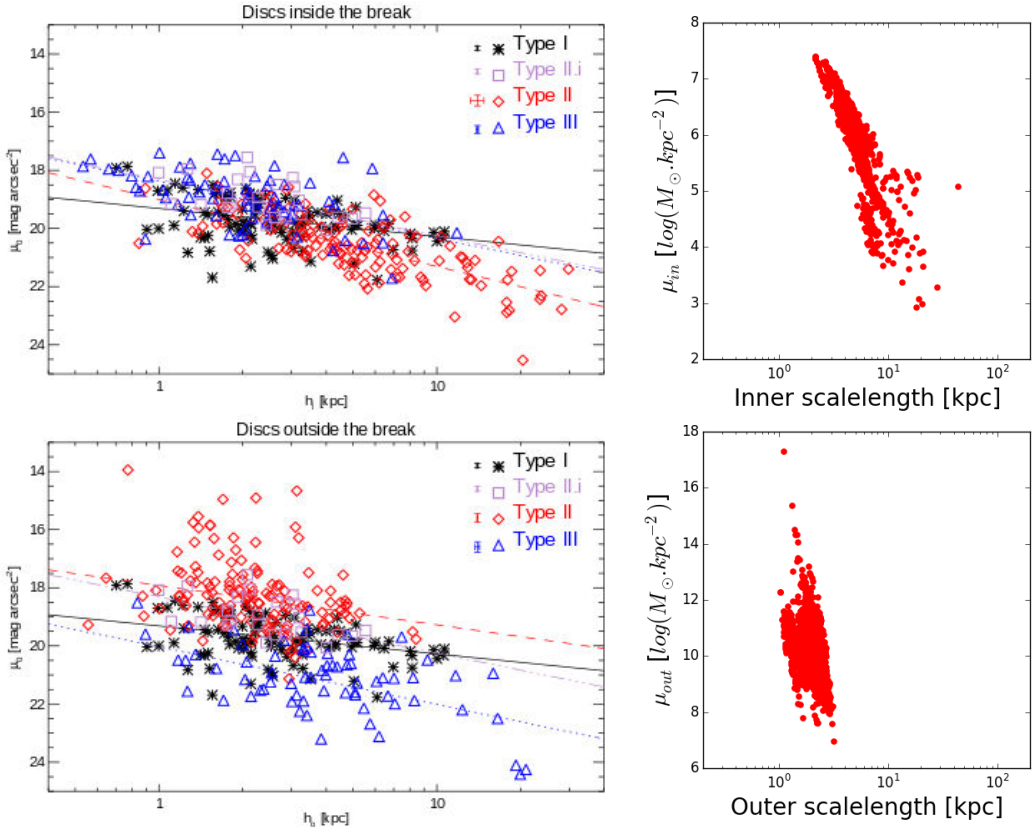

Figure 4.27.: Central surface brightness (or density) as a function of the scalelengths from Laine et al. (2014) (left panels) and for a sample of 100 of our simulations (right panels) at 20 different time steps. As in figure 4.26, only the reliable fits are plotted here, and the discs are downbending (type II).

So far I only checked the fit parameters of type II discs in this section, however we showed that three of our isolated galaxies displayed a type III profile (see section 4.4.4). I plotted the values of the type III fits, and compared them with the observations (figure 4.28) Although we do not have many points, the scalelengths as well as the break radii (which are not too large this time) are compatible with the observations, which confirms that our type III are realistic. We also have type III profiles in the *mdf* simulations close to the merging, but those profiles are often difficult to fit and change quickly over time, so that the fit results are usually not as reliable.

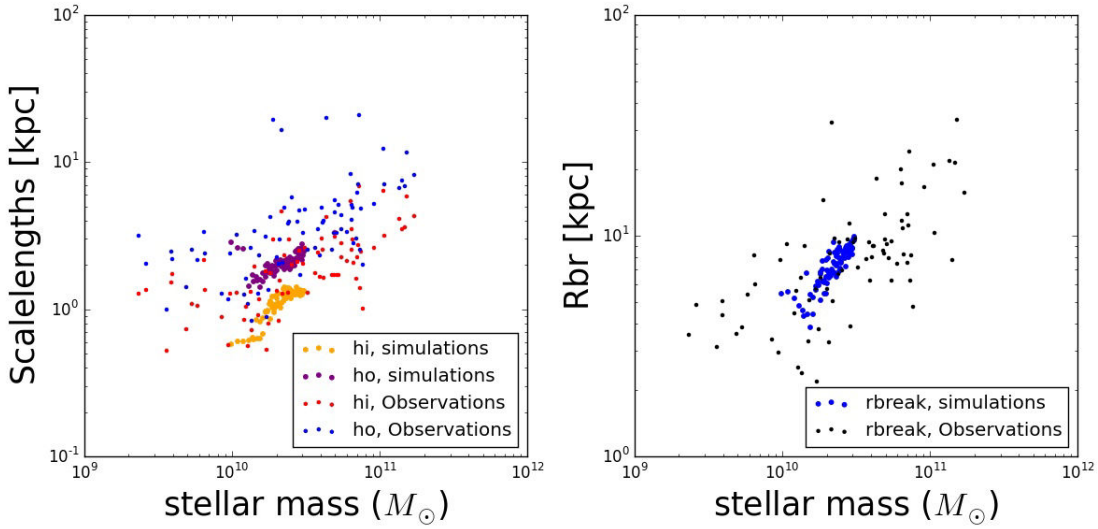

Figure 4.28.: Same as figure 4.24, but for type III idf profiles. Here I took 40 time steps for the simulations to have a larger number of points.

To conclude, our scalelengths show a good agreement with the observations of Muñoz-Mateos, Sheth, Gil de Paz, et al. (2013) and Laine, Laurikainen, Salo, et al. (2014), although the break radius tends to be among the highest values of the observations for type II discs.

4.5. Thick disc

The radial density profiles I have presented so far are the ones from the thin disc, using a vertical cut at 1 kpc. In this section I study the profile of the thick disc. I used a dozen simulations for this study, but in the following section I focus on one, the others showing similar results.

4.5.1. Thickness of the disc

We showed the presence of a thick disc in our simulated galaxies in Paper I (section 2.1.1), with a combination of age and dynamical constraints on the stellar component. However, there is another way to isolate the thick disc, using the fact that it is thicker than the thin disc, and thus becomes dominant at a certain height from the plane (see section 1.2.4.1). To find at which vertical distance from the plane the thick disc becomes dominant, I plotted the density profile as a function of z in our galaxies, at a given radius (as in figure 1.4 of section 1.2.4.1). The density is averaged over an anulus taken at the considered radius, just as the radial density profiles, but within different vertical layers. I took the absolute value of z, to have only positive values, which means that I take the

particles both above and under the galactic plane (at the same vertical distance). The plot is shown in figure 4.29 for one simulation at t=10 Gyr, and at 5.5 kpc radius. We see that the density decreases with height, which is expected, but there are two different parts of the profile, the inner part being decreasing faster than the outer one (similar to an upbending profile). The separation occurs at $z_c \sim 1.1$ kpc, and is the transition from the thin disc dominated part to the thick disc. This confirms that the choice of cutting at 1 kpc height to keep only the thin disc was consistent.

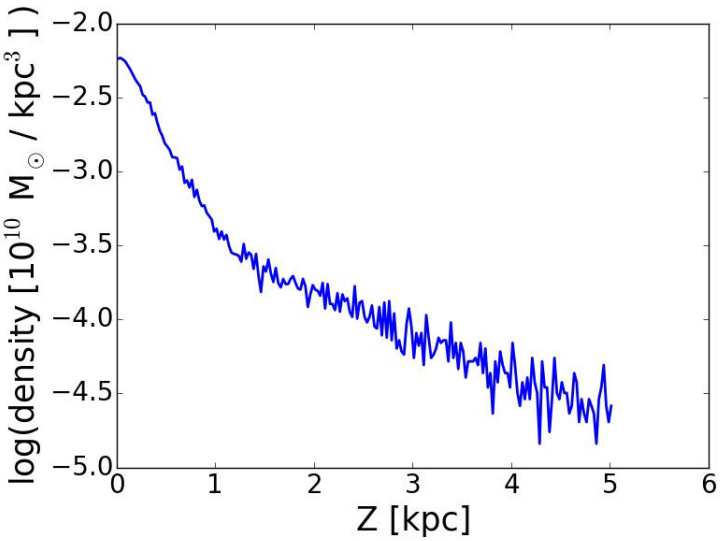

Figure 4.29.: Vertical density profile (density as a function of the height from the plane), at 5.5 kpc cylindrical radius.

Nevertheless, this z_c was derived at 5.5 kpc radius, and I found by making the same analysis at several radii that z_c seems to increase with the radius (figure 4.30, left panel). What could explain this trend? To understand it, I plotted the mean value of the thickness $< z >$ as a function of the radius, as being the value of z averaged for all the particles inside an anulus of the given radius (figure 4.30, right panel). The thickness is high in the inner parts, probably due to the boxy/peanut bulge, but beyond the bar the mean thickness of our galaxies increases monotonically with the radius. Therefore, the thickness of the disc (thin + thick) is higher in the outer parts, which explains the increase of z_c.

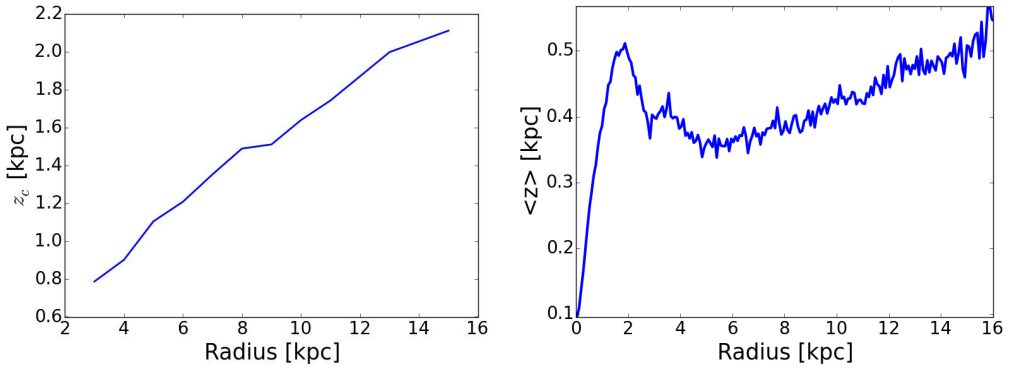

Figure 4.30.: Left panel: separation height between the thin and the thick disc, as a function of the cylindrical radius. Right panel: mean thickness of the disc, as a function of the radius.

4.5.2. Thick disc radial profile

Using z_c derived in the previous section, I could then derive the radial density profile of the thick disc part, that is, the part with $z > z_c$. z_c is dependent on the radius, therefore I had to implement a radius dependent cut in my $Fortran$ fitting program. I plotted in figure 4.31 the resulting radial profiles of the thick disc for two simulations. We can see that there seems to be a very extended central bulge-like part (until $\sim$ 15 kpc) followed by an exponential disc, with a possible downbending break, which is more or less clear depending on the simulation.

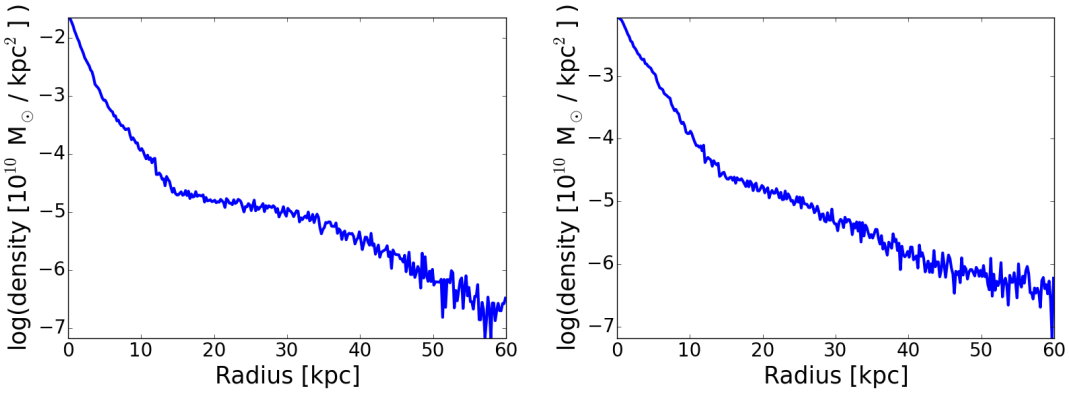

Figure 4.31.: Radial density profile of the thick disc part ($z > z_c$) for two different simulations at t=10Gyr.

This profile is rather tricky to decompose, there appears to be at least three different ways of fitting it.
- The first option is to suppose that it is a bulge + single exponential profile, with

a very extended bulge part, possibly being composed of two bulges, a classical and a boxy/peanut one. This is the simplest solution, and the fit works, even if the end of the profile is not well reproduced (figure 4.32, left panel). But the last 10 kpc are a very low density area, with only a few particles per annulus, so that the end of the profile is not reliable.
- The second option is to suppose that there is a downbending break, and fit a downbending disc with a break around 28 kpc (figure 4.32, right panel). Although the break is not as well defined as for the thin disc (especially for simulations such as the right panel of figure 4.31), the fit works for most simulations.
- Finally, it is possible to fit an upbending disc on this profile. This is based on the assumption that the central part is too extended to be only the bulge, and that a part of it could be a fast decreasing exponential inner disc. The fit works (figure 4.32, bottom panel), as the central part seems to show a slight change in its profile around 7 kpc. As in the first case, the end of the profile is not well reproduced.

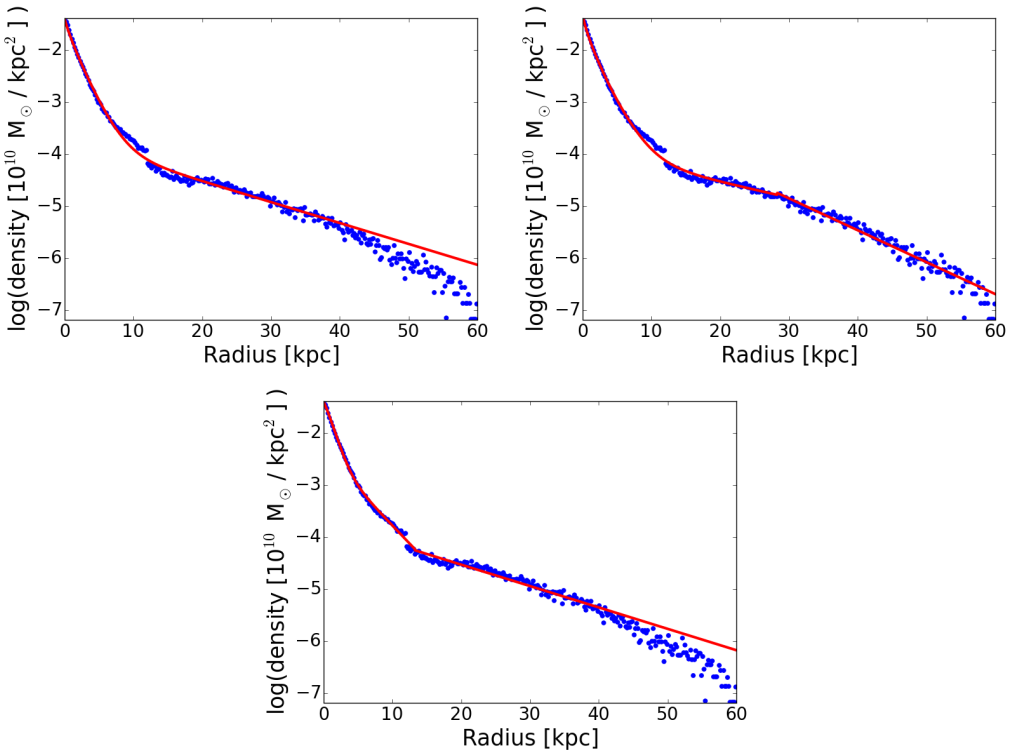

Figure 4.32.: Radial density profile of the thick disc part ($z > z_c$) for a simulation at t=10 Gyr, fitted (in red) with different methods. The top left panel shows a fit with a Sérsic bulge + single exponential (type I), the top right panel with a double downbending exponential function, and the bottom panel with an upbending disc.

Looking at the thin disc break radius (21 kpc for the snapshot shown in figure 4.32), there seems to be a small bump in the thick disc profile, which could be due to the spirals (the break often being located at the end of the spirals, see Paper IV in section 4.4.3.1) affecting slightly the thick disc. Nevertheless, there is no break in the thick disc profile at the thin disc break – I checked this result for several simulations. Assuming a type II thick disc, its break is farther out than the thin disc profile, while for a type III thick disc its break is located closer to the center. This is consistent with the two discs having a different formation history, as shown in Paper I (section 2.1.1). Indeed, the thin disc was formed from newly born stars after the merging, while the thick disc is constituted of older stars.

Comerón, B. G. Elmegreen, Salo, et al. (2012) also studied the surface brightness profiles of edge-on observed galaxies for the thin and the thick disc separately, to look for a truncation in the thick disc profile. They found that the thick disc truncates less often than the thin disc, but when it does, its break coincides with the thin disc one. We do not find this result, which might suggest that there is no downbending break in our thick discs, as the type II break is not always well defined. Furthermore, these authors found very few antitruncations (type III) in the thick disc, so that fitting our thick discs with type III profiles might not be consistent either.

To conclude, our thick disc profiles are not straightforward to interpret, as there are several ways of fitting them. A more systematic study on a larger sample is needed to find the nature of the thick disc profile.

Conclusion

In this thesis, I used the N-body/SPH major merger simulations presented in Athanassoula, Rodionov, Peschken, et al. (2016) to study the properties of the remnant galaxy. This paper shows how a spiral galaxy can be created from a gas-rich major merger at high redshift, using a hot gaseous halo to fuel the formation of a new disc in the remnant galaxy. Although most of my work concentrated on the analysis of the radial density profile of these remnants, I had the opportunity to investigate many different issues about galaxy formation and evolution. In particular, I studied the transition between the merger and the remnant disc growth, since the merging is not an instantaneous event and is not obvious to delimitate over time. There are several methods to find when the merging starts and end, including the distance between the centers of densities of the proto-galaxies, the star formation rate, and the black hole mass, each one having its own benefits. The start of the disc growth after the merging can be derived using the circularity parameter of stars at birth.
After the disc starts growing, I observed the presence of radial stellar migration, a significant amount of stars moving inwards or outwards over time. In particular, most of the stars ending up in the outer disc appear to have migrated outwards. This migration seems to be due to orbital resonances in the disc, the initial distribution of stars moving outwards appearing to be linked to the corotation resonance.
I also studied the pattern speed using the Tremaine-Weinberg method, and found that it works also in the case of thick discs.

In the second part of the thesis I presented my work on the density distribution, our galaxies showing a typical bulge + downbending disc (type II) profile at the end of the simulations. I first tried to reproduce the 2D density distribution of our galaxies using GALFIT and BUDDA, however the disc break appeared to be difficult to fit, so that I focused on the 1D radial profiles. I used a $Fortran$ program to fit these profiles, allowing to interactively select the fitting interval, with the desired function. The bulge part of the profile seems to be best fitted with two different Sérsic functions, one representing the classical bulge and the other a discy pseudo-bulge. The profile sometimes shows a bar in the inner part, which can be fitted using another Sérsic function.
To fit the disc part, I used a piece-wise fit, fitting the inner and the outer disc

separately, which gaves me three main parameters: the inner disc scalelength, the outer disc scalelength, and the break radius. These parameters are in good agreement with the observations, although the break radius generally tends to be slightly to high. The stellar break appears to coincide with the end of the spiral structure, as well as with a break in the gaseous density profile, the gas density showing a brutal drop in the stellar outer disc. This corresponds to a drop in the star formation rate as well, which could explain the downbending outer disc observed in the stellar profile. Looking at the scalelengths, I found that they correlate with the total angular momentum of the galaxy, high angular momentum merging systems producing remnant discs with large inner and outer scalelengths, and break radii (submitted paper). However, not all our galaxies have downbending discs. Soon after the merging, the remnant galaxy usually shows an upbending disc (type III), the profile being dominated by a spheroid formed by the merger. The downbending disc then appears gradually whith the disc growing. We also have three simulations of isolated galaxies (no merger) showing an upbending disc at the end of the simulation, which seems to be due to the presence of a spheroid as well, although its formation scenario is not clear. Finally, I studied the density profile of the thick disc, isolating it by using the vertical density distribution and by determining at which distance from the plane the thick disc becomes dominant. The resulting radial density profile is not straightforward to decompose, but the thin disc break does not seem to coincide with a break in the thick disc.

This work was done using mainly $python$ (and sometimes $Fortran$) to create numerous programs allowing me to analyze and visualize our simulations in many different ways.

Perspectives

The N-body simulations I presented in this thesis have many interesting features, showing very realistic morphology, dynamics and mass distribution. The presence of a hot gaseous halo, as well as their high resolution, makes them unique to study galaxy evolution after a major merger event. Therefore, there are many further points which are worth studying in these simulations, and which are not covered by the papers presented in this thesis. I give below some of these points, some of them being already in progress.
These research projects should lead to new papers in the next months.

I showed in this thesis the presence of stellar migration in our simulated galaxies. This migration takes place in the whole disc, and is particularly important for the outer parts, where a consequent fraction of the stars comes from the inner part (see section 2.2.1). This corresponds to outward migration, but there is also inward migration in the disc. It is necessary to further investigate what causes this stellar migration, and whether it is indeed linked to resonances, as the results of section 2.2.2 suggest. Furthermore, the amount and direction (inwards or outwards) of migration seems to vary as a function of the radius (section 2.2.1), and it would be interesting to understand why, and if it is linked to the presence of morphological components.
The migration seems to be linked to the global angular momentum (see sections 4.4.2.1, 4.4.2.2), stars migrating further when the spin parameter λ is higher. This needs further investigation, and another way to study the migration would be to look at angular momentum exchanges in the galactic disc.

A further point to understand is the formation of the type II break in our discs. Although we showed its formation over time in Appendix F, we have not yet found the mechanism responsible for its creation. It seems to be linked to spiral arms (see section 4.4.3.1), to coincide with a drop of star formation (section 4.4.1.2), but we need further investigation to understand how and why this leads to this typical type II surface density profile in our simulations.

The star formation also needs further work. I showed in section 4.4.1.2 the star formation rate as a function of the radius in the disc, and it would be interesting to fully understand what causes some areas to form more stars than others, look

at the dependence with the gaseous distribution, and link the star formation rate to some morphological features such as spirals. This will require to analyze and take into account the possible bias introduced by our star formation recipe.

The thick disc needs to be studied in more detail. We showed in Paper I (section 2.1.1) that there was a thick disc in our galaxies, formed mainly by stars born before the merging, so that the major merger seems to be the cause of the creation of a thick disc in our simulations. Nevertheless, we did not look at the thick disc any further, and its morphology and dynamics still need to be analyzed. I started looking at the thick disc stellar distribution in section 4.5.2, but a systematic study over more simulations is needed. Furthermore, it would be interesting to compare the thick disc population kinematically derived in Paper I to the one used in section 4.5.2 from the vertical density profile.

We made isolated galaxies simulations, which have barely been used so far, although the presence of a hot gaseous halo makes them interesting to study and to compare with other simulations and observations. We showed quickly that our isolated galaxies were realistic in Paper I (section 2.1.1), and I added them in my sample in Paper III (section 4.4.2.1), but a more detailed study of the idf and their differences with the mdf would be interesting, for example for the presence of the classical bulge and the thick disc. This would put constrains on which dynamical features and morphological components are likely to be directly linked to a major merger, or to a secular isolated evolution ($nature$ vs $nurture$).
The upbending (type III) profile found in three idf simulations also needs more investigation, to understand how it formed, and if it is related to the bar orbital resonances (see section 4.4.4).
Furthermore, looking at the type III profiles both in the idf and in the mdf at early times, a model of light emission is needed to allow a direct comparison to observations. We separated the old from the young stars to isolate the underlying type II disc, but this is only a rough approximation of the electromagnetic spectrum bands observed for real galaxies. The code $SUNRISE$ allows to model the light emitted by a simulated galaxy in several bands, which would allow us to look at the UV emissions for example to see if they show the underlying type II disc, as the young population does.

There are several initial conditions we tried to vary in our simulations, such as the spins of the protogalaxies, the merging orbit, the AGN properties, or the inclination angle between the two protogalaxies. This allowed us to have several hundred major merger simulations. Nevertheless, the number of possible combinations of all the initial conditions is much higher, and we are still making new simulations to fill some areas of the parameter space. The goal is to look at the effect of each parameter individually. For example, what is the effect of the inclination angle on the morphology of the remnant? Can we get some particular

features such as polar rings or bars for nearly perpendicular encounters? We already found a polar bar in our sample of simulations (section 2.1.3), which would need a specific inspection. For such an analysis we need to have more simulations to be able to consistently compare the simulations obtained by varying one initial parameter in particular.
With this aim in mind, we would also like to see the effect of varying the mass ratio of the two protogalaxies, the orbit, and the total mass. By changing the time of the merging, we could also explore if it has an impact on the remnant galaxy Hubble type, and if this allows to account (at least partly) for the Hubble sequence frequencies in the local Universe.

Finally, we are currently making new simulations including chemistry, to be able to further investigate the stellar populations in our galaxies, for example for the thick disc component. This would allow direct comparisons with the GAIA results for the Milky Way. I should run myself some of these new simulations, to be prepared for my postdoctoral position in Warsaw about simulating dwarf galaxies.

Bibliography

[1] E. Athanassoula. “The existence and shapes of dust lanes in galactic bars”. In: *Monthly Notices of the Royal Astronomical Society* 259 (Nov. 1992), pp. 345–364. DOI: 10.1093/mnras/259.2.345 (cit. on p. 49).

[2] E. Athanassoula. “What determines the strength and the slowdown rate of bars?” In: *Monthly Notices of the Royal Astronomical Society* 341 (June 2003), pp. 1179–1198. DOI: 10.1046/j.1365-8711.2003.06473.x. eprint: astro-ph/0302519 (cit. on p. 20).

[3] E. Athanassoula. “On the nature of bulges in general and of box/peanut bulges in particular: input from N-body simulations”. In: *Monthly Notices of the Royal Astronomical Society* 358 (Apr. 2005), pp. 1477–1488. DOI: 10.1111/j.1365-2966.2005.08872.x. eprint: astro-ph/0502316 (cit. on p. 21).

[4] E. Athanassoula. “Boxy/peanut and discy bulges: formation, evolution and properties”. In: *Formation and Evolution of Galaxy Bulges*. Ed. by M. Bureau, E. Athanassoula, and B. Barbuy. Vol. 245. IAU Symposium. July 2008, pp. 93–102. DOI: 10.1017/S1743921308017389 (cit. on pp. 22, 63).

[5] E. Athanassoula, R. E. G. Machado, and S. A. Rodionov. “Bar formation and evolution in disc galaxies with gas and a triaxial halo: morphology, bar strength and halo properties”. In: *Monthly Notices of the Royal Astronomical Society* 429 (Mar. 2013), pp. 1949–1969. DOI: 10.1093/mnras/sts452. arXiv: 1211.6754 (cit. on pp. 20, 60).

[6] E. Athanassoula, S. A. Rodionov, N. Peschken, et al. “Forming Disk Galaxies in Wet Major Mergers. I. Three Fiducial Examples”. In: *The Astrophysical Journal* 821, 90 (Apr. 2016), p. 90. DOI: 10.3847/0004-637X/821/2/90. arXiv: 1602.03189 (cit. on pp. 26, 135, 164).

[7] J. Bakos and I. Trujillo. “Deep Surface Brightness Profiles of Spiral Galaxies from SDSS Stripe82: Touching Stellar Halos”. In: *ArXiv e-prints* (Apr. 2012). arXiv: 1204.3082 [astro-ph.CO] (cit. on p. 72).

[8] I. K. Baldry, K. Glazebrook, J. Brinkmann, et al. “Quantifying the Bimodal Color-Magnitude Distribution of Galaxies”. In: *The Astrophysical Journal* 600 (Jan. 2004), pp. 681–694. DOI: 10.1086/380092. eprint: astro-ph/0309710 (cit. on p. 17).

[9] J. E. Barnes. “Encounters of disk/halo galaxies”. In: *The Astrophysical Journal* 331 (Aug. 1988), pp. 699–717. DOI: 10.1086/166593 (cit. on p. 18).

[10] J. E. Barnes. “Formation of gas discs in merging galaxies”. In: *Monthly Notices of the Royal Astronomical Society* 333 (July 2002), pp. 481–494. DOI: 10.1046/j.1365-8711.2002.05335.x. eprint: astro-ph/0201250 (cit. on p. 12).

[11] J. Binney. “On the rotation of elliptical galaxies”. In: *Monthly Notices of the Royal Astronomical Society* 183 (May 1978), pp. 501–514. DOI: 10.1093/mnras/183.3.501 (cit. on p. 21).

[12] J. Binney and S. Tremaine. *Galactic Dynamics: Second Edition*. Princeton University Press, 2008 (cit. on pp. 154, 158).

[13] G. R. Blumenthal, S. M. Faber, J. R. Primack, et al. “Formation of galaxies and large-scale structure with cold dark matter”. In: *Nature* 311 (Oct. 1984), pp. 517–525. DOI: 10.1038/311517a0 (cit. on p. 19).

[14] A. Borlaff, M. C. Eliche-Moral, C. Rodríguez-Pérez, et al. “Formation of S0 galaxies through mergers. Antitruncated stellar discs resulting from major mergers ”. In: *Astronomy & Astrophysics* 570, A103 (Oct. 2014), A103. DOI: 10.1051/0004-6361/201424299. arXiv: 1407.5097 (cit. on p. 12).

[15] F. Bournaud, C. J. Jog, and F. Combes. “Galaxy mergers with various mass ratios: Properties of remnants”. In: *Astronomy & Astrophysics* 437 (July 2005), pp. 69–85. DOI: 10.1051/0004-6361:20042036. eprint: astro-ph/0503189 (cit. on pp. 18, 21).

[16] A. Brooks and C. Christensen. “Bulge Formation via Mergers in Cosmological Simulations”. In: *Galactic Bulges* 418 (2016), p. 317. DOI: 10.1007/978-3-319-19378-6_12. arXiv: 1511.04095 (cit. on p. 21).

[17] F. Buitrago, I. Trujillo, C. J. Conselice, et al. “Early-type galaxies have been the predominant morphological class for massive galaxies since only z $\sim$ 1”. In: *Monthly Notices of the Royal Astronomical Society* 428 (Jan. 2013), pp. 1460–1478. DOI: 10.1093/mnras/sts124. arXiv: 1111.6993 (cit. on p. 20).

[18] Y. I. Byun and K. C. Freeman. “Two-dimensional Decomposition of Bulge and Disk”. In: *The Astrophysical Journal* 448 (Aug. 1995), p. 563. DOI: 10.1086/175986 (cit. on p. 68).

[19] C. M. Carollo, M. Stiavelli, P. T. de Zeeuw, et al. “Spiral Galaxies with WFPC2.I.Nuclear Morphology, Bulges, Star Clusters, and Surface Brightness Profiles”. In: *The Astrophysical Journal* 114 (Dec. 1997), p. 2366. DOI: 10.1086/118654 (cit. on p. 22).

[20] M. Chiba and T. C. Beers. “Kinematics of Metal-poor Stars in the Galaxy. III. Formation of the Stellar Halo and Thick Disk as Revealed from a Large Sample of Nonkinematically Selected Stars”. In: *The Astrophysical Journal* 119 (June 2000), pp. 2843–2865. DOI: 10.1086/301409. eprint: astro-ph/0003087 (cit. on p. 23).

[21] S. Comerón, B. G. Elmegreen, H. Salo, et al. “Breaks in Thin and Thick Disks of Edge-on Galaxies Imaged in the Spitzer Survey Stellar Structure in Galaxies (S^4G)”. In: *The Astrophysical Journal* 759, 98 (Nov. 2012), p. 98. DOI: 10.1088/0004-637X/759/2/98. arXiv: 1209.1513 (cit. on pp. 72, 134).

[22] G. Contopoulos. “How far do bars extend”. In: *Astronomy & Astrophysics* 81 (Jan. 1980), pp. 198–209 (cit. on p. 25).

[23] G. Contopoulos and T. Papayannopoulos. “Orbits in weak and strong bars”. In: *Astronomy & Astrophysics* 92 (Dec. 1980), pp. 33–46 (cit. on p. 25).

[24] T. J. Cox, P. Jonsson, J. R. Primack, et al. “Feedback in simulations of disc-galaxy major mergers”. In: *Monthly Notices of the Royal Astronomical Society* 373 (Dec. 2006), pp. 1013–1038. DOI: 10.1111/j.1365-2966.2006.11107.x. eprint: astro-ph/0503201 (cit. on p. 12).

[25] R. L. Davies, G. Efstathiou, S. M. Fall, et al. “The kinematic properties of faint elliptical galaxies”. In: *The Astrophysical Journal* 266 (Mar. 1983), pp. 41–57. DOI: 10.1086/160757 (cit. on p. 21).

[26] R. E. de Souza, D. A. Gadotti, and S. dos Anjos. “BUDDA: A New Two-dimensional Bulge/Disk Decomposition Code for Detailed Structural Analysis of Galaxies”. In: *The Astrophysical Journal Supplement Series* 153 (Aug. 2004), pp. 411–427. DOI: 10.1086/421554. eprint: astro-ph/0404103 (cit. on p. 78).

[27] P. Di Matteo, M. D. Lehnert, Y. Qu, et al. “The formation of a thick disk through the heating of a thin disk: Agreement with orbital eccentricities of stars in the solar neighborhood”. In: *Astronomy & Astrophysics* 525, L3 (Jan. 2011), p. L3. DOI: 10.1051/0004-6361/201015822. arXiv: 1011.3825 (cit. on p. 23).

[28] A. Dressler, A. Oemler Jr., H. R. Butcher, et al. “The morphology of distant cluster galaxies. 1: HST observations of CL 0939+4713”. In: *The Astrophysical Journal* 430 (July 1994), pp. 107–120. DOI: 10.1086/174386 (cit. on p. 17).

[29] B. G. Elmegreen, F. Bournaud, and D. M. Elmegreen. “Bulge Formation by the Coalescence of Giant Clumps in Primordial Disk Galaxies”. In: *The Astrophysical Journal* 688, 67-77 (Nov. 2008), pp. 67–77. DOI: 10.1086/592190. arXiv: 0808.0716 (cit. on p. 21).

[30] B. G. Elmegreen and D. A. Hunter. “Radial Profiles of Star Formation in the Far Outer Regions of Galaxy Disks”. In: *The Astrophysical Journal* 636 (Jan. 2006), pp. 712–720. DOI: 10.1086/498082. eprint: astro-ph/0509190 (cit. on p. 72).

[31] B. G. Elmegreen and C. Struck. “Exponential Galaxy Disks from Stellar Scattering”. In: *The Astrophysical Journal Letters* 775, L35 (Oct. 2013), p. L35. DOI: 10.1088/2041-8205/775/2/L35. arXiv: 1308.5236 (cit. on p. 70).

[32] P. Erwin, J. E. Beckman, and M. Pohlen. “Antitruncation of Disks in Early-Type Barred Galaxies”. In: *The Astrophysical Journal Letters* 626 (June 2005), pp. L81–L84. DOI: 10.1086/431739. eprint: astro-ph/0505216 (cit. on p. 72).

[33] P. Erwin, M. Pohlen, and J. E. Beckman. “The Outer Disks of Early-Type Galaxies. I. Surface-Brightness Profiles of Barred Galaxies”. In: *The Astrophysical Journal* 135 (Jan. 2008), pp. 20–54. DOI: 10.1088/0004-6256/135/1/20. arXiv: 0709.3505 (cit. on pp. 70–73, 79).

[34] P. B. Eskridge, J. A. Frogel, R. W. Pogge, et al. “The Frequency of Barred Spiral Galaxies in the Near-Infrared”. In: *The Astrophysical Journal* 119 (Feb. 2000), pp. 536–544. DOI: 10.1086/301203. eprint: astro-ph/9910479 (cit. on p. 20).

[35] A. M. N. Ferguson and C. J. Clarke. “The evolution of stellar exponential discs”. In: *Monthly Notices of the Royal Astronomical Society* 325 (Aug. 2001), pp. 781–791. DOI: 10.1046/j.1365-8711.2001.04501.x. eprint: astro-ph/0103205 (cit. on p. 70).

[36] K. C. Freeman. “On the Disks of Spiral and S0 Galaxies”. In: *The Astrophysical Journal* 160 (June 1970), p. 811. DOI: 10.1086/150474 (cit. on p. 70).

[37] D. Friedli and W. Benz. “Secular evolution of isolated barred galaxies. I - Gravitational coupling between stellar bars and interstellar medium”. In: *Astronomy & Astrophysics* 268 (Feb. 1993), pp. 65–85 (cit. on p. 49).

[38] K. Fuhrmann. “Nearby stars of the Galactic disc and halo - IV”. In: *Monthly Notices of the Royal Astronomical Society* 384 (Feb. 2008), pp. 173–224. DOI: 10.1111/j.1365-2966.2007.12671.x (cit. on p. 23).

[39] G. Gilmore and N. Reid. “New light on faint stars. III - Galactic structure towards the South Pole and the Galactic thick disc”. In: *Monthly Notices of the Royal Astronomical Society* 202 (Mar. 1983), pp. 1025–1047. DOI: 10.1093/mnras/202.4.1025 (cit. on pp. 23, 24).

[40] J. E. Gunn. “The evolution of galaxies”. In: *Astrophysical Cosmology Proceedings*. Ed. by H. A. Brueck, G. V. Coyne, and M. S. Longair. 1982, pp. 233–259 (cit. on p. 70).

[41] L. Gutiérrez, P. Erwin, R. Aladro, et al. “The Outer Disks of Early-type Galaxies. II. Surface-brightness Profiles of Unbarred Galaxies and Trends with Hubble Type”. In: *The Astrophysical Journal* 142, 145 (Nov. 2011), p. 145. DOI: 10.1088/0004-6256/142/5/145. arXiv: 1108.3662 (cit. on pp. 70, 72–74).

[42] F. Hammer, H. Flores, D. Elbaz, et al. “Did most present-day spirals form during the last 8 Gyr?. A formation history with violent episodes revealed by panchromatic observations”. In: *Astronomy & Astrophysics* 430 (Jan. 2005), pp. 115–128. DOI: 10.1051/0004-6361:20041471. eprint: astro-ph/0410518 (cit. on p. 20).

[43] F. Hammer, H. Flores, M. Puech, et al. “The Hubble sequence: just a vestige of merger events?” In: *Astronomy & Astrophysics* 507 (Dec. 2009), pp. 1313–1326. DOI: 10.1051/0004-6361/200912115. arXiv: 0903.3962 (cit. on p. 12).

[44] F. Hammer, H. Flores, Y. B. Yang, et al. “A forming, dust-enshrouded disk at z = 0.43: the first example of a massive, late-type spiral rebuilt after a major merger?” In: *Astronomy & Astrophysics* 496 (Mar. 2009), pp. 381–387. DOI: 10.1051/0004-6361:200810488. arXiv: 0901.0718 [astro-ph.GA] (cit. on pp. 12, 20).

[45] M. Haywood. “Radial mixing and the transition between the thick and thin Galactic discs”. In: *Monthly Notices of the Royal Astronomical Society* 388 (Aug. 2008), pp. 1175–1184. DOI: 10.1111/j.1365-2966.2008.13395.x. arXiv: 0805.1822 (cit. on p. 54).

[46] L. Hernquist. “Structure of merger remnants. I - Bulgeless progenitors”. In: *The Astrophysical Journal* 400 (Dec. 1992), pp. 460–475. DOI: 10.1086/172009 (cit. on p. 18).

[47] J. Herpich, G. S. Stinson, A. A. Dutton, et al. “How to bend galaxy disc profiles: the role of halo spin”. In: *Monthly Notices of the Royal Astronomical Society* 448 (Mar. 2015), pp. L99–L103. DOI: 10.1093/mnrasl/slv006. arXiv: 1501.01960 (cit. on p. 122).

[48] J. Herpich, G. S. Stinson, H.-W. Rix, et al. “How to bend galaxy disc profiles II: stars surfing the bar in anti-truncated discs”. In: *ArXiv e-prints* (Nov. 2015). arXiv: 1511.04442 (cit. on pp. 72, 126).

[49] P. F. Hopkins, K. Bundy, D. Croton, et al. “Mergers and Bulge Formation in ΛCDM: Which Mergers Matter?” In: *The Astrophysical Journal* 715 (May 2010), pp. 202–229. DOI: 10.1088/0004-637X/715/1/202. arXiv: 0906.5357 [astro-ph.CO] (cit. on p. 21).

[50] P. F. Hopkins, T. J. Cox, J. D. Younger, et al. “How do Disks Survive Mergers?” In: *The Astrophysical Journal* 691 (Feb. 2009), pp. 1168–1201. DOI: 10.1088/0004-637X/691/2/1168. arXiv: 0806.1739 (cit. on p. 12).

[51] P. Jonsson. “SUNRISE: polychromatic dust radiative transfer in arbitrary geometries”. In: *Monthly Notices of the Royal Astronomical Society* 372 (Oct. 2006), pp. 2–20. DOI: 10.1111/j.1365-2966.2006.10884.x. eprint: astro-ph/0604118 (cit. on p. 66).

[52] N. Katz. “Dissipational galaxy formation. II - Effects of star formation”. In: *The Astrophysical Journal* 391 (June 1992), pp. 502–517. DOI: 10.1086/171366 (cit. on p. 21).

[53] T. Kim, D. A. Gadotti, K. Sheth, et al. “Unveiling the Structure of Barred Galaxies at 3.6 μm with the Spitzer Survey of Stellar Structure in Galaxies (S^4G). I. Disk Breaks”. In: *The Astrophysical Journal* 782, 64 (Feb. 2014), p. 64. DOI: 10.1088/0004-637X/782/2/64. arXiv: 1312.3384 (cit. on p. 72).

[54] J. Kormendy and R. Bender. “A Revised Parallel-sequence Morphological Classification of Galaxies: Structure and Formation of S0 and Spheroidal Galaxies”. In: *The Astrophysical Journal Supplement Series* 198, 2 (Jan. 2012), p. 2. DOI: 10.1088/0067-0049/198/1/2. arXiv: 1110.4384 (cit. on p. 21).

[55] J. Kormendy and R. C. Kennicutt Jr. “Secular Evolution and the Formation of Pseudobulges in Disk Galaxies”. In: *Annual Review of Astrnomy and Astrophysics* 42 (Sept. 2004), pp. 603–683. DOI: 10.1146/annurev.astro.42.053102.134024. eprint: astro-ph/0407343 (cit. on pp. 21, 68).

[56] J. Laine, E. Laurikainen, H. Salo, et al. “Morphology and environment of galaxies with disc breaks in the S^4G and NIRS0S”. In: *Monthly Notices of the Royal Astronomical Society* 441 (July 2014), pp. 1992–2012. DOI: 10.1093/mnras/stu628. arXiv: 1404.0559 (cit. on pp. 20, 70, 72, 73, 126–128, 130).

[57] E. Laurikainen, H. Salo, and R. Buta. “Comparison of Bar Strengths and Fractions of Bars in Active and Nonactive Galaxies”. In: *The Astrophysical Journal* 607 (May 2004), pp. 103–124. DOI: 10.1086/383462. eprint: astro-ph/0111376 (cit. on p. 20).

[58] E. Laurikainen, H. Salo, and R. Buta. “Multicomponent decompositions for a sample of S0 galaxies”. In: *Monthly Notices of the Royal Astronomical Society* 362 (Oct. 2005), pp. 1319–1347. DOI: 10.1111/j.1365-2966.2005.09404.x. eprint: astro-ph/0508097 (cit. on p. 69).

[59] C. C. Lin and F. H. Shu. “On the Spiral Structure of Disk Galaxies.” In: *The Astrophysical Journal* 140 (Aug. 1964), p. 646. DOI: 10.1086/147955 (cit. on p. 22).

[60] S. R. Loebman, R. Roškar, V. P. Debattista, et al. “The Genesis of the Milky Way’s Thick Disk Via Stellar Migration”. In: *The Astrophysical Journal* 737, 8 (Aug. 2011), p. 8. DOI: 10.1088/0004-637X/737/1/8. arXiv: 1009.5997 (cit. on p. 23).

[61] L. A. MacArthur, S. Courteau, and J. A. Holtzman. “Structure of Disk-dominated Galaxies. I. Bulge/Disk Parameters, Simulations, and Secular Evolution”. In: *The Astrophysical Journal* 582 (Jan. 2003), pp. 689–722. DOI: 10.1086/344506. eprint: astro-ph/0208404 (cit. on p. 68).

[62] K. Menéndez-Delmestre, K. Sheth, E. Schinnerer, et al. “A Near-Infrared Study of 2MASS Bars in Local Galaxies: An Anchor for High-Redshift Studies”. In: *The Astrophysical Journal* 657 (Mar. 2007), pp. 790–804. DOI: 10.1086/511025. eprint: astro-ph/0611540 (cit. on p. 20).

[63] M. J. Miller and J. N. Bregman. “Constraining the Milky Way’s Hot Gas Halo with O VII and O VIII Emission Lines”. In: *The Astrophysical Journal* 800, 14 (Feb. 2015), p. 14. DOI: 10.1088/0004-637X/800/1/14. arXiv: 1412.3116 (cit. on p. 26).

[64] I. Minchev and B. Famaey. “A New Mechanism for Radial Migration in Galactic Disks: Spiral-Bar Resonance Overlap”. In: *The Astrophysical Journal* 722 (Oct. 2010), pp. 112–121. DOI: 10.1088/0004-637X/722/1/112. arXiv: 0911.1794 (cit. on p. 58).

[65] I. Minchev, B. Famaey, A. C. Quillen, et al. “Evolution of galactic discs: multiple patterns, radial migration, and disc outskirts”. In: *Astronomy & Astrophysics* 548, A126 (Dec. 2012), A126. DOI: 10.1051/0004-6361/201219198. arXiv: 1203.2621 (cit. on p. 73).

[66] C. Möllenhoff and J. Heidt. “Surface photometry of spiral galaxies in NIR: Structural parameters of disks and bulges”. In: *Astronomy & Astrophysics* 368 (Mar. 2001), pp. 16–37. DOI: 10.1051/0004-6361:20000335 (cit. on p. 68).

[67] B. K. Moorthy and J. A. Holtzman. “Stellar populations in bulges of spiral galaxies”. In: *Monthly Notices of the Royal Astronomical Society* 371 (Sept. 2006), pp. 583–608. DOI: 10.1111/j.1365-2966.2006.10722.x. eprint: astro-ph/0512346 (cit. on p. 21).

[68] J. C. Muñoz-Mateos, K. Sheth, A. Gil de Paz, et al. “The Impact of Bars on Disk Breaks as Probed by S^4G Imaging”. In: *The Astrophysical Journal* 771, 59 (July 2013), p. 59. DOI: 10.1088/0004-637X/771/1/59. arXiv: 1304.6083 (cit. on pp. 72, 126, 127, 130).

[69] M. Naeslund and S. Joersaeter. “Surface photometry of the edge-on spiral NGC 4565. I. V-band data and the extended optical warp.” In: *Astronomy & Astrophysics* 325 (Sept. 1997), pp. 915–922 (cit. on p. 71).

[70] P. A. Oesch, R. J. Bouwens, C. M. Carollo, et al. “Structure and Morphologies of z ˜ 7-8 Galaxies from Ultra-deep WFC3/IR Imaging of the Hubble Ultra-deep Field”. In: *The Astrophysical Journal Letters* 709 (Jan. 2010), pp. L21–L25. DOI: 10.1088/2041-8205/709/1/L21. arXiv: 0909.5183 (cit. on p. 19).

[71] Y. Ono, M. Ouchi, E. Curtis-Lake, et al. “Evolution of the Sizes of Galaxies over $7 < z < 12$ Revealed by the 2012 Hubble Ultra Deep Field Campaign”. In: *The Astrophysical Journal* 777, 155 (Nov. 2013), p. 155. DOI: 10.1088/0004-637X/777/2/155. arXiv: 1212.3869 (cit. on p. 19).

[72] C. Y. Peng, L. C. Ho, C. D. Impey, et al. “Detailed Structural Decomposition of Galaxy Images”. In: *The Astrophysical Journal* 124 (July 2002), pp. 266–293. DOI: 10.1086/340952. eprint: astro-ph/0204182 (cit. on p. 75).

[73] C. Y. Peng, L. C. Ho, C. D. Impey, et al. “Detailed Decomposition of Galaxy Images. II. Beyond Axisymmetric Models”. In: *The Astrophysical Journal* 139 (June 2010), pp. 2097–2129. DOI: 10.1088/0004-6256/139/6/2097. arXiv: 0912.0731 (cit. on p. 75).

[74] M. Pohlen, R.-J. Dettmar, R. Lütticke, et al. “Outer edges of face-on spiral galaxies. Deep optical imaging of NGC 5923, UGC 9837 and NGC 5434”. In: *Astronomy & Astrophysics* 392 (Sept. 2002), pp. 807–816. DOI: 10.1051/0004-6361:20020994 (cit. on pp. 70, 71).

[75] M. Pohlen and I. Trujillo. “The structure of galactic disks. Studying late-type spiral galaxies using SDSS”. In: *Astronomy & Astrophysics* 454 (Aug. 2006), pp. 759–772. DOI: 10.1051/0004-6361:20064883. eprint: astro-ph/0603682 (cit. on pp. 70–73, 79).

[76] P. J. Quinn, L. Hernquist, and D. P. Fullagar. “Heating of galactic disks by mergers”. In: *The Astrophysical Journal* 403 (Jan. 1993), pp. 74–93. DOI: 10.1086/172184 (cit. on p. 23).

[77] M. Romero-Gómez, J. J. Masdemont, E. Athanassoula, et al. “The origin of rR_1 ring structures in barred galaxies”. In: *Astronomy & Astrophysics* 453 (July 2006), pp. 39–45. DOI: 10.1051/0004-6361:20054653. eprint: astro-ph/0603124 (cit. on p. 23).

[78] R. Roškar, V. P. Debattista, T. R. Quinn, et al. “Riding the Spiral Waves: Implications of Stellar Migration for the Properties of Galactic Disks”. In: *The Astrophysical Journal Letters* 684, L79 (Sept. 2008), p. L79. DOI: 10.1086/592231. arXiv: 0808.0206 (cit. on p. 54).

[79] R. Roškar, V. P. Debattista, G. S. Stinson, et al. “Beyond Inside-Out Growth: Formation and Evolution of Disk Outskirts”. In: *The Astrophysical Journal Letters* 675, L65 (Mar. 2008), p. L65. DOI: 10.1086/586734. arXiv: 0710.5523 (cit. on pp. 54, 72).

[80] J. Schaye. “Star Formation Thresholds and Galaxy Edges: Why and Where”. In: *The Astrophysical Journal* 609 (July 2004), pp. 667–682. DOI: 10.1086/421232. eprint: astro-ph/0205125 (cit. on p. 72).

[81] J. A. Sellwood and J. J. Binney. “Radial mixing in galactic discs”. In: *Monthly Notices of the Royal Astronomical Society* 336 (Nov. 2002), pp. 785–796. DOI: 10.1046/j.1365-8711.2002.05806.x. eprint: astro-ph/0203510 (cit. on p. 58).

[82] J. L. Sérsic. *Atlas de galaxias australes*. 1968 (cit. on p. 68).

[83] M. A. Shaw and G. Gilmore. “The luminosity distributions of edge-on spiral galaxies. I - A two-dimensional model and its application to NGC 891 and 4565”. In: *Monthly Notices of the Royal Astronomical Society* 237 (Apr. 1989), pp. 903–927. DOI: 10.1093/mnras/237.4.903 (cit. on p. 68).

[84] E. Silva-Villa and S. S. Larsen. “The relation between surface star formation rate density and spiral arms in NGC 5236 (M 83)”. In: *Astronomy & Astrophysics* 537, A145 (Jan. 2012), A145. DOI: 10.1051/0004-6361/201117432. arXiv: 1111.1249 (cit. on p. 16).

[85] F. Simien and G. de Vaucouleurs. “Systematics of bulge-to-disk ratios”. In: *The Astrophysical Journal* 302 (Mar. 1986), pp. 564–578. DOI: 10.1086/164015 (cit. on p. 21).

[86] O. N. Snaith, M. Haywood, P. Di Matteo, et al. “The Dominant Epoch of Star Formation in the Milky Way Formed the Thick Disk”. In: *The Astrophysical Journal Letters* 781, L31 (Feb. 2014), p. L31. DOI: 10.1088/2041-8205/781/2/L31. arXiv: 1401.1835 (cit. on p. 23).

[87] V. Springel, T. Di Matteo, and L. Hernquist. “Modelling feedback from stars and black holes in galaxy mergers”. In: *Monthly Notices of the Royal Astronomical Society* 361 (Aug. 2005), pp. 776–794. DOI: 10.1111/j.1365-2966.2005.09238.x. eprint: astro-ph/0411108 (cit. on p. 48).

[88] V. Springel and L. Hernquist. “Cosmological smoothed particle hydrodynamics simulations: the entropy equation”. In: *Monthly Notices of the Royal Astronomical Society* 333 (July 2002), pp. 649–664. DOI: 10.1046/j.1365-8711.2002.05445.x. eprint: astro-ph/0111016 (cit. on p. 60).

[89] V. Springel and L. Hernquist. “Formation of a Spiral Galaxy in a Major Merger”. In: *The Astrophysical Journal Letters* 622 (Mar. 2005), pp. L9–L12. DOI: 10.1086/429486. eprint: astro-ph/0411379 (cit. on p. 12).

[90] V. Springel, N. Yoshida, and S. D. M. White. “GADGET: a code for collisionless and gasdynamical cosmological simulations”. In: *New Astronomy* 6 (Apr. 2001), pp. 79–117. DOI: 10.1016/S1384-1076(01)00042-2. eprint: astro-ph/0003162 (cit. on p. 60).

[91] I. Strateva, Ž. Ivezić, G. R. Knapp, et al. “Color Separation of Galaxy Types in the Sloan Digital Sky Survey Imaging Data”. In: *The Astrophysical Journal* 122 (Oct. 2001), pp. 1861–1874. DOI: 10.1086/323301. eprint: astro-ph/0107201 (cit. on p. 17).

[92] A. Toomre. “Mergers and Some Consequences”. In: *Evolution of Galaxies and Stellar Populations*. Ed. by B. M. Tinsley and R. B. G. Larson D. Campbell. 1977, p. 401 (cit. on p. 18).

[93] A. Toomre and J. Toomre. “Galactic Bridges and Tails”. In: *The Astrophysical Journal* 178 (Dec. 1972), pp. 623–666. DOI: 10.1086/151823 (cit. on p. 12).

[94] S. Tremaine and M. D. Weinberg. “A kinematic method for measuring the pattern speed of barred galaxies”. In: *The Astrophysical Journal Letters* 282 (July 1984), pp. L5–L7. DOI: 10.1086/184292 (cit. on pp. 59, 61).

[95] P. C. van der Kruit. “Optical surface photometry of eight spiral galaxies studied in Westerbork”. In: *Astronomy & Astrophysics Supplement Series* 38 (Oct. 1979), pp. 15–38 (cit. on p. 70).

[96] P. C. van der Kruit and L. Searle. “Surface photometry of edge-on spiral galaxies. I - A model for the three-dimensional distribution of light in galactic disks.” In: *Astronomy & Astrophysics* 95 (Feb. 1981), pp. 105–115 (cit. on p. 70).

[97] T. K. Wyder, D. C. Martin, D. Schiminovich, et al. “The UV-Optical Galaxy Color-Magnitude Diagram. I. Basic Properties”. In: *The Astrophysical Journal Supplement Series* 173 (Dec. 2007), pp. 293–314. DOI: 10.1086/521402. arXiv: 0706.3938 (cit. on pp. 17, 18).

[98] P. Yoachim and J. J. Dalcanton. “Structural Parameters of Thin and Thick Disks in Edge-on Disk Galaxies”. In: *Astrpohysical Journal* 131 (Jan. 2006), pp. 226–249. DOI: 10.1086/497970. eprint: astro-ph/0508460 (cit. on p. 23).

[99] P. Yoachim, R. Roškar, and V. P. Debattista. “Integral Field Unit Spectroscopy of the Stellar Disk Truncation Region of NGC 6155”. In: *The Astrophysical Journal Letters* 716 (June 2010), pp. L4–L8. DOI: 10.1088/2041-8205/716/1/L4. arXiv: 1005.0851 (cit. on p. 72).

[100] P. Yoachim, R. Roškar, and V. P. Debattista. “Spatially Resolved Spectroscopic Star Formation Histories of nearby Disks: Hints of Stellar Migration”. In: *The Astrophysical Journal* 752, 97 (June 2012), p. 97. DOI: 10.1088/0004-637X/752/2/97. arXiv: 1204.0026 (cit. on p. 72).

[101] Y. Yoshii and J. Sommer-Larsen. “On the formation of exponential discs”. In: *Monthly Notices of the Royal Astronomical Society* 236 (Feb. 1989), pp. 779–799. DOI: 10.1093/mnras/236.4.779 (cit. on p. 70).

[102] J. D. Younger, T. J. Cox, A. C. Seth, et al. “Antitruncated Stellar Disks via Minor Mergers”. In: *The Astrophysical Journal* 670 (Nov. 2007), pp. 269–278. DOI: 10.1086/521976. arXiv: 0707.4481 (cit. on p. 72).

Appendix

A. Merging morphology

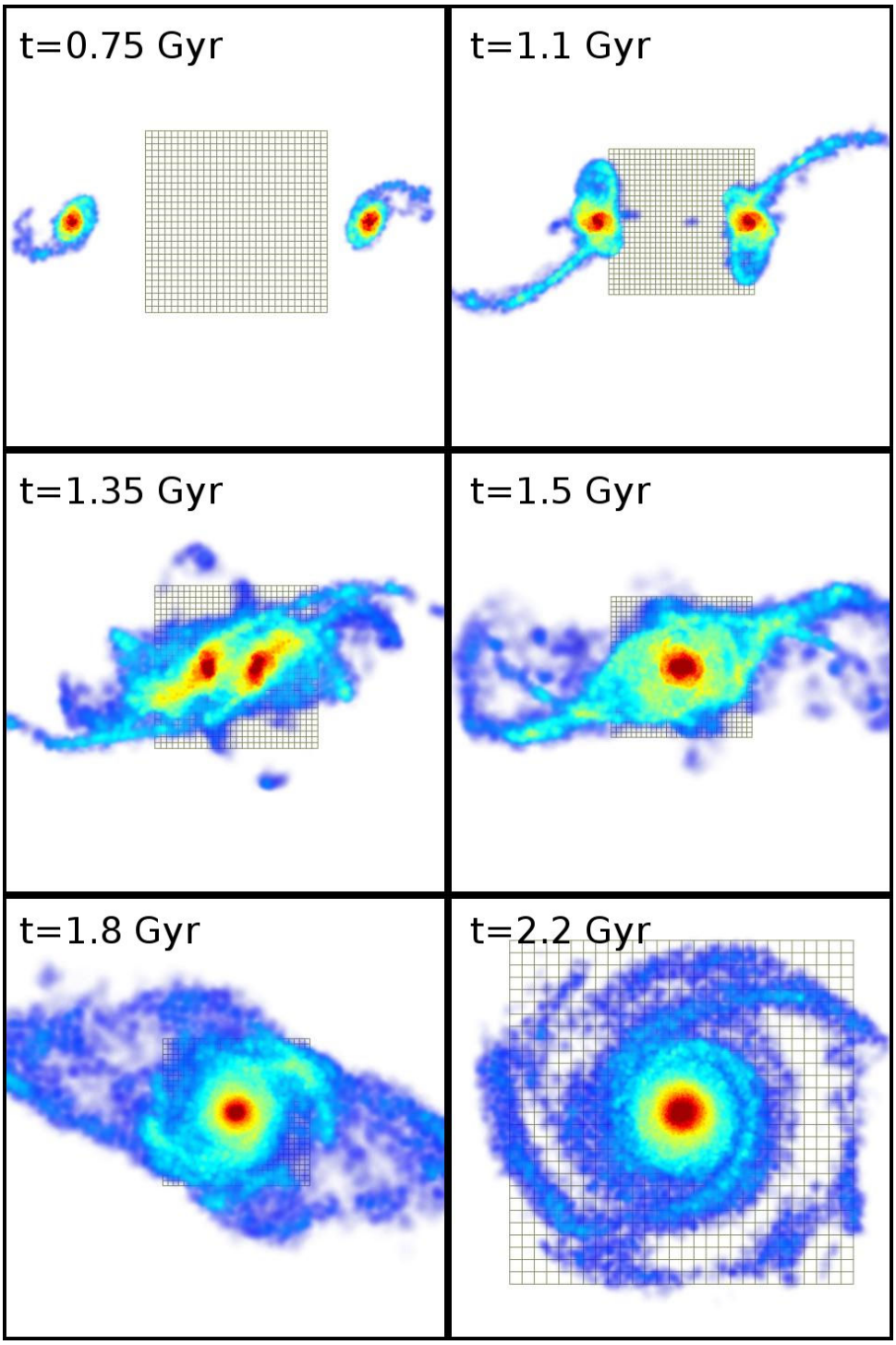

Figure A.33.: Evolution with time of the merging seen face-on for the stars of $mdf732$. The color coding is different in each pannel, as well as the scale, to best suit the morphology of the system. The grid is made of 1x1 kpc squares, with a total size of 28x28 kpc.

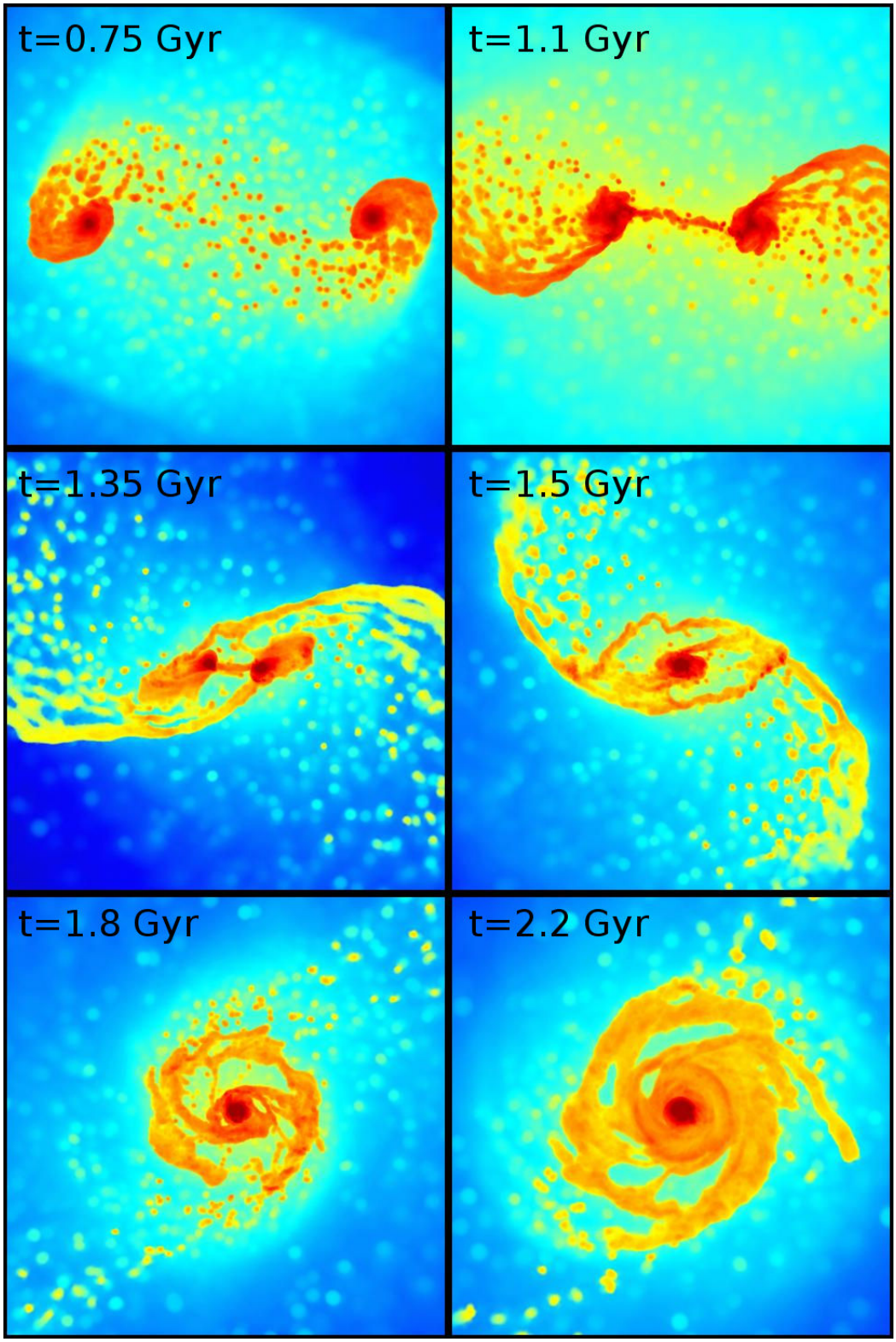

Figure A.34.: Same as figure A.33 but for the gas.

B. How to compute the circularity parameter ϵ

The circularity parameter of a particle is its z-component angular momentum, normalized by the angular momentum of the circular orbit having the particle's energy: $\epsilon = J_z/J_{circ}$. The difficult part is thus to find this circular orbit, to be able to derive its angular momentum. The first step is to derive the energy of the stellar particle, which can be expressed as:

$$E_p = E_{kin} + \phi \tag{A.1}$$

where E_{kin} is the kinetic energy of the particle and ϕ its gravitational potential (derived using $gyrfalcON$).
We now need to derive the energy of a circular orbit as a function of its radius r, to be able to find which circular orbit has the same energy as the particle. Using the circular velocity as a function of the radius (computed in the spherical approximation) it is easy to derive the kinetical energy of a circular orbit. Nevertheless, the computation of the gravitational potential of an orbit is less straightforward. In the spherical approximation, the total gravitational potential at radius r can be seen as the sum of the potentials of spherical shells with a radius smaller than r, and the shells with a radius greater than r. Thus, using Newton's theorems, one finds (J. Binney and Tremaine, 2008):

$$\phi(r) = -\frac{G}{r}\int_0^r dM(r') - G\int_r^\infty \frac{dM(r')}{r'} \tag{A.2}$$

where $dM(r) = 4\pi\rho(r)r^2dr$ represents the mass of a shell. For a discrete system of particles with radii r_i and masses m_i, this gives:

$$\phi(r) = -\frac{G}{r}\sum_{r_i<r} m_i - G\sum_{r_i>r}\frac{m_i}{r_i} \tag{A.3}$$

Computing the gravitational potential ϕ (and the kinetic energy) at several radii, we can get the energy of circular orbits as a function of their radius. We then only need to find the radius r_{circ} at which the circular energy takes the value of the particle's energy, which can be done by interpolating the circular radius as a function of the circular energy $r_{circ} = f_{interpol}(E_{circ})$, and solving $r_{circ} = f_{interpol}(E_{particle})$. The corresponding circular angular momentum is then $J_{circ} = r_{circ} * v_{circ}(r_{circ})$.

C. How to compute the guiding radius

The guiding radius of a particle is the radius at which it would orbit, if it had the same angular momentum but with a perfectly circular orbit. Therefore, the first step is to derive the angular momentum L_z of the particle along the z axis

since the circular orbit is in the galactic plane (xy plane). We then need to find which circular orbit has the same angular momentum. To do this, the reasoning is similar to Appendix B, but more straightforward since we only need the angular momentum of a circular orbit, instead of its energy. Using again the circular velocity as a function of the radius, we easily derive the circular angular momentum as a function of the radius. All we have to do now is to find at which radius the circular angular momentum takes the value of the particle angular momentum, which is the guiding radius. Using an interpolation of the circular radius as a function of the circular angular momentum, the guiding radius R_G of a particle with angular momentum L_z can be directly obtained by solving $R_G = f_{interpol}(L_z)$.

D. Bar evolution over time

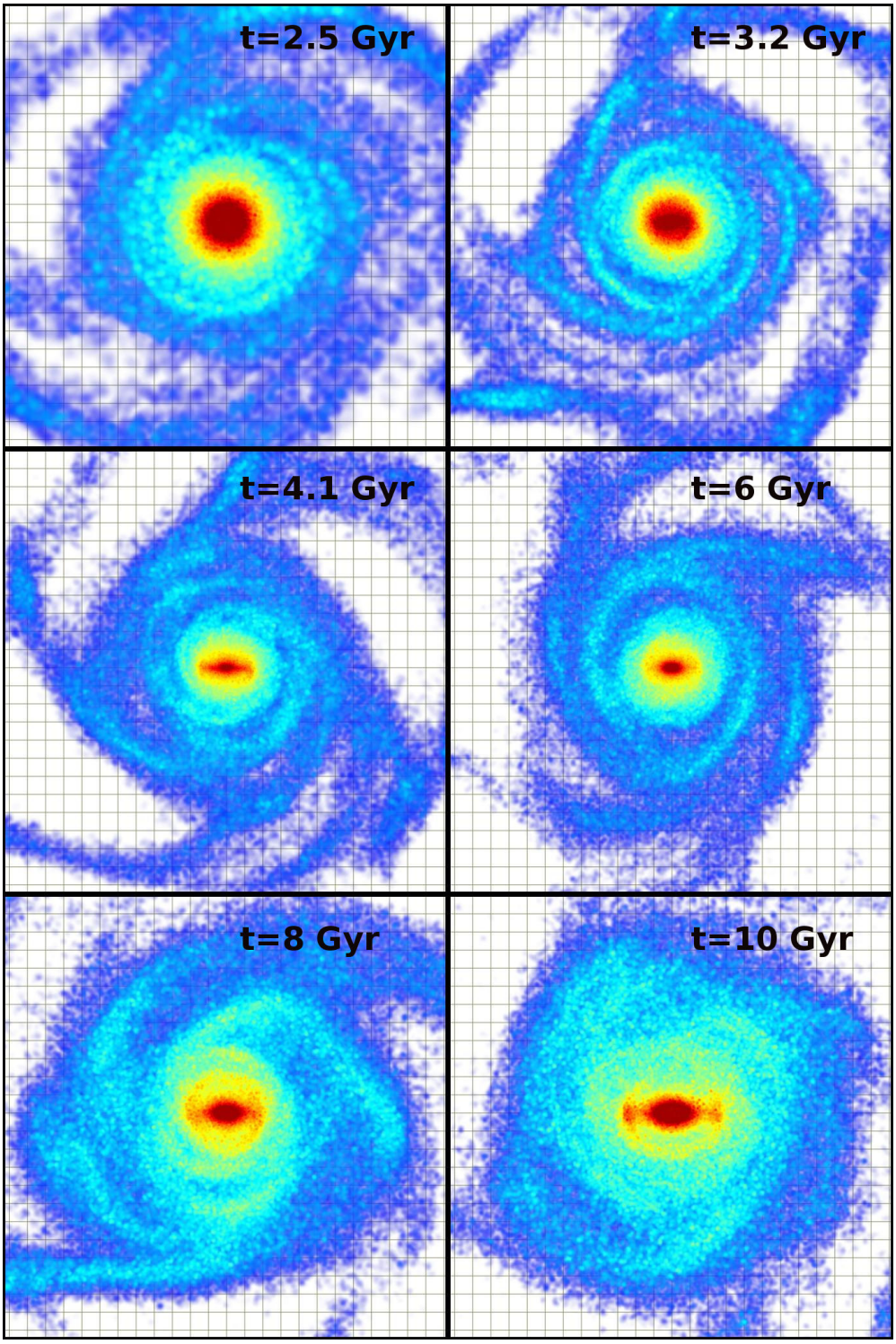

Figure A.35.: Evolution with time of the bar seen face-on for $mdf732$. The color coding is different in each pannel, it has been chosen to best suit the morphology of the bar. The grid is made of 1x1 kpc squares, and each pannel has the same size in kpc.

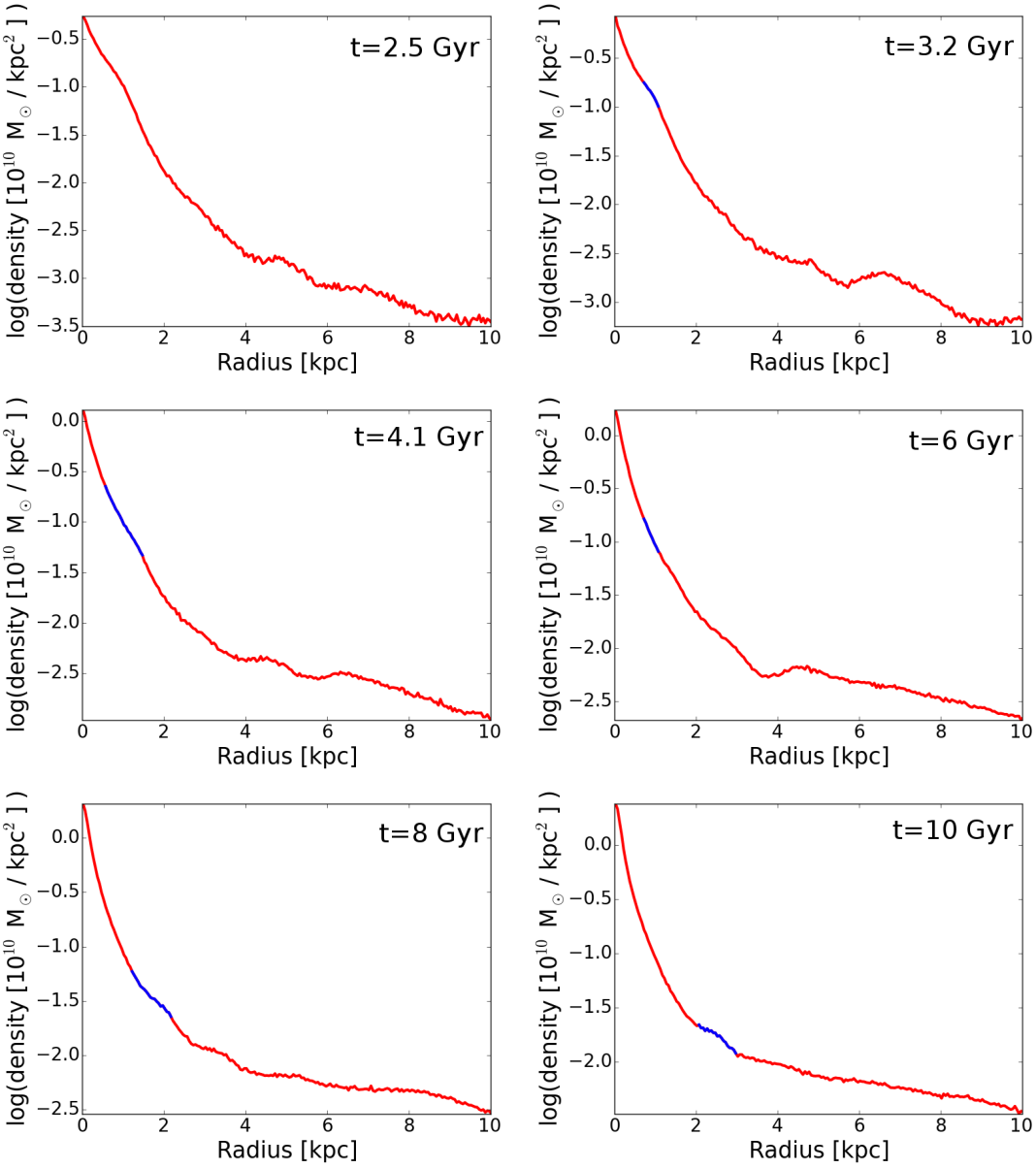

Figure A.36.: Evolution with time of the radial density profile in the central region for $mdf732$. The blue part corresponds to the region visually identified on the face-on images as the end of the bar.

E. Computation of the spin parameter λ

E.1. Whole System

I recall here the definition I used for λ in Paper III (section 4.4.2.1):

$$\lambda = \frac{J|E|^{1/2}}{GM^{5/2}} \tag{A.4}$$

where J is the total angular momentum, E the total energy, G the gravitational constant and M the total mass. While M and J are straightforward to derive, the computation of the total energy is slightly more complicated. It can be expressed as:

$$E = E_{kin} + E_{gp} + U \tag{A.5}$$

where E_{kin} is the kinetical energy, E_{gp} the gravitational potential energy, and U the gas internal energy. E_{kin} is also straightforward to compute, while U can be directly derived from $gyrfalcON$, and has a very weak contribution. On the other hand, the computation of the gravitational potential energy is more difficult, and is not only the sum of the gravitational potential of every particle (which can be derived using $gyrfalcON$ as well). There is an analytic solution for this, which is demonstrated in J. Binney and Tremaine (2008):

$$E_{gp} = \frac{1}{2}\int \rho(r)\phi(r)d^3r \tag{A.6}$$

where ρ is the density distribution, and ϕ the gravitational potential. This gives for a discrete system of particles of masses and gravitational potentials m_i and ϕ_i:

$$E_{gp} = \frac{1}{2}\sum_{i=1}^{N} \phi_i m_i \tag{A.7}$$

This $\frac{1}{2}$ fraction is easy to understand. The gravitational potential energy can be seen as the sum of all gravitational interactions between all the particles. By summing all the gravitational potentials for all the particles, I will count the interactions twice. Indeed in an interaction involving only a particle A and a particle B, the gravitational potential of A is the gravitational force between A and B, and so is the potential of B. By adding both potentials, I will end up counting the gravitational interaction twice. Therefore a factor $\frac{1}{2}$ is necessary to sum the interactions only once.
Using $gyrfalcON$, we can derive E_{gp} from equation A.7, and thus the total energy and λ.

E.2. One component

In the discussion of Paper III, I computed λ for the dark and the baryonic matter separately. While the computation of the total angular momentum, mass and kinetic energy is still the same (we just sum over the corresponding particles), the gravitational potential energy cannot be computed the same way. Indeed,

by computing the gravitational potential of the particles, all the interactions are taken into account, including the interactions between dark and baryonic matter. Therefore, if we sum over the dark matter particles only (to get λ_{DM}), the interactions between dark matter particles will be counted twice (see previous section), but not the interactions with the baryonic matter. Therefore the $\frac{1}{2}$ factor does not apply here, the result is more complicated than that.

The definition of the gravitational potential energy of the whole system can be written (Appendix E.1):

$$W_{tot} = \frac{1}{2} \int \rho(r)\phi(r)d^3r \tag{A.8}$$

where $\rho(r)$ and $\phi(r)$ are the density distribution and the gravitational potential, and can be written for a system with two components (1 and 2):

$$\begin{aligned} \rho(r) &= \rho_1(r) + \rho_2(r) \\ \phi(r) &= \phi_1(r) + \phi_2(r) \end{aligned} \tag{A.9}$$

which gives in A.8:

$$\begin{aligned} W_{tot} &= \frac{1}{2} \int d^3r \rho_1(r)\phi_1(r) + \rho_2(r)\phi_2(r) + \rho_1(r)\phi_2(r) + \rho_2(r)\phi_1(r) \\ W_{tot} &= W_{1,isolated} + W_{2,isolated} + \int \rho_1(r)\phi_2(r)d^3r \end{aligned} \tag{A.10}$$

since it can easily be shown that $\int \rho_1(r)\phi_2(r)d^3r = \int \rho_2(r)\phi_1(r)d^3r$ (using $\phi = -\frac{G}{R}\int \rho(r)d^3r$), and $\frac{1}{2}\int \rho_1(r)\phi_1(r)d^3r$ is the gravitational potential energy of the component 1 if it was isolated ($W_{1,isolated}$).

The next step is to compute the term $\int \rho_1(r)\phi_2(r)d^3r$. To do that, we will switch to discrete expressions since we are dealing with N-body models. In discrete terms:

$$\int \rho\phi d^3r = -\sum_{i=1}^{N} \sum_{\substack{j=1 \\ j\neq i}}^{N} G\frac{m_i m_j}{r_j - r_i} \tag{A.11}$$

where m_i, r_i are the masses and radii of the particles. Therefore, numbering the particles from 1 to N_1 for the component 1, and from $N_1 + 1$ to N_2 for the component 2:

$$\int \rho_1\phi_2 d^3r = -\sum_{i=1}^{N_1} \sum_{j=N_1+1}^{N_2} G\frac{m_i m_j}{r_j - r_i} \tag{A.12}$$

After playing around with the indexes, one gets:

$$\int \rho_1 \phi_2 d^3r = -\sum_{i=1}^{N_1} \sum_{j=i+1}^{N_2} G\frac{m_i m_j}{r_j - r_i} - \sum_{i=1}^{N_1} \sum_{j=1}^{i-1} G\frac{m_i m_j}{r_j - r_i} + 2W_{1,isolated} \tag{A.13}$$

The first term takes into account all the interactions of the component 1 with the system without counting them twice, therefore it is the gravitational potential energy of the component 1:

$$W_1 = -\sum_{i=1}^{N_1} \sum_{j=i+1}^{N_2} G\frac{m_i m_j}{r_j - r_i} \tag{A.14}$$

It is easy to show that the second term in equation A.13 is the gravitational potential energy of the component 1 if it was isolated, therefore:

$$\int \rho_1 \phi_2 d^3r = W_1 - W_{1,isolated} \tag{A.15}$$

So that by using equation A.10, one finally finds:

$$\begin{aligned} W_1 &= W_{tot} - W_{2,isolated} \\ W_2 &= W_{tot} - W_{1,isolated} \end{aligned} \tag{A.16}$$

This result is coherent: the total of the interactions of the component 1 with the whole system is the sum of all the interactions in the system (counted once), from which we substract the self-interactions of the component 2.

To compute λ for the dark (baryonic) matter only, I thus need to compute the gravitational potential energy of the whole system, and substract the gravitational potential energy of the isolated baryonic (dark) matter.

F. Evolution of the radial density profile from type III to type II

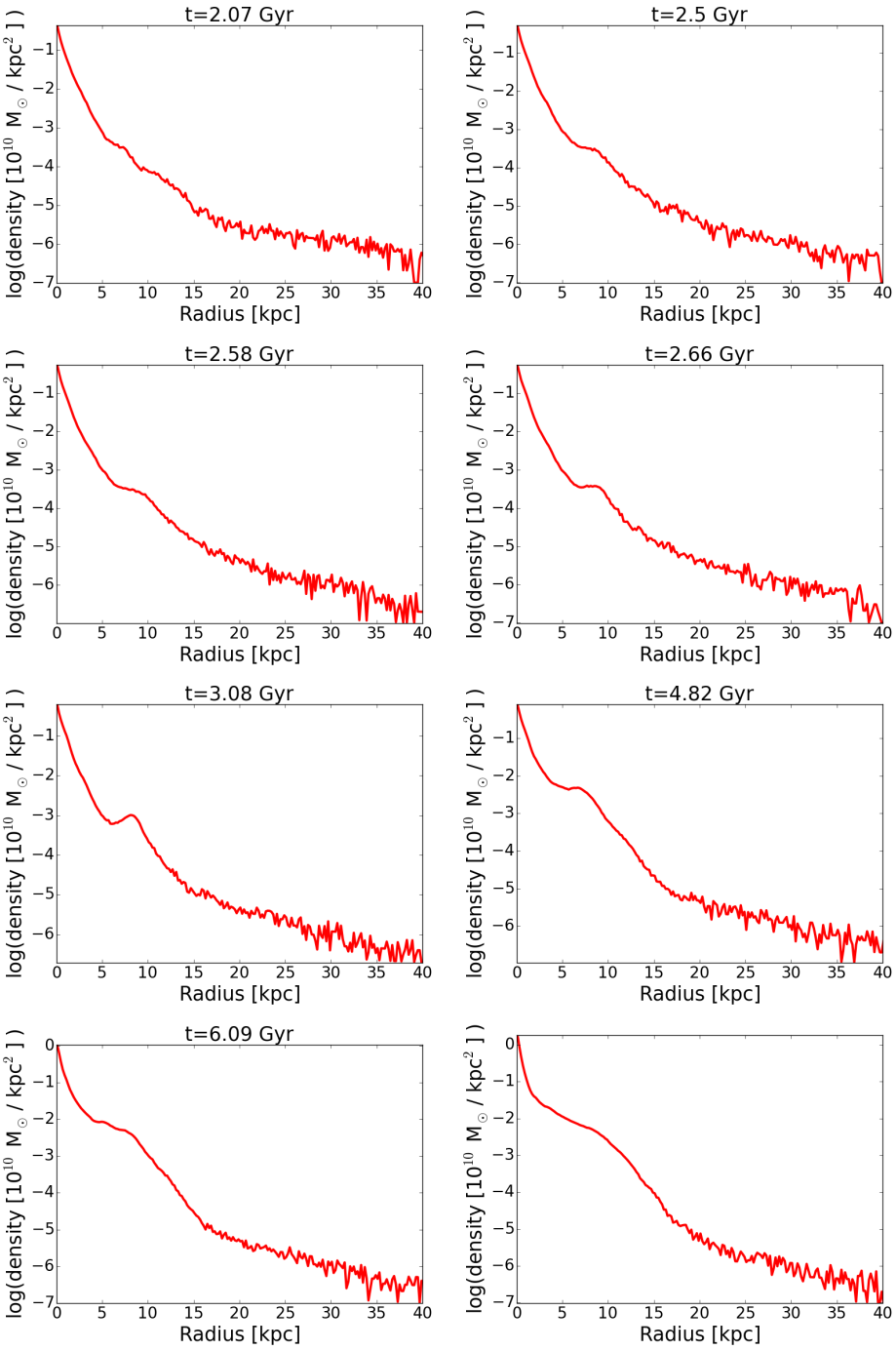

Figure A.37.: Radial density profiles as a function of time showing the transition from a type III to a type II disc. The top left pannel shows a clear type III with a break around 16 kpc, while the bottom right pannel shows a type II disc with a break around 10 kpc.

Résumé

Cette thèse explore la formation, l'évolution et la structure des galaxies spirales à l'aide de simulations, en mettant l'accent sur le disque. Après avoir rappelé les propriétés générales des galaxies à disque, je présente nos simulations hydrodynamiques à N-corps mettant en scène une fusion majeure entre deux galaxies à disque à haut redshift, chacune en possession d'un halo de gaz chaud. Les disques des progéniteurs sont détruits par la fusion, et un disque étendu se forme dans la galaxie ainsi obtenue à partir d'étoiles nouvellement formées, la formation stellaire étant alimentée par le halo de gaz. A la fin de la simulation, la nouvelle galaxie montre toutes les propriétés d'une galaxie spirale, prouvant pour la première fois avec des simulations comment une galaxie de type tardif peut être créée par une fusion majeure. Après avoir présenté l'article correspondant (Athanassoula, Rodionov, Peschken, et al. 2016) et décrit notre échantillon de simulations, je me concentre sur la période de la fusion. La fusion n'est pas instantanée, et déterminer quand elle commence et finit n'est pas évident. Je montre ici plusieurs moyens de caractériser cette période, ainsi que le début de la formation du disque. Le disque se développe ensuite grâce aux étoiles nouvellement formées, et beaucoup de ces étoiles migrent radialement, se déplaçant vers l'intérieur ou l'extérieur après leur naissance et jusqu'à la fin de la simulation. J'analyse cette migration, ainsi que sa probable origine liée aux orbites résonantes. Je présente ensuite une étude sur la mesure de la rotation angulaire de la barre en utilisant la méthode de Tremaine-Weinberg, et vérifie qu'elle fonctionne dans le cas des disques épais.

La seconde partie de cette thèse se concentre sur les profils de densité radiaux des galaxies formées dans nos simulations. Dans un premier temps sont présentées les propriétés générales des profils de brillance de surface dans les galaxies à disque, ainsi que leur intérêt pour l'étude de la structure galactique. Ces profils peuvent en effet être fittés pour obtenir un certain nombre de propriétés sur les galaxies, ce qui permet de les caractériser et les comparer. Une alternative à ces profils à une dimension est l'analyse bi-dimensionnelle de la distribution de densité, que je présente rapidement avec les codes GALFIT et BUDDA appliqués à nos simulations, avant de passer aux profils de densité radiaux. Je décris comment obtenir et fitter ces profils, ainsi que les difficultés rencontrées. Ces fits permettent d'étudier les propriétés de la barre et des différents bulbes dans nos

galaxies tels que les bulbes classique et discy, mais donnent aussi des informations sur le disque, qui est le sujet principal de cette thèse. Les profils du disque sont de type II à la fin des simulations, et il est intéressant de chercher à comprendre ce qui produit ce profil spécifique, à l'aide de la distribution de densité du gaz et du taux de formation stellaire. Les longueurs d'échelle obtenues avec les fits du disque prennent des valeurs très différentes d'une simulation à une autre, et j'explique ces différences dans un article soumis en utilisant le moment angulaire total dans nos simulations. Dans un autre article (en préparation), nous analysons l'évolution du profil du disque au cours du temps et trouvons des profils de type III peu après la fusion. Nous avons des simulations de galaxies isolées, et certaines d'entre elles montrent également un disque de type III, mais cette fois à la fin de la simulation. Je compare ensuite toutes les propriétés obtenues par mes fits aux observations, pour vérifier la fiabilité de nos résultats. Jusqu'à présent l'analyse faite sur la distribution de densité se concentrait sur le disque fin, mais nos galaxies montrent aussi un disque épais, qui est dominant à une certaine hauteur du plan galactique. Je présente une étude rapide du disque épais et de son profil de densité radial, ainsi qu'une comparaison avec le disque fin.

Abstract

This thesis explores the formation, evolution and structure of spiral galaxies using simulations, with an emphasis on the disc component. After reminding the general properties of disc galaxies, I present our N-body/SPH simulations involving a major merger between two disc galaxies at high redshift, both in possession of a hot gaseous halo. The discs of the progenitors are destroyed by the merger, and a well-extended disc forms in the remnant galaxy from newly born stars, star formation being fuelled by the gaseous halo. By the end of the simulation, the remnant galaxy shows all the properties of a spiral galaxy, evidencing in details how a late-type galaxy can be created from a major merger. After presenting the corresponding paper (Athanassoula, Rodionov, Peschken, et al., 2016) and describing our sample of simulations, I focus on the merging period. The merging is not instataneous, and knowing when it starts and ends is not straightforward. I show here different ways of characterizing this period, as well as the start of the disc formation. The disc then grows from newly born stars, and many of these stars show radial migration, moving inwards or outwards after their birth until the end of the simulation. I analyze this migration, as well as its probable orbital resonance origin. I then present a study on the measurement of the bar pattern speed using the Tremaine-Weinberg method, and test its robustness in thick discs.

The second part of this thesis focuses on the radial density profiles of the remnant galaxy in our simulations. First, general properties of surface brightness profiles in disc galaxies are introduced, as well as their interest for the study of the galactic structure. These profiles can indeed be fitted to derive a number of properties about the galaxies, which allows to characterize and compare them. An alternative to these one-dimensional profiles is the two-dimensional analysis of the density distribution, which I present shortly with the codes GALFIT and BUDDA applied to our simulations, before moving to radial density profiles.
I describe how to derive and fit those profiles, as well as the difficulties encountered. These fits allow to study the properties of the bar and of the different bulges in our galaxies such as the classical and the discy bulges, but also provide information about the disc, which is the main topic of this thesis. The disc profiles are downbending (type II) at the end of the simulations, and it can be interesting to investigate what produces this specific shape, with the help of the gaseous density distribution and the star formation rate. The scalelengths derived from the fit of the disc show a wide range of values from one simulation to another, and I explain these differences in a submitted paper using the total angular momentum in the simulations. In a further paper (in preparation) we analyze the evolution of the disc profile over time and find upbending (type III) profiles soon after the merging. We also ran simulations of isolated galaxies, and some of them show an upbending profile as well, but this time at the end of the simulation. I then compare all the properties derived from my fits to observations, to check the reliability of our results.
So far the analysis made on the density distribution was focusing on the thin disc, but our galaxies also show a thick disc, which is dominant at a certain height from the galactic plane. I present a short study of the thick disc and its radial density profile, as well as its comparison to the thin disc.